REINHOLD HETZEL

Experimental studies on electroluminescence and its driving parameters of GaN-based and AlGaInP-based light emitting diodes

DOCTORAL THESIS

For obtaining the academic degree of

Doktor der technischen Wissenschaften

Doctoral Programme of Technical Sciences

Technical Physics

Graz University of Technology

Supervisor:

Ao.Univ.-Prof. Dipl.-Ing. Dr.techn. Günther Leising

Institute of Solid State Physics

Graz, June 2014

Theories,

Models,

Methods,

Approaches,

Assumptions,

Results

and Findings

The Magnificent Seven
Damien Hirst (British, born 1965)
Lettered ping pong balls - designed to promote the show conceived by Damien Hirst at the Gagosian Gallery New York, in 2000.

To Ines

EIDESSTATTLICHE ERKLÄRUNG

AFFIDAVIT

Ich erkläre an Eides statt, dass ich die vorliegende Arbeit selbstständig verfasst, andere als die angegebenen Quellen/Hilfsmittel nicht benutzt, und die den benutzten Quellen wörtlich und inhaltlich entnommenen Stellen als solche kenntlich gemacht habe. Das in TUGRAZonline hochgeladene Textdokument ist mit der vorliegenden Dissertation identisch.

I declare that I have authored this thesis independently, that I have not used other than the declared sources/resources, and that I have explicitly indicated all material which has been quoted either literally or by content from the sources used. The text document uploaded to TUGRAZonline is identical to the present doctoral dissertation.

Datum / Date

Unterschrift / Signature

Preamble

During the PhD period specific segments occurring in this thesis was published in international papers. The leading author of the published papers is always the author of this thesis. Parts of the text of the publications were implemented in the contents of this thesis, whereas at the beginning of each chapter a mark referring to the particular publication is made. The originally published publications are attached in the appendix of this thesis. The copyright clearance for each publication was obtained from the respective publisher. A publication list including the link to the chapter in which the publication was implemented is established below. Further the contribution of each additional author is enclosed.

List of publications

1. **Current density impact on the emission behavior of GaN-based blue emitting LEDs in the temperature range of 4.2-400 K**, Authors: Reinhold Hetzel and Günther Leising, Phys. Status Solidi A, 1-8 (2014), DOI 10.1002/pssa.201431046

    - The accepted version of the paper can be found in chapter 6. Reinhold Hetzel was the leading author and writer of the entire text. Günther Leising was supervisor of the project, did proof reading and supported the understanding and interpretation of the gained results.

2. **Tunable natural light realized by phosphor-innovation light-emitting-diode technology**, Authors: Reinhold Hetzel, Stefan Tasch, and Günther Leising, Elektrotechnik & Informationstechnik, 1-6 (2012), DOI 10.1007/s00502-012-0105-1

    - Parts of the paper are implemented in chapter 1.1 and 3.2. Reinhold Hetzel was the leading author and writer of the entire text. Günther Leising was supervisor of the project, did proof reading and supported the understanding and interpretation of the gained results. Stefan Tasch did proof reading and inserted ideas to improve the discussion.

3. **Spectral Behavior and Coherence Length of GaN-, and AlGaInP-based Light-Emitting-Diodes**, Authors: Reinhold Hetzel and Günther Leising, Proc. SPIE 9003, Light-Emitting Diodes: Materials, Devices, and Applications for Solid State Lighting XVIII, 900318 (2014), DOI 10.1117/12.2037875

    - Parts of the paper are implemented in chapter 9. Reinhold Hetzel was the leading author and writer of the entire text. Günther Leising was supervisor of the project, did proof reading and supported the understanding and interpretation of the gained results.

4. **Methods for Obtaining the Junction Temperature of LEDs**, Authors: Reinhold Hetzel and Günther Leising, Proceeding LED Professional Symposium, 208-215 (2013)

    - Parts of the paper are implemented in chapter 5. Reinhold Hetzel was the leading author and writer of the entire text. Günther Leising was supervisor of the project, did proof reading and supported the understanding and interpretation of the gained results.

5. Patent: **Anordnung zum Emittieren von in seiner Farbtemperatur variierbarem weissem Licht**, Authors: Reinhold Hetzel and Günther Leising, Reference number: 10 2013 109 651.4, Date of submission: September 4th 2013

    - The English summary of the patent can be found in chapter 11.

6. Patent in preparation: **Verfahren zum Betreiben einer zum Emittieren von in seiner Helligkeit und Farbtemperatur einstellbarem Licht eingerichteten Anordnung**, Authors : Reinhold Hetzel, Hans Hoschopf and Günther Leising, Date of submission (expected): July 2014

    - The English summary of the patent can be found in chapter 8.

Abstract

Light emitting diodes (LEDs) have enormous potential to provide high quality of light combining it with a significant reduction of the energy consumption in general lighting applications. Much longer lifetimes and higher efficiencies made incandescent as well as fluorescent lighting systems becoming a dying segment. However, there are still many remaining questions concerning LEDs reliability and performance issues. In particular, the understanding of the emission processes occurring in solid state lighting, which govern lifetime and efficiency, are still not sufficiently developed.

In the present thesis a completely calibrated measurement setup was evolved which allows investigating the emission response with respect to the pn-junction temperature. A careful distinction between thermal as well as current density impacts is achieved by operating LEDs under short forward voltage pulses of 500 ns. With the help of an additional development which extended the temperature range to very low values, specific radiative recombination mechanisms were accessible.

The electroluminescence spectra of blue emitting GaN-based LEDs as well as red emitting AlGaInP-based LEDs in the temperature region between 4.2 K and 400 K were investigated. GaN-based LEDs show a strong band filling effect in the elevated temperature region as well as a strong exciton localization which dominates the radiative recombination at low temperatures. The emission behavior of AlGaInP-based LEDs is strongly temperature dependent, however stable in terms of the injected current density. Low temperature investigations brought forward the coupling of free excitons to impurity states in this semiconductor alloy.

Analytical tools like focused ion beam (FIB) as well as energy dispersive X-ray spectroscopy (EDX) were used to determine the structure of the LEDs. The location of the pn-junction was ascertained by electron beam induced current (EBIC) measurements.

Coherence length of the two types of LEDs was determined via a Fabry-Perot interference setup and the validity and limitations of the conventional determination method from the emission linewidth and lineshape are discussed.

Also present in this thesis is a method which allows to derive photoluminescence properties like quantum yield as well as the fluorescence lifetime of color conversion materials which are used for white light LED systems.

Kurzfassung

Licht emittierende Dioden (LEDs) haben ein enormes Potential den Energieverbrauch in der Allgemeinbeleuchtung drastisch zu reduzieren. Ausschlaggebend dafür sind, im Vergleich zu herkömmlichen Leuchtmitteln wie Glühbirnen oder Energiesparlampen, die bedeuten höhere Effizienz als auch die signifikant längere Lebensdauer. Allerdings sind im Bezug auf Leistung und Beständigkeit noch einige Fragen ungeklärt, vor allem bezüglich des Verständnisses der strahlenden Rekombination.

In dieser Dissertation wurde ein vollkommen kalibriertes Messsystem entwickelt, welches erlaubt das Emissionsverhalten von LEDs in Abhängigkeit der pn-Sperrschichttemperatur zu analysieren. Eine strenge Unterscheidung zwischen Stromdichte- und Temperatureffekten wurde durch Injektion von kurzen Vorwärtsspannungspulsen mit einer Pulsbreite von 500 ns erzielt. Durch eine Weiterentwicklung dieses Messsystems ist auch eine Analyse im Kryogenik-Bereich möglich.

Das Verhalten von Elektrolumineszenz-Spektren von blau leuchtenden LEDs auf Basis von GaN und rot emittierenden LEDs auf Basis von AlGaInP wurde im Temperaturbereich von 4.2 K und 400 K analysiert. GaN LEDs zeigen ein starkes Füllen der Bänder in Abhängigkeit von der Stromdichte. Zusätzlich dominieren lokalisierte Exzitonen das Emissionsverhalten bei sehr niedrigen Temperaturen. Die, auf AlGaInP-basierenden, LEDs sind sehr instabil bezüglich der Temperatur, jedoch zeigen sie kaum eine Veränderung des Emissionsspektrums in Abhängigkeit von der Stromdichte. Tieftemperaturuntersuchungen zeigen eine starke Wechselwirkung zwischen freien Exzitonen und auftretenden Defekten im Halleiterverband.

Zur Untersuchung der jeweiligen Struktur der Proben wurden Focused Ion Beam (FIB) Aufnahmen in Kombination mit energiedispersiver Röntgenspektroskopie (EDX) herangezogen. Weiters wurde die Lage des pn-Übergangs mittels Electron Beam Induced Current (EBIC) bestimmt.

Eine Kohärenzlängenanalyse der beiden LEDs wurde mit einen Fabry-Perot Interferometer durchgeführt, wobei die konventionelle, numerische Ermittlungsmethode mit experimentell erhaltenen Daten verglichen und gegenübergestellt wurde.

Ebenfalls dargestellt in dieser Dissertation ist eine Methode zur Bestimmung von Photolumineszenz-Eigenschaften wie Quantenausbeute und Fluoreszenz-Lebensdauer von Farbkonversionspasten welche für Weiß-Licht-LED Systeme verwendet werden.

Acknowledgment

At this point I would like to take the opportunity and thank all people who contributed to this work, first of all my supervisor, Prof. Günther Leising, for his ongoing support and continuous patience as well as for the freedom that was placed into my work.
Further I want to thank the whole LUMITECH team for supporting this PhD thesis as well as for funding. Special thanks to Stefan Tasch, Alexander Rinderhofer, Friedrich Wagner, Hans Hoschopf, Manuel Schwarz, Peter Haumer, Daniel Mitrovic, Martin Wolf, Stefanie Kern, and Sonja Svetits.
Lots of thanks to all people of the institute of Solid State Physics for making this time period so diverting. In particular I want to thank Harald Kerschbaumer and Elisabeth Stern for making things going much easier and much faster. Special thanks to Robert Krauß and Martin Kornschober for building all kind of various experimental parts. Also thanks to Birgit Kunert and Lisa Ulrich for the lab support.
During most of my PhD period I was pleased to stay in the *k-room* (thanks to Roland Resel for this opportunity) where I was contemporary witness of the most stunning, sometimes quite disturbing discussions about global challenges and general scientific issues. Special thanks to the old *k-room* consisting out of Tatjana Djuric, Michael Dohr, Armin Moser, Alfred Neuhold, and Alexander Pichler as well as the newcomers Paul Christian, Andrew Jones, Christoph Lercher, Stefan Pachmajer, Christian Röthel, Katrin Unger, and Michael Zawodzki. Thank you for making this office so unique. Particularly special thanks to Armin and Christian for many Matlab problem solving supports which significantly decreased the amount of time of my data analysis.
Furthermore I want to thank Prof. Leising's group members Patrick Mayrhofer, Alexander Tovstopyat and Christian Straka for discussions. I thank Martin Faccinelli and Stefan Kirnstötter for EBIC measurements and their support for result interpretation, further Sebastian Rauch and Harald Plank of the FELMI for the FIB investigations of my samples, and Florian Lackner of the experimental physics department for providing the liquid helium.
Special thanks to David Egger and Simon Ausserlechner for encouragement during the whole period of time which includes a couple of after work drinks and literally thousands of coffees.
Finally I want to thank my whole family, in particular my parents as well as my sister Daniela, who gave me the opportunity to tread such path. This work is dedicated to Ines who is responsible for keeping me on track during the whole PhD period. Providing permanent encouragement and patience is the only reason making all of this possible. Sincerely thanks to her!

Contents

Part I.

General Overview

1. Introduction

1.1. New century of light

Parts of the introduction are taken and adapted from *Tunable natural light realized by phosphor-innovation light-emitting-diode technology* by Hetzel et al. [1]. The original work can be found in the appendix of this thesis.

The first published evidence for solid state lighting was noted by Round in 1907 where SiC crystals emitted light with different color by the appliance of an electric field [2]. Nearly 50 years later Braunstein reported in 1955 the direct radiative recombination of electron-hole pairs in several semiconductor alloys [3]. The first Light Emitting Diode (LED) which was emitting in the visible range of the electromagnetic spectrum was reported in 1962 by Nick Holonyak et al [4]. They achieved red light emission with a $Ga(As_{1-x}P_x)$ semiconductor superstructure. Since then the development of LEDs was continued and the LED technology became available in opto-couplers, alphanumeric displays and pocket calculators at the beginning of the 1970s. Since the late 1960s, the lumen per lamp efficiency for the most powerful commercially available red LEDs increased roughly by a factor of $1.5 \cdot 10^5$ [5]. During the last decade, the efficiency of the commercially offered white LEDs increased by a factor of $1.0 \cdot 10^3$ [5]. This exponential rise of the light output and the efficiency made the technology available for a large field of new applications. Amongst others, LED technology is now settled in the automotive and medical sector and is well established in the entertainment industry e.g. for large area display applications. Additionally, since LED light provides high luminous efficacies of 150 lm/W and more [6] the conventional incandescent light bulb (around 12 lm/W) gets replaced by this technology. It is expected that most of the classical light sources will be replaced by LEDs soon. Several types of semiconductor alloys being available today allow LEDs to operate at wavelengths from deep ultra violet (UV) up to the near infrared region (IR) covering the entire visible spectrum (VIS).
Major advantages like long lifetime (beyond tens of thousands of hours) and high efficiencies make LEDs more and more common in the field of general illumination for homes and offices. Furthermore, in contrast to thermally radiating light sources (tungsten bulbs, halogen lamps, etc.), LEDs offer dimming capabilities while keeping the

spectral distribution constant [7]. To benefit from the LED technology in these areas, the development of high quality white light was one of the basic challenges.
Light emitted by the sun is essential for life on earth and therefore the standards on artificial lighting systems must be quite high to compete with the natural light quality. Dynamic lighting systems enable changing individually and continuously illuminance and color temperature over the day. Therefore, a high quality dynamic lighting system emulates natural light which allows to bring specific natural light conditions, with all its amenities, into buildings. Hence, the now commonly accepted human biological clock is getting more and more important. The intrinsic period of the biological clock is about 24.2 hours long which is slightly longer than our 24 hours day. The biological clock synchronizes every day by external ”Zeitgeber” (English: ”time givers”) which are e.g. social stimulations, sleep behavior and eating habits. However, known so far, light is the most important Zeitgeber which controls the human circadian clock [8]. Once light enters the human eye sensor, photons strike light sensitive photoreceptor cells in the retina. The obtained information gets transmitted through the retinal ganglion cells (RGCs) to the human brain. This image-forming visual system contains rod and cone photoreceptor cells. For the photopic vision (color vision) three types of cones (L, M, S), for the scotopic vision (night vision) only one type of rod cells are responsible. Each human eye contains in sum around 6.5 million cones and roughly 120 million rods, respectively [9]. However, in 2001 Brainard [10] and Thapan [11] discovered a third type of photoreceptor that regulates the melatonin concentration over the day which is mainly responsible for setting the circadian rhythm. This non-image-forming system does not arise from rods or cones. The opsin-like protein melanopsin triggers the non-image-forming visual functions [12]. The circadian rhythm - also called sleep-wake cycle - controls, amongst others, the hormone level of melatonin and cortisol, the core body temperature, and the heart rate [13], [14]. Hence, the circadian rhythm reflects physical properties and defines different chronotypes. Especially short wavelength light (blue to green) suppresses the hormone melatonin efficiently which leads to a shift of the sleep-wake cycle [15]. Lockley et al. showed further that exposure to light, using a monochromatic light source with a wavelength of 460 nm (linewidth (FWHM) = 10 nm), results in a phase delay of the circadian rhythm of about 3 hours, compared to a phase shift of about 1.7 hours for 555 nm, respectively. As a result, polychromatic light sources offering a high color temperature (e.g. 6500 K) show a significant stronger impact on the melatonin suppression than light sources with lower correlated color temperature (CCT) values (e.g. 3000 K)[16]. The remaining question at this point is, by what means does the melatonin suppression influence the actual living situation? Cajochen [17] showed a positive linear correlation between the subjective alertness and the suppression of melatonin. Suppressing the melatonin concentration results in less tiredness and therefore, in higher alertness ratings. Further, daytime exposure to bright light showed a significant decrease of sleepiness [18]. Especially for shift- and late

night-workers dynamic lighting can help to get rid of sleep problems, fatigue and deactivation. A study from 2007 revealed that an increase of the CCT of general illumination systems in offices from 2900 K to 17000 K leads to higher concentration and alertness of office workers. On the other hand the fatigue as well as the sleepiness decreased. Essentially, the subjective work performance of the office workers increased by 19.4 % [19]. Recent studies showed that dynamic lighting systems improve the performance of high school students [20]. Appropriate use of different lighting programs with CCT ranges from 3800 K to 11000 K in class rooms lead to a positive effect regarding reading speeds and error reduction in concentration tests. Other fields where light plays an important role are health care facilities and hospitals. Studies pointed out that artificial daylight illumination significantly improves the well-being and the life quality of elderly people in health care facilities [21], [22]. Residents show better vitality and orientation and claimed to have a better sleep quality by applying dynamic lighting systems in common social environments (e.g. living room). Sust et al. [22] also indicated that the residents of health care facilities start to communicate more in such environments.

To summarize, several studies point out the importance of light, especially the consequences of light quality on the physical and the psychological system of the human body. Therefore one main future challenge for general lighting is the improvement of high quality variable lighting systems. LEDs are the only light sources available right now which provide on the one hand high quality light in terms of color rendering and supporting the circadian rhythm and on the other hand long lifetimes and high efficiencies.

1.2. Scope of this thesis

This thesis focuses on the understanding of fundamental processes occurring in LEDs. Keeping in mind the application to achieve white light emitters, a blue emitting GaN-based LED as well as a red emitting AlGaInP-based LED were examined.
During this thesis a measurement setup was developed which allows to investigate LEDs under certain driving as well as temperature conditions. In chapter 5 the measurement setup with all the required calibration measurements is presented.
Sample investigation was performed using analyzing tools like focused ion beam (FIB) in combination with electron dispersive x-ray spectroscopy (EDX) as well as electron beam induced current spectroscopy (EBIC). The fundamentals of the methods are summarized in section 3.4 (FIB and EDX) and in section 3.5 (EBIC), the obtained measurement results can be found in chapter 4.
Chapter 6 and chapter 7 present the obtained results and the detailed analysis of the thermal as well as current density impact on the emission behavior of the blue emitting GaN-based LEDs (chapter 6) as well as red emitting AlGaInP-based LEDs (chapter 7). The coherence investigation on those two types of LEDs including the established Fabry-Perot setup can be found in chapter 9.
Further, color conversion materials which are used for white light emitters were investigated and analyzed. In chapter 10 a measurement setup to determine the quantum yield is presented. Additionally optical properties (lifetime and quantum yield) of investigated color conversion materials (phosphorous materials) are shown.
Parts of the thesis were implemented in two different patents whereas the key aspects of the patents are summarized in chapter 8 and chapter 11.

2. Color science

This chapter contains selected topics concerning color science and colorimetry. The described aspects are just enough to gain an overview and an idea of those topics and to understand the mentioned parameters in this thesis. For this chapter the author refers to the comprehensive, extensive and detailed summary of color science of *Wyszecki & Stiles* (reference number [23]) as well as to the pages 331-385 out of *Cameron, J. R. & Skofronick, J. G.* (reference number [9]) which gives an overview on the physics of the eye and vision.

2.1. The human eye

Light emitted or reflected by an object hits the human eye which processes this information to the human brain. Therefore the human eye is the interface which connects the physical environment and the perception. Furthermore light parameters are directly connected to the sensitivity of the human eye which will be elaborated below.
The visible spectral range is determined by the detection region of the human eye. In this thesis the expression ”light” is always referred to the visible spectral range which is approximately in the wavelength range between 380 nm and 780 nm. Figure 2.1 shows the main elements of the human eye. Light hits the cornea and gets absorbed by the pupil, which is surrounded by the iris. The lens focuses the light beam on the retina. The size of the diameter of the pupil depends on and adjusts to the light level. Generally the diameter can vary between 3 mm to 8 mm, where it takes for the pupil around 1 to 3 seconds to adjust to its minimum size if the light intensity increases significantly. However on the other hand it takes more than 5 minutes to reach again the maximum value if the light level is decreased again. Generally, the incoming light gets refracted mainly by the cornea, the lens, the aqueous fluid and the vitreous body whereas the index of refraction of those elements varies between n = 1.33 to n = 1.41 [9]. Not indicated in figure 2.1 are blood vessels which are responsible for the oxygen supply.
One very important part of the human eye is the retina which contains photosensitive cells called *rods* and *cones*. Each eye contains about 120 million of rods and about 6.5 millions of cones, respectively. If a photon hits the photoreceptor cell, the photon triggers a signal which will be transformed to the brain. Rods provide vision at low light

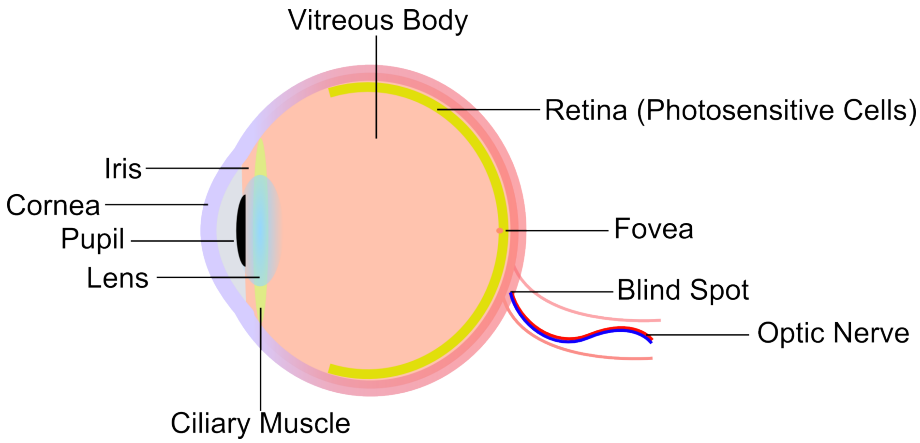

Figure 2.1.: Basic structure of the human eye. Light is transmitted through the cornea, absorbed by the pupil and focused by the lens on the retina which contains the photosensitive receptor cells.

levels (below 0.034 cd/m^2); cones are dominant in the high illumination level (above 3.4 cd/m^2). Those two parts can be separated into two kinds of visions, one is labeled *scotopic* (where rods are dominant), and the other one is called *photopic* (where cones are dominant). The region in-between, where both photoreceptor cells are responsible for signal triggering, is called *mesopic* vision.

Figure 2.2 distinguishes between the sensitivity range of the two receptor cells in the human eye (standard observer following reference [24] for the photopic and [23] for the scotopic based on measurements by Wald (1945) and by Crawford (1949)). As indicated in figure 2.2 the sensitivity peak of the rods is around 510 nm and shifted to lower wavelengths relative to the photopic vision. Important to mention is that both sensitivity curves are normalized to each other in this illustration. The difference in sensitivity between rods and cones is between 1000 and 10000, depending on the spectral range as well as on the observer. Therefore the sensitivity of rods is significantly higher than those of the cones.

In principle, in case of the rods, just two photons are required to trigger a signal. This however means that in total the illuminant needs to provide around 20 photons in front of the cornea, due to the fact that 3 % of the incoming photons are getting reflected at the surface of the cornea, 50 % are getting absorbed somewhere in the eye and only approximately 20 % of the remaining photons strike the photoreceptor cells in the end. So in conclusion just 10 % of the incoming photons are triggering a signal.

If the light level increases, cones provide vision. There are three types of cones which are responsible for color perception of the human eye which are called long (L), middle (M) and short (S). The sensitivity of those three cones depends on the spectral range and is depicted in figure 2.3. Taking the convolution of these three sensitivity curves leads to the eye sensitivity curve which is also known as the $V(\lambda)$ curve. Figure 2.2

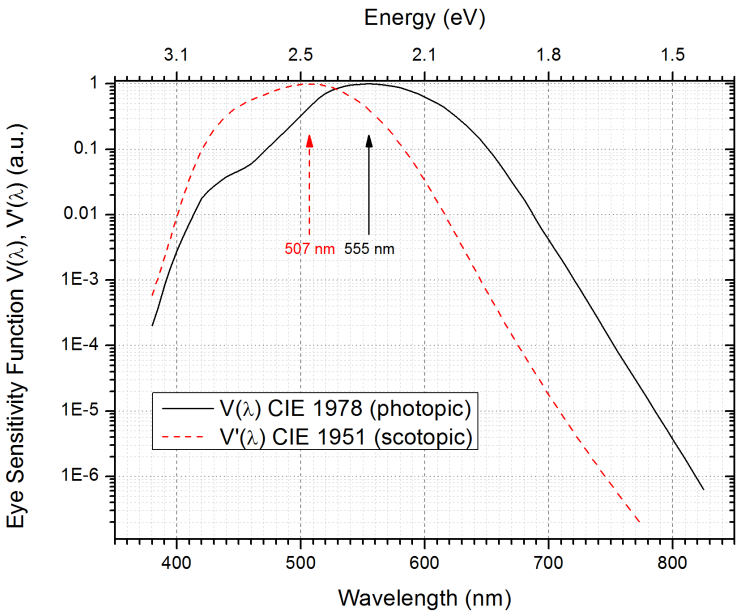

Figure 2.2.: Eye sensitivity function of a standard observer (defined and classified by the *International Commission on Illumination* CIE (Commission Internationale de l'Eclairage)). Photopic vision is provided by the cones, scotopic by the rods, respectively. Following reference [24] (photopic) and [23] (scotopic).

illustrates the $V(\lambda)$ curve which reflects the sensitivity of the human eye of a standard observer relative the wavelength of the incoming light (defined and classified by the *International Commission on Illumination* CIE (Commission Internationale de l'Eclairage)). All photometric parameters are related to this eye sensitivity curve (further attention to this topic is given in section 2.2).

As discussed in the introduction of this work (section 1.1) there is a third type of photoreceptor which does not control vision, but is responsible for regulation of the circadian rhythm of the human body. This photoreceptor acts as "Zeitgeber" (English: "time giver") and reflects physical properties. Amongst others, the hormone level of melatonin, cortisol and serotonin as well as heart rate and core body temperature gets highly influenced by this receptor. The action spectrum of this third type is blue shifted relative to the scotopic and photopic vision and has it maximum at around 460 nm. Figure 2.4 depicts this action spectrum (also called circadian efficacy) following DIN V 5031-100 [25] as well as the photopic sensitivity function of the human eye.

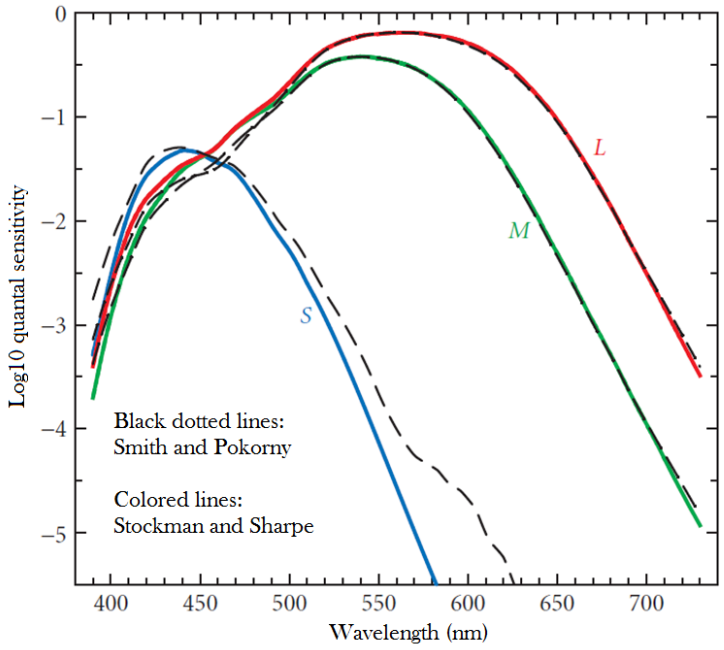

Figure 2.3.: Sensitivity behavior of the long (L), middle (M) and short (S) cone of a standard observer. Convolution lead to the three types lead to the $V(\lambda)$ curve. Taken from [26].

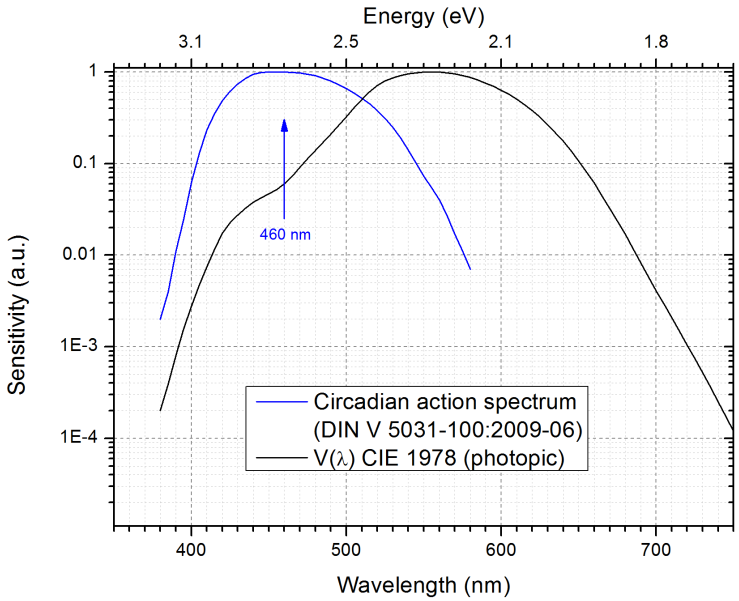

Figure 2.4.: Circadian action spectrum peaking at around 460 nm following DIN V 5031-100 [25] relative to the $V(\lambda)$ curve.

2.2. Colorimetry

This section treats the fundamental parameters which allow to describe and characterize a light source regarding its color properties. Colorimetry numerically defines visual stimuli out of the spectral power distribution the light source provides. The challenge is to find general valid parameters which describe color properties regarding the needed requirements. The prerequisite of such definition must satisfy that an observer with normal color vision agrees completely with the general defined color quantities (under the same experimental conditions). This can be achieved by defining experimental laws based on empirical generalizations. Therefore all the mentioned parameters are based on measurements which were performed and defined for a standard observer with a standard color vision.
The section gives a general overview concerning this topic based on reference number [23], [26], and [27]. Reference number [28] allows to access the tabular database of all important color functions (data in this thesis was accessed from [28] between 03/17/2014 and 03/21/2014).

2.2.1. Tristimulus values - color matching functions

The numerical description of the color stimuli of an observer can be described by the color matching functions (CMFs). As discussed in the previous section the human vision is based on three classes of photoreceptor cells which absorb the incoming photon and trigger a signal. This signal depends on the absorption rate which itself depends on the energy (i.e. the wavelength) as well as on the amount of photons. To define the response of a subject relative to the energy of the incoming photons the CMFs are established.
The CMFs presented here are based on a X, Y, Z coordinate system. This system is also known as the ”non real” or ”imaginary” color stimuli system. The reason for establishing an imaginary system is to circumvent negative stimulus values (which is the case in the R, G, B system). The CMFs reflect the human trichromatic system, therefore each color can be described by just three quantities.
As mentioned before the X, Y, Z coordinate system does not involve negative values and therefore is very convenient for further calculation. For that reason this system is used in this thesis and therefore presented in this section.
There are two common methods to establish the CMFs; one is called *Maximum Saturation Method* and the other one *Maxwell's Method*. In both methods the subject adjusts the color in a test field to the color provided in the comparison field. The subject has to achieve the same color (impression) in the test field as shown in the comparison field by mixing two primary (*Maximum Saturation Method*) or three primary colors (*Maxwell's*

Method). The color shown in the comparison field is monochromatic and its wavelength varies throughout the experiment. Usually the primary colors are also monochromatic however experiments were also executed with polychromatic light sources as well. The amount of the three primaries required to match the test field color with the comparison field color will then be used to define the CMFs. By additive mixing of these three (dimensionless) values each color (impressions) can be produced. Figure 2.5 shows the currently proposed CIE CMFs as well as the original one from 1931 modified by Judd (1951) and Vos (1978) [24]. Those CMFs are valid for a centrally viewed field with a diameter of 2°.

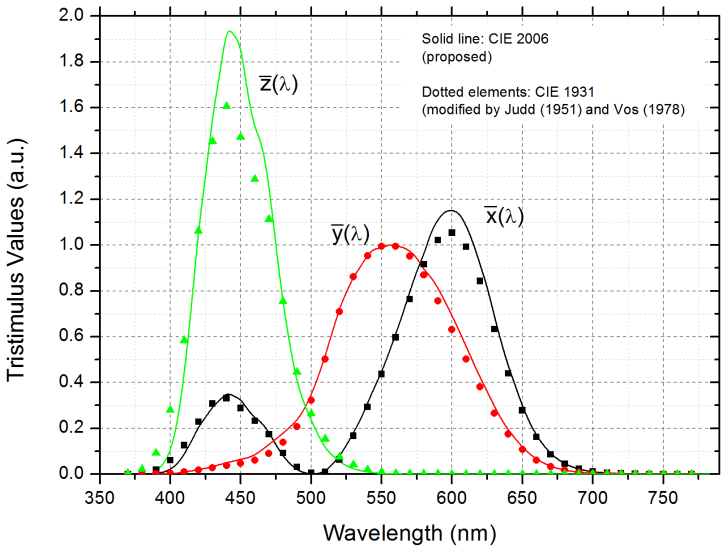

Figure 2.5.: 2° Color matching functions with respect to the wavelength. Dotted elements: CIE 1931, modified by Judd (1951) and Vos (1978) [24], Solid line: transformed from Stockman & Sharpe (2000) LMS cone fundamentals [29].

The right now proposed CIE 2006 CMFs are linear transformations of the 2° cone fundamentals of Stockman & Sharpe 2000 [29], ratified by the CIE (2006) as the new physiologically-relevant fundamental CIE CMFs.
The transformation between the CMFs and the cone fundamentals $\bar{l}(\lambda)$, $\bar{m}(\lambda)$, $\bar{s}(\lambda)$ is given by equation 2.1, 2.2 and 2.3.

$$\bar{x}(\lambda) = 1.94735469\ \bar{l}(\lambda) - 1.41445123\ \bar{m}(\lambda) + 0.36476327\ \bar{s}(\lambda) \tag{2.1}$$

$$\bar{y}(\lambda) = 0.68990272\ \bar{l}(\lambda) + 0.34832189\ \bar{m}(\lambda) \tag{2.2}$$

$$\bar{z}(\lambda) = 1.93485343\ \bar{s}(\lambda) \tag{2.3}$$

$$\tag{2.4}$$

The eye sensitivity function $V(\lambda)$ is defined by equation 2.5:

$$\bar{y}(\lambda) = V(\lambda) \tag{2.5}$$

For a given spectral power distribution the three stimulus values X, Y, Z can then be calculated by using equation 2.6, 2.7 and 2.8.

$$X = \int_{380}^{780} I(\lambda)\ \bar{x}\ (\lambda)\ d\lambda \tag{2.6}$$

$$Y = \int_{380}^{780} I(\lambda)\ \bar{y}\ (\lambda)\ d\lambda \tag{2.7}$$

$$Z = \int_{380}^{780} I(\lambda)\ \bar{z}\ (\lambda)\ d\lambda \tag{2.8}$$

whereas $I(\lambda)$ is the spectral power distribution of the light source. Out of these stimulus values the chromaticity values can then be defined as:

$$x = \frac{X}{X+Y+Z} \tag{2.9}$$

$$y = \frac{Y}{X+Y+Z} \tag{2.10}$$

$$z = \frac{Z}{X+Y+Z} \tag{2.11}$$

whereas

$$x + y + z = 1 \tag{2.12}$$

This means that an emission spectrum with a certain spectral power distribution can be assigned two a 2 dimensional map plotting x and y (the third value can be calculated out of the other two). This mapping allows to assign a spectral power distribution to a certain color point. In figure 2.6 the chromaticity diagram of the CIE 2012 (proposed) is shown. The monochromatic colors or pure colors can be found on the perimeter of the diagram and are labeled with the perspective wavelength number. The equal energy point EE corresponds to the a constant spectral distribution ($x = \frac{1}{3}$, $y = \frac{1}{3}$, $z = \frac{1}{3}$) and is often also named *white point*. Further indicated in figure 2.6 is the position of the black

body radiator with a certain temperature (see section 2.2.3). The line which connects the two ends of the spectra locus is called purple line representing the additive mixture of extreme short wavelength light and long wavelength light. No wavelength numbers are labeled on this line because there is no monochromatic light which creates this kind of highly saturated color, only the mixture allows to produce such colors.
With this CIE diagram light sources regarding their color impression can be classified. If the chromaticity point of the spectral power distribution of the investigate light source lies in the middle of the spectrum close to the EE point the light source will be classified as a white light source. The chromaticity points of white light sources are in the environment to the Planckian locus.

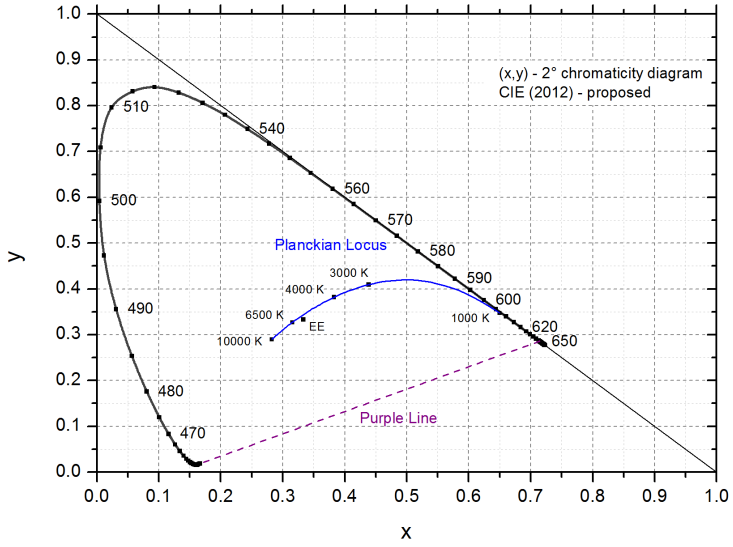

Figure 2.6.: The CIE (2012) 2° "physiologically-relevant" chromaticity coordinates following Stockman & Sharpe (2000) [29]. EE refers to the equal energy point.

It is important to mention at this point that the difference between two chromaticity points in the x, y chromaticity diagram is not uniform. This means that the color change in one direction occurs much more rapid than in the other direction. Therefore another color coordinate system was established which is called the *uniform chromaticity diagram* or u', v' diagram. This diagram can be calculated by using equations 2.13 and 2.14:

$$u' = \frac{4x}{-2x + 12y + 3} \tag{2.13}$$

$$v' = \frac{9y}{-2x + 12y + 3} \tag{2.14}$$

Figure 2.7 shows the CIE 1976 u',v' uniform chromaticity diagram. The non-uniformity of the distance between certain color coordinates in the x,y system is not completely eliminated, however the color difference between two geometric distances is approximately proportional between these points.
Both systems are applied in the lighting industry, therefore both versions of the chromaticity coordinate system are presented in this work (x,y and u',v') .

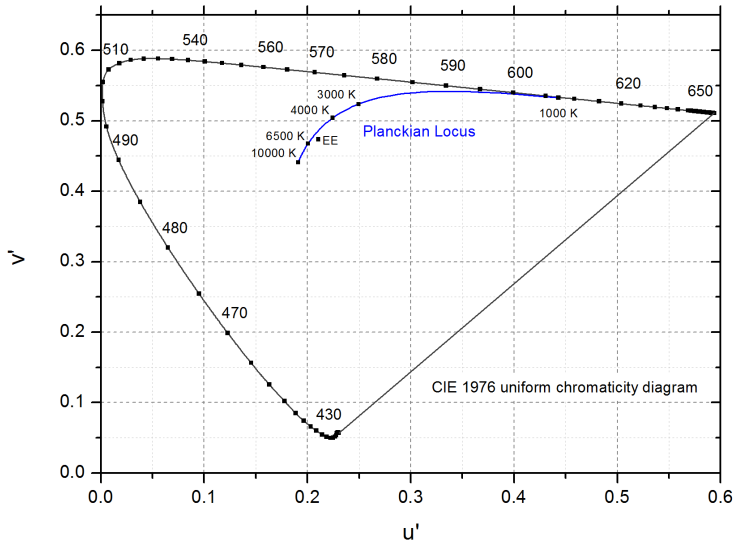

Figure 2.7.: The CIE 1976 u',v' uniform chromaticity diagram calculated out of equation 2.13 and 2.14.

Note: The chromaticity coordinates (in either case) are numbers which refer to a certain color (perception) and do not reflect any spectral distribution of the light source. Out of a spectral power distribution x,y or u',v' coordinates can be calculated by using equation 2.6 to 2.11 or equation 2.13 and 2.14, respectively. However there is no bijective function between x,y / u',v' coordinates and the spectral power distribution. Therefore out of the x,y / u',v' coordinates no conclusion of the spectral power distribution of the light source can be drawn.
This means that two light sources with the same coordinates just agree with their color impression, however the general color quality (e.g. color rendering properties) can be completely different. Without the spectral distribution of the two light sources they can hardly be compared to each other.

2.2.2. MacAdam ellipses

In 1942 MacAdam analyzed the distance between two chromaticity points which are hardly distinguishable anymore. He defined regions where within these regions the color difference can not be distinguished by the observer anymore [30]. It turned out that those regions are shaped like ellipses. Therefore those chromaticity points which lie in between these ellipse are not distinguishable by the observer anymore and can be seen as an identical color impression.
Figure 2.8 shows the ellipses (ellipses are plotted 10 times larger due to illustration reasons) in the CIE 1931 chromaticity diagram. The size of an ellipse depends on the color coordinate (note: this illustration is in the non uniform x,y chromaticity system).

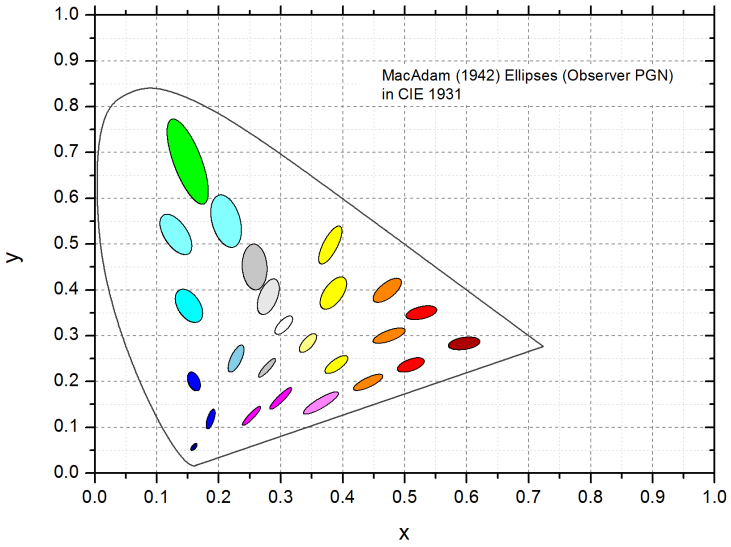

Figure 2.8.: MacAdam ellipses plotted in the CIE 1931 non uniform x,y chromaticity system. Observer: Perley G. Nutting Jr (PGN). The axes of the ellispe are plotted 10 times larger due to illustration reasons.

In the lighting industry the ellipses defined in the CIE 1931 (plotted in figure 2.8) are known as 1 step SDCM ("Standard Deviation Color Matching"). This means that no color difference between the light source and the specified chromaticity coordinate is observable (it lies inside the MacAdam ellipse) by a standard observer. The difference between the actual chromaticity color coordinate of a light source and its defined target color is specified in certain SDCM steps. The SDCM is the standard deviation σ which means that with the increasing number of steps the actual color difference is getting larger in comparison to the target value. 1 step SDCM means a standard deviation of 1σ

which is defined by the MacAdams ellipse itself. A 2 step SDCM means 2σ away from the target, 3 step SDCM 3σ values away and so on. Therefore a larger SDCM number refers to a larger standard deviation and therefore to a large color difference of the light source with respect to the target color.

2.2.3. Color temperature

The color temperature of a light source is referred to a temperature value which defines the color of white light. The term color temperature is only valid for a black body radiator. If a black body radiator is getting heated it will start to glow red at a certain temperature. This emitted visible spectrum can be then assigned to the temperature value of the black body radiator which is called color temperature. If the temperature of the emitter is increased the emission spectrum changes and eventually the emitter will glow bluish for high temperature values. This behavior is depicted in figure 2.9, following equation 2.15. In equation 2.15 $I(\lambda)$ refers to the intensity with respect to wavelength λ, h to the Planck constant, c to the speed of light, k to the Boltzmann constant and T to the temperature of the black body. A low color temperature value alludes that red light dominated the emission (often referred as *warm* white light), a high color temperature means that the blue emission is dominant (often referred as *cold* white light).

$$I(\lambda) = \frac{2\pi hc^2}{\lambda^5} \frac{1}{e^{\left(\frac{hc}{\lambda kT}\right)} - 1} \tag{2.15}$$

In figure 2.6 and 2.7 the Planckian locus describes the color coordinates of such black body spectra.
For a non black body emitter (e.g. LED, fluorescent tube, discharge lamp, etc.) a color temperature value can not be defined. Nevertheless to characterize the white light sources regarding their type of color (i.e. warm white or cold white) a so called *correlated color temperature* (CCT) is assigned. To calculate this CCT value the chromaticity values of the light source are determined and compared in the CIE diagram with the chromaticity values of the black body radiator. This color temperature value which matches with the Planckian locus will be than assigned as the CCT. If the chromaticity coordinate of the light source is not lying directly on the Planckian locus, isotherms (lines with constant color temperature) perpendicular to the Planckian locus allow to define the CCT of the light source. Those lines are called Judds lines and are perpendicular lines to the Planckian locus in the u',v' chromaticity diagram.
Out of the CCT no correlation to the actual spectral distribution can be drawn. Only the impression of whiteness can be assigned relative to the impression obtained by a black body radiator. Out of the CCT no color quality can be extracted.
One approximation to calculate the CCT out of the spectral distribution was proposed

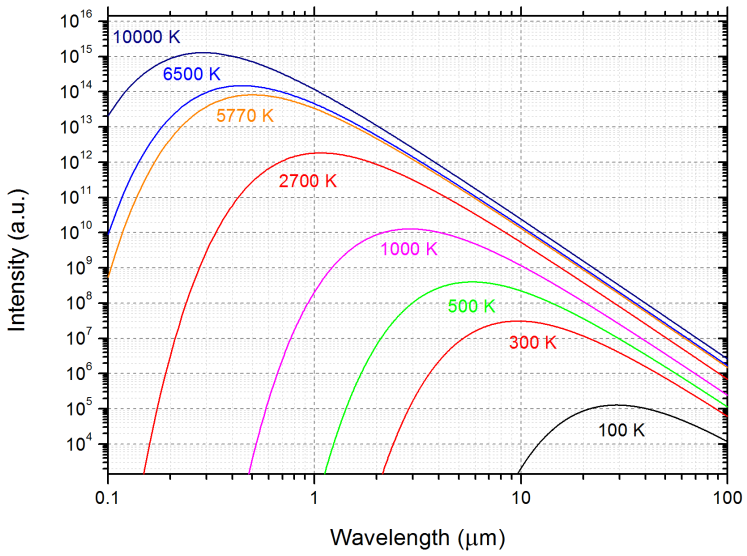

Figure 2.9.: Emission distribution of a black body radiator for several temperatures following equation 2.15.

by McCamy [31] (equation 2.16):

$$CCT(x,y) = -449n^3 + 3525n^3 - 6823.3n + 5520.33 \tag{2.16}$$

where $n = \frac{(x-xe)}{(y-ye)}$ and x/y are the chromaticity points of the light source. The epicenter of convergence are xe = 0.3320 and ye = 0.1858.

2.2.4. Color rendering

To identify the color quality of a light source a parameter has to be established. This certain parameter has to identify the ability of a light source to represent the natural appearance of an object if the object is illuminated by the light source. Several types of color rendering indices were proposed in the last couple of years (e.g. color quality scale (CQS) [32] or gamut area index (GAI) [33]). However, due to several non-agreements of third parties involved, non of them gained ground in the lighting community. Therefore in this work the classical and still accepted color rendering index (CRI) is presented. The CRI depicts the ability of a light source to render certain colors of an object relative to a reference light source. The reference light source is chosen in way that if the test light source lies on the Planckian locus in the chromaticity diagram, a black body radiator with the same nominal color temperature is taken as reference. If the chromaticity

point lies apart from the Planckian locus, a black body radiator with the same CCT is chosen or alternatively, the standardized D65 illuminant (also called daylight illuminant with 6504 K color temperature defined by the CIE) is used. The maximum CRI value is 100 which indicates high color quality. Every black body radiator has a CRI value of 100.
To gain the CRI value for a test light source, 14 types of test color samples are established. Those test color samples get illuminated with the reference source as well as with the test light source. The difference in color change ΔE_i of the chromaticity coordinates will then be noted. The index i indicates the amount of test samples (1 to 14). Following equation 2.17 the CRI for each test sample can be calculated.

$$\text{CRI}_i = 100 - 4.6\Delta E_i \tag{2.17}$$

The so called *general* CRI_G is taken by averaging the CRI of the first 8 test samples (which are often referred to non-saturated colors) given by equation 2.18:

$$\text{CRI}_G = \frac{1}{8}\sum_{i=1}^{8}\text{CRI}_i \tag{2.18}$$

If more test samples (number 9 to 14) are averaged in the calculation of the CRI it is labeled separately (e.g. CRI_{1-14}). Figure 2.10 shows the power reflectivity of the 8 non-saturated test samples [34], figure 2.11 of the saturated test samples 9 to 14, respectively.

Another devoted abbreviation of the color rendering index (CRI) is R_a. The R_a is equal to the general CRI_G which averages the first 8 test samples. If more specific test samples are involved, the index i will refer to the test sample set (R_i). Typically if a light source is specified, often only the CRI_G (R_a) is outlined. The abbreviation R_a is commonly used in German speaking countries.

Note: The CRI is just an indication which allows to compare certain light sources. On average one can say that a CRI of at least 90 should be required for indoor lighting applications.

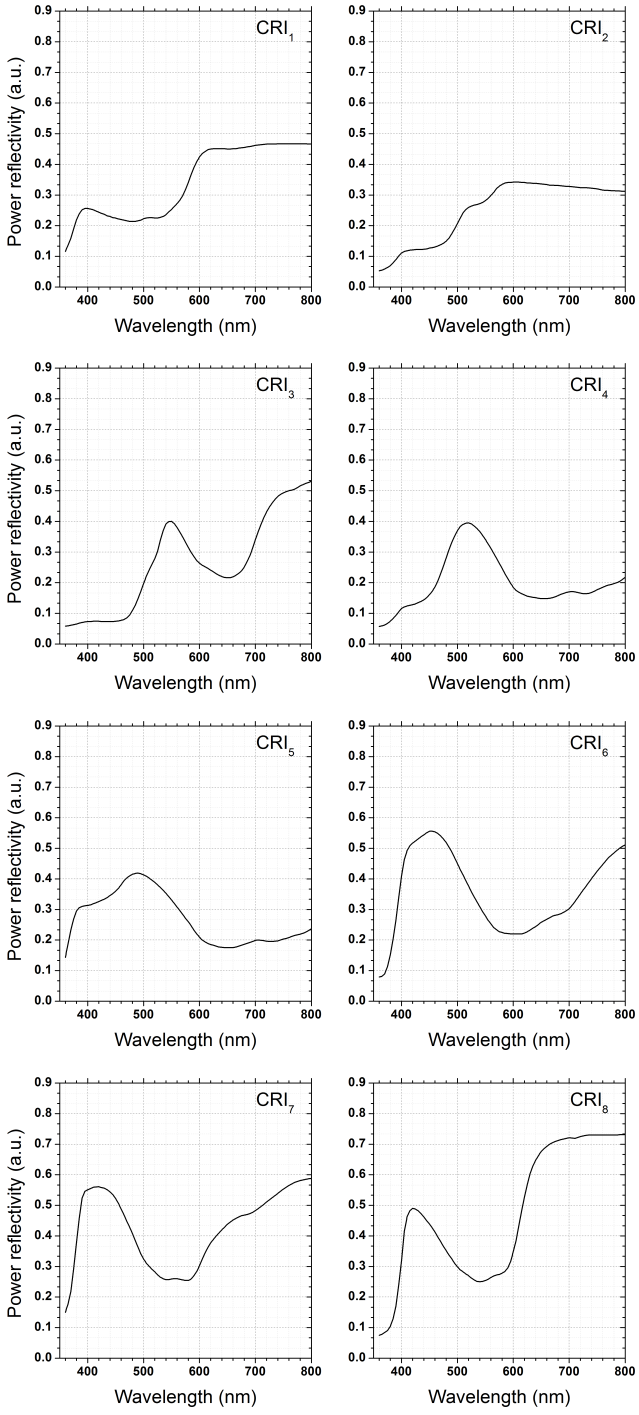

Figure 2.10.: Power reflectivity versus wavelength of the 8 test samples [34] which allows to determine the general color rendering index (CRI_G / R_a) of a light source.

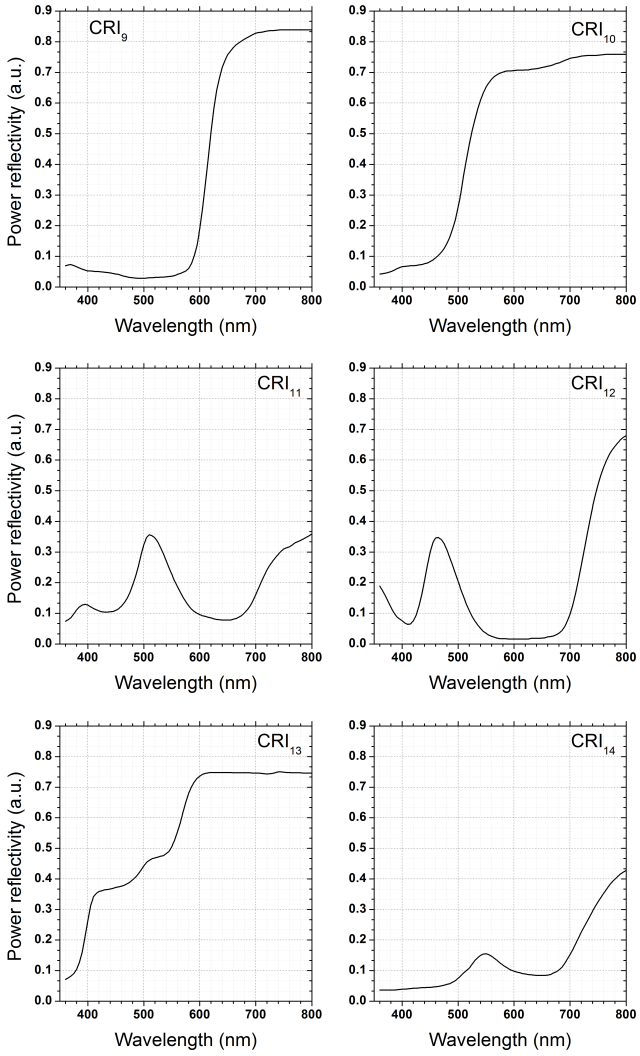

Figure 2.11.: Power reflectivity versus wavelength of the test samples number 9 to 14 [34] which allows to determine specific (saturated) color rendering indices (CRI_i / R_i) of a light source.

2.2.5. Dominant wavelength & color purity

The dominant wavelength λ_D is defined as the saturated color which lies on the intersection of a straight line between the EE point and the chromaticity point of the light source and the perimeter (figure 2.12).
The color purity P is defined as the fraction between the distance between EE point and the x,y of the light source and the distance between EE point to the dominate wavelength λ_D (equation 2.19).

$$P = \frac{\overline{EE - (x,y)_{\text{source}}}}{\overline{EE - \lambda_D}} = \frac{a}{a+b} \tag{2.19}$$

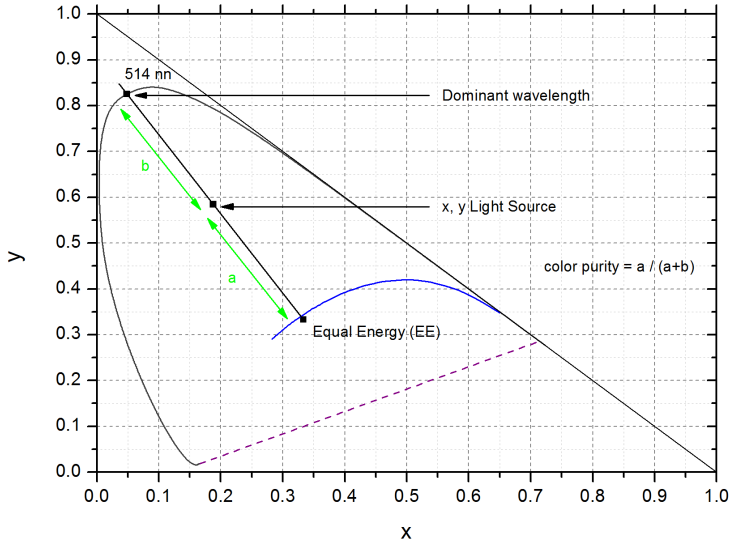

Figure 2.12.: Graphical definition of the dominant wavelength and the purity of a light source in the CIE 1931 diagram.

An algorithm which allows to numerically obtain the color purity and the dominant wavelength was proposed by Judd in 1933 and can be found in reference [35].

2.2.6. Photometric units

Table 2.1 lists the basic photometric units and its comparison to the radiometric ones. The difference between photometric and radiometric is that the photometric units take the already discussed $V(\lambda)$ curve (which includes the sensitivity of the human eye) into account and the radiometric do not.

Table 2.1.: Selected photometric and radiometric units. Full names of the abbreviation: lm: lumen, cd: candela, lx: lux, sr: steradiant.

Photometric unit	**Dimension**	**Radiometric unit**	**Dimension**
Luminous flux (Lumen)	lm	Radiant flux	W
Illuminance (Lux)	$\mathrm{lm/m^2 = lx}$	Irradiance	$\mathrm{W/m^2}$
Luminous intensity (Candela)	lm/sr = cd	Radiant intensity	W/sr
Luminance	$\mathrm{cd/m^2}$	Radiance	$\mathrm{W/(sr\ m^2)}$

3. Fundamentals & analytical tools

In this chapter a compendium of the fundamentals of optoelectronic is presented. Further the basics of the analytical tools used to investigate the samples are explained. The aim of this chapter is provide a principle overview of the physics and on the measurement techniques used in this work.

3.1. Semiconductor principles

To get an overview about principles of semiconductor physics the author highly recommends and refers to the course materials *243. Semiconductor Optoelectronic Devices* of Prof. David A. B. Miller [36].

3.1.1. Semiconductor alloys

For optoelectronic devices III-V compound semiconductors are used (e.g. III: Al, Ga, In, V: N, P, As). The crystal structures of such compounds do form a so called *zinc blende* structure (closely related to the diamond structure) or a *wurtzite structure*. The zinc blende structure is an interlocking of two face centered cubic lattices (fcc), however, different to the diamond structure, there are two different atoms in the unit cell. A very famous optoelectronic example of such crystal structure is GaAs. III-V nitrides like GaN, AlN and InN form the wurtzite structure which consists out of two interlocking hexagonal closed packed (hcp) lattices [37]. The crystal structures of zinc blende and wurtzite structure are depicted in figure 3.1. Whether zinc blende nor wurtzite structure do have a center of inversion, due to the fact that two atoms appear in the crystal structure. Therefore, by performing a translation, the atom at position (x, y, z) does not lead to the same atom at position (-x, -y, -z). Subsequently such structures do exhibit a polarity. Wurtzite structures grown on hexagonal substrates (0001) become piezoelectrically active if they are under thermal stress [38].
For optoelectronic devices, semiconductor materials with a direct band gap are used. This means that the minimum of the conduction band E_C lies directly above the maximum of the valence band E_V. The distance between those two extrema is then called

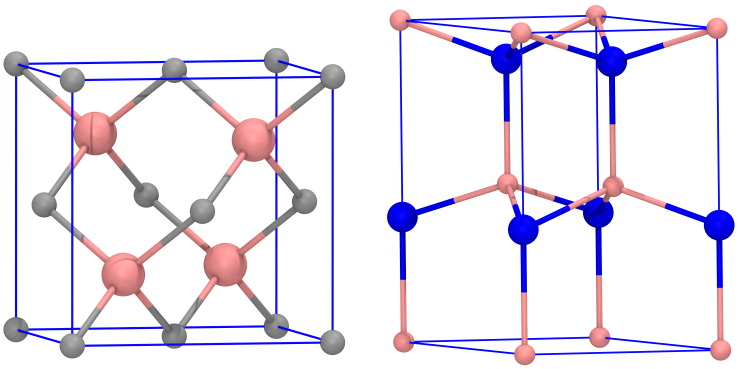

Figure 3.1.: Left panel: Zinc blende structure (e.g. GaAs, InP) consisting out of two interlocking face centered cubic lattices with two atoms in the unit cell. Right panel: Wurtzite structure (e.g. GaN, AlN) containing two interpenetrating hexagonal closed packed lattices.

band gap energy E_g. Figure 3.2 illustrates a schematic energy-momentum diagram ($E - \mathbf{k}$ diagram) for a direct semiconductor. If the minimum of the conduction band is not at the same position (in k-space) as the maximum of the valence band the semiconductor is called indirect.

For GaN the valence band is degenerated. This is due to the fact that the bottom of the conduction band is formed by the s-levels of gallium atoms (original atom) and the top of the valence band is formed from the three p-levels (px, py, pz in direction x, y, z) of the nitrogen atoms. The interaction of the electron spin with the orbits (spin orbit coupling) separates and therefore splits off one of the three valence bands. This leads to an occurrence of a so called split off hole (SOH) in the band diagram. The two remaining holes, degenerated at the top of the valence band, are on the one hand heavy holes (HH) and on the other hand light holes (LH), respectively [36], [38].

The difference between heavy holes and light holes is given by their effective mass m^* which is defined in equation 3.1, whereas $\hbar$ is equal to the Planck constant divided by 2π.

$$\frac{1}{m^*} = \frac{1}{\hbar^2}\frac{d^2E}{dk^2} \tag{3.1}$$

Out of equation 3.1 one can conclude that the effective mass is indirect proportional to the curvature of valence band (cf. figure 3.2). Therefore heavy holes have a larger effective mass and the curvature is not as bend as for the light holes with a lower effective mass. Combining the effective mass with the energy leads to the circumstance that the energy of heavy holes is smaller than the one of the light holes (equation 3.2).

$$E = \frac{\hbar^2 k^2}{2m^*} \tag{3.2}$$

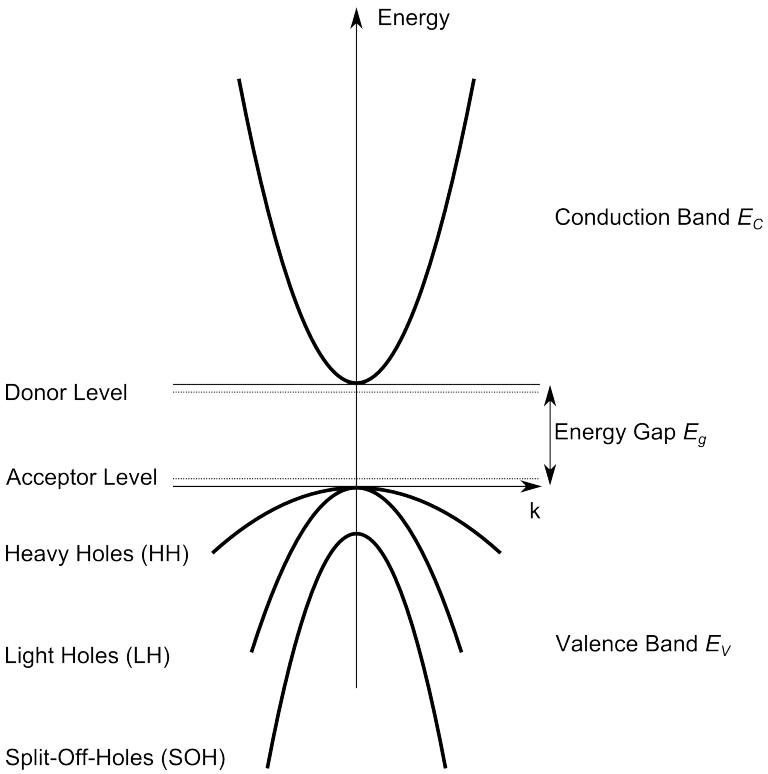

Figure 3.2.: Band diagram (energy versus momentum vector **k**) of a direct semiconductor material. Adapted from [36], [39], and [40].

Further indicated in figure 3.2 are the respective energy positions of the donor and acceptor levels. Doping with donor atoms lead to an n-type semiconductor material (extrinsic semiconductor with a large electron concentration). One doping example is a combination of a group V element with a group IV semiconductor (e.g As or P in Si which makes Si to an n-type semiconductor). On the other hand an acceptor atom is referred to a dopant which makes the semiconductor material to a p-type one (extrinsic semiconductor with a large hole concentration) as for example a group III element implemented in a group IV semiconductor (Al or B in Si which makes Si to an p-type semiconductor).
The donor level lies directly beneath the conduction band and the acceptor level is located closely above the valence band, respectively. The position of the respective levels can be explained with shallow donors that exhibit usually enough thermal energy to ionize (e.g. at room temperature) and therefore mobile electrons are lifted into the conduction band. The positively charged (immobile) donor ions remain closely below the conduction band. In the complete ionization state (thermal equilibrium) the electrons are equal to the concentration of the donor ions. For the acceptor dopants the same is valid however relative to the valence band [39], [41].

3.1.2. Recombination processes

If an electron located in the conduction band makes a transition down to the valence band (where a hole is located) the electron-hole pair is getting annihilated. This effect is called recombination. Recombination is the opposite process of charge generation where an electron from the valence band gets lifted up into the conduction band leaving behind the remaining hole in the valence band. Such generation could occur due to vibrations of lattice atoms which lead to bond breaking. In thermodynamic equilibrium generation as well as recombination of charge carriers are equal, therefore the overall carrier concentration stays the same [39].
If now excess carriers are introduced into the direct semiconductor, the probability of recombination is increasing significantly. On the other hand, if we illuminate a semiconductor sample with light containing a certain energy, the probability of generation of charge carriers is increased as well. This effect is then called absorption. Figure 3.3 illustrates a direct charge generation process (G) as well as an absorption (A) of an incoming photon in a semiconductor material. E_C and E_V are the conduction and the valence band energies, respectively.
However, in light emitting diodes the emission of light is based on the phenomenon of radiative recombination of charge carriers (spontaneous recombination). In the radiative recombination process a photon with a certain energy can be created by annihilation of an electron-hole pair (R_E in figure 3.3). The amount of excess electron-hole pairs are getting produced by injection of charge carriers into the semiconductor material. This emission process based on charge carrier injection is called electroluminescence. The energy of the photon depends on the energy position of the respective excited state. In figure 3.3 the energy of the emitted photon is equal to the band gap energy ($h\nu = E_C$-E_V). The photon flux Φ (emitted photons per seconds) of an LED can be defined by the electron-hole pair injection rate R generated in the volume V convoluted with the internal quantum efficiency η_i (equation 3.3 [42]).

$$\Phi = \eta_i R V \tag{3.3}$$

The internal quantum efficiency η_i strongly depends on temperature, defect concentration, doping, as well as on the semiconductor material itself [42]. Since typically the internal quantum efficiency is not equal to unity, undesired non-radiative processes in semiconductors can occur as well. Such non-radiative recombination centers often occur from defects (foreign atoms, dislocations, etc.) which introduce energy levels (traps) directly in the band gap of the semiconductor. Such defects within the band gap effectively trap and capture charge carriers and prevent radiative recombination. These non-radiative recombination form deep traps in the band gap was firstly analyzed by Shockley, Read and Hall and is therefore called Shockley Read Hall (SRH) recombina-

tion. In figure 3.3 such recombination process is labeled R_S whereas E_T is the energy of the trap in the band gap.
Another non-radiative recombination process which limits the efficiency of LEDs is called Auger recombination (R_A in figure3.3). The energy from the electron hole recombination is transferred to a free electron (or free hole) which lifts the free electron high up in the conduction band (or the hole deeply in the valence band) [27]. The Auger process is becoming more dominant for small bang gap materials [43].
Not shown in figure 3.3 is the non-radiative recombination by surface states. At the surface of the semiconductor crystal the periodicity is getting disturbed. Therefore the energy diagram changes at the surface which further leads to non-radiative recombination centers [27].

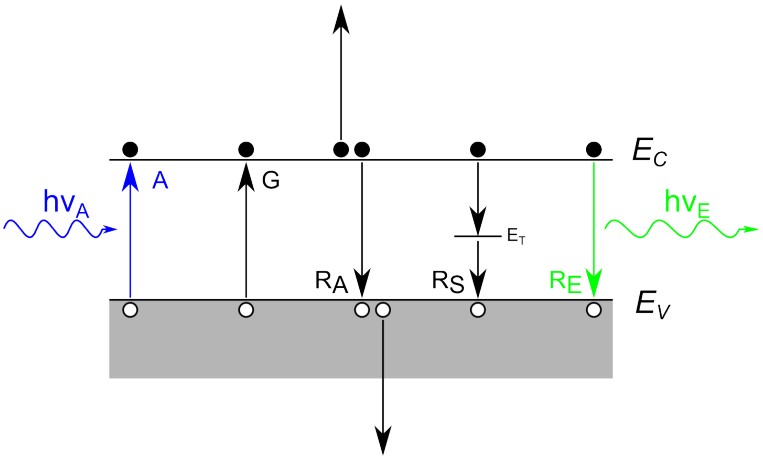

Figure 3.3.: Absorption (A) and charge generation (G) as well as selected radiative and non-radiative recombination processes (R_A Auger recombination, R_S Schokley Read Hall recombination, R_E radiative emission) occurring in semiconductor materials. Adapted from [27] and [39].

Right know the reduction of the internal efficiency with respect to temperature and injection current (so called efficiency droop) is a highly debated issue and by far not completely understood. For further reading about this particular topic the author refers to several recent publications which discuss experimental and simulation data: [43], [44], [45], [46], [47].

In an indirect semiconductor a direct recombination is very unlikely due to the difference in momentum of the electron in the conduction band and the hole in the valence band. A direct recombination where energy as well as momentum is conserved is only possible in combination with lattice interaction (emission of phonons) [39].

3.1.3. pn-junction

This summary is a compendium based on reference number [37], [39], [48] and [49], however the physics of the pn-junction is in principle available in every fundamental semiconductor physics literature not listed here.

An LED is based on the radiative recombination of electrons and holes in a so called pn-junction. A pn-junction results out of an interaction between a p-type (p-doped) and an n-type (n-doped) semiconductor material. Bringing those two types together causes that the majority charges of the n-type material (electrons) to diffuse into the p-type region (where holes are the majority charge carriers). The positively charged holes are canceled out by the diffusing electrons and therefore a region without majority carriers is occurring (virtually) whereas parts of the n-type region is charged positively due to the remaining positively charged atoms (remaining positively charged donors) and parts of the p-type region is negatively charged due to the remaining negatively charged atoms in the p-type region (remaining negatively charged acceptors). The diffusion current occurs due to the difference of the dopant concentration in thermodynamic equilibrium and flows from the n-type to the p-type material.
Due to this diffusion current an electric field occurs which direction is pointing from the n-type to the p-type region. However this (negative) electric field drives electrons from the p-type region back to the n-type region. This type of current is called drift current and is pointing in the opposite direction relative to the diffusion current. At some point there is a steady state situation between diffusion current and drift current and a so called space charge layer (depletion region) is formed.
This situation is depicted in figure 3.4 whereas E is the electric field and N_D and N_A are referred to the donor and acceptor concentrations, respectively. The voltage across the junction in thermodynamic equilibrium (without external bias) is called built in voltage V_B.
By applying an external electrical field, this space charge region can be enhanced or reduced. Operating the pn-junction in reverse bias (V_r) leads to injection of holes on the n-type side and electrons on the p-type side, respectively. This circumstance will increase the width of the depletion region and the total electrostatic potential across junction increases by V_r. Subsequently the total electrostatic potential V across the junction in revers bias is the sum of $V_B + V_r$.
On the other hand, if the junction is operated in forward bias V_f, electrons are injected on the n-type side as well as holes are injected on the p-type side, respectively. Therefore the depletion region width is getting reduced. The total electrostatic potential across junction V decreases by V_f and is given by $V_B - V_f$.

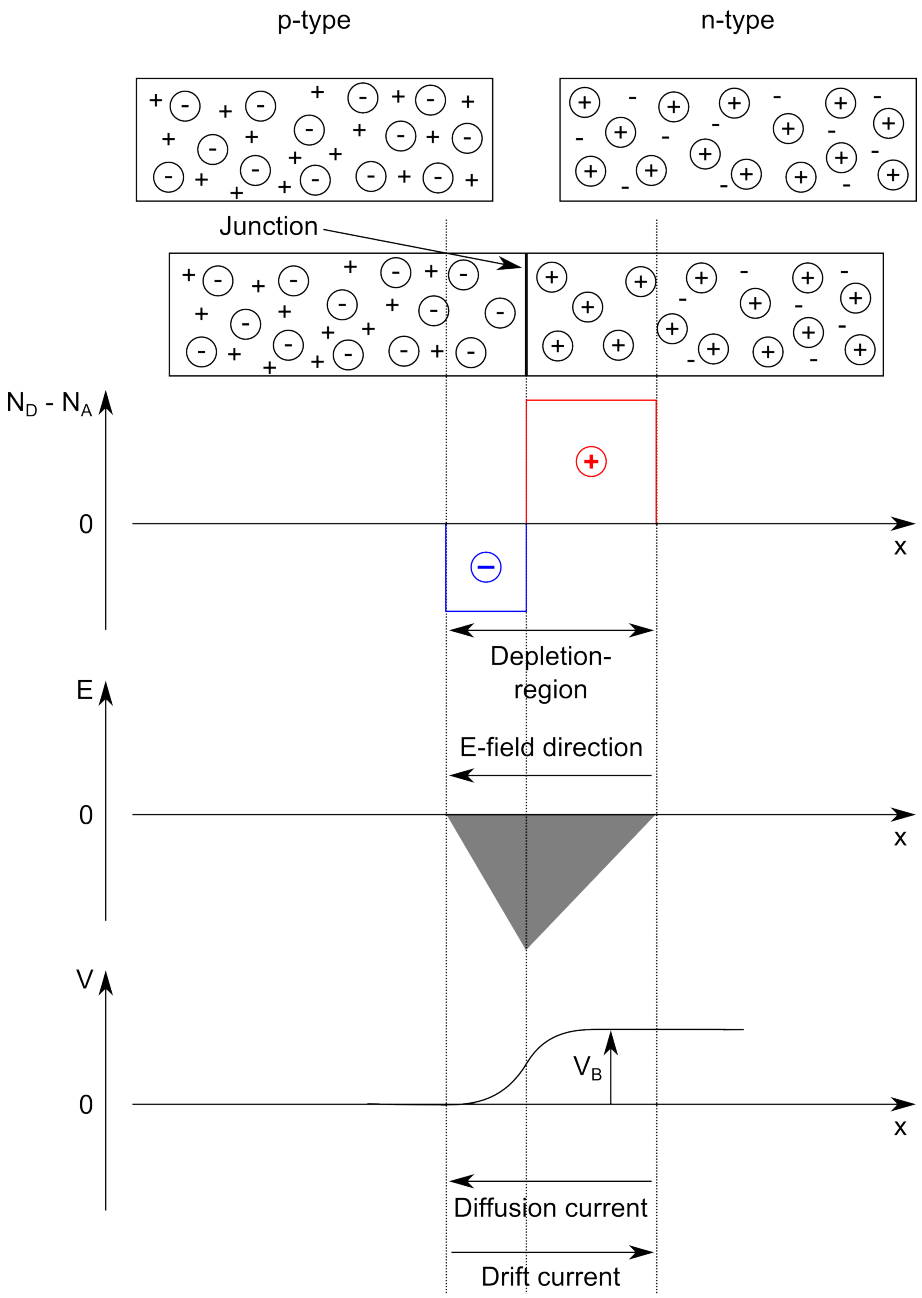

Figure 3.4.: Schematic illustration of the pn-junction. N_D and N_A are referred to the donor and acceptor concentrations, V_B to the built in voltage, respectively.

3.1.4. Heterostructures

A schematic cross section of an LED is shown in figure 3.5. On a substrate an n-type semiconductor layer is grown followed by a p-type layer whereas both layers are contacted using gold electrodes. As discussed above the pn-junction is responsible for the radiative emission of light. The pn-junction usually not just consists out of one single n-type and one singly p-type layer, rather various types of different layers are arranged to obtain a highly efficient LED.
Such layer structure consist out of a so called heterostructure (heterojunctions) whereas more than one type of semiconductor material is grown on each other. Specifically a quantum well (QW) or more precisely a multiple quantum well (MQW) structure is obtained by bringing together a narrow band gap material with a wide band gap material. The advantages for using heterostructures are ([36]):

- Confinement of the electrons and holes in QWs makes the device more efficient.
- Different types of materials exhibit different refraction indices and therefore allow wave-guiding.
- Band gap tuning to control emission behavior / absorption processes is possible.

Very important for growing heterojunctions is that the lattice constant of the used materials is very similar because a big lattice mismatch leads to defects which increase the probability of non-radiative recombination centers, therefore reducing the efficiency of the LED.
The band line up of a typical heterostructure can be found in figure 3.5. In this example the MQW structure consists out of two types of semiconductors namely a narrow band gap GaInN and a wide band gap GaN. The confinement layer is out of AlGaN. The electrons (and holes) will be confined and can recombine in the potential wells which are produced by this different kinds of semiconductor materials. Very often an electron blocking layer (EBL) is inserted for reducing the electron leakage (separate AlGaN layer in this illustration). This layer prevents that electrons escape from the active layer and the confinement interface. This becomes crucial at high temperatures where the carriers are thermally activated as well as if the height of the QW is quite low. Carrier leakage is quite a big problem for the efficiency decrease in LEDs [43].

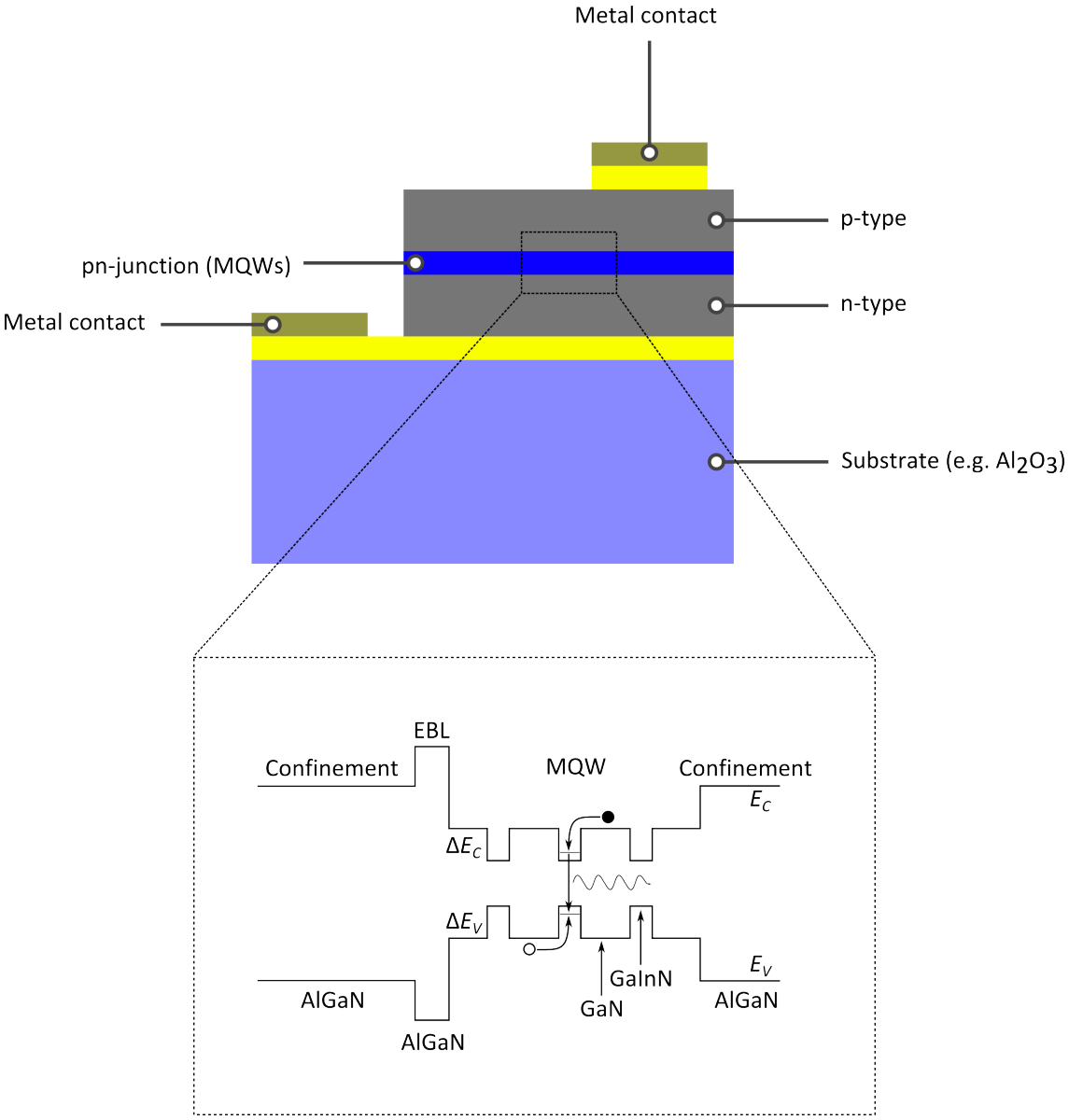

Figure 3.5.: Schematic illustration of the structure of an LED as well as the band diagram of an undoped multiple quantum well (MWQ) structure including an electron blocking layer (EBL). The band off-sets between the two different semiconductor material is labeled ΔE_C and ΔE_V (adapted from [27]).

3.2. White light LED

Parts of this section are taken and adapted from *Tunable natural light realized by phosphor-innovation light-emitting-diode technology* by Hetzel et al. [1]. The original work can be found in the appendix of this thesis.

There are two general approaches to generate white light which are summarized in figure 3.6 (adapted from [27]). One technique is by additive mixing of two or more colors from different light sources (left panel in figure 3.6). Alternatively wavelength converters allow to modify spectra in a way that white light is emitted (right panel in figure 3.6). The approach, illustrated on the right hand side of figure 3.6, occurs via fluorescence. In this case the LED (usually UV or blue LED) excites a phosphor (light converting luminescence particles e.g. Yttrium Aluminum Granat (YAG) doped with rare earth materials) which emits light in a certain visible wavelength range. Figure 3.7 demonstrates the characteristic spectrum of a color converted LED. The blue peak in the spectrum at approximately 450 nm occurs due to the unconverted light fraction of the exciting blue LED.

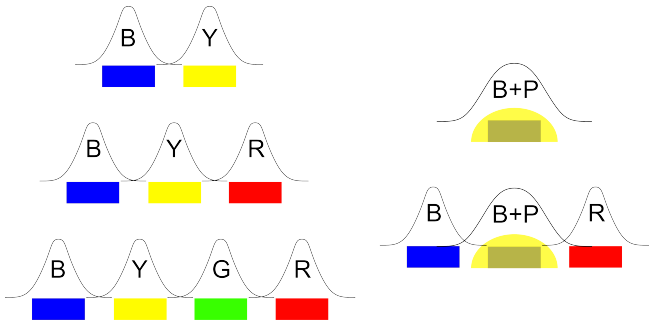

Figure 3.6.: Approaches to generate white light (blue emitting LED (B), yellow emitting LED (Y), green emitting LED (G), red emitting LED (R), color converted LED (P)). Left panel: Additive color mixing of different LEDs emitting in two or more visible wavelength regions. Right panel: Use of color converters (Adapted from [27]).

Combining a color converted LED with red and blue LEDs allows on the one hand to achieve high CRI values and on the other hand to tune the CCT over a broad region. Figure 3.8 shows an example of an LED module combining three blue, six color-converted and eight red LEDs, respectively (LUMITECH's Phosphor Innovation (PI) LED Technology). This setup allows CRI values above 90 over the allocated CCT region, from 2700 K to 6500 K. To change the CCT, the emission intensity of the single types of LEDs (R, P or B) is changed. Further, to address the appearance of an object, the LED module in figure 3.8 allows, by slightly varying the color composition of the emitting light, to

adjust the CRI value of the object and therefore emphasizes the object.
The spectral distributions of such an LED module for several CCTs are shown in the bottom panel in figure 3.8. In general, the CRI increases with the number of LED sources distributed over the visible spectral range [27]. One major benefit, color converted LEDs provide, is the combination of high efficiencies and broadband emission (figure 3.7) which is mainly responsible for the high CRI values compared to multi-LED additive mixing.

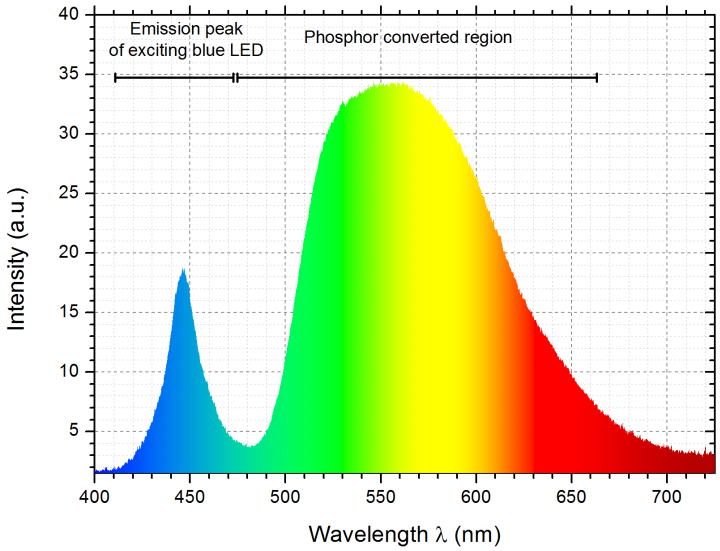

Figure 3.7.: Spectrum of a color converted LED. The blue peak exists due to the unconverted light fraction of the exciting blue LED.

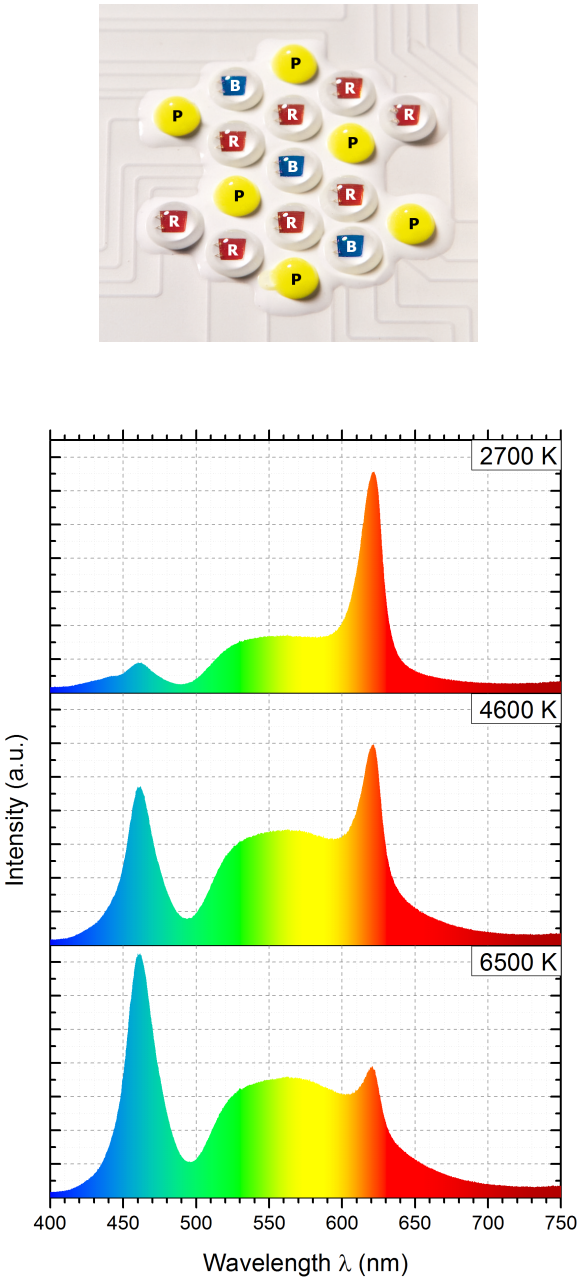

Figure 3.8.: Top panel: LED module using six color converted (P) LEDs in combination with three blue (B) and eight red (R) LEDs. This allows tuning the CCT from 2700 K to 6500 K and provides a CRI above 90 over the whole tunable CCT region (Courtesy of LUMITECH Produktion und Entwicklung GmbH). Bottom Panel: Emission spectrum of the LED module presented for different CCTs. For low CCTs a significant fraction of the visible spectrum lies in the red region, for high CCTs the blue part of the spectrum is dominant, respectively.

3.2.1. LED driver systems

To operate LED light engines basically two types of driver electronics are available. To reduce the temperature impact of the injection current on the pn-junction most of the driver systems are operating the LED in a pulsed mode. Such so called pulsed driver systems inject forward voltage/current pulses with certain duty cycles. The duty cycle is defined as the ratio between the pulse width and the repetition rate of the pulses. To change the light output (dimming) the pulse height remains constant, however the pulse width is getting reduced. Therefore the duty cycle determines the light output level.
On the other hand constant voltage/current drivers inject direct current (DC) whereas the light output can be tuned by changing the current level (height). The main reason that such driver systems are not the system of choice is due to the enormous temperature increase of the pn-junction during operation. Temperature changes lead to shifts of color coordinates and unstable emission spectra. However such driver system do not reveal any kind of flicker effect (stroboscopes).
During this thesis a patent was developed which allows to stabilize the emission behavior of a DC operated LED system. The key aspects of the submitted patent can be found in in chapter 8.
Figure 3.9 illustrates the two driver concepts.

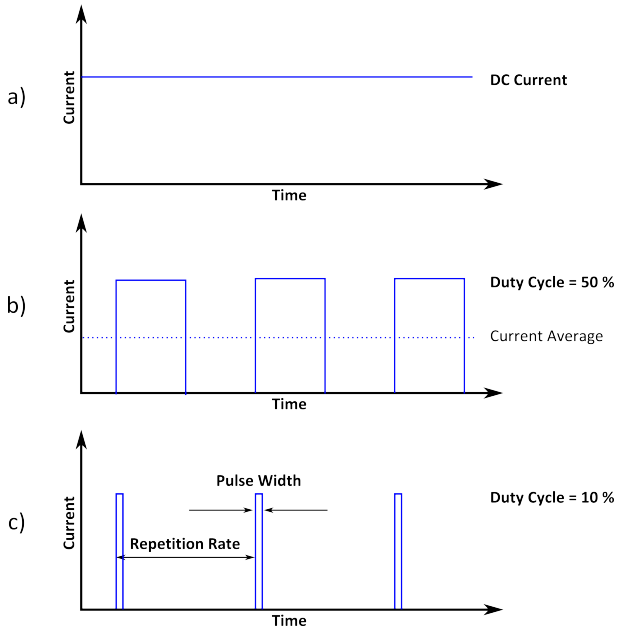

Figure 3.9.: Driver concepts to operate LED light engine. a) DC driver. b) and c) Pulse driver with a 50% and a 10% duty cycle.

3.3. Luminescence

Color conversion materials used to produce white light emitting light engines are based on luminescence. Basic properties like quantum yield and lifetime of color conversion materials were obtained during this thesis. The fundamentals are presented in this section are following reference number [50], the experimental results can be find in chapter 10.

Luminescence is a phenomenon in nature where light is getting emitted from electronically excited states. Luminescence can be divided into two categories, one is called *Phosphorescence* and the other one *Fluorescence*. Excitation into energetically higher electronic states can for instance occur due to absorption of photons. Absorption and emission processes can be illustrated in a Jablonski diagram as shown in figure 3.10. An absorbed photon can be excited to a higher vibrational level S1 or S2. The level of excitement depends on the energy of the incoming photon. Afterwards a relaxation to the lowest excited level S1 due to internal conversion processes usually occurs. Emission from the bottom of S1 to the ground state S0 is then referred to fluorescence whereas the typical fluorescence lifetime is in the nanosecond range [50]. The excited S states are singlet states.
On the other hand phosphorescence occurs from triplet states T1 to the ground state. Such relaxation times are much longer and occur in the millisecond or second range. In the excited triplet state the spin orientation of the excited electron is the same as in the ground state. Therefore the electron undergoes a spin conversion from the singlet state (where opposite spin orientation relative to the ground state is present) to the triplet state (intersystem crossing). The reason for the long lifetimes of the electron in the triplet state is due to the fact that transitions from the T1 to the singlet ground state S0 are forbidden (same spin orientation).
As indicted in figure 3.10 the emission from S1 / T1 is shifted to lower energies. The difference between absorption and emission energy (whereas the emission energy is typically lower than the absorption energy) is called Stokes shift. For color conversion materials used for LED lighting this Stokes shift should be as small as possible due to the fact that energy (and therefore efficiency) is getting lost between excitation and emission.

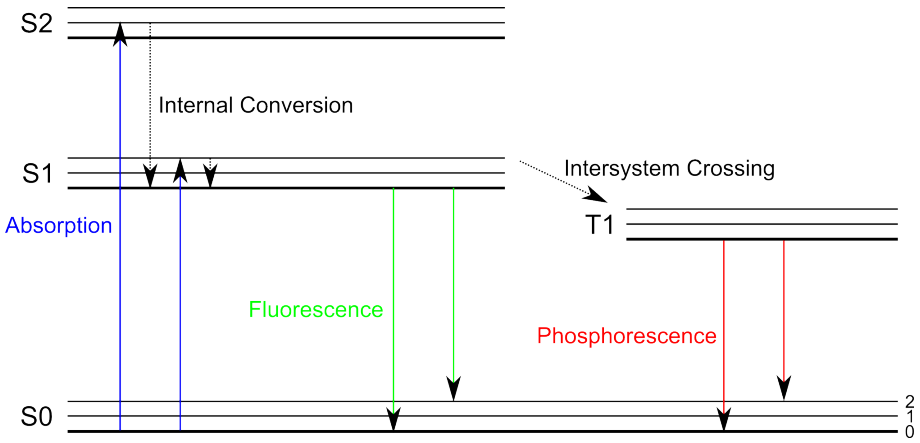

Figure 3.10.: Jablonksi diagram schematically describing Fluorescence (emission from singlet state S1) and Phosphorescence (emission from triplet state T1). Adapted from reference number [50].

3.3.1. Fluorescence lifetime

In this thesis the fluorescent lifetime was determined out of the phase-modulation lifetime measurement (this method is also called frequency-domain method). The principle idea of such setup is presented in this section. For the measurement results and the actual measurement setup please refer to section 10.1.
Figure 3.11 sketches the concept of the frequency-domain method. The excitation source gets modulated in the frequency range of the expected lifetime of the sample (typically in the kHz - MHz region). The sample will emit in the same matter as the modulation of the excitation source. If the lifetime of the sample is in the same range as the modulation frequency of the excitation source a shift of the emission response will occur. This can be noticed by a phase shift of the emission response relative to the modulation of the excitation source. Further the emission intensity will decrease because emission occurs when the minimum of excitation is reached. The modulation factor can be obtained out of the ratio between peak maximum of the excitation a and the peak height of the emission b, respectively (equation 3.4):

$$m = \frac{b}{a} \tag{3.4}$$

In the experiment discussed above the fluorescent intensity $I(t)$ relative to time t is discovered. This intensity is proportional to the number of exited molecules $n(t)$ which exponentially decreases with the lifetime τ (equation 3.5)

$$n(t) = n_0 e^{\frac{-t}{\tau}} \tag{3.5}$$

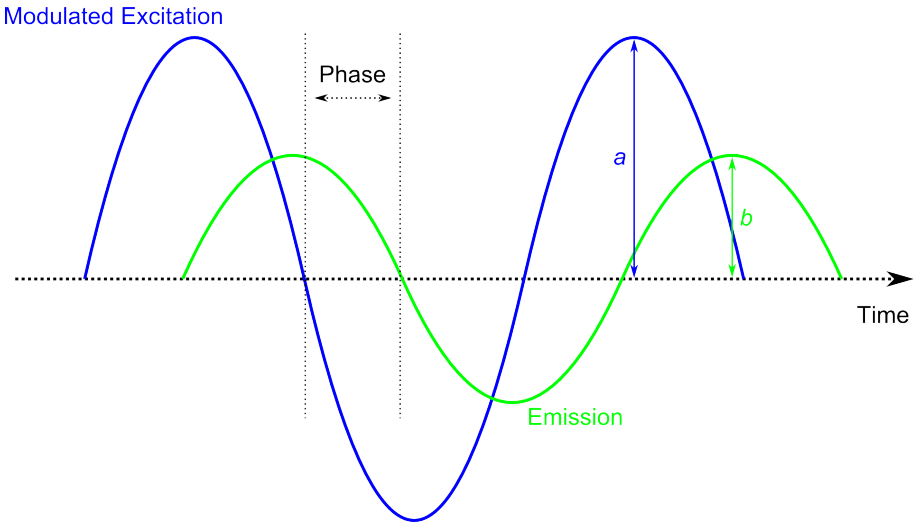

Figure 3.11.: Principle idea of fluorescent lifetime determination via frequency-domain method. The phase shift as well as the intensity change with respect of the emission response relative to the excitation source is obtained. The modulation m is given out of the ratio of the peak heights a and b (equation 3.4). Figure adapted from reference number [50].

whereas n_0 is the initial population. The fluorescent intensity can then be written (equation 3.6):

$$I(t) = I_0 e^{\frac{-t}{\tau}} \tag{3.6}$$

The average amount of time the fluorophore stays in the excited states can be written as shown in equation 3.7:

$$< t >= \frac{\int_0^\infty tI(t)dt}{\int_0^\infty I(t)dt} \tag{3.7}$$

whereas for a single exponential decay equation 3.8 is valid:

$$< t >= \tau \tag{3.8}$$

The phase shift ϕ as well as the modulation m can be obtained experimentally. Those parameters can be used to obtain the lifetime of the sample taking equation 3.9 and equation 3.10 into account.

$$\tan(\phi) = \omega\tau_\phi \tag{3.9}$$

$$m = \frac{1}{\sqrt{1+\omega^2\tau_m^2}} \tag{3.10}$$

whereas ω is the modulation frequency and τ_ϕ and τ_m are the lifetimes gained out of the respective phase ϕ or out of the modulation m.

3.3.2. Fluorescence quantum yield

The quantum yield reflects the light conversion efficiency of a certain material. In the case of color converting materials this value should be as close to unity as possible to gain highly efficient light engines. The quantum yield is generally defined as the fraction of the number of photons emitted relative to number of photons absorbed (equation 3.11):

$$\Phi = \frac{\#\text{number of photons emitted}}{\#\text{number of photons absorbed}} \tag{3.11}$$

more specifically (equation 3.12)

$$\Phi = \frac{\Gamma}{\Gamma + k_{nr}} \tag{3.12}$$

whereas Γ is the rate constant (emission rate) and k_{nr} the rate of the non-radiative decay. The quantum yield can be close to 1 if the non-radiative decay is very small, however due to the Stokes shift there will be always energy lost between excitation and emission.

Demas and Crosby [51] accurately defined the quantum yield of a compound as *"the fraction of molecules that emit a photon after direct excitation by the source"*. This is not exactly the same definition as discussed in equation 3.11 and equation 3.12, however for our purposes the definition shown in equation 3.11 is sufficient enough.

A quite recently published review summarizes and compares certain methods for the determination of the quantum yield [52]. In this thesis the presented results were determined by the comparison with the quantum yields of a reference standard sample Φ_R. Equation 3.13 then leads to the quantum yield Φ_S of the investigated sample S:

$$\Phi_S = \Phi_R \frac{F_S(\lambda_{ex})}{F_R(\lambda_{ex})} \frac{f_R(\lambda_{ex})}{f_S(\lambda_{ex})} \frac{n_S^2}{n_R^2} \frac{q_R(\lambda_{ex})}{q_S(\lambda_{ex})} \tag{3.13}$$

whereas R and S are standing for reference standard and sample, respectively. Further n_R and n_S are the index of refraction of the solvent of reference standard and sample, q_S and q_R are the photon fluxes at sample position for reference standard and sample at chosen wavelength λ_{ex}. If possible, the excitation wavelength λ_{ex} of sample and reference standard should be the same, however if this is not the case, by measuring the respective photon fluxes this can be adjusted (q values).

$f_S(\lambda_{ex})$, $f_R(\lambda_{ex})$ are the absorption factors given by equation 3.14:

$$f(\lambda_{ex}) = 1 - 10^{-A(\lambda_{ex})} \tag{3.14}$$

whereas $A(\lambda_{ex})$ is the absorbance at the excitation wavelength λ_{ex}. The factor F is the integrated spectral fluorescence photon flux defined by equation 3.15:

$$F = (hc_0)^{-1} \int_{\lambda_{em_1}}^{\lambda_{em_2}} \frac{I(\lambda_{em})}{s(\lambda_{em})} \lambda_{em} d\lambda_{em} \tag{3.15}$$

$I(\lambda_{em})$ is the blank corrected emission intensity, $s(\lambda_{em})$ the spectral responsitivity of the detector, and $(hc_0)^{-1}\lambda_{em}$ the conversion factor from an energy scale to a photon scale.
To increase the accuracy of the measurement, various concentrations of reference and sample solutions have to be measured. Afterwards one can plot the spectral fluorescence photon flux plot F versus the absorption f for the various concentrations. The gradient of the linear fit through the measurement data directly leads to term $\frac{F_S(\lambda_{ex})}{f_S(\lambda_{ex})}$ (indirectly to $\frac{f_R(\lambda_{ex})}{F_R(\lambda_{ex})}$) in equation 3.13.
For the experimental procedure and the measurement results please refer to section 10.2.

3.4. Focused ion beam (FIB) & electron dispersive X-ray spectroscopy (EDX)

In this thesis samples have been investigated by a focused ion beam (FIB) microscope as well as analyzed by the use of an electron dispersive X-ray (EDX) spectroscope. In this section only the principles of those two analyzing tools will be presented (based on the review of Steve Reyntjens and Robert Puers [53] for FIB microscopy and [54] for EDX measurements). The performed measurements can be found in section 4.1.

FIB investigations are applied in the semiconductor industry to perform failure analysis, material research and process inspection. Further samples can be structured for micromachining applications or prepared for transmission electron microscopy (TEM) investigations.
A FIB consists in principle out of an *ion column*, a *vacuum*, a *gas injection system* and a *work chamber*. In the ion column Ga+ ions are produced and emitted. Liquid Ga in a chamber in combination with a high electric field (10^8 V/cm) allows to emit Ga+ ions from a liquid droplet on a thin tungsten needle. The ion column is very similar to the electron column in a scanning electron microscope (SEM) however, instead of electrons, typically Ga+ ions are used as particle source. The whole ion chamber is under a vacuum pressure of around 10^{-7} mbar.
The ion beam gets collimated and focused through several lenses and apertures. The

ion beam energy is typically around 10 keV to 50 keV, the current in between 1 pA to 10 nA. The sample is mounted on a work stage within the work chamber. Typically a five-axis stepping motor allows to move the stage in several directions and it allows rotation around a certain axis. In most FIB systems a gas injection system is implemented which can be used for etching or for deposition of certain materials.
When the ion beam hits the sample surface several physical (energy loss of the ions due to interaction with atoms and electrons of the sample) and chemical processes (breaking of bonds) occur. The energy loss can be transferred to heat (phonons) or can induce damages to the sample (atom displacement). In addition neutral and ionized substrate atoms can be sputtered, therefore removal of parts of the sample is possible by the use of a high current beam (so called milling).
In case of milling the ion beam is scanning the sample surface and etching of certain shapes into the surface is possible. For enhancement of the etching rate selected gas through the gas nozzle can be inserted (e.g. Cl_2, Br_2).
Moreover through this gas nozzle certain materials can be deposited by the FIB system on behave of the chemical vapor deposition (CVD). The precursors gas is getting adsorbed and the materials are getting decomposed through the ion beam. One example is illustrated in figure 3.12 where platinum (Pt) on a gold circuit path on an LED surface was deposited.

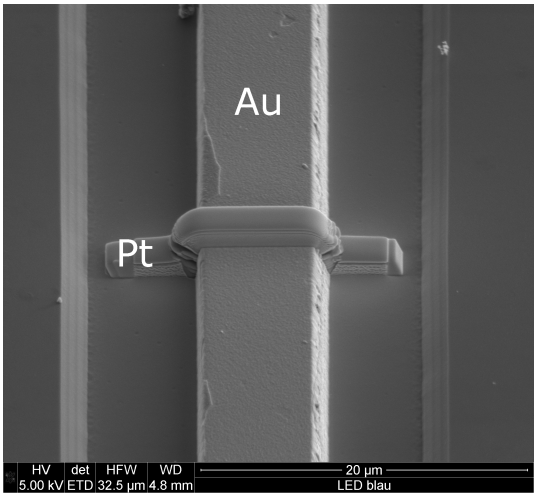

Figure 3.12.: Deposited platinum (Pt) on the gold circuit path (Au) which is located on the surface of a GaN-based LED.

The energy of the ion can be also transferred to secondary particles (electrons, ions and atoms) which are getting emitted from the sample surface. The energy measurement of those secondary particles enables imaging while the ion beam is scanning the surface of the sample. It should be mentioned at this point that imaging with the FIB also leads to

undesired milling as well as to implementation of Ga+ ions in the sample. The implementation depth depends on the incident angle as well as on the beam energy.
The system used to investigate the presented samples in this thesis is in a dual beam configuration whereas a scanning electron microscope (SEM) is combined with the FIB. The electron column of the SEM is tilted 52° to the ion column. Such system allows a live view of the FIB process using the SEM.

Electron dispersive X-ray spectroscopy (EDX)

The sample compilation was analyzed by using an electron dispersive X-ray spectroscope (EDX). This technique allows to chemically analyze and map the occurring elements in the sample.
EDX spectroscopy is based on fluorescence. Via X-rays or electrons an electron in the inner shell of the material can be excited by photo-ionization. An electron from an higher shell will then refill this generated hole whereas through the recombination process either radiative emission of non-visible light (X-rays) or an Auger emission is occurring. The fluorescent emission is characteristic for each element, therefore by measuring the energy, an elemental assignment to the energy levels can be performed. The Auger emission is non-radiative and dominant for elements with low nuclear charge values Z. For Z values above 30 the X-ray emission becomes dominant. This leads to the circumstance that for low Z values this technique becomes less appropriate due to the decrease of radiative emission (increase of the Auger emission).
The penetration depth can be increased if X-rays instead of electrons are used as excitation. Moreover X-ray excitation can be performed under ambient conditions.
For electron irradiation on the other hand ultra high vacuum is a prerequisite, however a very high spatial resolution can be achieved.
In figure 3.13 an EDX measurement of a GaN-based LED crosscut is illustrated. The excitation energy of this measurement was 15 keV.

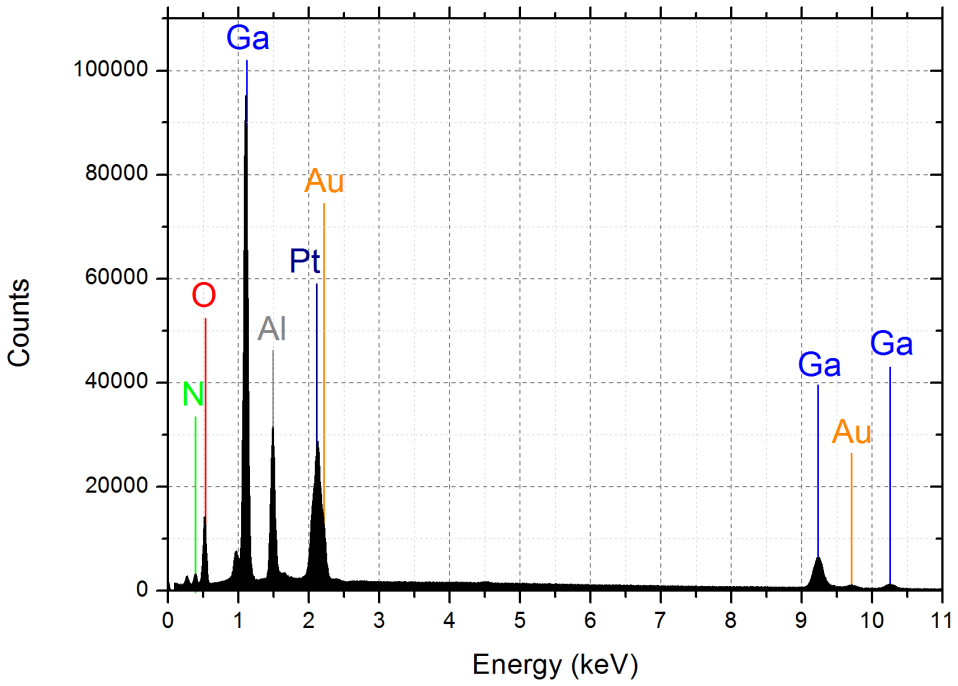

Figure 3.13.: Example of an EDX measurement of a cross cut through a GaN-based LED. The excitation energy is 15 keV. The fluorescent emission energy is characteristic and can be assigned to certain elements.

3.5. Electron beam induced current (EBIC)

The following text is based on a review article by Leamy, reference number [55].

Electron beam induced current (EBIC) is a general tool to investigate basic properties of semiconductor materials. The location of pn-junctions, recombination centers as well as layer inhomogeneity can be detected and imaged. Further, diffusion lengths and carrier lifetimes in semiconductor materials can be obtained.
An EBIC system contains basically a scanning electron microscope (SEM) where an external amplifier circuit measures the so called EBIC signal. Electron bombardment on the sample leads to an ionization of the atoms and therefore generates charge carriers (electrons and holes) in the sample. The EBIC system is sensing the current which is produced by the electron beam (figure 3.14).

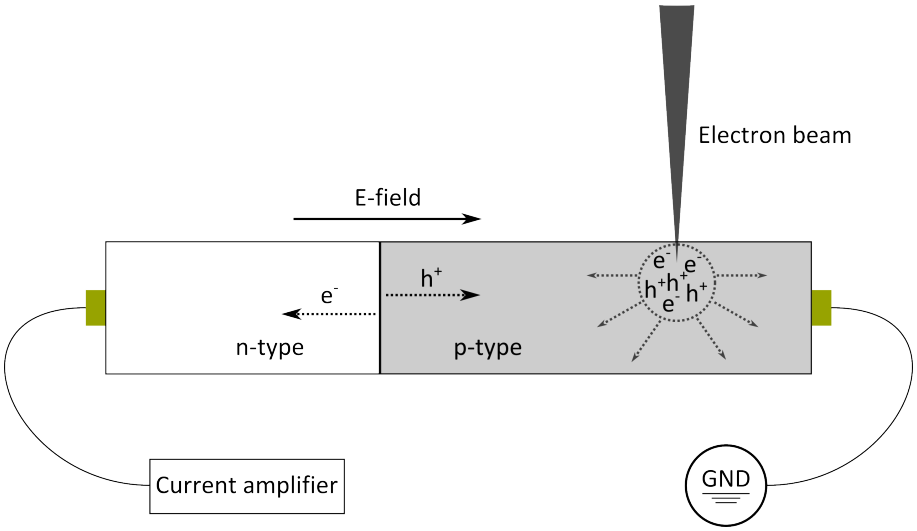

Figure 3.14.: Measurement scheme of an EBIC system. Charge carriers are produced by the electron beam, get separated by an an internal electric field and collected by an external circuit.

One prerequisite for detection of an EBIC signal is that the investigated sample supports an internal electric field (e.g. pn-junction, Schottky contact, etc.). Charge carriers which are produced by the electron beam get separated by the internal electric field and drift to the contacts where they can be detected by an external circuit (amplified circuit). If the electron beam produces charge carriers away from the internal electric field, those will diffuse to the edges of the space charge region and will get separated afterwards. Depending on the position where the electron beam produces the charges relative to the position of the internal electric field, the strength of the EBIC signal varies. I.e. a high

internal electric field leads to a strong EBIC signal, a low electric field to a small signal, respectively. The position of the electron beam relative to the sample can be varied and the behavior of the EBIC signal relative to the (scanning) electron beam position can than be recorded and imaged.
In a pn-junction a depletion zone arises where (virtually) no mobile charge carriers are located (see section 3.1.3). If charge carriers are generated directly at the pn-junction they will drift to the edges of the depletion zone and induce a charge at the external surface of the sample. The collected current flows in direction of the electric field (built in field) and occurs due to drift of minority carriers and not due to the drift of majority carriers. The electric field is pointing from the n-type region to the p-type region, which means that a positive measured EBIC signal has to be measured on the p-type side, a negative signal on the n-type side, respectively.
Figure 3.15 shows an actual SEM picture of an AlGaInP-based LED which is contacted by two measuring needles which record the EBIC signal. One needle is connected to the current amplifier circuit, the other one to the ground. Depending which of the needles is connected to the amplifier circuit, whether a positive or a negative signal is measured.

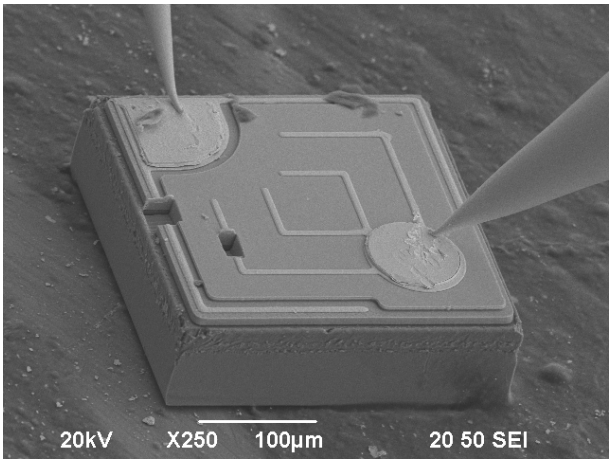

Figure 3.15.: Scanning electron microscope picture of an AlGaInP-based LED inducing two measurement needles to record the EBIC signal. One is connected to the circuit amplifier the other one to ground.

Part II.

Experimental Investigation

4. Sample investigation & sample preparation

Two types of LEDs were mainly investigated regarding their temperature and current properties. One type is emitting in the blue range (GaN-based) of the visible spectrum and one in the red region (AlGaInP-based), respectively. The reason for investigating those types is, that for a tunable white light system such LED constellation is needed (see section 3.2). The samples were investigated by applying several analyzing tools. This section deals with the examination of the basic properties of this two types of LEDs. The distributor specifications of the two types of LEDs are shown in table 4.1.

Table 4.1.: Distributor specifications of the GaN-based and AlGaInP-based LEDs.

	GaN	**AlGaInP**
Producer / corporation	TE Opto	Epistar
Product number	ETCJ8-0BAG1-F1	ES-AESOAX14
Maximum DC forward current (mA)	240	50
Maximum reverse voltage (V)	5	10
Maximum junction temperature (°C)	140	125
Dominant wavelength min/max at 25°C (nm)	450 / 460	610 / 620
Typical spectral bandwidth at 25°C (nm)	25	18
Chip dimension (W x L x H) (μm)	510 x 1020 x 150	355 x 355 x 100
Size bonding pad N / P (μm)	82.5 / 82.5	100 / 100
Electrodes	Au	Au
Substrate	Al_2O_3	Al_2O_3

Optical microscope pictures of the two types of LEDs are shown in figure 4.1. The image magnification of the red LED is 200 times, of the blue LED 50 times, respectively. The dimensions of the LEDs were checked using the optical microscope; for the blue emitting GaN-based LED 520 x 1010 μm, for the red AlGaInP-based LED 295 x 300 were μm measured. To electrically contact those LEDs, a 30 μm thick gold wire was bonded on the bonding pad as well as to a printed circuit board.
To gain information about the uniformity of the emission of the LEDs, they were operated under the optical microscope with a very low DC current level which was 5 μA for the blue emitting and 2 μA for the red emitting LED, respectively. This uniformity is

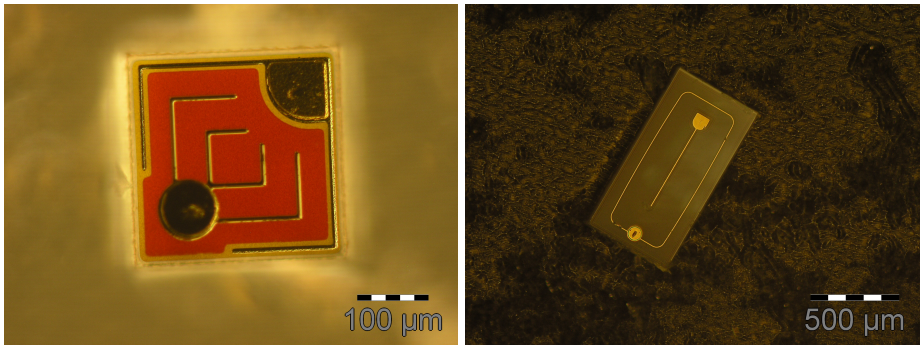

Figure 4.1.: Optical microscope images of the red emitting AlGaInP-based LED (left panel, image magnification 200 times) and the GaN-based LED (right panel, image magnification 50 times).

important due to the fact that for several experiments a very thin fiber optics was placed on top of the LED surface and therefore it has to be ensured that the position of the fiber optics relative to the diode surface does not influence the measuring result. Figure 4.2 again shows the LEDs now contacted and during operation driven at very low current levels.

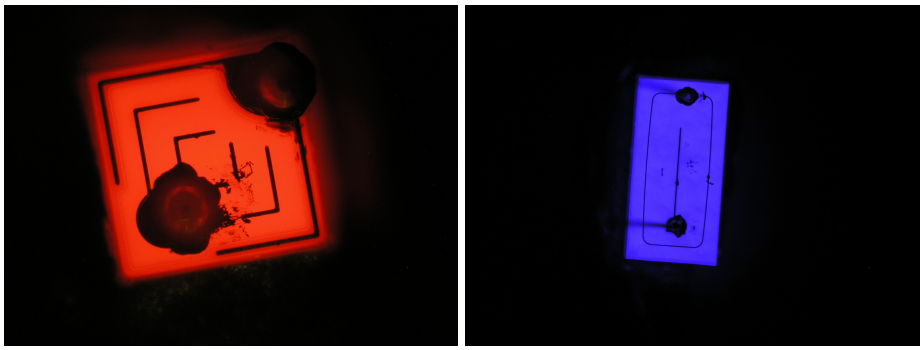

Figure 4.2.: Optical microscope images of the operated red emitting AlGaInP-based LED (left panel, image magnification 200 times) and the GaN-based LED (right panel, image magnification 50 times). The DC current level was 2 µA for the red emitting AlGaInP-based and 5 µA for the blue emitting GaN-based, respectively.

4.1. FIB & EDX investigations

To gain insight into the LED structure, focused ion beam (FIB) investigations in combination with energy-dispersive X-ray spectroscopy (EDX) were performed. A basic summary of those two techniques can be found in section 3.4.

4.1.1. GaN-based LED

Two FIB crosscuts through each electrode (top and bottom electrode) of the LED have been performed. Figure 4.3 shows a scanning electron microscope (SEM) picture of the GaN-based LED surface including the two FIB tranches on each electrode whereas the ring electrode (outer electrode) is referred to the top electrode (p-electrode). The straight electrode located midway relative to the LED surface is referred to the bottom electrode (n-electrode). Out of this image one can see the proportion between the thick sapphire substrate relative to the very thin semiconductor layer on top. The LED was mounted with conducting graphite to an aluminum sample holder.
The crosscut of the top electrode (marked in figure 4.3) as well as the EDX mapping can be found in figure 4.4. The EDX mapping region is indicated as a rectangle in the overview plot.
The semiconductor layers are grown on a pre-patterned Al_2O_3 sapphire substrate. The pattern can be identified by the triangles in the FIB crosscut. On top of the substrate an approximately 8 μm thick GaN layer structure is followed by an 150 nm thin AlN-based layer. The layer structure was obtained out of the performed EDX measurement. The height of the gold electrode is around 2.5 μm. In between the gold electrode and the AlN-based layer a distinct layered structure is observable. FIB in combination with EDX did not allow us to gain more information about the detailed structure of these layers (QW structure). On top of the gold electrode a platinum layer was deposited to perform the FIB cut. This platinum layer reduces charging effects and prevents samples from damage during the sputtering process.

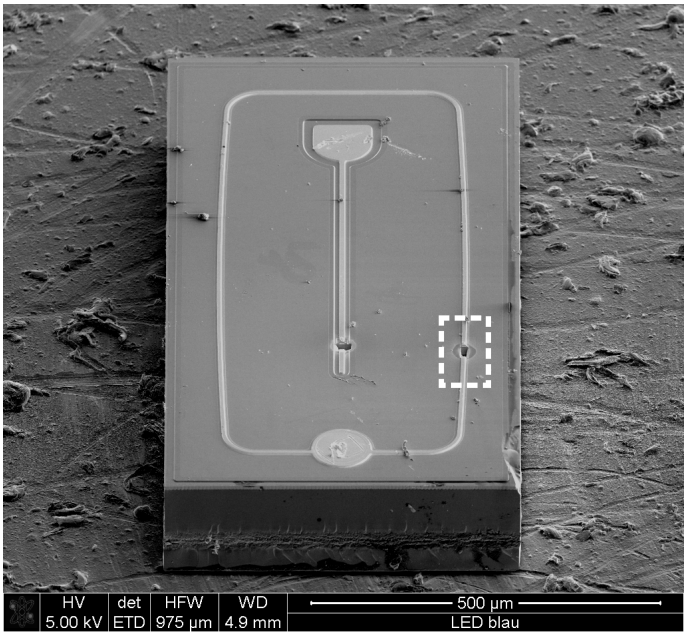

Figure 4.3.: Overview scan of the blue emitting GaN-based LED in a FIB microscope. Two FIB-cut trenches can be identified; one on the top electrode (ring electrode, on the right hand side, marked) and one at the bottom contact (in middle of the image).

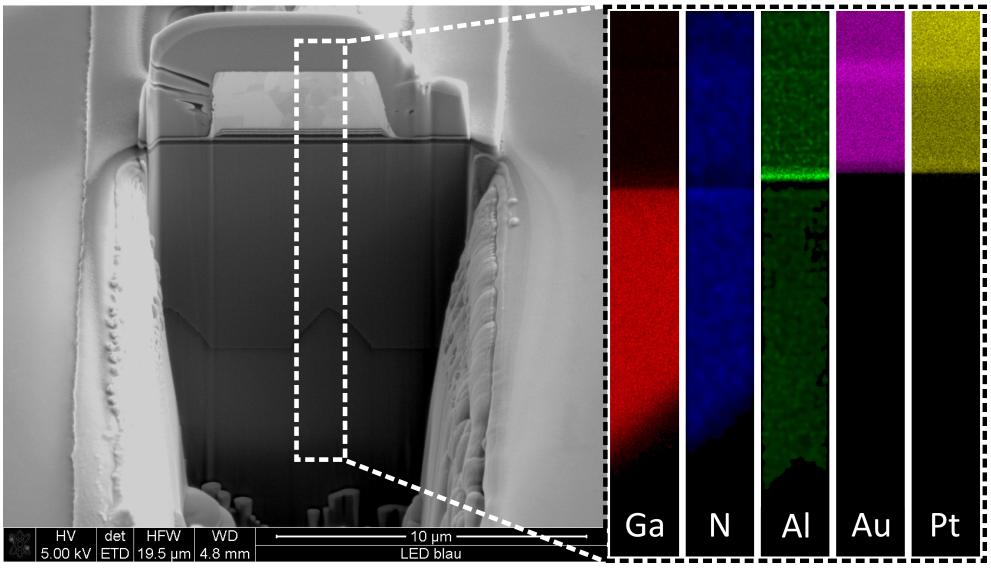

Figure 4.4.: Left panel: Image of the crosscut through the top electrode of the GaN-based LED (FIB cut position indicated in figure 4.3). The rectangle indicates the EDX mapping region. Right panel (starting from left to right): EDX mapping of certain elements, Ga, N, Al, Au and Pt. The platinum was deposited to protect the sample during sputtering of the FIB trenches.

The pre-patterning of the substrate can be also identified in figure 4.5. On can see the pre-patterned substrate in the SEM image during the FIB crosscut preparation (bottom panel) as well as in the optical microscope picture shown in the top panel of figure 4.5.

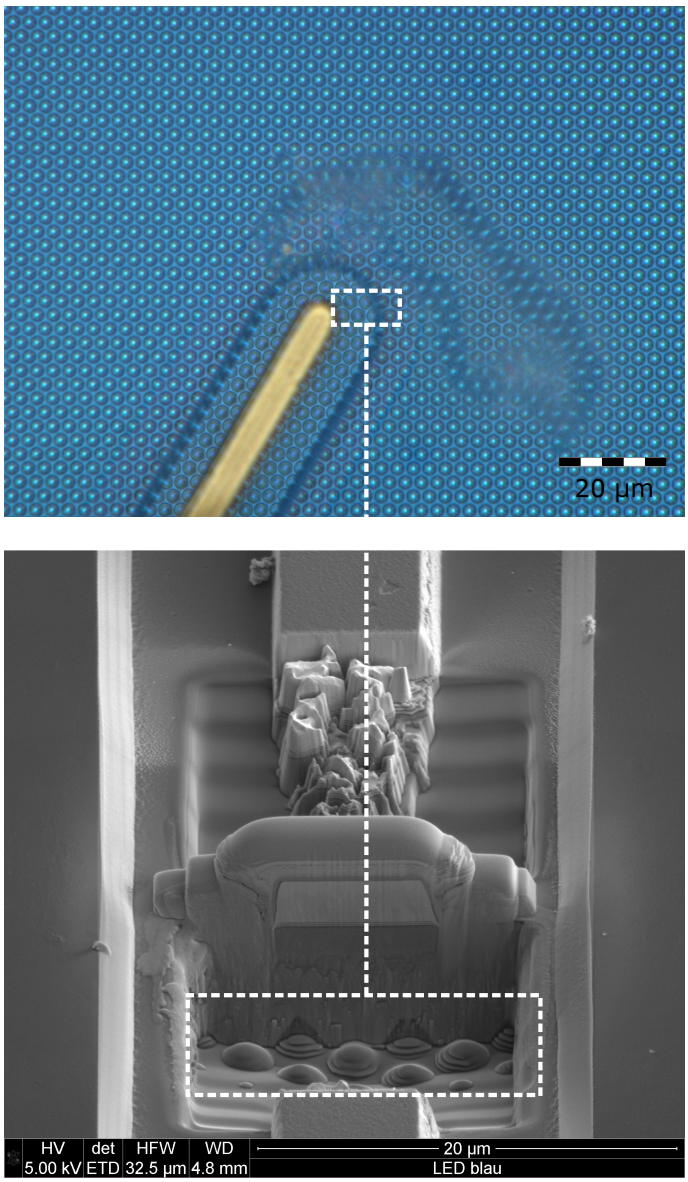

Figure 4.5.: Top panel: Optical microscope of the surface of the GaN-based LED. The pre-patterning of the substrate surface can be identified through the transparent semiconductor layer. Bottom panel: SEM image during the FIB cutting process. The rectangular highlights the pre-patterned structure of the substrate.

Further the surface of the GaN-based LED was investigated performing EDX measurements on a surface position on the sample (not on the electrode). To gain surface sensitive information the acceleration voltage of the electron beam was varied between 15 keV and 2 keV. Large acceleration voltages of the electron beam increase the penetration depth, therefore it is very hard to distinguish if the signal (emission) is related to the surface or to the bulk materials. By varying the voltage and comparing those results with the EDX measurement performed in the crosscut, conclusions about the surface materials can be drawn.
The elemental spectra for three acceleration voltages (2 keV, 5 keV and 15 keV) are depicted in figure 4.6. Out of this measurement we obtained that the surface of the blue emitting GaN-based LED is covered with a transparent silicon oxide SiO_2 layer. The evolving C peak in the 2 keV measurement arises from carbon contamination.

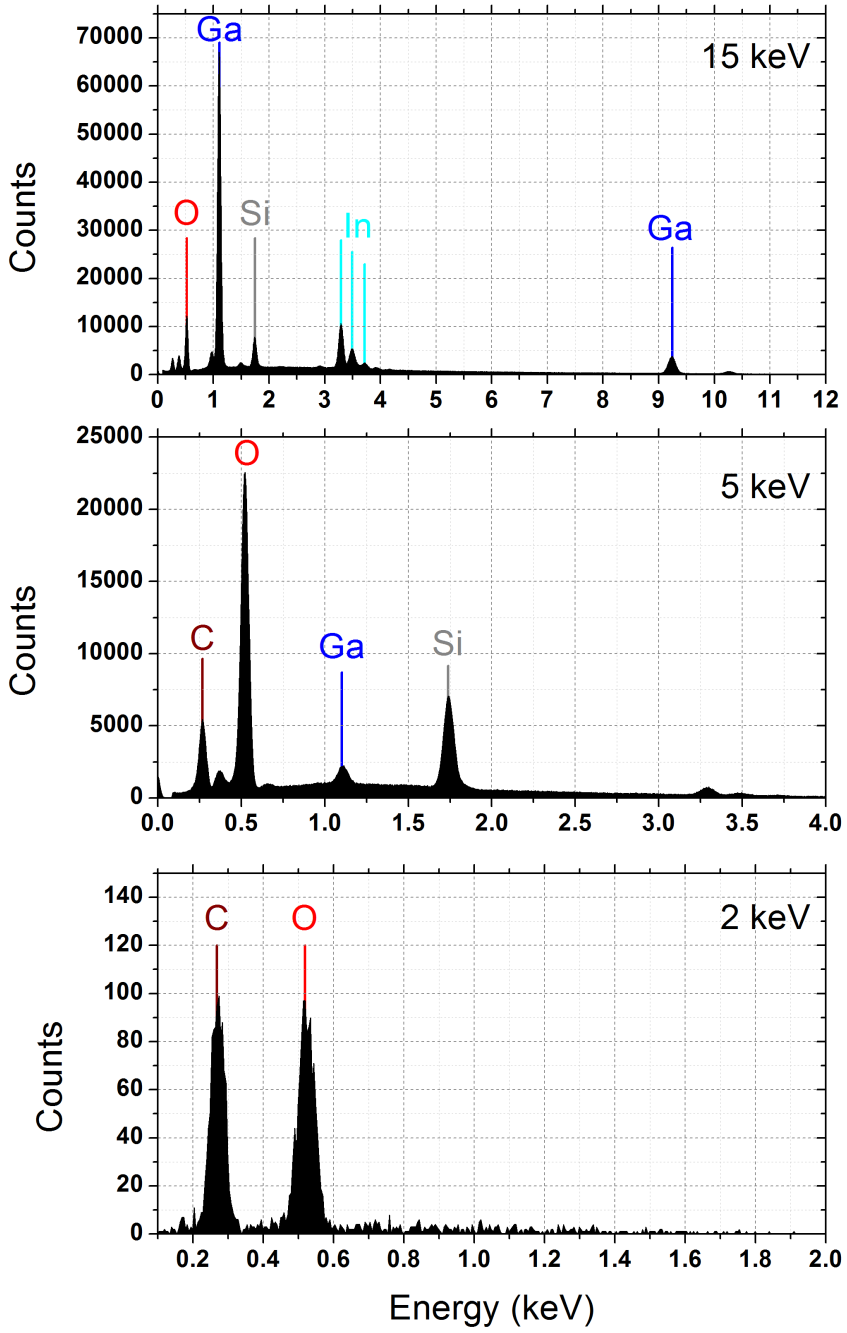

Figure 4.6.: EDX investigations of the surface of the GaN-based LED. The acceleration voltage was varied from 15 keV (top) to 5 keV (middle) and 2 keV (bottom) to reduce the penetration depth of the electron beam.

4.1.2. AlGaInP-based LED

Figure 4.7 shows the overview of the red emitting AlGaInP-based LED. Again two FIB cuts were performed whereas platinum was deposited beforehand. The overall thickness of the device is 100 μm whereas the thickness mainly arises from the substrate. In the overview image two distinct semiconductor layers (assignment see below) on top of the substrate can be identified.
The topside electrode contains the round shaped bonding pad and is referred to the n-electrode. The bottom electrode is the p-electrode, respectively. The LED was mounted again with conducting graphite on an aluminum sample holder. The vesica on the surface next to the FIB crosscut of the top electrode (right panel in figure 4.7) arise from the interaction of the ion beam and the surface material.

In figure 4.8 the top electrode is illustrated including the EDX mapping. In this case the sapphire substrate is not specially patterned (in terms that it will be observable with the applied techniques). However, a 1.1 μm buffer layer is placed on top of the substrate. On top of the buffer layer a 9.5 μm thick GaP layer is followed by a 2.7 μm thick AlInP layer. The gold electrode height is just 1 μm. The platinum layer deposited shows a distinct two layer structure which can be assigned to the different depositing rate used (lower evaporation rate at the beginning).

Again surface sensitive EDX analysis was performed, whereas the electron beam voltage was varied between 2 keV and 15 keV. We found an thin transparent SiO_2 passivation layer on top of the LED (see figure 4.9). The evolving C peak in the 2 keV measurement arises from carbon contamination.

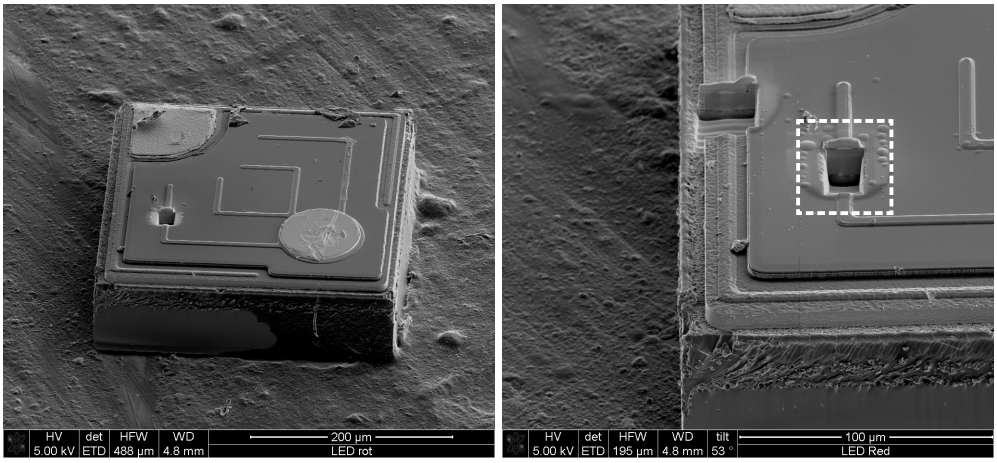

Figure 4.7.: Overview of the red emitting AlGaInP-based LED; the right panel shows the zoom where the FIB trenches are located. Rectangular indicates the FIB cut through the top electrode (FIB investigation is shown in figure 4.8).

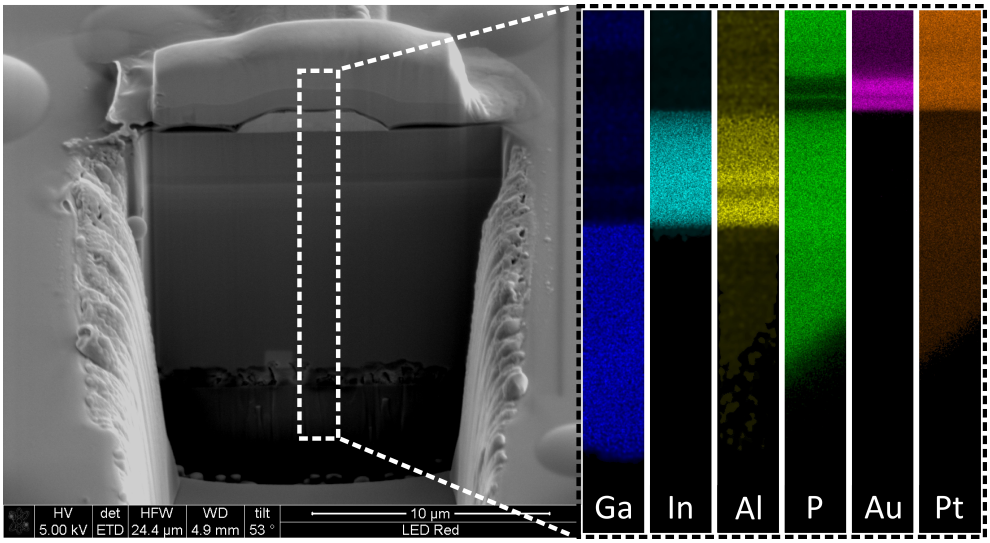

Figure 4.8.: Left panel: Image of the crosscut through the top electrode of the AlGaInP-based LED. The rectangle indicates the region where EDX analysis was performed. Right panel (starting from left to right): EDX mapping of certain elements, Ga, In, Al, P, Au and Pt. The platinum was evaporated to protect the sample during sputtering of the FIB trenches.

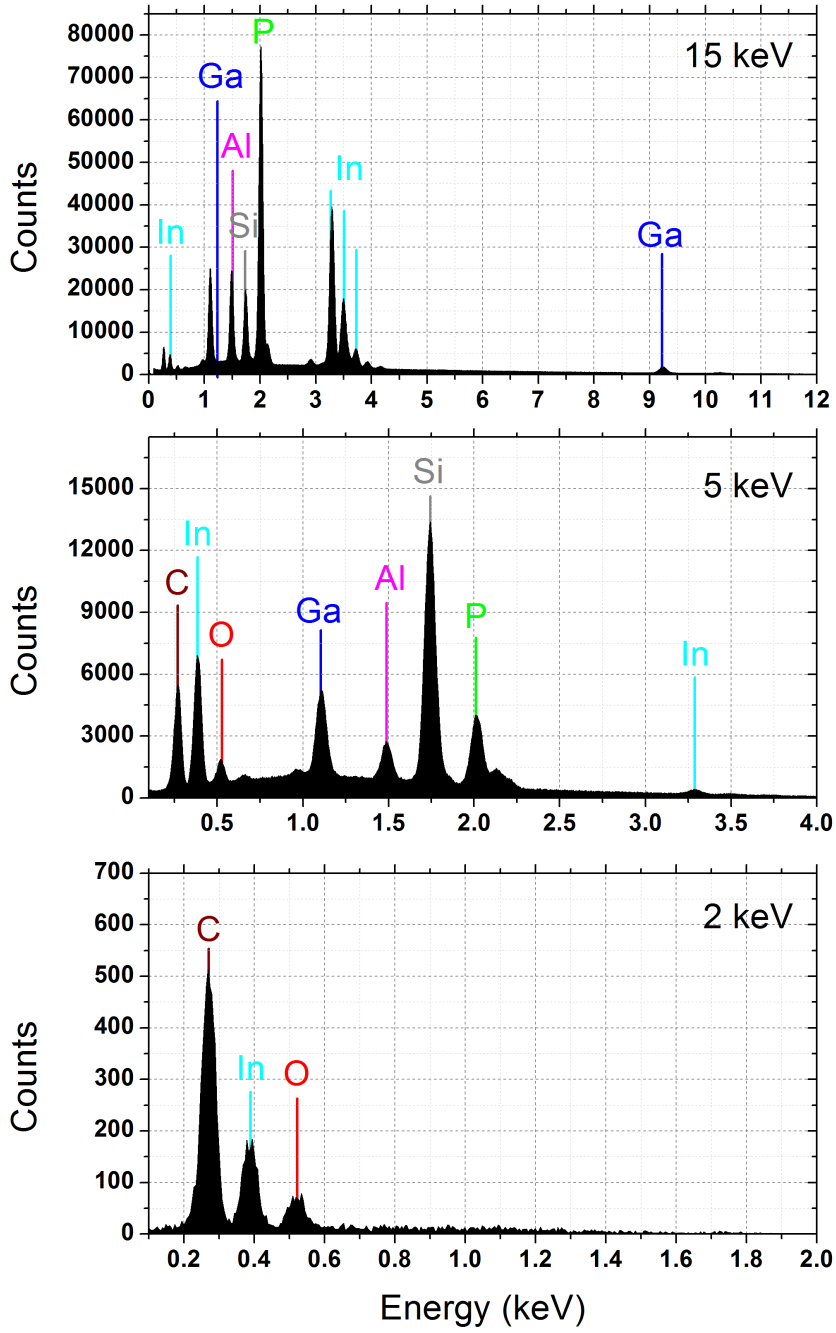

Figure 4.9.: EDX investigations of the surface of the AlGaInP-based LED. The acceleration voltage was varied from 15 keV (top) to 5 keV (middle) to 2 keV (bottom), respectively.

4.2. EBIC investigations

The fundamental principles of the electron beam induced current (EBIC) method are illustrated in section 3.5.
Due to the FIB cut preparation, investigations of the cross section using EBIC were possible. The EBIC signal can be plotted in various ways, for clarity some common ways of graphical illustration are summarized:

- Contour plots: The scanning position of the electron beam relative to the investigated area is plotted. Lines with the same current are displayed and color coded regarding their current level. Different colors refer to different current levels. Regions where the numbers of lines are increasing show enhanced current activity. Due to illustration reasons, the EBIC signal is sometimes plotted on a logarithmic scale instead of a linear one. However the direction of the electric field is lost due to the fact that the sign is not considered anymore on a logarithmic scale.
- Gray scale plots: The recorded EBIC signal for each scanning position (electron beam position) is displayed using gray scale color coding. For negative signals white regions correspond to no signal; grayish colors to high currents, respectively. The situation of the color coding is plotted vice versa for positive EBIC current signals (white indicates low negative values, gray no signal).
- Surface plots: In this 3 dimensional plot the absolute EBIC signal is plotted on the z-axis. Further the current levels are color coded as well. The x and y directions correspond to the surface position of the electron beam relative to the sample.

The corresponding scanning electron microscopy (SEM) picture is always included in the figure.

4.2.1. AlGaInP-based LED

Figure 4.10 shows the contour plot to the corresponding SEM picture of a red emitting AlGaInP-based LED. The EBIC investigations were performed at the crosscut beneath the top electrode which is also indicted in figure 4.10. The EBIC signal shows negative current values which indicates that the doping region close to the top electrode is n-type. Since the EBIC signal was obtained from the top electrode, a negative value means that the electric field is pointing from the top electrode to the bottom electrode. Therefore the top electrode has to be the n-electrode. This agrees with the information out of the data sheet. Figure 4.11 shows the corresponding gray scale plot, which highlights the pn-junction of the device.
Out of figure 4.12 and figure 4.13 we can address the pn-junction of the AlGaInP-based red emitting LED. Figure 4.12 and figure 4.13 are a zoom into the crosscut shown in figure 4.10 and figure 4.11. Figure 4.12 shows the corresponding SEM image including the contour plot, figure 4.13 the respective gray scale plot and the surface plot. The magnification of the SEM image shown in figure 4.12 and figure 4.13 is 15000 times. The pn-junction is located where the maximal EBIC signal is measured and therefore lies in the middle of the 3 μm thick AlInP layer (which is grown on top of the 10 μm thick GaP layer, see section 4.1.2).
Due to the fact that the EBIC signal decreases rapidly, one can assume that the diffusion length of the charge carriers is quite small. The acceleration voltage of the electron beam was 20 keV.

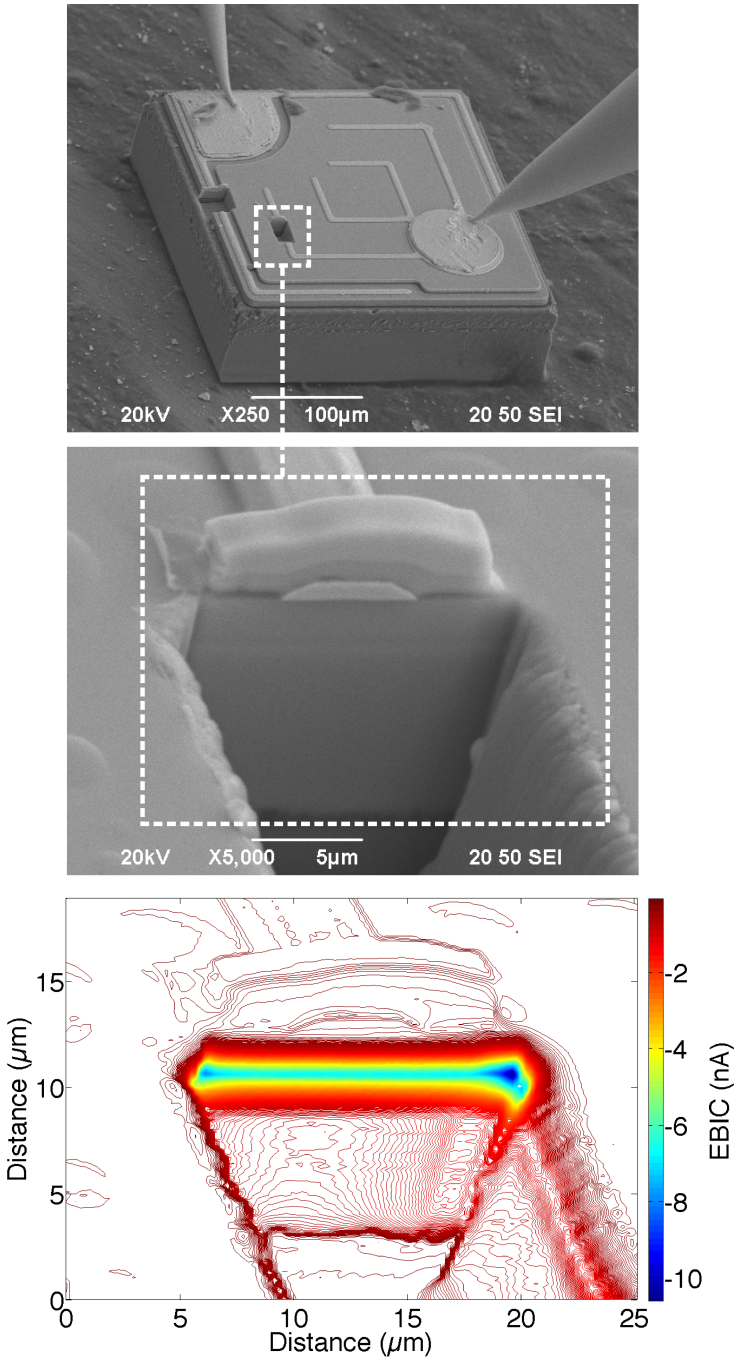

Figure 4.10.: Top: Overview image of the AlGaInP-based LED. Rectangular indicates the FIB trench were EBIC measurements were carried out. Middle: Scanning electron microscope (SEM) picture of the FIB cut through the top electrode. The acceleration voltage was 20 keV, the magnification 5000 times. Bottom: Contour plot of the same region. Low negative EBIC signal indicates the location of the pn-junction.

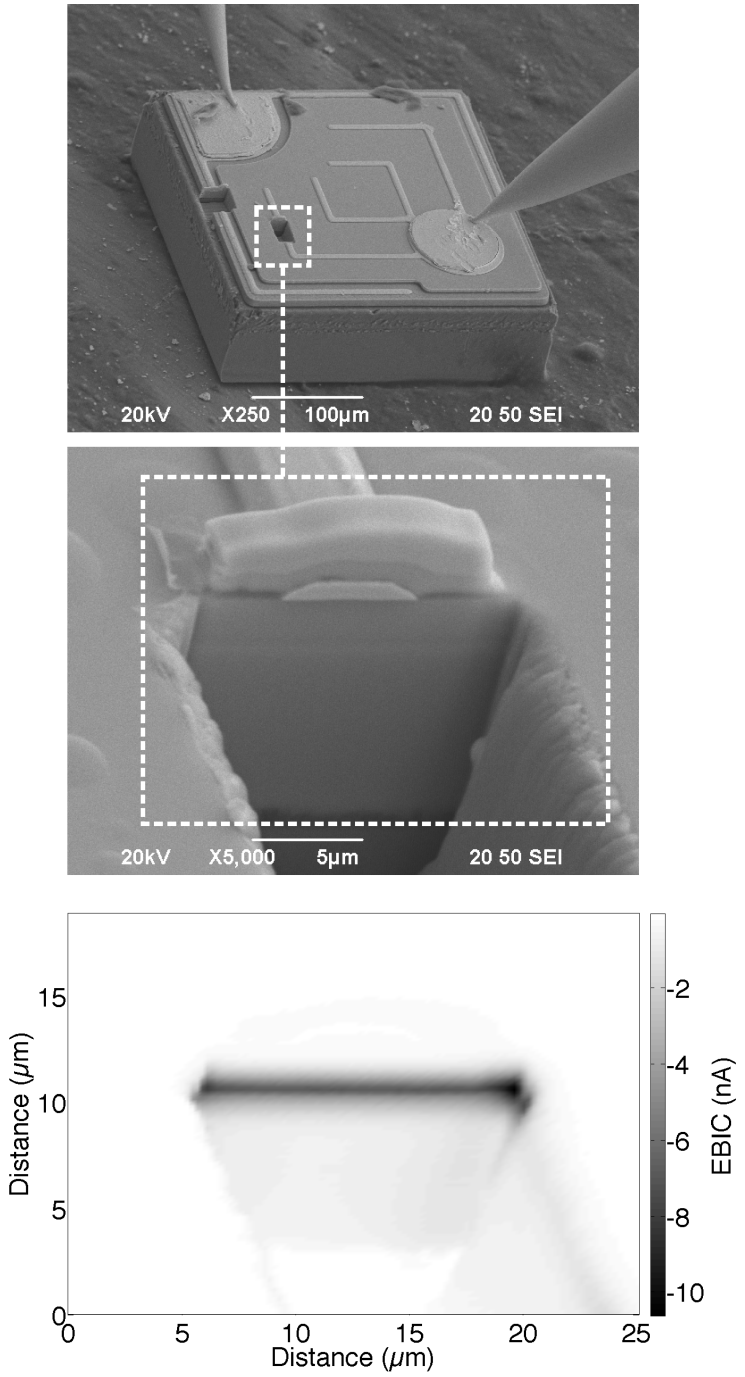

Figure 4.11.: Top: Overview image of the AlGaInP-based LED. Rectangular indicates the FIB trench were EBIC measurements were carried out. Middle: Scanning electron microscope (SEM) picture of the FIB cut through the top electrode. The acceleration voltage was 20 keV, the magnification 5000 times. Bottom: Respective gray scale plot indicating the location of the pn-junction

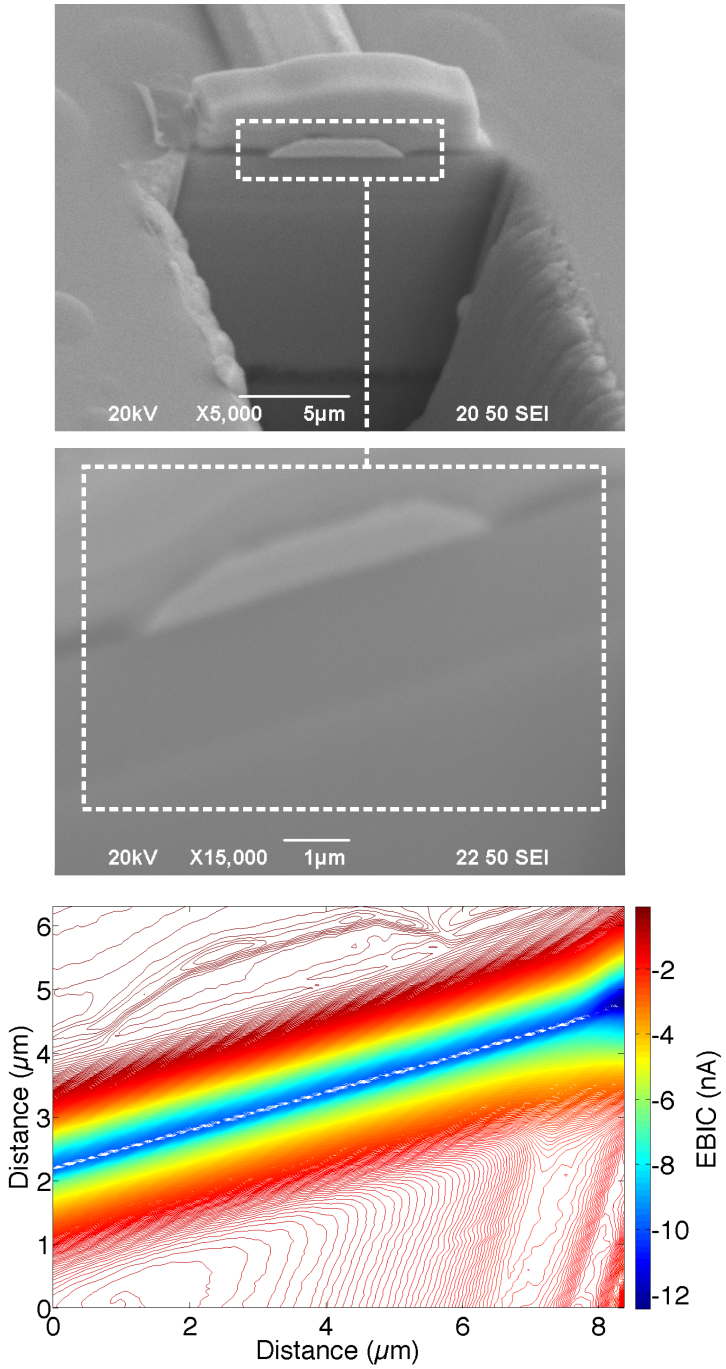

Figure 4.12.: Top: Scanning electron microscope (SEM) picture of the FIB cut through the top electrode of an AlGaInP-based LED. Middle:SEM image of the zoom into the FIB cut. The acceleration voltage was 20 keV, the magnification 15000 times. Bottom: Contour plot of this region. Low negative EBIC signal indicates the location of the pn-junction.

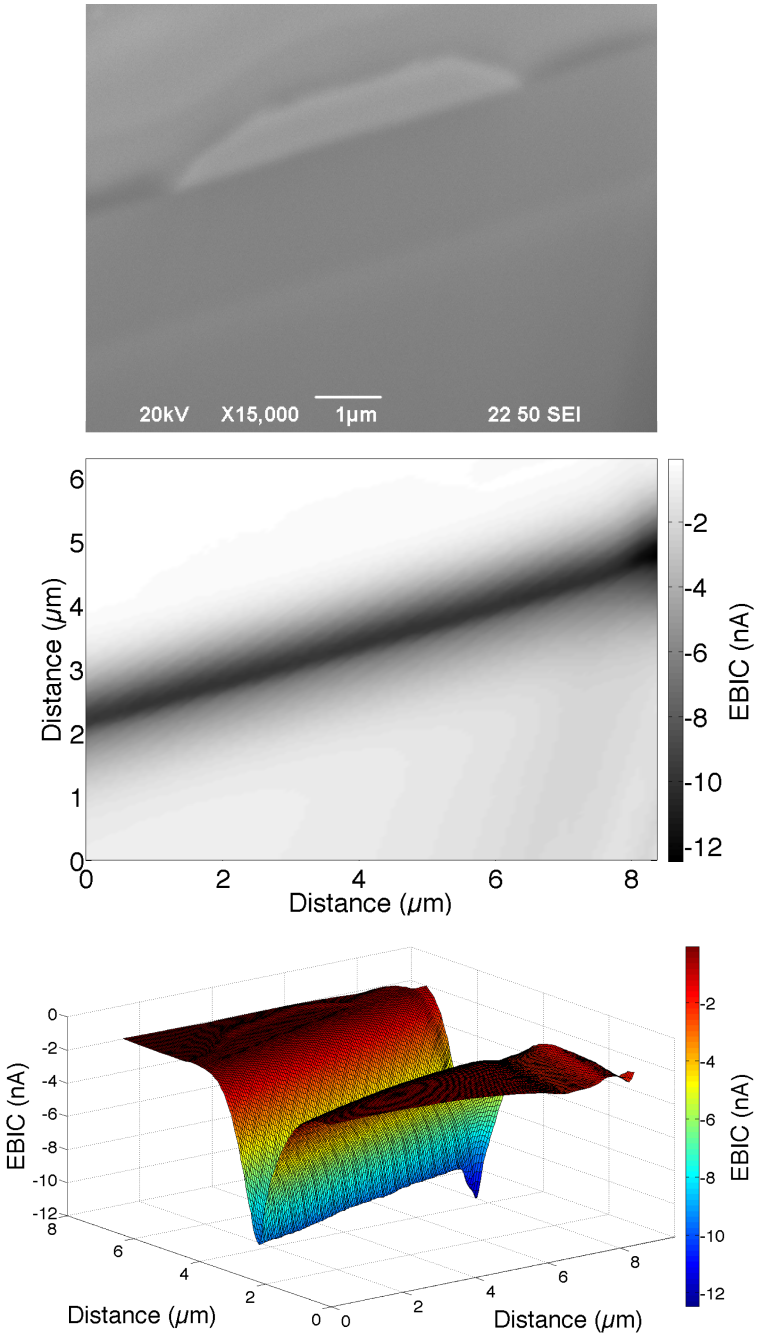

Figure 4.13.: Top: Scanning electron microscope (SEM) picture of the zoom into the FIB cut through the top electrode of an AlGaInP-based LED. The acceleration voltage was 20 keV, the magnification 15000 times. Middle: Gray scale plot of the region shown in the SEM image. Low negative EBIC signal indicates the location of the pn-junction. Bottom: Respective surface plot.

4.2.2. GaN-based LED

Figure 4.14 shows overview SEM image of the contacted GaN-based LED for EBIC investigations. Further the FIB trench including the zoom into the FIB cut is illustrated. The corresponding EBIC signal is plotted versus the electron beam position and shown in a color coded contour plot. Figure 4.15 shows the corresponding gray scale plot and surface plot to the SEM image (magnification 15000 times, beam energy 20 keV). The pn-junction lies very close below the top electrode where the 150 nm thin AlN layer is located.
The EBIC signal was again obtained from the top electrode. Since in this case a positive signal is measured the top electrode refers to the p-type electrode. The electron beam acceleration voltage was 5 keV.

Figure 4.16 and figure 4.17 illustrate the EBIC signal of the surface of the GaN-based LED. The corresponding SEM picture shows the surface position as well as a dust grain located on top of it (which can be also located in each EBIC signal plot because the signal drops to low values at such position when the electron beam hits the surface). The acceleration voltage during EBIC measurement was 20 keV.
Special mentioning is the regular and periodic variation of the EBIC signal on the surface of the LED (surface plot in figure 4.17). This variation occurs due to the inhomogeneous distribution of recombination centers in the GaN layer. This result has not to be confused with the patterning of the sapphire substrate shown in section 4.1.1. The penetration depth X of the electron beam is around 1.45 µm, however the patterning starts to occur in a depth of around 7 µm (measured from the surface to the bulk). The penetration depth X was calculated with equation 4.1 (following reference number [56]) whereas E_0 is the beam energy in keV (20 keV) and ρ_m the mass density of the specimen in g/cm^3 (6.15 g/cm^3).

$$X = \frac{0.1 E_0^{1.5}}{\rho_m} \tag{4.1}$$

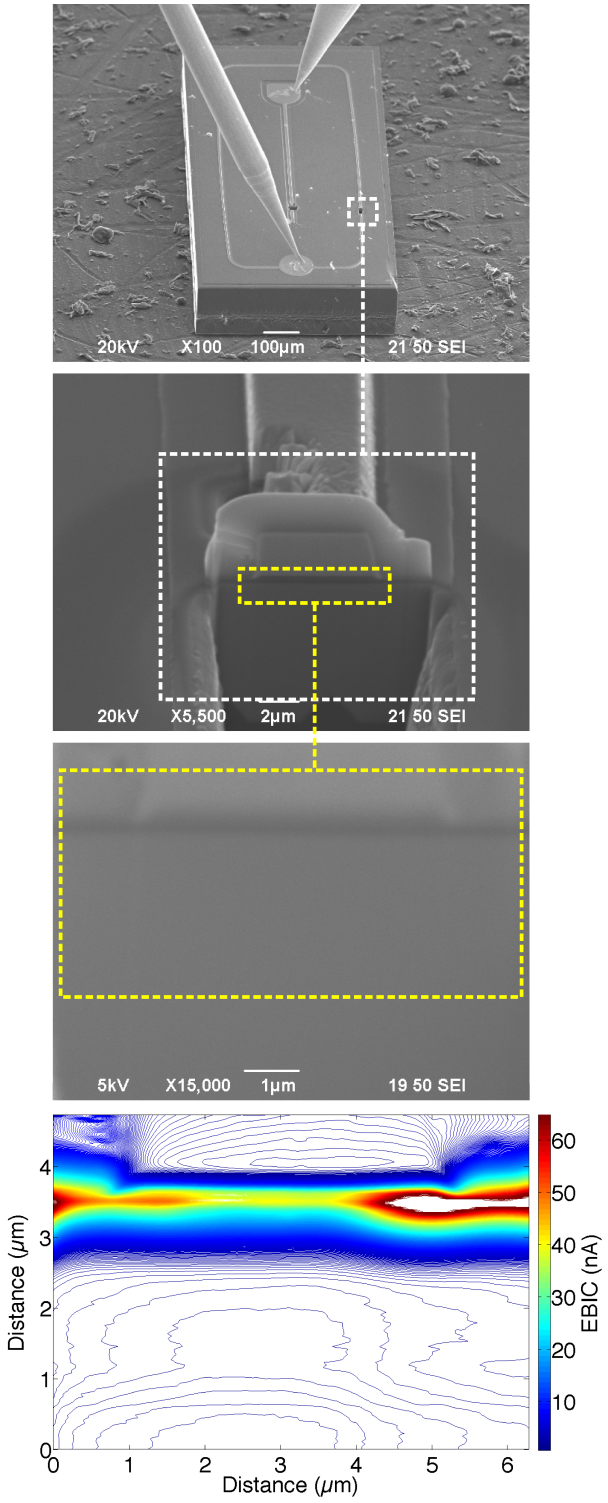

Figure 4.14.: Top: Overview scanning electron microscope (SEM) picture of the FIB cut through the top electrode of a GaN-based LED. Middle two plots: Zoom into the FIB trench. Bottom: Contour plot of the SEM image with a magnification of 15000 times. The acceleration voltage was 5 keV. High EBIC signals indicate the location of the pn-junction. Bottom: Respective surface plot.

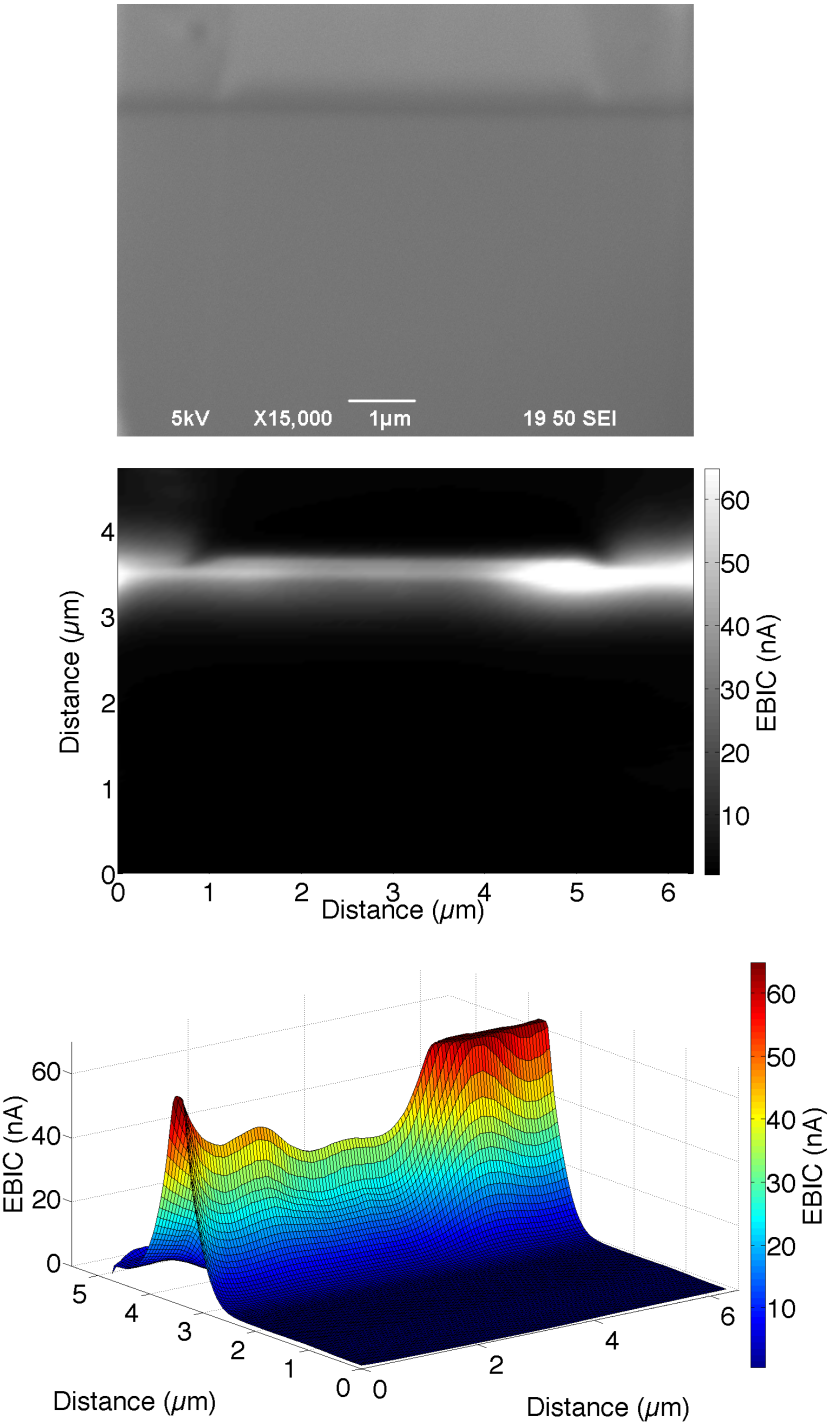

Figure 4.15.: Top: Scanning electron microscope (SEM) picture of the zoom into the FIB cut through the top electrode of an GaN-based LED (see figure 4.14). The acceleration voltage was 5 keV, the magnification 15000 times. Middle: Respective gray scale plot. Bottom: Respective surface plot.

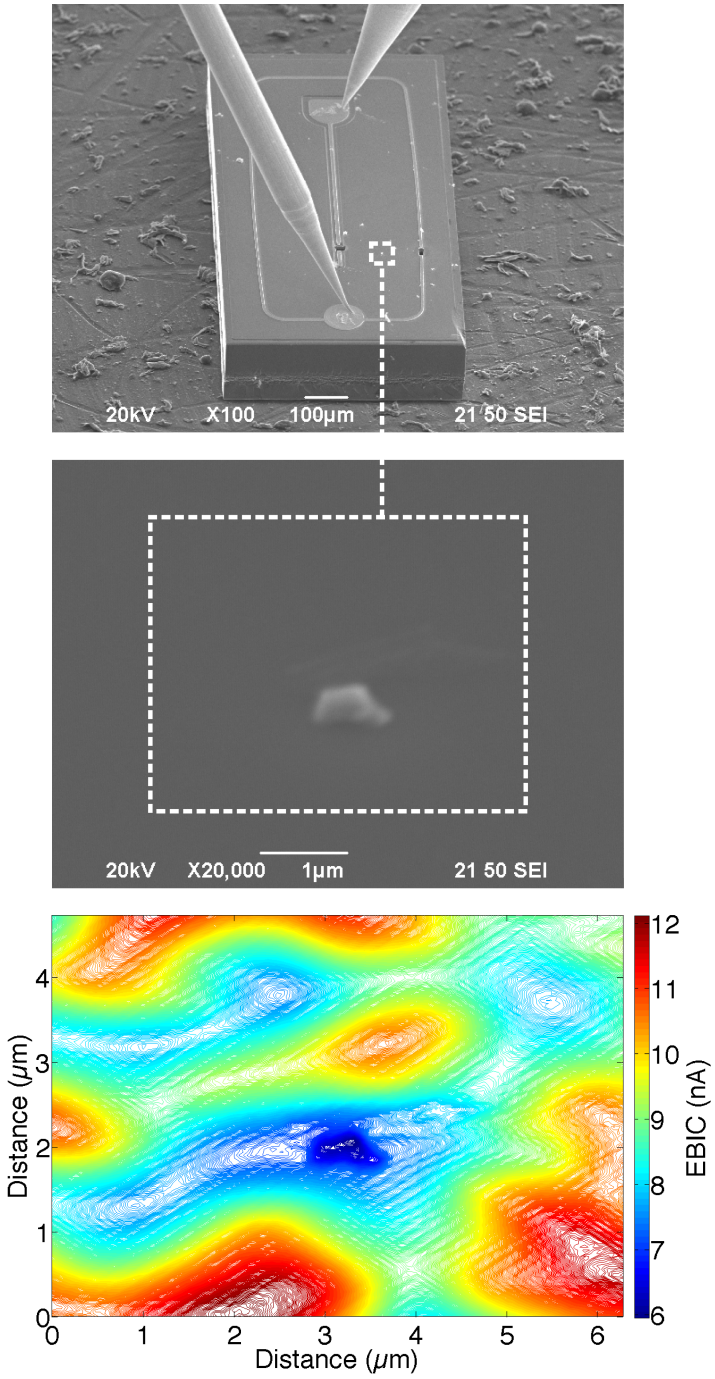

Figure 4.16.: Top: Overview scanning electron microscope (SEM) picture including the indication were the EBIC measurement of the surface of a GaN-based LED was performed. Middle: Magnified SEM image (acceleration voltage was 20 keV, the magnification 20000 times). Bottom: Contour plot of the respective region.

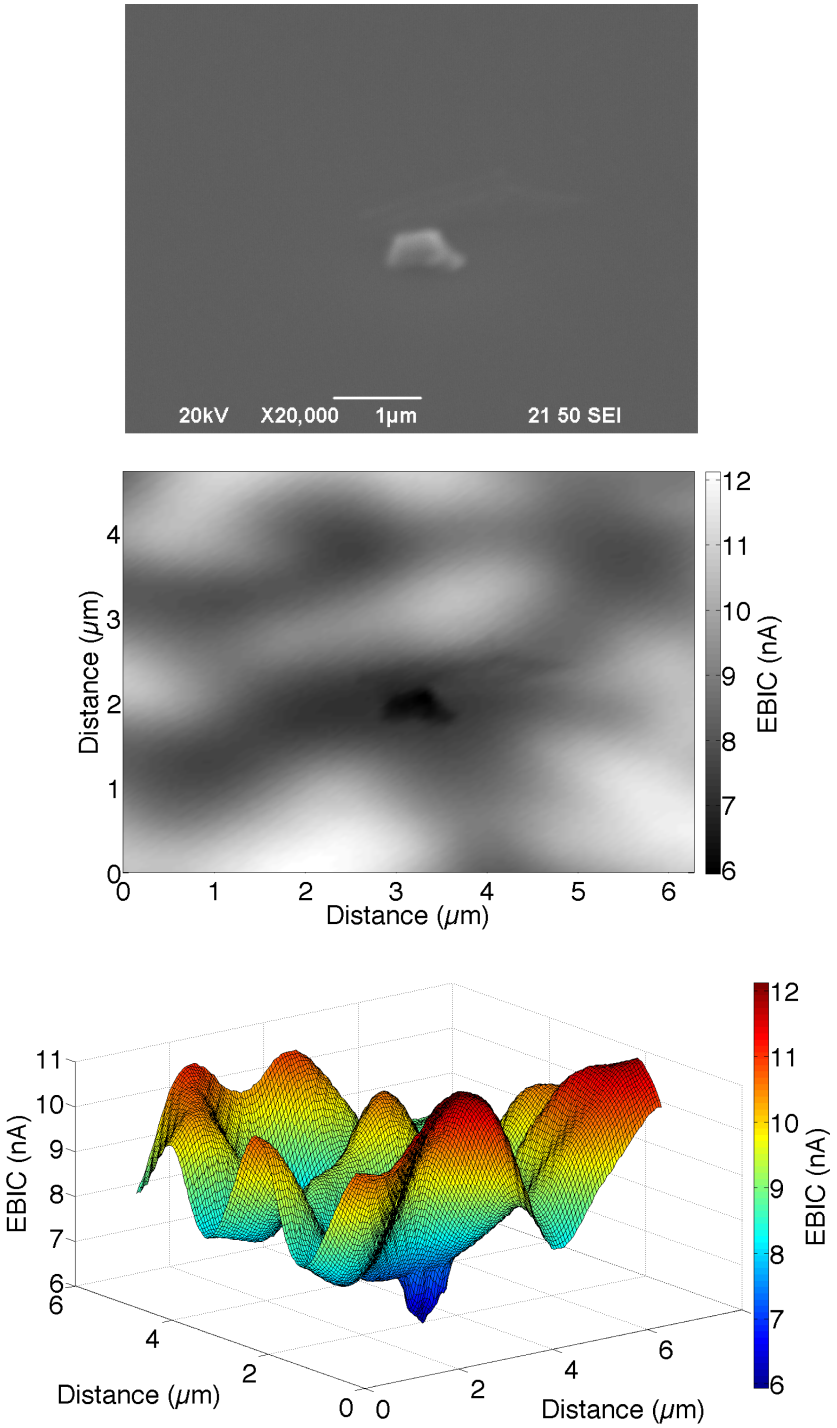

Figure 4.17.: Top: SEM image of the surface of a GaN-based LED (overview plot in figure 4.16). Middle: Respective gray scale image. Dust grain located on the surface can be identified as a dark spot (low signal). Bottom: Respective surface plot. The acceleration voltage was 20 keV, the magnification 20000 times.

4.3. LED damage

Injection of current (densities) outside the specification boundaries could lead to device damages of the sample surface as well as of the contacts. Figure 4.18 shows example images of burned LEDs. Left panel shows the burned surface of a red emitting AlGaInP-based LED. In this case the current density was too high which leads to a burned surface next to the electrodes. Right panel shows a burned bonding contact on a GaN-based LED which got loose due the exceeding current.

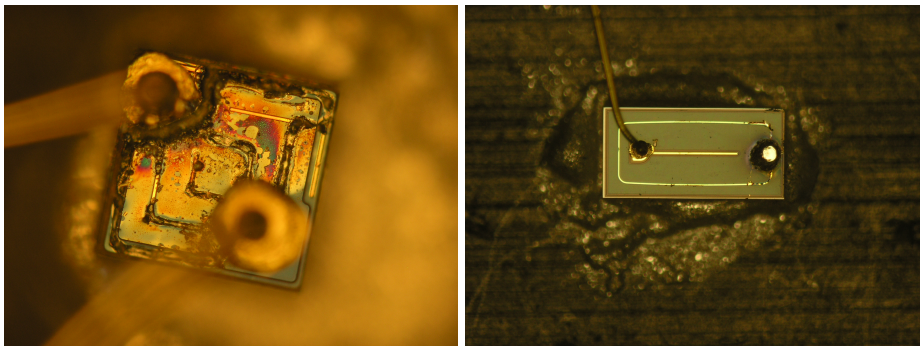

Figure 4.18.: Optical microscope images of two examples of LED damage due to high current density (left panel: red emitting AlGaInP-based LED, right panel: blue emitting GaN-based LED).

5. Determination of the junction temperature of LEDs

There are several attempts to obtain the junction temperature (JT) of LEDs. This section will list the advantages and disadvantages of several measurement methods and will present a measurement setup which allows determining the JT highly accurate.
Segments of this chapter are taken and adapted from the conference proceeding *Methods for Obtaining the Junction Temperature of LEDs*. The published version can be found in the appendix of this thesis.

5.1. Conventional measurement methods

In principle thermo-resistances (e.g. Pt100), thermocouples or diodes are sensing instruments which allow measuring the temperature with quite high accuracy. The difficulty applying such tools is that depending where the sensing element is located and mounted, rather the environment temperature than the actual JT is measured. The keyword in this section is thermal equilibrium. Direct measurement methods can only be applied if the whole system (sample and sensing element) is under thermal equilibrium. However, the influence of the driving parameters on the JT (i.e. current injection) is still not taken into account. Figure 5.1 shows the temperature of the device environment of an LED light engine measured with a K-type thermocouple (Nickel Chromium vs. Nickel Aluminum, reference temperature 0°C). The DC forward current of the device was 400 mA, 600 mA, and 1300 mA, respectively. The thermocouple was located on a heat sink next to the LED device which consists of four phosphor-converted-LEDs and two red-LEDs. After approximately 3600 seconds (60 minutes) a thermal equilibrium of the device environment is reached, however no conclusion about the actual JT of the active region of any of the LEDs can be drawn. One approach to gain insight into the actual JT would be to solve the quite complex heat equation of the whole device area. However this would still only give an estimate of the JT due to the fact that the driving parameters cannot be taken into account. Furthermore, due to practical reasons, such method will be hard to establish in applied fields.

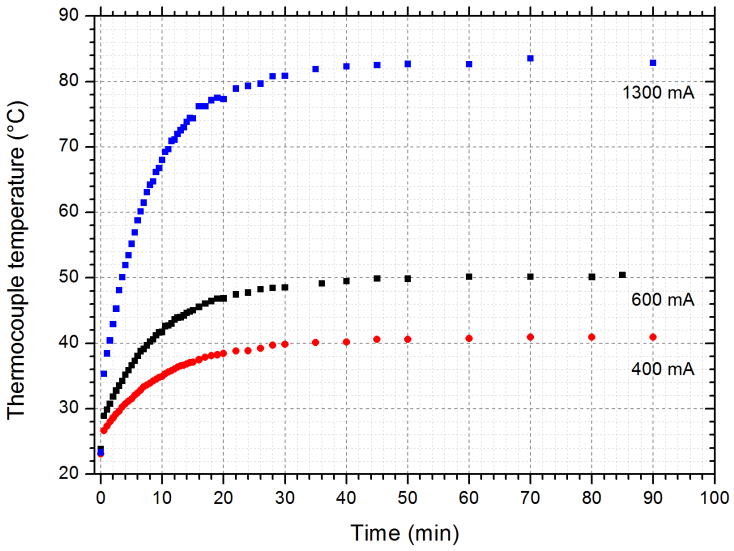

Figure 5.1.: Temperature dependence vs. time of an LED module containing 4 phosphor converted and 2 red LEDs. Measurements were performed with a K-type thermo couple located on a heat sink next to the LED device.

One much more convenient way to measure temperatures are contactless methods based on the detection of infrared (IR) radiation. Every body exhibiting a temperature above 0 K emits IR radiation following Planck's radiation law (see section 2.2.3).
In the lighting industry it is quite common to use IR cameras to determine temperature behavior of LEDs. One big advantage of IR cameras is that no contact between the sensing element and the sample is needed. Further a temperature distribution over the whole field of view of the camera can be measured. Due to the fast processing time of modern IR cameras, temperature changes can be basically measured in real time. IR images published in this thesis were recorded with the following IR camera (Optris PI 160):

- Detector: Amorphous silicon (bolometer)
- Detector size: 160 pixel x 120 pixel (Pixel size 25 µm x 25 µm)
- Spectral Range: 7.5 µm - 13 µm
- Image frequency: 120 Hz
- Temperature detection ranges: -20°C-100°C, 0°-250°C and 150°C-900°C
- Field of view (FOV) objective: 23° (horizontal) x 17° (vertical)
  focal length f = 10 mm

- Lens Material: Germanium

Figure 5.2 shows an IR transmission measurement of the germanium lens of the Optris PI 160. The particular wavelength behavior of the lens has to be taken into account and is automatically embedded in the software. If another lens is used the IR image has to be calibrated regarding the new objective.

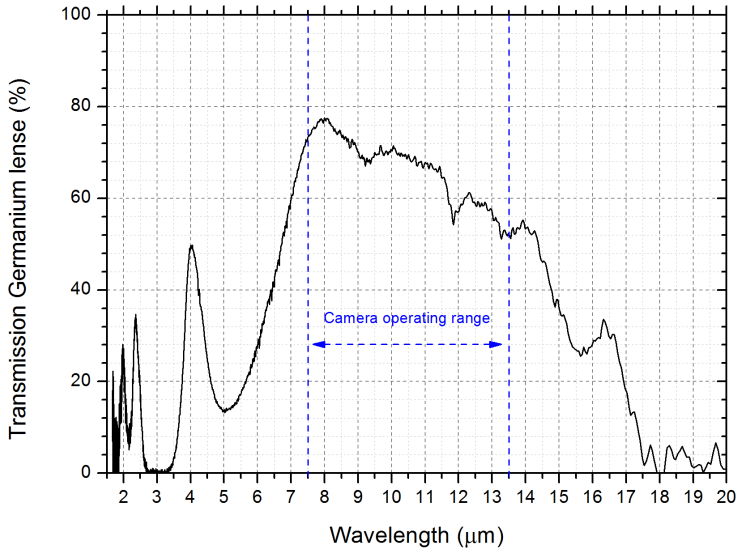

Figure 5.2.: IR transmission measurement of a coated Germanium lens used for IR temperature measurements. The measurement was performed with a BOMEM MB-102, whereas the sample environment was purged with CO_2 and H_2O filtered air.

Although IR cameras are quite convenient, the accurate temperature measurement is not straight forward. The following section list the main issues of IR cameras which have to be taken into account.

1. Emittance of an object ϵ (Emissivity):

   The emittance ϵ is defined as the change of the emission intensity of an real object relative to a black body radiator. The ϵ value depends on the wavelength, as well as on the temperature and on the angle of incidence. Furthermore the surface condition (surface texture) strongly influences the emittance as well.
   Figure 5.3 shows an IR image of an LED module mounted on an aluminum heat sink. No operation voltage is applied, therefore the whole light engine is in thermal equilibrium (environment temperature). Several parts that occur in the color coded IR image occur distinguishable and therefore exhibit at different assigned temperature values. The heat sink where the printed circuit board (PCB)

is mounted can be easily distinguished from the PCB itself, further gold contact/circuit paths on the PCB can be distinguished as well. Due to the fact that the IR camera (image) is not calibrated regarding the various emittance values of the certain materials investigated, the IR image contains wrong temperature values. For the example shown in figure 5.3, the temperature values vary within 4°C. To obtain correct temperature values, the emission coefficients of all materials have to be taken into account and each pixel of the recorded IR image has to be calibrated regarding the emittance ϵ.

As mentioned above, the ϵ value strongly depends on wavelength λ, direction θ and temperature T as well as on the surface condition. Without taking the exact ϵ value into account leads to wrong absolute temperature values. Because of the fact that the ϵ value depends on temperature also relative changes in temperature can often hardly be recorded. As an example the ϵ value of aluminum can basically vary between 0.01 and 0.99 depending on temperature, wavelength and surface treatment. To determine the JT of LEDs the ϵ value of the specific semiconductor alloy, as well es the T dependence has to be known.

Table 5.1 lists selected values of the normal total emittance for certain materials [57].

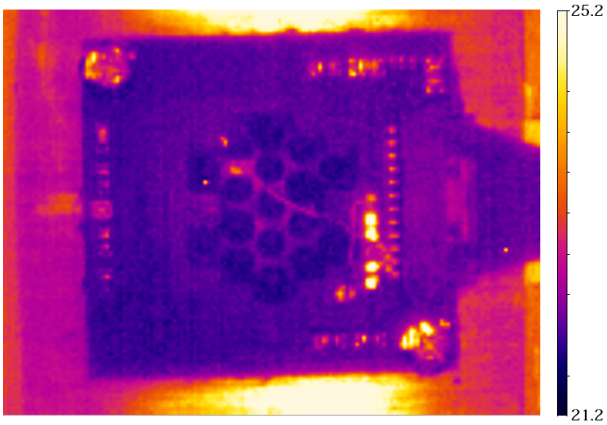

Figure 5.3.: Color coded IR image of an LED module mounted on a aluminum heat sink which is turned off and in thermal equilibrium. The values labeled next to the color bar are listed in °C.

Table 5.1.: Normal total emittance ϵ of selected materials at certain temperatures T and conditions (from [57]).

Material	T (K)	Emittance ϵ	Information
Aluminum	311	0.045-0.056	Foil, embossed
Chromium	367	0.08	Plated on iron, polished
Copper	373	0.052	Polished
Gold	300	0.68	Very pure, polished, λ=0.46 μm
Silicon	1000	0.64	Etched λ=0.65 μm
Silver	1213	0.35 - 0.044 [1]	Film, tungsten substrate

2. Surface temperature:

   Customary an LED is mounted on a substrate surrounded by a glob top material. Glob top materials are usually transparent (exceptions are phosphor converted LEDs were the glop top material is utilized as a matrix for the phosphorous particles) and are assigned to protect the LED chip and LED bonding contact of external influences (mechanical as well as contamination). IR cameras are measuring surface temperatures, therefore a mixture of the surface temperature of the LED and of the glob top surface is measured.
   One major problem is the IR absorbance of the glob top material. Left y-axis of figure 5.4 shows Planck's radiation curve plotted for reasonable LED temperatures during operation (300 K, 320 K, and 340 K). The detection range of the silicon detector of the IR camera is shown on the x-axis. The absorbance of a commonly used glop top material[2] is plotted on the right y-axis in figure 5.4. The absorbance of the silicon rubber compound is significant which leads to absorbance of IR radiation within the globe top material. This results in complete wrong temperature values if the absorbance behavior of the particular glob top material is unknown.

Those reasons are mainly responsible for the fact that an IR cameras cannot be used to determine accurately the JT of an LED. Even if no globe top material is implemented, the strong dependence of the emittance value on temperature, wavelength and surface properties (texture, quality, etc.) makes a sophisticated temperature determination hardly possible. Moreover at best the surface temperature rather than the JT is measured.
Therefore another setup was developed in this thesis and is presented in the next section.

[1] ϵ=0.35 (λ=0.55) - 0.044 (λ=0.65)
[2] Two component silicon rubber (ratio 1:1, 20 min cure time at 80°C), "Momentiv" XE 14-B7892

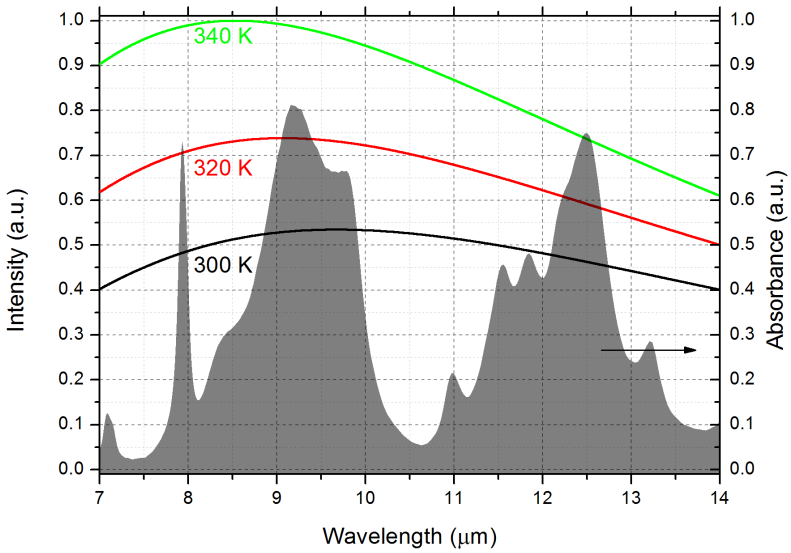

Figure 5.4.: Comparison of black body radiation and absorbance spectrum of a silicon hydrocarbon polymer used as glob top material in the detection range of an amorphous silicon IR detector. The IR spectrum was recorded with a BOMEM MB-102, whereas the sample environment was purged with CO_2 and H_2O filtered air.

5.2. Obtaining the JT of LEDs in the range between 230 K and 400 K

The principle parts of the measurement setup for obtaining the JT are shown in figure 5.5. The measurement of the emission spectra and the driving parameters were performed in thermal equilibrium in a chamber oven with precise temperature control (Weiss – Vötsch VT4002). The temperature range was set between -40°C and 120°C with an accuracy of 0.1°C. One additional Pt100 resistor was mounted on a separate heat sink which was located in the oven to ensure the predetermined oven temperature. Before the measurements were performed, the samples were stored for at least 30 minutes in the chamber to guarantee the thermal equilibrium of the devices. To avoid icing effects, the temperature oven was flushed with dry air during the whole experiment. To probe the LED device it must be driven in a manner that there is a negligible temperature increase due to the driving power. Therefore, the LED device is operated with a current which is generated by voltage pulses with a very small duty cycle (0.1%, pulse width = 500 ns, repetition time = 500 μs). Consequently we can assume that the JT is equal to the measured oven temperature. The forward voltage pulses were produced with a pulse generator (HP 214 B); using a series resistance Rs the forward current of

the device was determined (the series resistance was selected individually: 9.78 Ω for 20 mA & 50 mA, 19.52 Ω for 100 & 150 mA or 46.31 Ω for 300 & 500 mA, respectively). The voltage pulses were logged with a digital oscilloscope (Hameg HMO 3524). The emission spectra were recorded with a CCD spectrometer (Thorlabs CCS 100) containing a grating with 1200 lines per mm, blazed at 500 nm.
The x-axis of the spectrometer was calibrated with a mercury argon lamp, the y-axis with a tungsten lamp, respectively. The linearity of the CCD was checked using optical density filters. Calibration of the x-axis, y-axis, and the linearity of a CCD spectrometer can be found in section 5.4.
An aperture in front of the entrance slit of the spectrometer was used to define the acceptance angle ($\alpha = 5.72°$). The current-voltage characteristics were measured with a Keithley 2601B source measure unit.

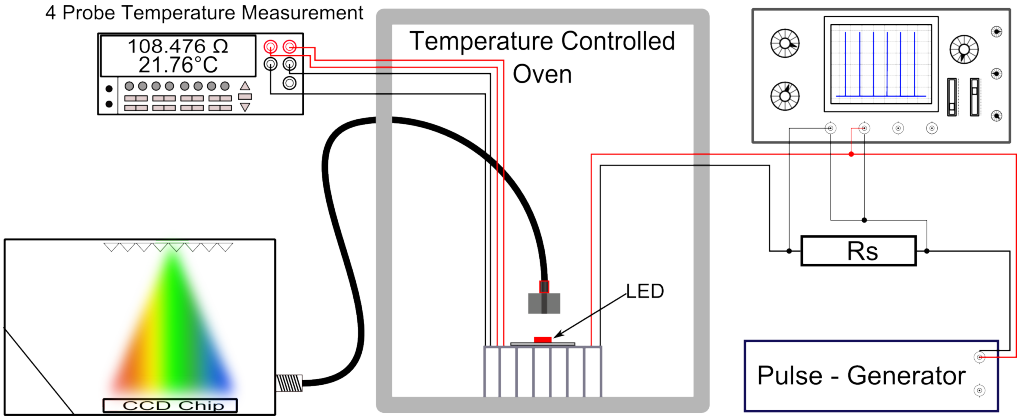

Figure 5.5.: Setup for determining the JT in the temperature range between 230 K and 400 K. The LEDs are located in a temperature controlled oven and operated by a pulse generator. The temperature of the LEDs is checked with an additional Pt100. The emission is recorded with a CCD spectrometer.

Figure 5.6 shows the pulse equivalent circuit of the measurement setup described in figure 5.5. The narrow pulse width of the forward voltage pulses is achieved by superimposing high frequency components. Therefore, in contrast to the DC equivalent circuit, capacitance as well as the inductances of the coax cable and of the circuit paths/board have to be considered. Furthermore, we also distinguish between horizontal as well as vertical resistances in the diode. The current I_d in figure 5.6 represents four current components namely the leakage current, the radiative current, the non-radiative current as well as the carrier-overflow current [58]. The description of the denotation used in figure 5.6 can be found in table 5.2.

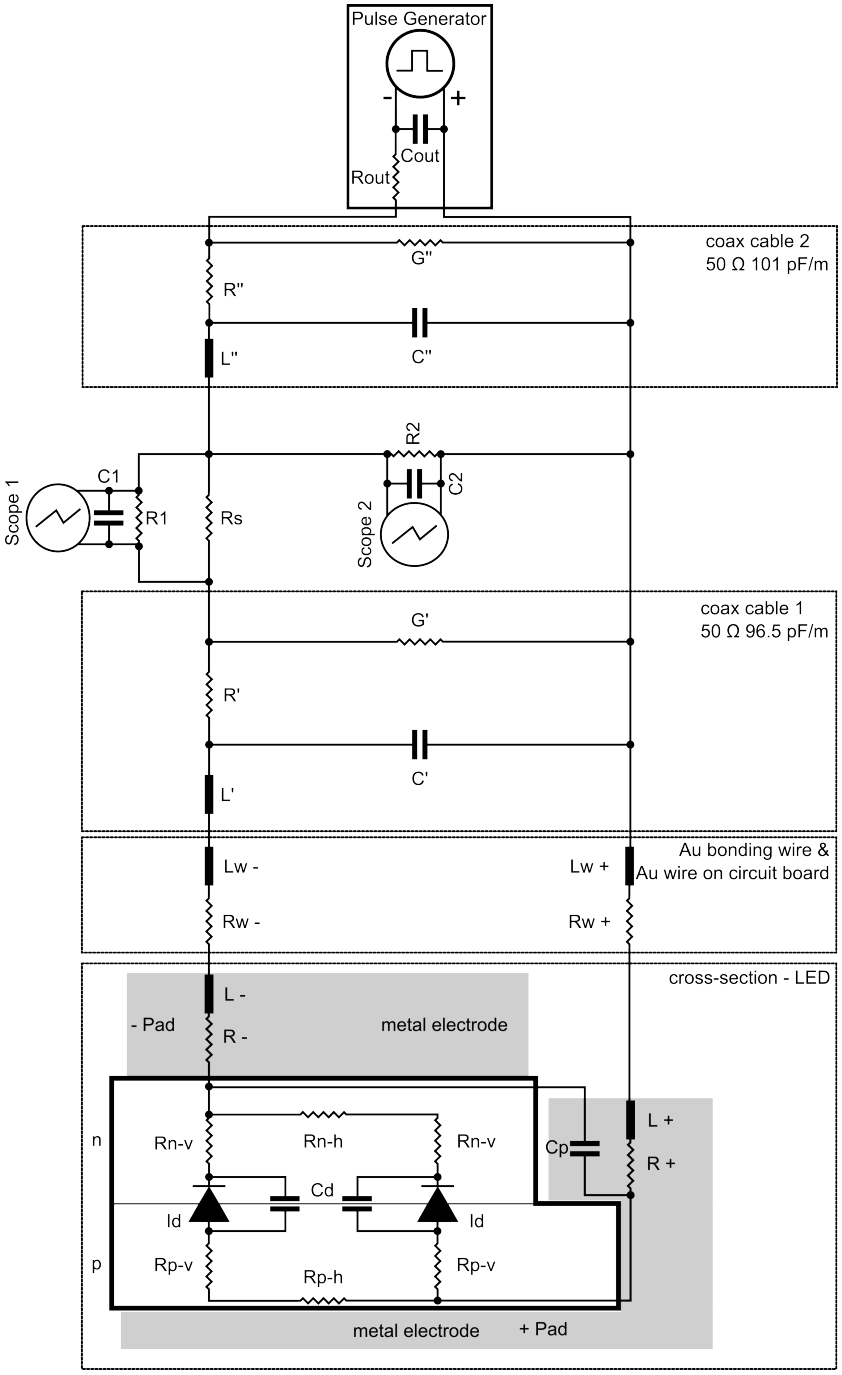

Figure 5.6.: Pulse equivalent circuit of the whole measurement setup described in figure 5.5, including the equivalent circuit of the LED, the circuit board as well as the supply contacts (coax cable). The description of the denotation can be found in table 5.2.

Table 5.2.: The description of the denotation of the equivalent circuit in figure 5.6

Label	Explanation
R + / R -	Resistance of metal electrode of LED
L + / L -	Inductance of metal electrode of LED
Rn-v / Rp-v	Vertical resistance of the n-type / p-type semiconductor material
Rn-h / Rp-h	Horizontal resistance of the n-type / p-type semiconductor material
Id	Current components
Cd	Conductance occurring from the depletion zone
Cp	Conductance occurring from the electrodes (pads)
Rw + / Rw -	p-side (+) / n-side (-) resistance of Au bonding wire & Au wire on PCB
Lw + / Lw -	p-side (+) / n-side (-) inductance of Au bonding wire & Au wire on PCB
Rs	Series resistance for forward current determination
R' / R"	Resistance of coax cable 1 (') / 2 (")
L' / L"	Inductance of coax cable 1 (') / 2 (")
C' / C"	Capacitance of coax cable 1 (') / 2 (")
G' / G"	Conductance of the dielectric material between inner and outer conductor of coax cable 1 (') / 2 (")
R1 / R2 / Rout	Input (output) resistances of scope 1 (R1) / 2 (R2) / pulse generator (Rout)
C1 / C2 / Cout	Input (output) capacitances of scope 1 (C1) / 2 (C2) / pulse generator (Cout)

The DC equivalent circuit is much simpler and can be derived from the pulse equivalent circuit because neither capacitances nor inductances play a significant role and therefore just resistances have to be taken into account.

5.2.1. Diode mounting

The LED dice on a sapphire substrate were mounted with thermally conducting silver epoxy[3] (cure time 80°C for 30 minutes) on an aluminum heat sink. To ensure great heat dissipation, the heat sink dimensions (5.0 mm x 6.3 mm x 4.8 mm) were chosen in a way that the areas of the device are much smaller than the area of the heat sink. Through a thin 30 μm Au bonding wire the devices were connected to a PCB. The contact pads on the LED dice as well as on the PCB consists out of Au. Figure 5.7 shows the mounting setup of the device. For most of the experiments the chip dimensions (length x width x height) were 1000 μm x 500 μm x 150 μm (blue emitting GaN-based) or 300 μm x 300 μm x 100 μm (red emitting AlGaInP). Additional and detailed information about the investigated samples can be found in section 4.

[3] Silver Loaded Epoxy Adhesive - Resin, Article Number: RS 186-3616 Supplier: RS Components Ltd, Birchington Road, Corby, Northants, NN17 9RS, UK

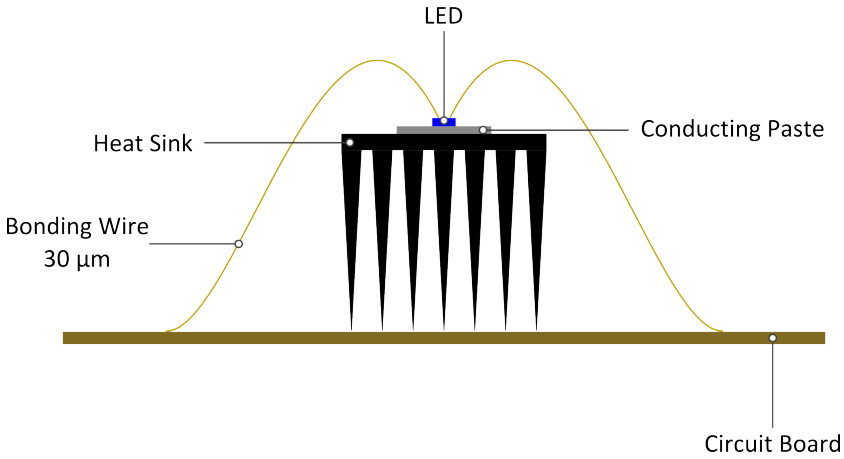

Figure 5.7.: Schematic illustration of the LEDs mounted on the heat sink and connected via gold bonding wires to the PCB.

5.3. Low temperature investigations

To gain insight into the emission behavior and emission processes of LEDs the diodes were measured under low temperature conditions. To ensure the low temperature the LEDs were dipped into a bath containing liquid helium-4 (4.2 K) or liquid nitrogen (77 K). Hence the JT of the LED was preset. The volume of the bath was very large comparing to the very small device volume; therefore, thermal equilibrium was reached directly after dipping the samples into the bath. The LEDs were mounted as described above (figure 5.7) and then mounted on a plastic sample holder (figure 5.8). Figure 5.9 shows the whole low temperature measurement setup. The sample holder was carried by a 2 m long hard glass rod. A 4 m long waveguide (Newport F-MLD; core diameter: 100 µm, cladding diameter: 140 µm, NA = 0.290) out of glass was used to measure the emission spectra of the LEDs in the liquid bath environment. The connection between the glass fiber optics and the spectrometer was made with a common SMA905 connector. The spectrometer including the 4 m long glass fiber was calibrated regarding x-axis as well as y-axis. To ensure the position of the fiber optics relative to the LED chip during the measurement, transparent Vaseline (Rohde Sanacid Vaseline) was used on top of the LED as well on the fiber optics. The reason for using transparent Vaseline was due to the fact that it was possible to remove the Vaseline after the measurement (see section 5.3.2). To reduce the viscosity of the Vaseline, it was heated with an IR lamp (150 W) for a couple of minutes until it was easy to distribute it over the device. The cure time of the Vaseline was around 60 seconds.

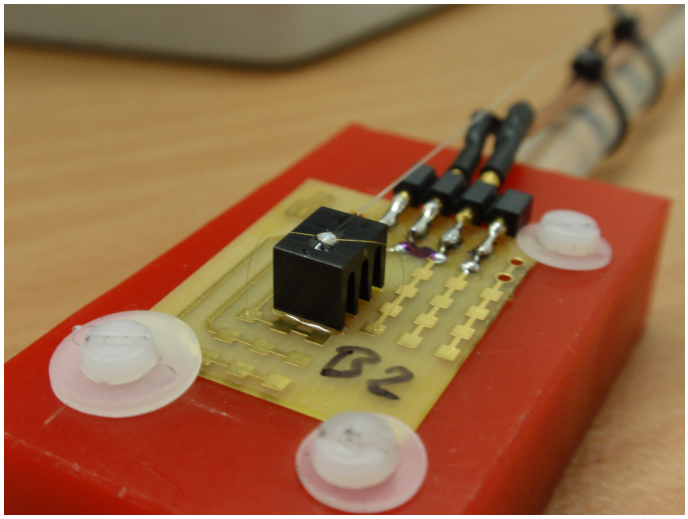

Figure 5.8.: Sample holder including LEDs used for the low temperature investigations. The LEDs are mounted on the aluminum heat sink and connected to the PCB. The fiber optics was mounted on the LED dye using transparent Vaseline.

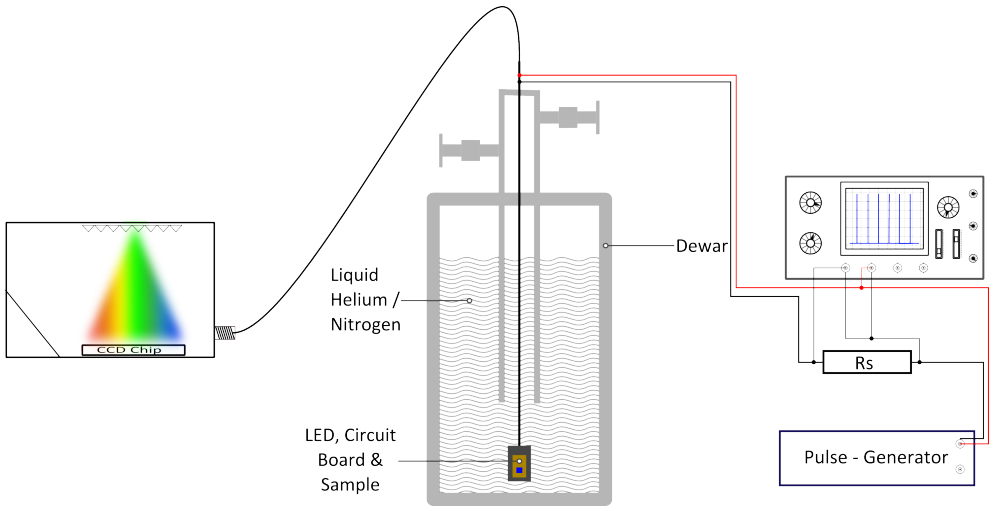

Figure 5.9.: Illustration of the low temperature setup for the investigation of the emission behavior of the LEDs in liquid environment. The LEDs are mounted on a sample holder whereas the electrical connections as well as the optical components are guided through a glass rod.

5.3.1. Emission behavior of Vaseline

To ensure that the measured emission spectra are non-influenced by the intrinsic emission behavior of the Vaseline, excitation-emission spectra of the Vaseline at room temperature was determined (Figure 5.10). The Vaseline shows a distinct emission peak around 420 nm which is in the similar emission range as the investigated blue emitting

GaN-based samples. Therefore, to ensure that our measured spectra do not get noised by the emission behavior of the Vaseline, the quantum efficiency of the Vaseline was determined.

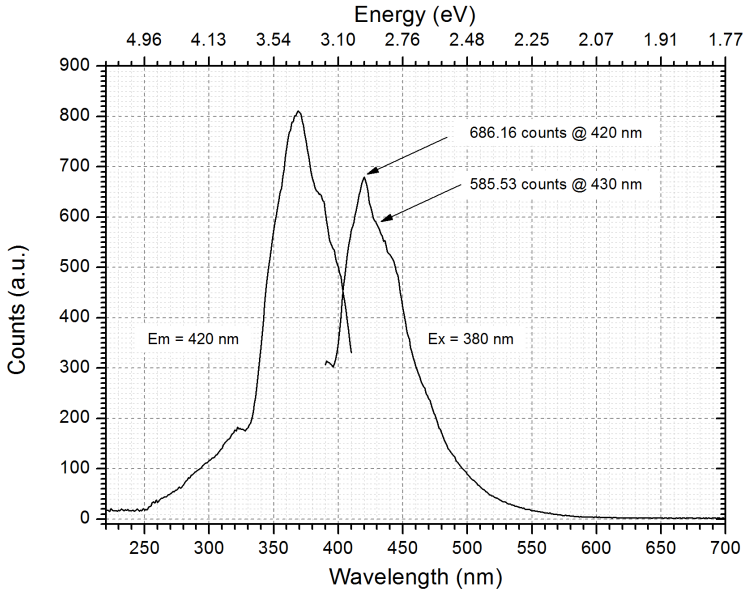

Figure 5.10.: Excitation-emission spectrum of the Vaseline. The emission monochromator (Em) was set to 420 nm for the excitation measurement, the excitation monochromator (Ex) was set to 380 nm for obtaining the emission spectrum, respectively.

The excitation-emission spectrum was recorded with a Shimdazu RF 5301 spectrofluorophotometer (measurement conditions: slit width of excitation/emission monochromator = 1.5 nm, sensitivity = ”High”, speed = ”Medium”). A commercially available GaN LED[4] peaking at around 420 nm was used as reference sample. The reference LED was mounted on a sample holder and inserted into the spectrofluorophotometer at the same position were usually the sample cuvette (including the Vaseline) is located. The current of the reference LED was tuned in a way that the spectrofluorophotometer was measuring the same number of counts which were emitted by the Vaseline inserted (under the same measurement conditions i.e. sensitivity, slit size, monochromator position, etc.). Afterwards the emission power of the tuned reference LED was measured with a power meter (Thorlabs PM 100D; Detector: Silicon photodiode S120VC).
Due to the fact that the emission spectrum of the LED does not exactly agree with the emission spectrum of the Vaseline, the number of counts were optimized regarding two wavelength positions at 420 nm and 430 nm (with respect to the two peak positions of

[4]GaN LED 3 mm Round (WU-1-61 BC), 513177.02, Conrad B/N 183911

the emission in figure 5.10). Figure 5.11 shows the emission spectrum of the Vaseline as well as the spectrum optimized for 420 nm and 430 nm, respectively. The forward current I_f of the reference LED was 122 µA for 420 nm and 116 µA for 430 nm. The emission power (obtained with the Thorlabs PMD 100) was 0.007 µW (0.009 µW/cm^2) for I_f = 122 µA (420 nm) and 0.005 µW (0.007 µW/cm^2) for I_f = 116 µA (430 nm), respectively. Due to the low current level, the turn on time of the reference LED did not change the output power (turn on time investigation was carried out between 1 min and 35 min).

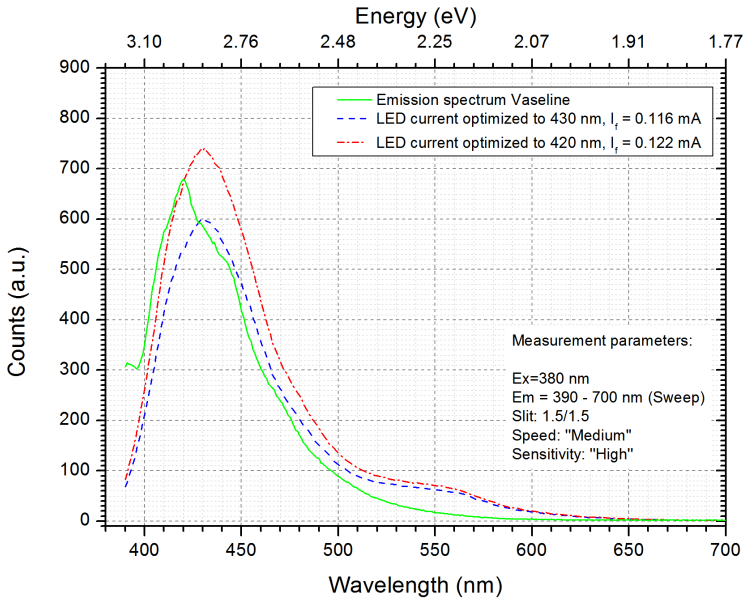

Figure 5.11.: Emission spectrum of the Vaseline as well as of the reference LED. The current of the LED (and therefore the output power of the LED) was tuned in a way that the emission peak fits the emission peak of the Vaseline. The excitation monochromator (Ex) was set to 380 nm, the emission monochromator (Em) was sweeping from 390 nm to 700 nm. The slit size of excitation/emission monochromator was set to 1.5 nm.

Out of the emission power of the reference LED, the quantum yield can be calculated if the excitation power of the spectrofluorophotometer is known. Therefore the excitation power of the spectrofluorophotometer at the excitation maximum of 380 nm was determined with a power meter at sample position (Thorlabs PM 100D; Detector: Silicon photodiode S120VC). Measurements lead to an average excitation power (at sample position) of the spectrofluorophotometer source of 83.0 µW (117.5 µW/cm^2). Equation 5.1 shows the calculation of the quantum yield η. Inserting the determined emission power of the LED P_{Emission} (between 0.007 µW/cm^2 and 0.009 µW/cm^2) as well as the

excitation power $P_{\text{Excitation}}$ of the spectrofluorophotometer (117.5 μW/cm^2) into equation 5.1 leads to a quantum yield between η=0.006 % (for 0.007 μW/cm^2) and η=0.008 % (for 0.009 μW/cm^2).

$$\eta[\%] = \frac{P_{\text{Emission}}}{P_{\text{Excitation}}} \cdot 100 \tag{5.1}$$

The experimental approximation to calculate the quantum yield of the used Vaseline clearly shows that the influence of the emission behavior of the Vaseline on the sample is negligible. The quantum yield values were obtained for an excitation wavelength of 380 nm which is the peak excitation wavelength of the Vaseline (figure 5.10). For a different excitation the quantum yield decreases further.
This concludes that Vaseline can be used as mounting and connection material for visible LEDs in combination with the fiber optics.

5.3.2. Vaseline demount

To remove the Vaseline from the LED dice after low temperature investigations were carried out, the following procedure was established:

1. LED sample holder has to be placed under an IR lamp (150 W) for around 5 minutes (distance IR lamp-LED: 8 cm) to decrease the viscosity of the Vaseline.
2. Heating of toluene on a separate heating plate until approximately 100°C are reached.
3. Carefully washing the Vaseline with the heated toluene from the substrate by using a glass needle.
4. If interference fringes on the LED surface can be still identified (as shown in the top panel in figure 5.12) step 1) to 3) have to be repeated until hardly any residuals are observable (figure 5.12 bottom panel).

5.3.3. Resistance measurements

During the liquid helium temperature measurements a significant part of the supply wires was located in the liquid bath. The resistance change due to the low temperatures was measured to ensure that no systematic errors influence the measurement results of the LED. The resistance measurement was performed by injecting pulsed current as well as direct current. Pulsed measurements were performed with a 20 Ω series resistance (series resistance was located outside the liquid environment at room temperature during the whole measurement), a forward voltage pulse width of 500 ns and a repetition rate of 500 μs, respectively. The direct current level was varied between 0 mA and 300

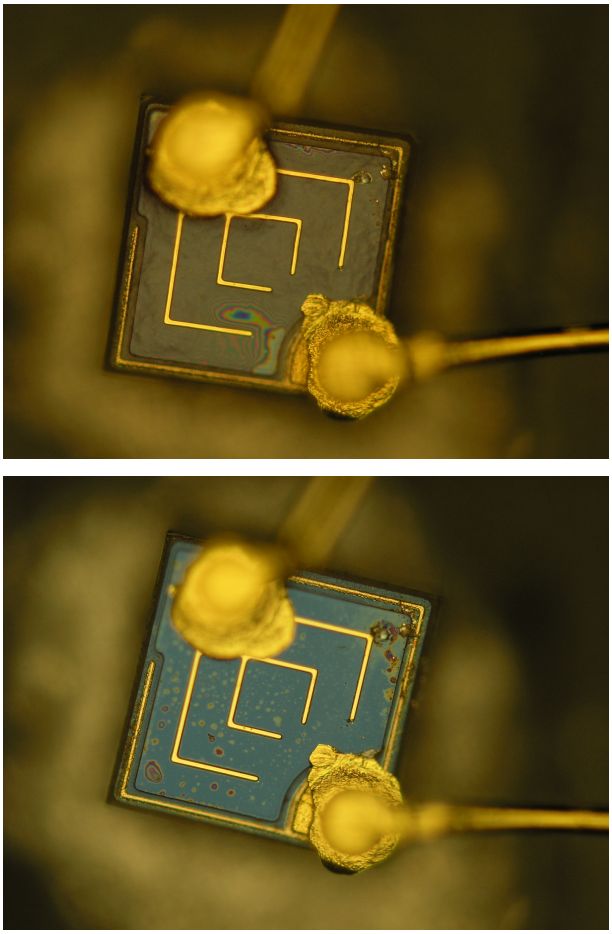

Figure 5.12.: Optical microscope image of the LED surface after the Vaseline removal process was executed once (top image) and twice (bottom image). If interference fringes are still observable (top image) residuals remain on the surface. The magnification of both images is 200 times.

mA. The total number of measurement points was 200, the injection time per measurement point was 10 ms.

Figure 5.13 shows the measurements performed at room temperature (RT = 298.5 K) and helium temperature (4.2 K) for pulsed injection current as well as for direct current. The minor deviation between DC and pulsed measurement arises from the measurement uncertainty of the determination of the forward voltage from the pulsed measurements. As expected, the resistance decreases with decreasing temperature which can be directly obtained out of the slope of the V-I characteristics. The resistance of the supply wires changes from 2.66 Ω (2.88 Ω DC) to 1.84 Ω (1.81 Ω DC) due to the low temperature environment.

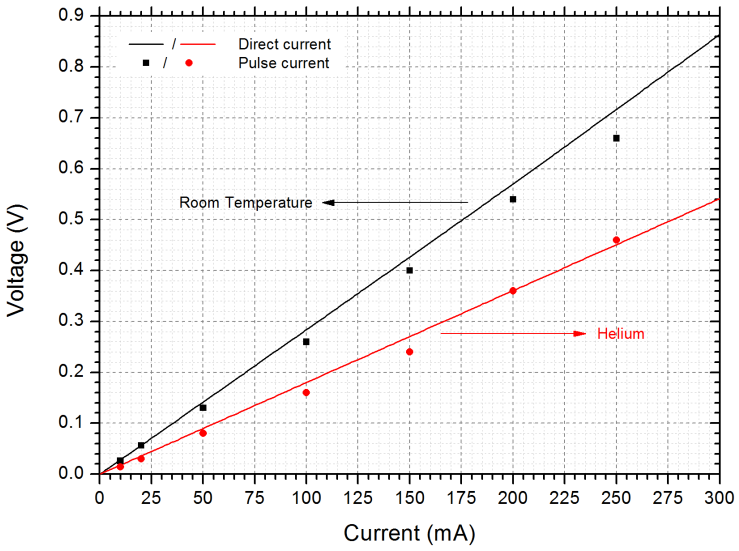

Figure 5.13.: Resistance determination of the contact wires at room temperature and liquid helium environment. Solid lines indicate the DC injected signal, dots the pulsed measured signal respectively.

5.3.4. Polarization and direction effects

In figure 5.8 the fiber optics is located normal to the substrate surface. To ensure that the detection angle of the fiber optics relative to the sample surface does not influence the measured emission response of the diode, the emission spectra of the LED with respect to the angle of the detection fiber was obtained.
The LEDs were mounted on a goniometer which allowed to change the angle of the detector relative to the samples in between -90° and +90°. The samples were mounted in a way that the goniometer moved relative to the vertical axis as well as to the horizontal axis of the LED. With a step size of 10° the emission spectra were recorded and compared to each other. The sample was afterward rotated 90° and the measurements were performed again. Neither for the blue emitting GaN-based LED nor for the red emitting AlGaInP-based LED a change of the shape of the emission spectra with respect to sample orientation and detector angle was measured.
Further a polarizer was included in front of the detector and the whole measurement was repeated. No impact on the shape of the emission pattern of the two types of LEDs was found for any polarization direction.

5.4. Calibration of a CCD spectrometer

To ensure correct and accurate measurements with a CCD spectrometer, calibration of the x and y axis has to be done in regular intervals and for every setup (e.g. fiber optics, aperture, etc.). All of the measured spectra shown in this work were calibrated regarding the listed points below.

5.4.1. Background spectrum correction

The background spectrum of a CCD spectrometer consists out of two parts, one is the dark current (thermal noise) of the CCD, one the background counts of residual light in the measurement setup. The recorded emission spectra have to be corrected regarding these so called background spectrum. In this thesis both mentioned parts (thermal noise and background counts) are referred to the expression *background spectrum*.
To correct the emission spectrum, the background spectrum has to be recorded and subtracted immediately after the measurement. Very important is that for each recorded spectrum an assigned background spectrum has to be measured as well.
The reason for recording as many background spectra as emission spectra is that the dark current of the spectrometer changes with time, in particular significantly right after the spectrometer is turned on. To circumvent the spectrometer should be turned on for some time prior measurements are carried out. The time interval strongly depends on the particular spectrometer. Top panel in figure 5.14 shows the behavior of the background spectrum of an Ocean Optics USB2000+, for different turn on times including the average signal count values. It takes around 120 minutes until the dark current remains constant.
The commonly in this work used Thorlabs CCS 100 does not show such a strong dark current behavior (bottom of figure 5.14). For clarity the background spectra after 30 seconds and after 2 hours are shown in the plot. The spectrometer can be used right after turning on. However it is still suggested to wait a few minutes before the first measurement is performed.

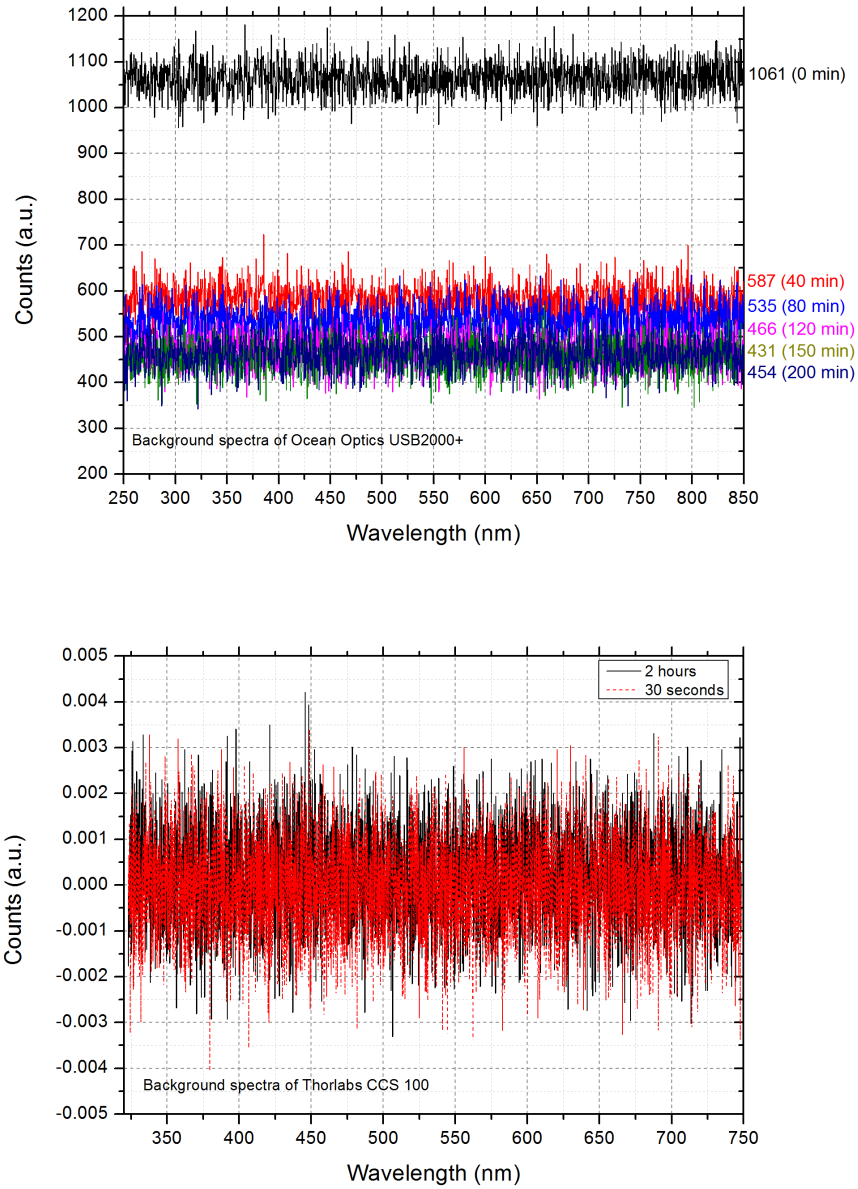

Figure 5.14.: Background spectra (thermal noise of the CCD and background counts of the remaining light) of two types of spectrometers. In the top panel the average count number with the respective to turn on time is listed.

5.4.2. x-axis calibration

To ensure that the recorded emission wavelength position is measured correctly, an x-axis calibration has to be performed. The x-axis or wavelength calibration was carried out with a Pen Ray - Mercury Argon Lamp (LSP035 LOT Oriel Group). The line width of such calibration sources is very small (i.e. 0.001 nm) and the spectral peak positions are assigned to certain wavelength values. Measuring the emission pattern of such calibration lamp with the spectrometer and comparing it to published literature wavelength values allows to calibrate the wavelength axis.
For further reading about the specification of mercury argon lamps the author refers to reference number [59] and [60].
For the particular spectrometer used, the actual calibration data has to be delivered to the various software:

- Thorlabs CCS 100: The calibration can be directly done in the delivered Software ”SPLICCO” by measuring the actual emission wavelength of the mercury argon lamp and inserting the real (literature) values into the software. The software tool will automatically recalculate the new positions and correct the spectrometer.
- Ocean Optics USB2000+: A linear regression of 3rd order has to be done which allows to obtain the ”calibration coefficient”. This coefficient has to be inserted into the Ocean Optics USB2000+ driver software (”USB EEPROM Programmer”). To perform the linear regression, the wavelength, the pixel number and the predicted wavelength have to be recorded. With a common analysis software (EXCEL, ORIGIN, etc.) a linear regression can be performed which leads to the coefficients needed.

The x-axis calibration should be performed in regular time periods (e.g. each 3 months).
It is highly recommended to perform the calibration with the same equipment (e.g.waveguide, aperture, etc.) which is used in the actual measurement setup as well.
Note: The warm up time of the Mercury Argon lamp was 20 minutes and the measurement were performed at room temperature.

5.4.3. y-axis calibration

The y-axis of the spectrometer was calibrated using a tungsten lamp standard (Osram Wi 17/G 9.0 V 16.9 A (C068), calibrated 11/21/2011). To perform the y-axis calibration one has to make sure that the same assembly (waveguide, aperture, etc.) which is used for the measurements is also used for calibration. Therefore the y-axis was calibrated for each different measurement setup. This means that if a waveguide/fiber optics exchange takes place or a different aperture is used, the y-axis calibration has to be re-performed.
The y-axis calibration provides the relative height of the recorded emission intensity. For the calibration, the tungsten lamp has to be under predefined conditions (delivered by Osram) which are listed in table 5.3. The distance between the aperture and the lamp was recorded during each calibration and was usually around 30 cm. The calibration was always performed at room temperature. The background spectrum was recorded directly after the measurement. The calibration was performed for 1 scan as well as averaging over 10 scans, 30 scans, 50 scans, and 100 scans, respectively. The calibration lamp stoving time was at least 20 minutes under calibration conditions.
The emission spectrum was recorded with the spectrometer and compared to the delivered emission spectrum. Out of the fraction between the background corrected emission spectrum of the tungsten calibration lamp and the delivered calibration curve, the respective calibration spectrum is obtained. The delivered calibration spectrum of the tungsten lamp is illustrated in figure 5.15.

Table 5.3.: Measurement conditions to operate the calibration standard.

Parameter	Value	Information
DC Current (A)	14.439	Setting parameter
Voltage (V)	6.858	4-pol measurement
Stoving time (min)	20	

Note: To prevent fusing of the lamp, the current/voltage has to be carefully increased and decreased during the turn on/off process.

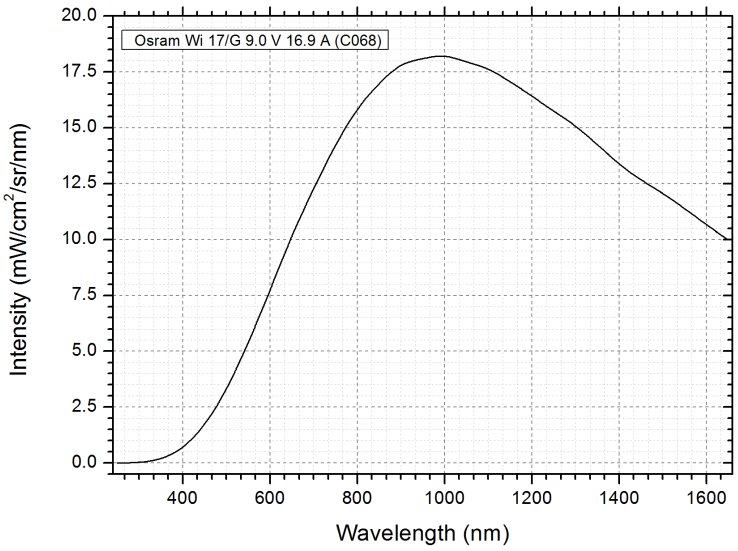

Figure 5.15.: Calibration spectrum of a tungsten standard under measurement conditions shown in table 5.3.

5.4.4. Detector linearity

The count value measured with a CCD detector at a certain wavelength does not automatically show a linear evolution with respect to intensity. This means that e.g. for a certain wavelength, double CCD counts do not guaranty that the light source provides double intensity. To compare emission spectra, the linearity of the CCD detector has to be measured and checked.
To perform such calibration, the transmission behavior of certain selected optical density filters (ODF) was measured in an UV/VIS spectrometer (PerkinElmer Lambda 9 or Shimadzu UV/VIS 1800). Out of this measurement the transmission T of each ODF for a specific wavelength (at 620 nm) was determined. Further the transmission T of an ODF was measured with the respective CCD spectrometer. To do so the ODF was set in front of the spectrometer, and a spectrum of a red emitting LED (peak wavelength at 620 nm) was logged and compared to the emission spectrum without ODF inserted. Taking equation 5.2 into account leads to T:

$$T = \frac{I}{I_0} \tag{5.2}$$

whereas I is the measured intensity with an ODF inserted, I_0 the intensity without ODF. The transmission values obtained with the CCD spectrometer are compared with the transmission behavior measured with the UV/VIS spectrometer. The results are plotted

in figure 5.16.
Both spectrometers (Ocean Optics USB2000+ as well as Thorlabs CCS 100) were calibrated. The measurement conditions can be found in table 5.4 for the Ocean Optics USB2000+ and for the Thorlabs CCS 100, respectively.

Table 5.4.: Parameters to obtain the linearity of the Thorlabs CCS 100 and Ocean Optics USB2000+ CCD detector.

Parameter	Thorlabs	Ocean Optics
T of optical density filters (%)	$2.8 < T < 93.4$	$1.2 < T < 98.3$
Driving parameters of red LED	10 mA DC, 1.79 V	300 mA Pulse
Turn on time of LED (min)	> 20	> 30
UV/VIS spectrometer	Shimadzu UV/VIS 1800	PerkinElmer Lambda 9
Distance LED to aperture (mm)	56	30
Distance ODF to aperture (mm)	2	2

The Thorlabs CCD detector shows a linear behavior over the whole region (top panel in figure 5.16). Though, due to the fact that no measurement data is available below 2.8 % and above 93.4 % the linearity out of the interval can not be ensured. Therefore the signal intensity should be adjusted in a way that the intensity of the signal is at least 3 % and not higher than 93 % of the total available range (i.e. by changing the integration time of the detector).
The Ocean Optics USB2000+ CCD detector shows a distinct behavior (bottom panel in figure 5.16). Only in the range between 11.9 % to 65.8 % linearity is ensured. Therefore the signal intensity should be adjusted in a way that it lies in between this regime.

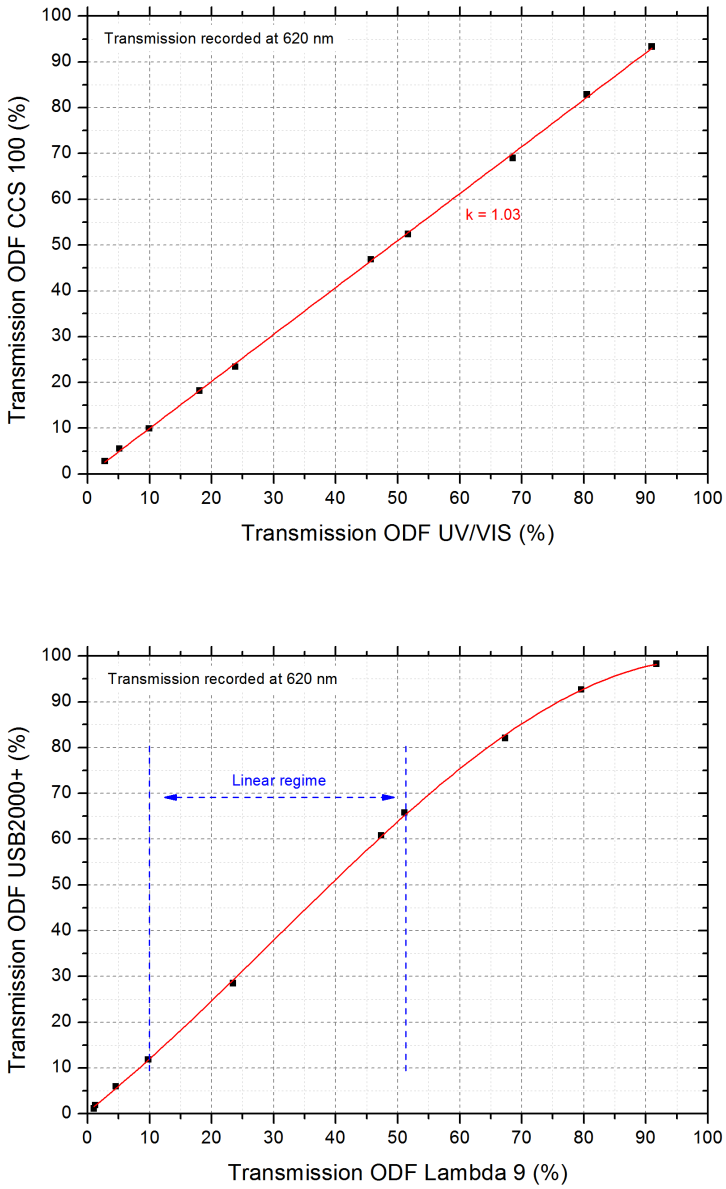

Figure 5.16.: Behavior of the linearity of the CCD detector of the Thorlabs CCS 100 (top panel) and the Ocean Optics USB2000+ (bottom panel) spectrometer.

5.5. Rising / falling times of LEDs

In the presented setup a very short forward voltage pulse is injected into the devices. The pulse width is 500 ns and the pulse repetition rate is 500 μm, which leads to a duty cycle of 0.1 %. The question now arises if the investigated devices can follow the short pulse width of 500 ns. Therefore the rising and falling time of the LEDs was determined. The LEDs were operated with forward voltage pulses of 500 ns. A high speed silicon PIN photodiode[5] was placed in front of the LED and measured the emission response. Table 5.5 lists the photodiode specifications. To record the voltage output of the photodiode, a 350 MHz scope was used. As listed in table 5.5 the typical rising time of the silicon photodiode is 2.5 ns. This fits with the specification of the scope quite well because its maximum resolution is around 2.9 ns (350 MHz).
To obtain the rising time τ_r of an LED, the time constant between 10 % and 90 % of the signal gain is measured. The obtain the falling time τ_f the same distance is measured on falling edge of the signal.
The rising time τ_r and the falling time τ_f for the GaN-based LED and for the AlGaInP-based LED were obtained. Figure 5.17 shows the results for the two respective types of LEDs. For the GaN-based LED (top panel of figure 5.17) a rising time τ_r of around 117 ns and a falling time τ_f of 95 ns was found. The average signal width (at 50 % of the maximum signal value) is 471 ns. For the red emitting AlGaInP-based LED a rising time τ_r of around 72 ns and a falling time τ_f of 68 ns was measured. The average signal width (at 50 % of the maximum signal value) is 486 ns.
In figure 5.17 the time response of the photodiode was shifted around -23.7 ns towards the forward voltage spectrum of the LED. This shift was measured in each performed measurement and is referred to a systematical error. One explanation for this systematical error is that the forward voltage injection pulse is measured directly after its production. However the response of the silicon photodiode is measured later in the measurement setup, therefore this time delay is measured as well. Further the response of the photodiode has also taken into account.

Table 5.5.: Melles Griot High-Speed Silicon PIN photodiode specifications.

Range of spectral response (nm)	350-1100
Rise time (ns)	2.5 typ; 3.5 max
Noise equivalent power (W/$\sqrt{\text{Hz}}$)	2.2 $\cdot 10^{-14}$
Dark current at -9 Vdc (nA)	5.5 typ
Response at 830 nm (A/W)	0.35 typ; 0.4 max

[5] Melles Griot, Product number 13 DAH 005

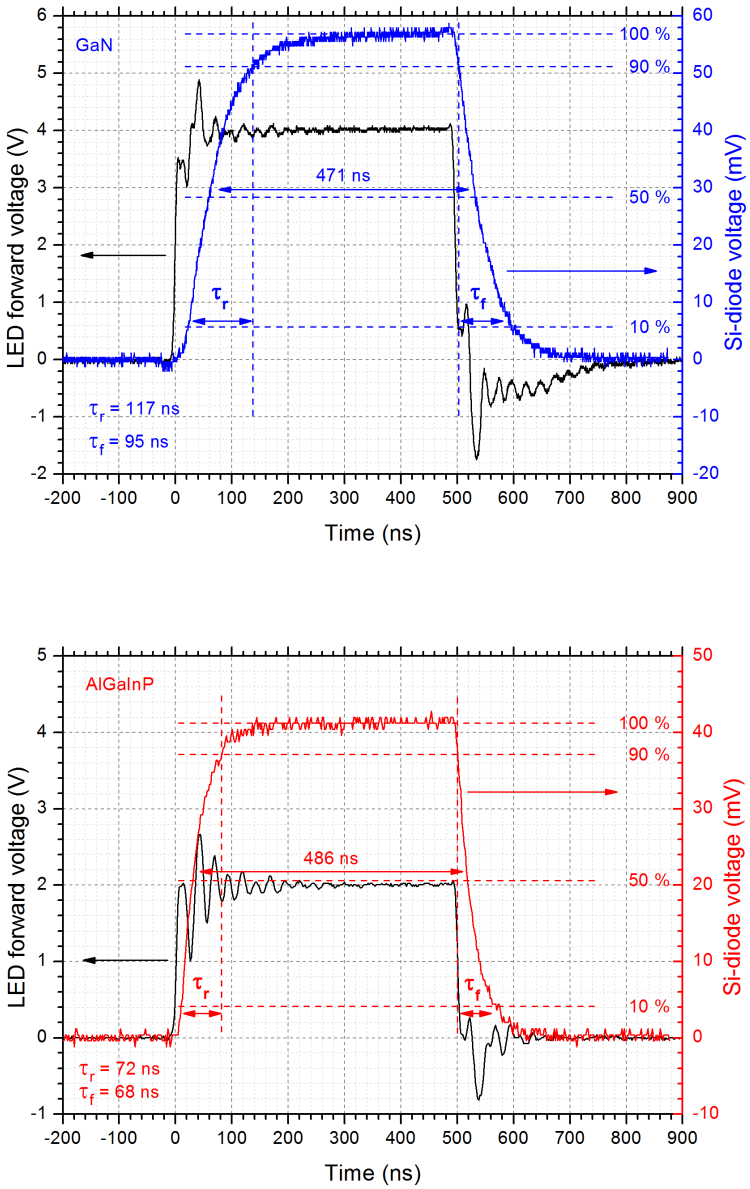

Figure 5.17.: Emission behavior of the GaN-based (top panel) and AlGaInP-based (bottom panel) LED operated with a 500 ns forward voltage pulse. The LED rising time (τ_r) as well as falling time (τ_f) are extracted out of the time distance between the signal value at 10 % and 90 %.

5.6. Influence of the 500 ns pulse on surface heating

To ensure that there is no increase of the device temperature (junction temperature) with respect to the pulsed injection current, a time dependent measurement of the surface temperature of the two types of LEDs has been performed. The LED dice were mounted on a ceramic substrate with poor thermal conductivity. Therefore the produced heat will not be transferred to a heat sink and the LED will heat up immediately if too much power is injected. Figure 5.18 shows the samples mounted on the ceramic substrate and bonded with 30 µm thin gold wires to a PCB.

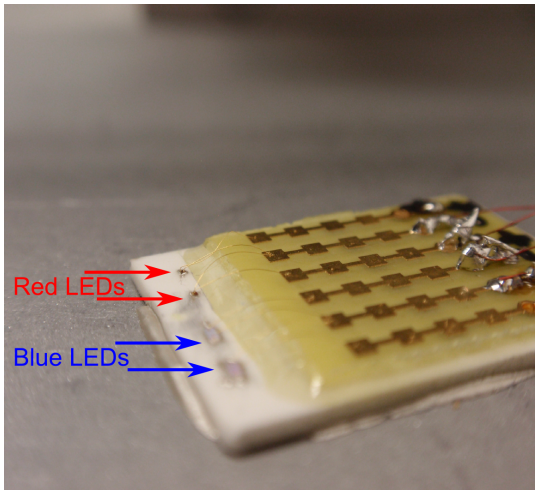

Figure 5.18.: Red emitting AlGaInP-based and blue emitting GaN-based LEDs mounted on a ceramic substrate and bonded to a PCB.

With an IR camera (Optris PI 160) a time dependent temperature measurement of the LEDs has been performed. The LEDs were operated with the maximum forward pulsed current used in the experiments (250 mA for the GaN-based LED, 150 mA for the AlGaInP-based LED). The results are shown in figure 5.19 whereas the inserts show the respective IR and visible images including the measurement areas. Two measurement areas were defined; Area 1 refers to a spot on the ceramic substrate, Area 2 to the actual diode. The reason of the temperature difference between Area 1 and Area 2 is due to the different emission coefficient of ceramic and diode. Each second a temperature value was recorded.
It is observable out of figure 5.19 that no change of the surface temperature with respect to time is measured if pulsed injection current is applied. This result supports our approach that thermal equilibrium of the diode is not disturbed by the injection of very short voltage pulses in combination with a low duty cycle.

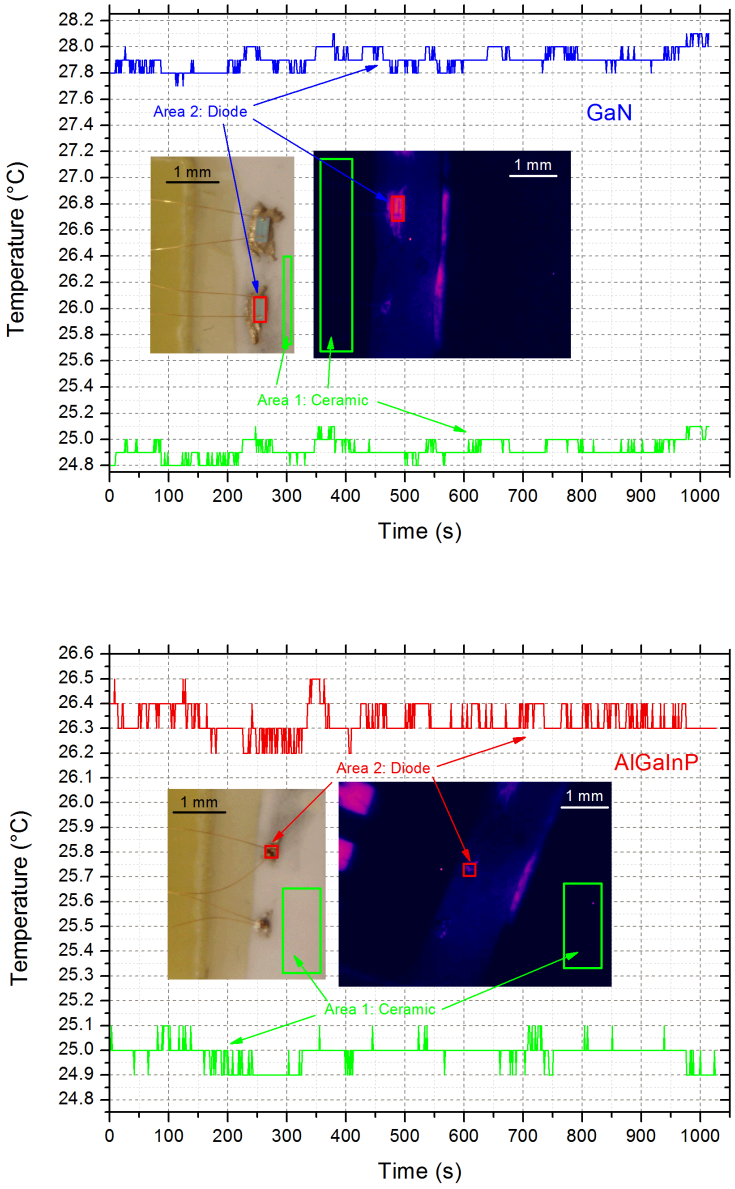

Figure 5.19.: LED surface temperature versus time measured with an IR camera. Top panel: GaN-based LED under a 250 mA pulsed injection current. Bottom panel: AlGaInP -based LED under a 150 mA pulsed injection current. Pulse width = 500 ns, duty cycle = 0.1 % for both types of LEDs. T = 0 seconds denotes that the LED is turned off, T = 1 second denotes that the LED is turned on. Area 2 denotes the position of the LED, Area 1 the ceramic environment.

Part III.

Results and Discussion

6. Current density impact on the emission behaviour of GaN-based blue emitting LEDs in the temperature range of 4.2 K to 400 K

This chapter 6 (except section 6.6) is presented in its original form (as accepted). No contents regarded changes were made, only the shape was adapted to the formatting of the thesis. Copyright clearance of the full text was obtained from the publisher. The text of the paper was completely written by the author of this thesis. The second and last author of the paper, Günther Leising, was the supervisor of the project. Further contents discussion as well as correction and proof reading was performed by him.

6.1. Abstract

Blue emitting GaN-based light emitting diodes (LEDs) show a distinct spectral behavior with respect to temperature and injection current density. Operating LEDs with short current pulses of 500 ns provide a steady state situation which allows investigating the emission behavior of LEDs at a certain device temperature thereby maintaining thermal equilibrium. The LEDs were examined in a temperature range between 4.2 K and 400 K and in a current density range between 2 A/cm^2 and 50 A/cm^2. Low temperature investigations showed a blue shift of the electroluminescence spectra (EL) with respect to junction temperature which is assigned to the radiative recombination of localized excitons. In the elevated temperature region a distinct red shift due to energy gap shrinkage was observed. Further we expect an exciton lifetime reduction at 4.2 K.
Additionally the influence of the driving parameters (pulsed injection current or direct current (DC)) in the presence of piezoelectric fields is discussed and separated into band filling effect and occurrence of fields which screen the quantum confined Stark effect (QCSE). Low temperature investigations indicate that band filling is mainly responsible for the blue shift of the EL spectra with respect to the injection current.

6.2. Introduction

Recent insights into the human non-image forming visual system gained tremendously the interest in tunable white light engines (changing color temperature) in the last couple of years. Hence the requirements for modern light emitting diodes (LEDs) are stable emission spectra, independent of the modality of current injection (pulse width modulated (PWM) or direct current (DC)). These driving parameters are mainly responsible for the temperature increase of the pn-junction which leads to unwanted spectral variations during operation of the LEDs [1]. In white light illuminants especially blue emitters play a prevailing role because they are used as primary emitter and also as excitation source for the phosphor conversion technology. GaN layers reveal great thermal stability as well as crystalline robustness which make this III-V direct semiconductor compound widely used for short wavelength light emission in optoelectronic devices for general illumination purposes [61],[62]. The understanding of the detailed nature of the emission process occurring in blue emitting LEDs and its particular behavior under different driving conditions is mandatory to design LED modules with stable and constant color coordinates.

The emission response is influenced by several internal device parameters. One important parameter, which dictates efficiency drops and influences the emission characteristics of LEDs is the junction temperature (JT) of the device [63]. However, the JT of LEDs is very difficult to access as neither sensing elements nor Infrared (IR) cam-eras can be used for determination. Sensing elements probe the temperature remote from the junction; IR cameras suffer from the problem that images have to be calibrated regarding the often unknown emission coefficients and they look at best at the surface temperature and not at the JT of the device. If measured on the final LED module, emitted IR radiation gets absorbed in the globe top material which consists typically of hydrocarbon/silicon polymers. Implementing phosphor conversion materials (i.e. rare earth doped sulphides, nitrides, aluminum garnets etc.) into the globe top matrix will further sufficiently increase the IR absorption. Consequently in the last couple of years methods have been developed which allow determining the JT out of the peak wavelength shift, the slope of the high energy wing or the forward voltage behavior of the LED [64], [65], [66], [67]. Those measurements are performed at thermal equilibrium in a temperature controlled oven.

We describe the current density impact on the temperature and therefore on the emission behavior of GaN-based LEDs by comparing pulsed and DC injection operated LEDs. We distinguish between pure temperature effects and pure carrier (current) impacts on the emission characteristics of GaN layer structures which we achieve by operating the LEDs with short current pulse widths and low duty cycles. To achieve thermal equilibrium at low temperatures, the spectral response of the LEDs was measured in a liquid helium and nitrogen bath.

6.3. Experimental setup and sample preparation

The measurements were performed at 4.2 K and 77 K and in the range between 230 K and 400 K. To ensure the intended device temperature (JT), all measurements were performed in thermal equilibrium. Low temperature measurements were carried out by contact cooling in a liquid helium bath (4.2 K) and a liquid nitrogen bath (77 K). The investigated LEDs consist of 8 μm thick GaN grown on a 140 μm thick Al_2O_3 substrate followed by an AlGaN/InGaN/GaN multiple quantum well (MQW) structure. A transparent SiO_x passivation layer is located on top of the whole diode area. The LEDs were mounted with a two component thermally conducting paste on an aluminum heat sink (5.0 mm x 6.3 mm x 4.8 mm) and contacted with 30 μm thick Au bond wires down to a printed circuit board (PCB). The device dimensions were 500 μm x 1000 μm with a device thickness (substrate and semiconductor layer) of 150 μm. The emission spectra were recorded with a spectrometer containing a 1200 lines/mm grid blazed at 500 nm. The spectrometer contains a CCD image sensor with a total number of 3648 pixels (pixel dimension 8 μm x 200 μm). Intensity calibration of the spectrometer (including fiber optics) was performed with a tungsten lamp standard; the wavelength calibration with a mercury argon lamp. The photometric linearity of the CCD detector was determined which causes that the signal intensity must be in the range between 5 % and 90 % of the total available measurement interval. For each recorded spectrum, the corresponding dark current was measured immediately afterwards and subtracted for data analysis. For the low temperature measurements (4.2 K & 77 K) a 250 μm diameter fiber optics (NA=0.29) was fixed on top of the LED using transparent glue. Emission/excitation photoluminescence measurements of the glue were carried out to ensure that the used glue does not affect the emission characteristics of the samples. Moreover we quantified that the shape of the emission spectra and the peak position is independent of the detector angle relative to the sample position. We furthermore did not observe any preferred polarization direction of the collected light.
For the measurements in the range between 230 K and 400 K a temperature-controlled chamber was used (temperature accuracy 0.1 K). To ensure the preset temperature of the chamber an additional Pt100 resistance on a separate heat sink was placed inside. During the whole experiment the chamber was purged with dry air to avoid icing effects. In front of the entrance slit of the fiber optics input side an aperture with an acceptance angle of 5.72° was inserted. The samples were stored for at least 30 minutes per measurement point in the chamber to ensure thermal equilibrium between the junction and the chamber environment.
To operate the samples, forward current pulses (HP 214 B pulse generator) as well as DC current (Keithley 2601 B source measure unit) were injected. The forward current pulse width was 500 ns and the repetition rate was 500 μs (duty cycle 0.1 %), respectively. A 20 Ω series resistance was installed in the setup to determine the injection current. The

pulsed injection current (density) was varied between 10 mA (2 A/cm^2) and 250 mA (50 A/cm^2). Current voltage characteristics in DC mode were recorded consecutively from 0 mA to 200 mA with a 10 ms current injection time per measuring point. The DC current emission spectra were recorded after the device was turned on for 3 s.

6.4. Results and discussion

One key parameter of light emitting junctions is the JT of the heterostructured LED. The JT is understood as the lattice temperature of the semiconductor alloy. Carriers injected into the quantum wells are denoted to hot carriers which possess a higher temperature than the JT [68]. Those injected hot carriers undergo certain pathways of thermalisation. One thermalisation process occurs due to carrier-carrier scattering of the injected hot carriers as well as due to the interaction with already present charge carriers [69], [70]. Moreover an energy transfer from the hot carriers to the lattice by the emission of phonons takes place [69], [70]. Thermalisation due to carrier-carrier scattering occurs quite fast (< 100 fs) e.g. for GaN 15-20 fs (at 25 K) were reported [68], [71]. Thermalisation by the emission of phonons is occurring in the ps range where for GaN values between 0.2 ps and 2.5 ps [70], [72], [73], [74] and for InGaN epitaxial films 5 ps [69] at room temperature were reported.
For AlGaN/GaN heterostructures 1.4 ps and for AlInN/AlN/GaN heterostructures a hot carrier energy relaxation time of 6 ps (at room temperature) were experimentally determined [75], [76]. So, current pulse widths of 500 ns are orders of magnitude longer than the reported hot carrier relaxation times. Therefore carrier temperature is expected to be equal to the JT. On the other hand, combining this current pulse width of 500 ns with a very low duty cycle of 0.1 % allows neglecting the contribution of the average integrated power impact on the JT and leads to a steady state situation. Operating LEDs with pulsed injection currents and a very low duty cycle in combination with a short current pulse width (500 ns) allows us to study the current impact on the charge carrier distribution in the potential wells of the MQW structure at certain preset temperature values. Further we gain insights into impact of the JT on the electroluminescence (EL) spectra.

6.4.1. Junction temperature investigations

Figure 6.1 illustrates the behavior of the emission-peak energy E_p with respect to the JT for several pulsed injection currents, which was obtained from the respective measured EL spectra. For temperatures above 230 K a red shift of the EL spectra with respect to the

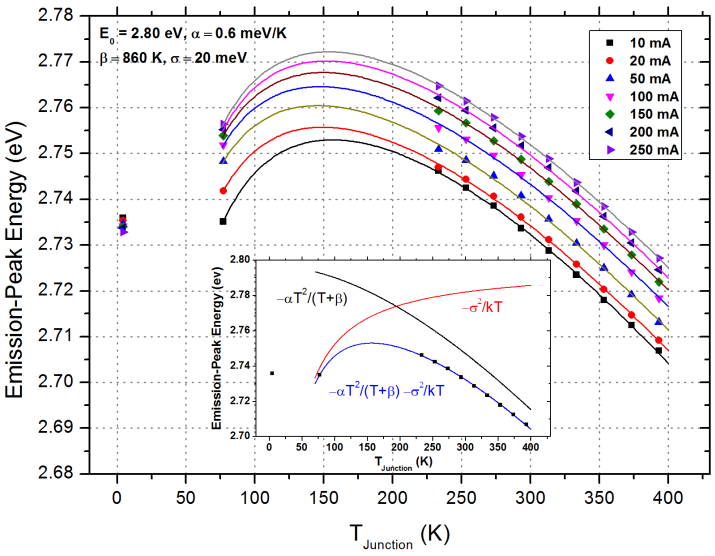

Figure 6.1.: Behavior of the emission-peak energy E_p as a function of the junction temperature $T_{Junction}$ and the pulsed injection current. The solid lines are the fitting curves based on equation 6.2. Insert shows the individual contribution of the respective terms of the model in equation 6.2 for a 10 mA injection current.

JT occurs, which shows a nonlinear behavior (quadratic) up to 300 K and a linear relation for higher temperatures. This red shift can be attributed to a temperature induced energy gap shrinkage of the MQW structure which can be understood as an interaction of the temperature dependent expansion of the lattice as well as the temperature dependent electron lattice interaction [77]. In this temperature region between 230 K and 400 K we measured a broadening of the emission spectra of approx. 8 nm which occurs from the interaction of charge carriers with phonons (acoustical as well as optical) and unavoidable alloy composition fluctuations [67], [78]. We found an additional distinct red shift of the EL spectra with decreasing temperatures (i.e. blue shift with increasing temperature) for the low temperature range (4.2 K & 77 K) which is an indication for exciton localization [40], [79], [80], [81], [82], [83], [84]. In semiconductor materials excitons are localized at low temperatures and quasi-free at high temperatures [85]. Structural defects (e.g. composition fluctuations, impurity density states, and lattice defects) lead to highly efficient traps for excitons [80], [81], [82], [84], [86]. Hence the captured exciton loses its kinetic energy and therefore the photon emission energy that corresponds to the recombining bound electron-hole pair is reduced by the binding energy. This leads to induced electronic states in the energy gap of the material and therefore to a red shift at low temperatures (where excitons dominate the radiative recombination). Equation 6.1 presents the total exciton energy E_f in the ground state,

whereas E_X stands for the binding energy of the exciton, m_e/m_h for the electron/hole mass, E_g reflects the actual energy gap, k the Boltzmann constant and $\hbar$ is equal to the Planck constant divided by 2π [40]. For trapped excitons the kinetic energy term vanishes and the total exciton energy E_f is given by the actual gap energy E_g minus the binding energy of the exciton E_X.

$$E_f = E_g - E_X + \frac{\hbar^2 k^2}{2(m_e + m_h)} \tag{6.1}$$

To gain insight into the degree of the localization of the excitons (which apparently dominate the emission at low temperatures) we apply a model in figure 6.1, which describes the behavior of the peak emission with respect to temperature as suggested in [81] and [87]. The emission-peak energy as a function of temperature $E_p(T)$ can be then fitted with equation 6.2

$$E_p(T) = E_{g,0} - \frac{(\alpha T)^2}{T + \beta} - \frac{\sigma^2}{kT} \tag{6.2}$$

whereas $E_{g,0}$ represents the fundamental gap energy at the limit T = 0 K, α and β are the Varshni parameters and T is the JT of the device, respectively. The last term $-\frac{\sigma^2}{kT}$ describes the Stokes-type red shift whereas from the σ value the degree of localization of the excitons can be obtained [79], [80], [81], [84], [87]. We found a σ value of around 20 meV which is a qualitative indication of a high degree of localization and in good accordance to previous reported results [79], [81], [87]. As indicated in figure 6.1, equation 6.2 is just applicable for the temperature range at and above 77 K which again agrees with previously reported results in [79], [81], [87]. However, equation 6.2 cannot describe the distinct behavior of the EL-peak at 4.2 K which will be elaborated below.

Insert in figure 6.1 separates the respective contribution of the two terms in equation 6.2. The first term $-\frac{(\alpha T)^2}{T+\beta}$ includes the Varshni parameters and allows the description of the energy gap shrinkage with increasing temperature whereas the second term $-\frac{\sigma^2}{kT}$ includes the excitonic behavior. Out of the applied model we obtained Varshni parameters of around 0.6 meV/K for α and 860 K for β which are comparable to reported literature values for such types of materials [79], [84], [88], [89].

6.4.2. Injection current influence

At 77 K and in the temperatures region between 230 K and 400 K a distinct blue shift when increasing the injection current is observed (figure 6.1). Two kinds of effects can be dominantly assigned to this current-induced blue shift namely the band filling effect (BFE) as well as the screening of the occurring piezoelectric (PE) field [90], [91].

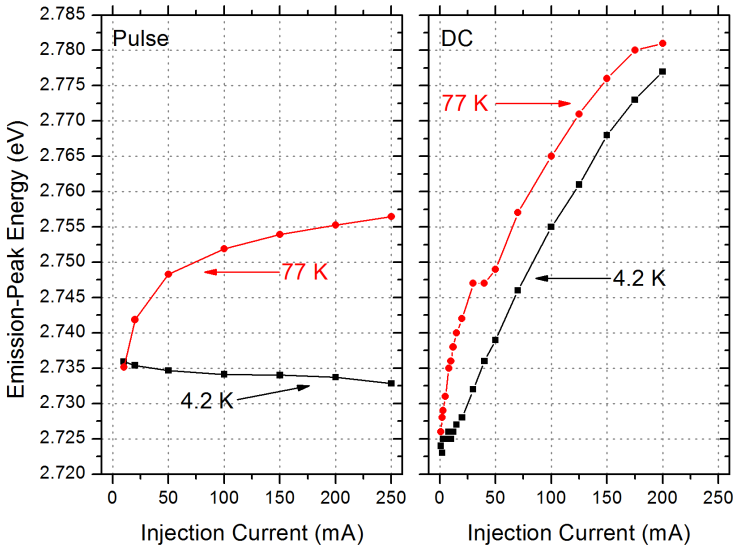

Figure 6.2.: Influence of pulsed (left panel) and DC (right panel) injection current levels on the emission-peak energy E_p at 4.2 K and 77 K.

Charge carriers at higher confined levels in a MQW structure contribute to the radiative recombination process, due to the fact that lower states are occupied [92], [93]. Therefore a shift to higher energies with respect to the charge carrier injection can be expected and assigned to the BFE. The BFE usually shifts the emission-peak energy linearly to higher energies when increasing the injection current [92]. This behavior is explained by the step-like density of states in the quantum well structure [42], [93].
However as reported previously the lattice mismatch of GaN, AlN and InN gives rise to PE fields which tilt the potential wells and therefore reduces the effective energy gap energy [94], [95], [96], [97]. The injection of charge carriers creates a field that counteracts the PE field and therefore reduces the occurring quantum confined Stark effect (QCSE) [92], [97], [98], [99]. As reported in [100] lattice mismatches as well as the difference in thermal expansion coefficients furthermore lead to strain and therefore to PE fields in GaN-based semiconductor alloys. Table 6.1 lists literature values for the piezoelectric modules ϵ_{33} and ϵ_{31} [101] as well as the thermal expansion coefficients α_n (normal to c-axis) and α_p (parallel to c-axis) at room temperature for GaN, AlN and InN, respectively [102], [103]. From Table 6.1 we find that the origin of PE field can be mainly assigned to the lattice mismatch. Nevertheless we note that the behavior of the thermal expansion coefficient for wurtzite III-V nitrides at low temperatures is quite complex due to the fact that negative values for temperatures below 50 K for InN [104] and at 75 K and below for AlN [105] were reported. However as described in [104],

the difference between the several expansion coefficients of those materials diminishes for very low temperatures (below 10 K). This concludes that the combination of different thermal expansion coefficients with the distinct lattice mismatches leads to PE fields which tilt the quantum well, where it can be expected that the lattice mismatch is the predominant effect.

Table 6.1.: Thermal expansion coefficients α_p/α_n [102], [103] and piezoelectric modules $\epsilon_{33}/\epsilon_{31}$ [101] for GaN, AlN and InN at room temperature.

	α_p at 300 K (10^-6/K)	α_n at 300 K (10^{-6}/K)	ϵ_{33} (C/m^2)	ϵ_{31} (C/m^2)
GaN	3.34	3.43	0.73	-0.49
AlN	3.48	4.35	1.46	-0.6
InN	2.751	3.83	0.97	-0.57

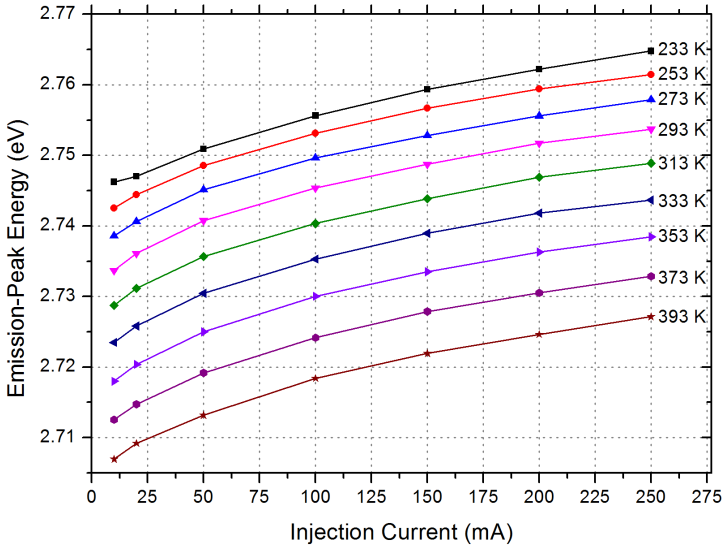

Figure 6.3.: Influence of pulsed injection current on the emission-peak energy E_p in the range of 230 K and 400 K.

The behavior of the emission-peak energy of the EL spectra with respect to the injection current for the low temperature region (4.2 K and 77 K) is shown in figure 6.2, for the high temperature region (230 K to 400 K) in figure 6.3, respectively. Neither for measurements performed at 77 K nor in between 230 K and 400 K, we find a strictly linear behavior of the emission-peak energy (which would be an indication for pure band filling) with respect to the pulsed injection current over the whole applied current range

(left panel in figure 6.2 and figure 6.3). Only for higher pulsed injection current levels (i.e. above 100 mA) a linear behavior can be observed (left panel in figure 6.2 and figure 6.3).
Further the increase of the full width at half maximum (FWHM) of around 16 meV with respect to the injection current at 77 K (figure 6.4) is an indication for band filling as the peak line width would be reduced if the QCSE is screened (as reported in [86], [99]).
At 4.2 K a very small red-shift (!) of 3 meV (corresponding to 0.1 % change of the respective emission-peak energy) with respect to the injection current is measured (left panel in figure 6.2). This supports our explanation that the screening of the PE field is not responsible for the blue shift with increasing current at elevated temperatures [79]. If screening of the occurring PE fields would be mainly responsible for the blue shift, such shift will be also observable at 4.2 K, besides, the FWMH will get reduced as well. However neither a blue shift (left panel in figure 6.2) nor a FWHM change (figure 6.4) is observed. Therefore we conclude that band filling is the dominant process for the blue shift of the EL spectra with increasing current at 77 K and above. However, since the emission-peak energy does show a non-linear behavior in the low current regime ($<$ 100 mA) and for temperatures above 77 K, an interplay between BFE and screening of the PE field in the low current range cannot be entirely excluded. The impact of PE fields in the low current region ($<$ 100 mA) and at elevated temperatures (at and above 77 K) cannot be further specified by taking the emission-peak behavior at 4.2 K into account.
We expect that the lifetime of the excitons decreases significantly at low temperatures, since neither the emission-peak energy (left panel in figure 6.2), nor the spectral shape (left panel in figure 6.5) do change significantly when increasing the pulsed injection current at 4.2 K (which was applied in the range between 10 mA and 250 mA) [85], [106]. Due to the decreasing lifetime of bound excitons at 4.2 K the recombination occurs from low lying energy levels. This reduction in carrier lifetime is also supported by the fact that no blue shift (and therefore no BFE) is observable at 4.2 K.
We note that for temperatures above 230 K the behavior of the emission-peak energy with respect to the injection current is slightly different and independent of the JT (figure 6.3). Deviations between low temperature (77 K) and high temperature (above 230 K) performance might be due to the fact that trapped excitons are not mainly involved in the radiative recombination process at such high temperatures anymore [85].

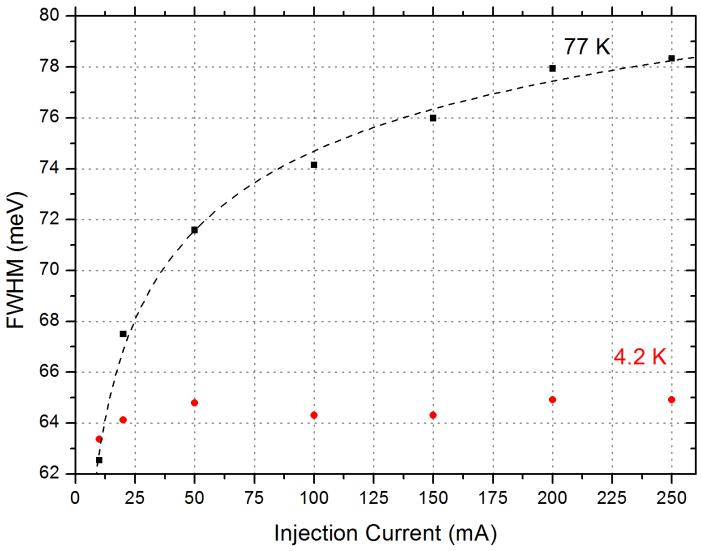

Figure 6.4.: Full width at half maximum (FWHM) with respect to pulsed injection current at 4.2 K and 77 K.

Essential to mention is that even low DC currents heat up the JT of the device, therefore non-thermal equilibrium situations are present and all discussed effects (lattice heating, carrier lifetime changes, screening of the PE field, band filling, etc.) do occur simultaneously and are hardly distinguishable anymore. With increasing temperature the lifetime of the charge carriers increase which allow them to relax into lower energy levels and explains the slightly red shifted emission spectra in figure 6.2 between pulse and DC injection current (< 30 mA) [106]. Therefore, a redistribution of the charge carriers occurs. However the lifetime gets also influenced by the amount of charge carriers, because more charge carriers in the quantum well reduce the average spatial separation between electrons and holes which reduces the lifetime [92]. This explains the different results of DC and pulse measurements performed at 4.2 K and 77 K in figure 6.2 especially for high current levels. Figure 6.5 shows the spectral behavior at 4.2 K depending whether pulse or DC current is injected.
These findings support our approach that the only way to extract reliable informations from the emission data is by depositing low pulse power. We further found a big difference between the measured current voltage characteristic of pulsed operated and DC driven LEDs for temperatures between 4.2 K and 300 K. Although the recording time of the current voltage characteristics of the LEDs was very short (10 ms) a distinct shift to lower voltages and therefore to higher temperatures was measured.

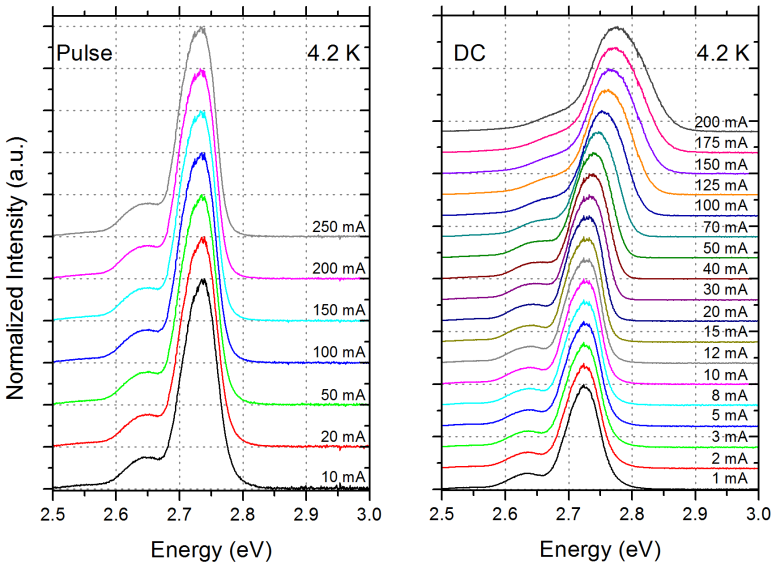

Figure 6.5.: Spectral behavior of GaN-based LEDs at 4.2 K. Left panel shows pulsed current injection, right panel DC current injection, respectively. The spectra are shifted vertically for clarity.

6.5. Conclusion

Our measurements on GaN-based LEDs showed that thermal as well as electrical effects highly influence the emission behavior. Due to our approach using pulsed injection current with a very low duty cycle and a short pulse width we could distinguish between prevailing thermal related shifts as well as carrier (current) dominated induced shifts. In the very low temperature region (4.2 K & 77 K), the emission-peak energy of GaN-based LEDs is red shifted with decreasing temperature (i.e. blue shifted with increasing temperature) due to the dominating radiative recombination of localized excitons from traps. Furthermore we expect that the exciton lifetime decreases significantly at 4.2 K. At 230 K trapped excitons do not dominate the radiative emission anymore and thermalize out of the quantum wells. Hence the observed red shift with increasing JT occurs due to the decrease of the effective energy gap.
We found that the blue shift with respect to injection current density can be dedicated mainly to band filling instead of screening of the QCSE. Important to mention is that the JT as well as the lifetime of the charge carriers is strongly influenced by DC current. Therefore investigations of the emission behavior of LEDs have to be performed using short current/voltage pulses and low duty cycles. To reach a steady state situation and ensure a defined JT in the low temperature region, investigations were performed in

liquid environment which is the only possibility to ensure thermal equilibrium at such low temperatures. Optical and electrical parameters gained from the presented experimental method can be in assigned to a 2-dimensional calibration array which allows the determination of the JT during operation of an LED by recalling those parameters. This gives the opportunity to counteract against current as well as temperature induced shifts of the color coordinates during operation of LED modules. Further evaluating the JT out of spectral data is more preferred than extracting it out of the forward voltage behavior (so called forward voltage method), due to the fact that the equivalent circuit of the measurement setup used for calibration is not equal to the commonly used PWM or DC driver circuits.

Acknowledgments

The authors would like to acknowledge LUMITECH Produktion und Entwicklung GmbH for providing samples as well as the Austrian Research Promotion Agency (FFG) for financial support. Further they thank Harald Plank and Sebastian Rauch for FIB and EDX measurements (Institute for Electron Microscopy and Nanoanalysis (FELMI) of Graz University of Technology).

6.6. Additional measurements

6.6.1. Phonon replica

The corresponding EL emission spectra of the GaN-based LED measured at 77 K are shown in figure 6.6. Left panel shows the pulsed operated LED in the range between 10 mA and 250 mA, right panel the DC operated spectra in between 1 mA and 200 mA, respectively. As discussed in the previous section, a blue shift of the emission spectra with respect to the injection current occurs which can be mainly assigned to band filling. Further at low temperatures excitons dominate the emission. The blue shift of the EL spectra when operating the LEDs under DC conditions is due to overlapping of several effects (screening of the PE-field, non thermal equilibrium situation, band filling, etc.) whereas a distinction is hardly possible. However this was already discussed in section 6.4.
In figure 6.6 as well as in figure 6.5 a peak on the low energy side (with respect to the main emission) is observed. This peak depends on the temperature and is disappearing for higher temperature values. This behavior is illustrated in figure 6.7 where the EL spectra with respect to temperature for a pulsed current of 10 mA and 250 mA are depicted.

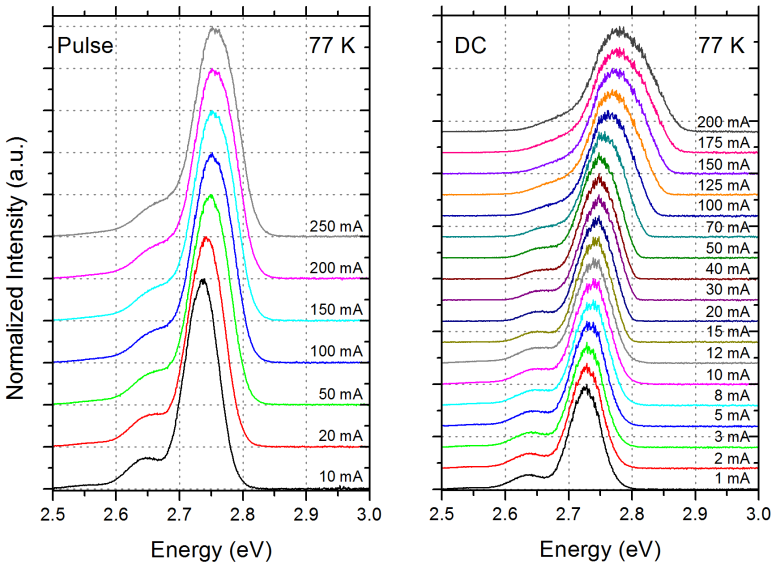

Figure 6.6.: Spectral behavior of GaN-based LEDs at 77 K. Left panel shows pulsed current injection, right panel DC injection, respectively. The spectra are shifted vertically for clarity.

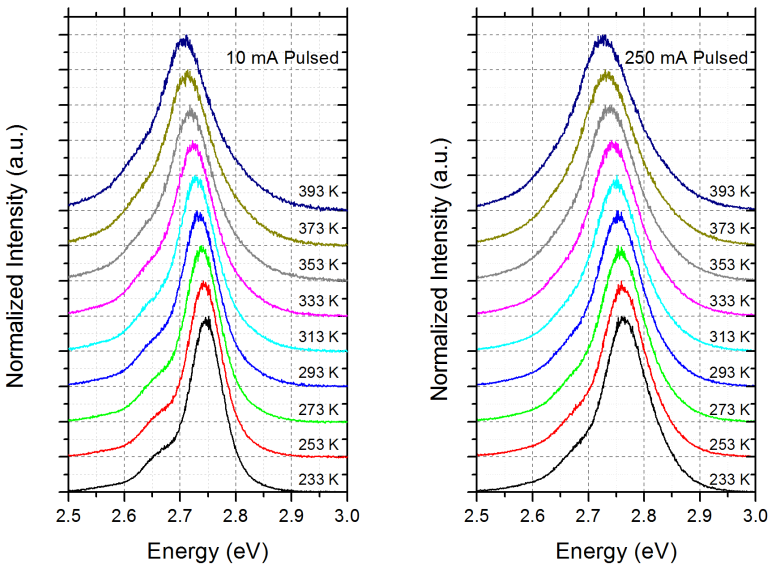

Figure 6.7.: Spectral behavior of GaN-based LEDs in the elevated temperature range between 233 K and 393 K. Left panel shows a 10 mA pulsed current injection, right panel shows a 250 mA pulsed current injection, respectively. The spectra are shifted vertically for clarity.

This low energy side peak can be assigned to *phonon replica* which means that a strong coupling between excitons and phonons exists [107]. To provide momentum conservation the radiative recombination of excitons is phonon assisted. The energy of the phonon assisted recombination is then given by equation 6.3 whereas E_0 is the zero phonon emission line (0LO) at low temperatures, $\hbar\omega_{ph}$ the longitudinal optical (LO) phonon energy and n a multiple integer (following reference [108]):

$$E_n = E_0 - n\hbar\omega_{ph} \tag{6.3}$$

Out of equation 6.3 one can see that the phonon assisted emission E_n is slightly red shifted (lower energy) than the main emission line E_0 (0LO). This phonon assisted recombination is strongly linked to the exciton therefore the LO phonon peak is disappearing with increasing temperature. However phonon replica are still observed (weakly) above room temperature which indicates a high crystal quality of the investigated samples [107].

We obtained the LO phonon energy out of the measurement at 4.2 K. Two side bands (satellites) are observable whereas the LO phonon energy was extracted out of the difference between the first LO mode (1LO) and the main EL peak emission E_0 which is also referred to the zero phonon peak (0LO). The second LO mode (2LO) is hardly appearing, therefore fitting of the emission peak was quite difficult and defective.
Figure 6.8 shows the EL spectrum of the GaN-based LED operated with 10 mA pulsed current at 4.2 K. The main emission peak was fitted with a Split-Gaussian function (asymmetric FWHM; in our fit model 0.037 eV on the left side and 0.026 eV on the right side), the LO phonon assisted peaks with a Gaussian distribution respectively. The difference between main emission (0LO) and the 1LO mode is around 91 meV which perfectly fits with previous reported literature results. For InGaN/GaN MQW between 89 meV and 92 meV were reported [107], [109], [110], [111], [112] for AlGaN/GaN heterostructures 89 meV were reported [113], respectively.
The distance between 1LO mode and 2LO mode is around 105 meV which is slightly higher than the difference between 0LO and 1LO mode. As discussed above this is due to the inaccuracy of the fitting, because the peak is hardly observable.
Out of the relative height of the 0LO mode and the respective LO phonon modes the exciton phonon coupling can be evaluated [114]. To express the relative strength of the LO sidebands, the Huang-Rhys factor S is introduced in equation 6.4 ([111]):

$$I_n = I_0 \frac{S^n}{n!} \tag{6.4}$$

whereas I_n is the intensity of the n-th LO phonon replica and I_0 the intensity of the 0LO

line. Out of the intensity ratio $\frac{2LO}{1LO}$ the S parameter was obtained:

$$S = 2\frac{I_2}{I_1} = 2\frac{0.017}{0.14} = 0.24 \tag{6.5}$$

The value again fits well with literature results for similar structures and lies far above the value for bulk GaN (S $\approx$ 0.007), which indicates a strong coupling of the phonon to the exciton at low temperatures [114].

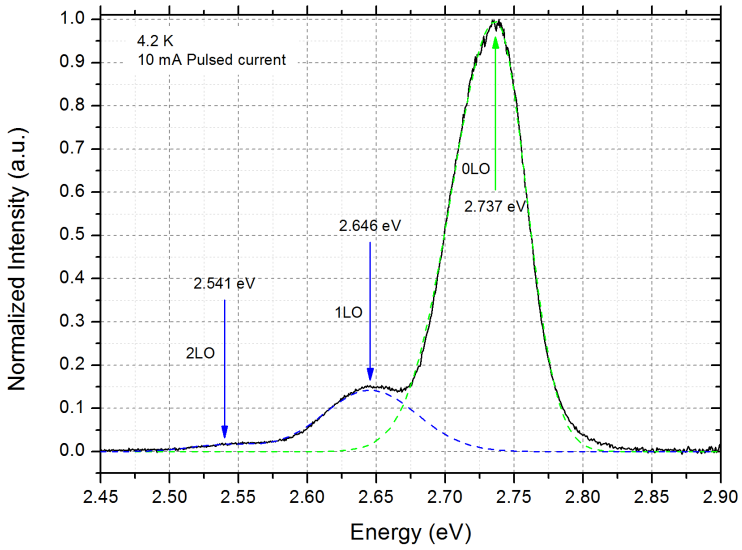

Figure 6.8.: El-spectrum of a GaN-based LED at 4.2 K operated with a 10 mA pulsed injection current. Peak fitting (dotted line) of the main emission peak (also called zero phonon line 0LO) was obtained by a Split-Gaussian function, first phonon mode (1LO) and second phonon mode (2LO) with an Gaussian function, respectively.

6.6.2. Current-voltage behavior of GaN

The current voltage behavior (I-V) of the GaN-based LED in the range between 230 K and 400 K is depicted in figure 6.9. The solid lines indicate the DC recorded I-V curves, the dots indicate the pulsed current injection measurements. For DC operation 200 measurement points with a DC injection time of 10 ms were applied. The measurement range was within the specifications of 0 mA and 200 mA. The pulsed measurements were recorded in the range between 10 mA and 250 mA, so slightly out of the specifications, but due to the pulsed operation the deposited power is still significant low.
Interestingly for low temperatures (233 K and 253 K) and high current values (above

20 mA) the DC recorded values do not fit with the pulse injection ones. The DC curves get shifted to lower voltages with respect to the pulsed injection measurement. This is an indication that the JT is significantly increasing and therefore the I-V characteristic shifts. The shift of the forward voltage with respect to injection current can be assigned to the self heating effect of the diode [115], [116].
This becomes crucial especially for very low temperature investigations. The insert in figure 6.9 illustrates the I-V characteristic at 4.2 K (DC as well as pulsed operated). The I-V curve for the DC operated LED shows a slight fold back behavior which is due to the temperature increase of the pn-junction. The difference between DC and pulse operated I-V characteristics is significant large even for low current densities.
The behavior of the I-V characteristics demonstrates the importance of depositing low power into the device to ensure the JT. Even very short DC current injection leads to a significant increase of the JT.

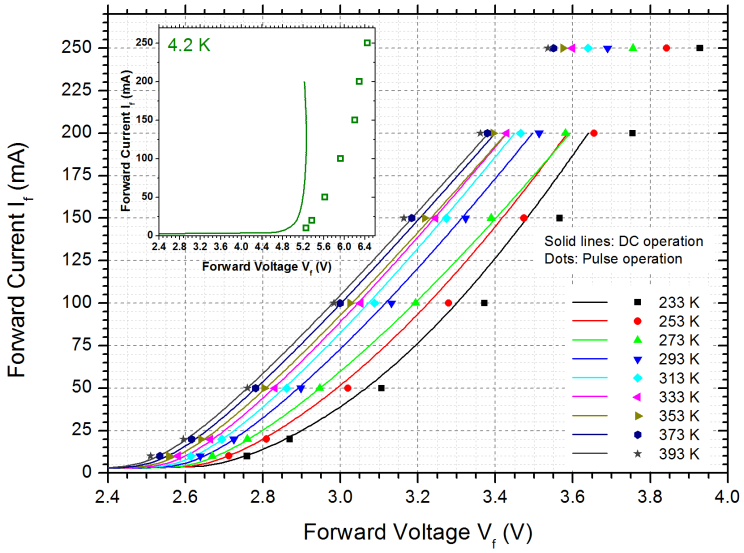

Figure 6.9.: Current-voltage behavior of the GaN-based LED in the temperature range between 230 K and 400 K. Solid lines indicate a DC operated LED, dots indicate a pulsed operated LED. Insert shows the behavior at 4.2 K.

Forward voltage behavior

A very common method to determine the JT of the device is the evaluation of the behavior of the forward voltage with respect to temperature. This can be done by a calibration measurement where the forward voltage with respect to the environmental temperature

of the oven (device in thermal equilibrium by operating it with very short voltage pulses) is recorded for several injection current levels. As shown for instance in reference number [65], [66], [117], and [118], usually the behavior of the forward voltage with respect to JT (oven temperature) follows a linear fit whereas its slope is independent of the injection current level.
We investigated the forward voltage behavior for JT determination in a reasonable and applicable temperature range of 233 K (-40°C) to 393 K (120°C). The dependence is plotted in figure 6.10 including the fit model. In this large temperture range we did not find a linear behavior, further the voltage behavior is not completely independent of the injection current level. We applied a quadratic fit model which allows to describe the certain behavior quite well. The obtained fit values can be found in table 6.2.
The previous reported linear behavior is only valid in a quite small temperature region (approximately between 20°C and 80°C) which is a too narrow range in terms of application. For a large temperature range another model has to be applied. However it still might be not sufficient extracting the JT directly out of the forward voltage behavior. Different approaches for determining the JT by the use of the change of EL-spectral behavior (e.g. peak wavelength, FWHM, high energy slope, etc.) should be considered as well.

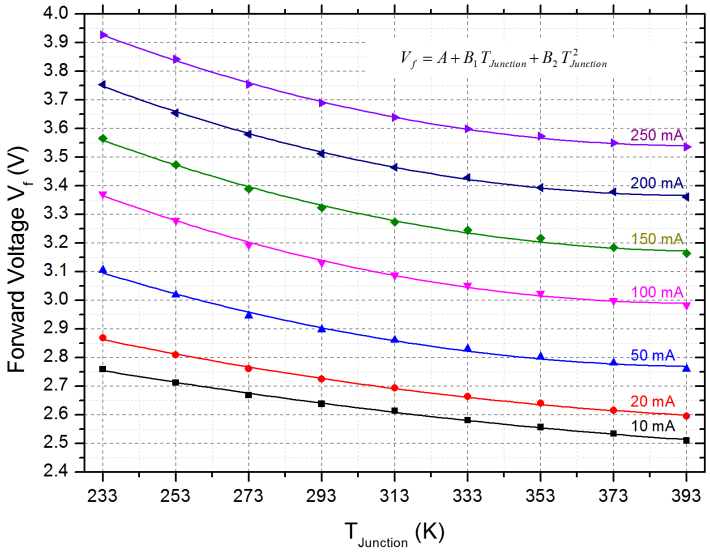

Figure 6.10.: Forward voltage V_f with respect to junction temperature $T_{Junction}$ for pulsed injection current. The fit parameters to the respective fit model are listed in table 6.2.

Table 6.2.: Fit parameter of model applied in figure 6.10 for several forward currents I_f. Model: $V_f = A + B_1\ T_{\text{Junction}} + B_2\ T^2_{\text{Junction}}$; A, B_1, and B_2 are the fit parameters and σ the respective standard deviations.

I_f **(mA)**	A	σ_A	B_1	σ_{B_1}	B_2	σ_{B_2}
10	2.77	$2.3 \cdot 10^{-3}$	$-2.1 \cdot 10^{-3}$	$0.7 \cdot 10^{-4}$	$0.6 \cdot 10^{-5}$	$0.7 \cdot 10^{-6}$
20	2.96	$4.3 \cdot 10^{-3}$	$-3.0 \cdot 10^{-3}$	$1.3 \cdot 10^{-4}$	$1.2 \cdot 10^{-5}$	$1.4 \cdot 10^{-6}$
50	3.20	$3.4 \cdot 10^{-3}$	$-3.5 \cdot 10^{-3}$	$1.0 \cdot 10^{-4}$	$1.4 \cdot 10^{-5}$	$1.1 \cdot 10^{-6}$
100	3.40	$4.3 \cdot 10^{-3}$	$-3.5 \cdot 10^{-3}$	$1.3 \cdot 10^{-4}$	$1.4 \cdot 10^{-5}$	$1.4 \cdot 10^{-6}$
150	3.58	$2.5 \cdot 10^{-3}$	$-3.5 \cdot 10^{-3}$	$0.7 \cdot 10^{-4}$	$1.5 \cdot 10^{-5}$	$0.8 \cdot 10^{-6}$
200	3.76	$2.2 \cdot 10^{-3}$	$-3.6 \cdot 10^{-3}$	$0.6 \cdot 10^{-4}$	$1.5 \cdot 10^{-5}$	$0.7 \cdot 10^{-6}$

6.6.3. Conclusion

The additional peak, red shifted relative to the main emission, occurring at low temperatures can be assigned to phonon replica which indicates a strong coupling between excitons and phonons. The distance between the zero phonon line (main emission line, 0LO) and the first phonon satellite (1LO) is around 91 meV which matches well with previous reported results.
DC operation of LEDs leads to a significant self heating effect which shifts the voltage to lower values. The effect becomes more dominant with decreasing temperature. This illustrates the dominant influence of DC operation on the JT of the device.
Apart from previous reported results, a non linear behavior of the forward voltage with respect to JT and pulsed injection current was observed. It is highly recommended to evaluate, if obtaining the JT directly out of the forward voltage behavior leads to correct temperature values.

7. Current density impact on the emission behavior of AlGaInP-based red emitting LEDs in the temperature range of 4.2 K to 400 K

7.1. Introduction

To achieve high quality white light in terms of high color rendering, a homogeneous distribution of the emission spectrum is needed (as discussed in section 3.2). This is only possible if a red emitter is inserted and the light source does provide a reddish emission. In principle there are two types of red emitters, primary emitters (e.g. LED) or color converting emitters which are excited by an UV or blue emitting LED. To circumvent the large Stoke shift by the use of red emitting color conversion materials, primary red emitting LEDs are usually preferred. Moreover, for a tunable white light system, which allows to change the color temperature throughout operation, a red emitting light source is needed to control the emission spectra in a way that the color temperature of the light source can be changed in a large range.
AlGaInP alloys are very promising to allow light emission starting from the long wavelength side (i.e. 650 nm) to the yellowish-green region (i.e. 560 nm) of the visible spectrum [119], [120]. Due to their high luminous efficacy of over 100 lm/W they are adopted in several applications, starting from automotive lighting, traffic lighting as well as color displays [120], [121]. An $(Al_xGa_{1-x})_{0.5}In_{0.5}P$ is lattice matched with GaAs which results in the fact that GaAs is often used as a substrate material for AlGaInP heterostructures [121].
However the behavior of the emission of AlGaInP LEDs strongly depends on several external parameters. One important parameter which will be discussed in this section is the junction temperature (JT) of the device [122]. Further the current density, the energy distribution of charge carrier as well as the coupling carrier strength strongly influence the emission behavior and performance of those types of LEDs [121].
The particular emission behavior of AlGaInP-based LEDs is still not well understood,

therefore in this section the current density impact on the emission behavior of AlGaInP-based LEDs will be described. In detail a separation between current impacts as well as temperature effects is achieved by operating the LEDs with very short pulse widths and small duty cycles. The investigated temperature region ranges from 4.2 K to 400 K, whereas low temperature investigations provide deeper insights into the ongoing radiative recombination process in such type of alloy.

7.2. Experimental setup and sample preparation

The experimental procedure was similar as described in section 6.3. Low temperature investigations were carried out in liquid helium-4 (4.2 K) and liquid nitrogen (77 K) by contact cooling in a liquid environment. The investigations in the temperature range between 230 K and 400 K were performed in thermal equilibrium in a temperature controlled chamber (temperature accuracy of 0.1 K). The devices were stored for at least 30 minutes in the oven before measurements were carried out, therefore the JT equals the lattice temperature of the devices. To ensure the preset temperature of the chamber, an additional Pt100 resistance on a separate heat sink was placed inside. During the whole experiment the chamber was purged with dry air to avoid icing effects. In front of the entrance slit of the fiber optics input side, an aperture with an acceptance angle of 5.72° was inserted.
The investigated LEDs consist of a 14 µm thick AlGaInP structure grown on an 86 µm thick Al_2O_3 substrate, whereas in the AlGaInP structure a 10 µm thick GaP layer was followed by a 3 µm AlInP layer. A transparent SiO_x passivation layer is located on top of the whole diode area. The LEDs were mounted with a two component thermally conducting paste on an aluminum heat sink (5.0 mm x 6.3 mm x 4.8 mm) and contacted with 30 µm thick Au bond wires down to a printed circuit board (PCB). The contact pads are out of Au as well. The device dimensions were around 300 µm x 300 µm with a device thickness (substrate and semiconductor layer) of approximately 100 µm. The emission spectra were recorded with a spectrometer containing a 1200 lines/mm grid blazed at 500 nm. The spectrometer contains a CCD image sensor with a total number of 3648 pixels (pixel dimension 8 µm x 200 µm). Intensity calibration of the spectrometer (including fiber optics) was performed with a tungsten lamp standard; the wavelength calibration with a mercury argon lamp. The photometric linearity of the CCD detector was determined which causes the signal intensity to be in the range between 5 % and 90 % of the total available measurement interval. For each recorded spectrum, the corresponding dark current was measured immediately afterwards and subtracted for data analysis. For the low temperature measurements (4.2 K & 77 K) a 250 µm diameter fiber optics (NA=0.29) was fixed on top of the LED using transparent glue. Emission/excitation photoluminescence measurements of the glue were carried out to

ensure that the used glue does not affect the emission characteristics of the samples. Moreover we quantified that the shape of the emission spectra and the peak position is independent of the detector angle relative to the sample position. We furthermore did not observe any preferred polarization direction of the collected light.
To operate the samples, forward current pulses (HP 214 B pulse generator) as well as DC current (Keithley 2601 B source measure unit) were injected. The forward current pulse width was 500 ns and the repetition rate was 500 µs (duty cycle 0.1 %), respectively. A 20 Ω series resistance was installed in the setup to determine the injection current. The pulsed injection current (density) was varied between 10 mA (11 A/cm^2) and 150 mA (167 A/cm^2) as well as between 20 mA (22 A/cm^2) and 500 mA (555 A/cm^2). Current voltage characteristics in DC mode were recorded consecutively from 0 mA to 40 mA with a 10 ms current injection time per measuring point. The DC current emission spectra were recorded after the device was turned on for 3 s.

7.3. Results and discussion

As described in section 6.4 the JT is understood as the lattice temperature of the LED. A pulse width of 500 ns was applied which is magnitudes of orders higher than typical relaxation times for the hot electrons (thermalization process) which is occurring in ps and fs ranges [68].
Figure 7.1 shows the behavior of the peak energy versus the junction temperature T_{Junction} and pulsed injection current for the investigated temperature range between 4.2 K and 400 K. In comparison to the results we obtained for the GaN-based blue emitting LED, the pulsed injection current does not influence the behavior of the main emission-peak energy. Therefore no particular strong band filling as well as no screening of piezoelectric field is observed.
Further free, rather than localized excitons, dominate the radiative emission at low temperatures which can be obtained from the fact that no red shift with decreasing temperature is observed in our samples [123]. The fit model given in equation 7.1 very well describes the behavior of the peak energy E_p with respect to the the junction temperature T whereas $E_{g,0}$ represents fundamental band gap energy at $T = 0$ K, and α and β the Varshni parameters [124]. In contrast to the fit model presented in section 6.4 for the GaN-based LEDs (where excitons which are localized at low temperatures dominate the emission), the term which describes the exciton localization $-\frac{\sigma^2}{kT}$ is set to zero, which indicates no exciton localization (at first sight, detailed discussion is followed below). The obtained fit values out of equation 7.1 are 0.8 meV/K for α and 560 K for β (presented in figure 7.1) which are in the same range as previous reported results for such type of semiconductor alloy [125], [126].

$$E_p(T) = E_{g,0} - \frac{(\alpha T)^2}{T + \beta} \tag{7.1}$$

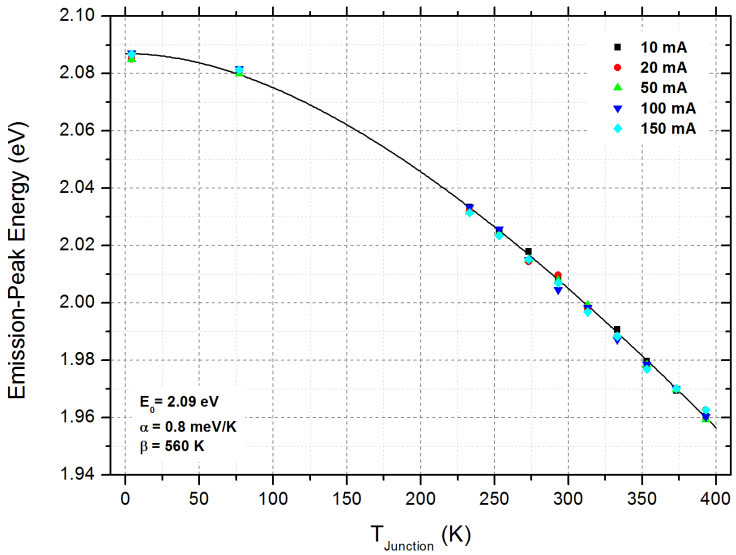

Figure 7.1.: Behavior of the emission-peak energy E_p as a function of the junction temperature T_{Junction} and the pulsed injection current. The solid line is the fitting curve based on equation 7.1. The fit model was applied for the 10 mA measurement data.

The spectral response of the emission with respect to JT in the elevated temperature region is shown in figure 7.2. One can see that if plotting the y-axis on logarithmic scale the slope of the high energy wing changes with respect to JT. This change can be recorded during a calibration measurement by injection of short forward voltage/current pulses. To determine the actual JT of a device during operation of the LED (LED is driven as designated), the slope of the actual emission spectra can be then compared to the slopes recorded in the calibration measurement. This allows to obtain the JT of an LED during operation directly out of the emission spectra [67], [118].
Inserted in figure 7.2 is the sensitivity of the L-cone fundamental (see section 2.2). The sensitivity of the L-cone drops significantly in the red region of the visible spectrum. Therefore a temperature induced red shift of the emission spectrum leads to a subjective brightness decrease since the sensitivity of the human eye is getting reduced. This indicates the importance of thermal management of solid sate lighting.

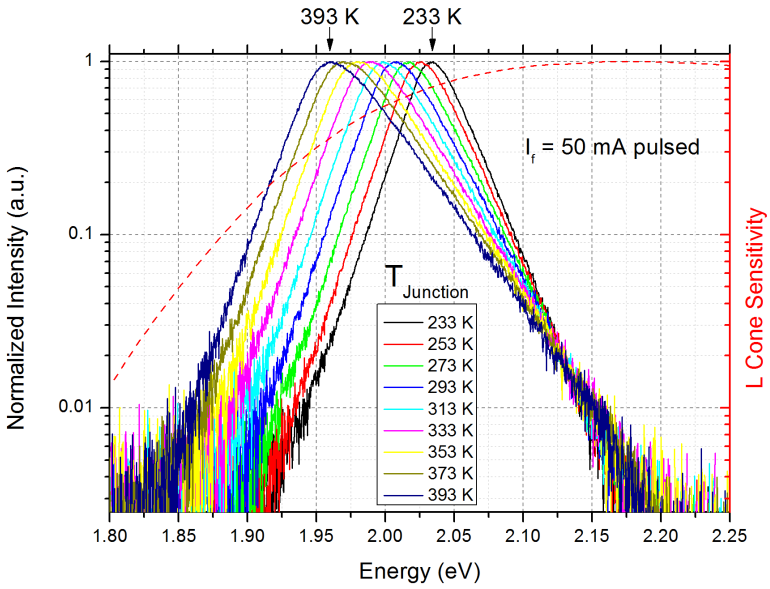

Figure 7.2.: Normalized emission spectra with respect to junction temperature T_{Junction} for an pulsed injection current level of 50 mA. The pulse width was 500 ns, the repetition rate was 500 µs, respectively (duty cycle of 0.1 %). The dotted line (referred to the right y-axis) represents the L-cone fundamental.

Figure 7.3 illustrates the FWHM change with respect to JT. The absolute value of the FWHM depends on the injection current level, however the slopes are independent of the respective injection current (0.05 nm/K). In the temperature range between 230 K and 400 K a linear shift of the peak energy with respect to temperature (insert of figure 7.3) independent of the injection current was observed. Again both parameters obtained out of the emission spectra (peak wavelength and FWHM change) can be used to determine the JT of a device while it is driven as designated and compared to the calibration measurement.

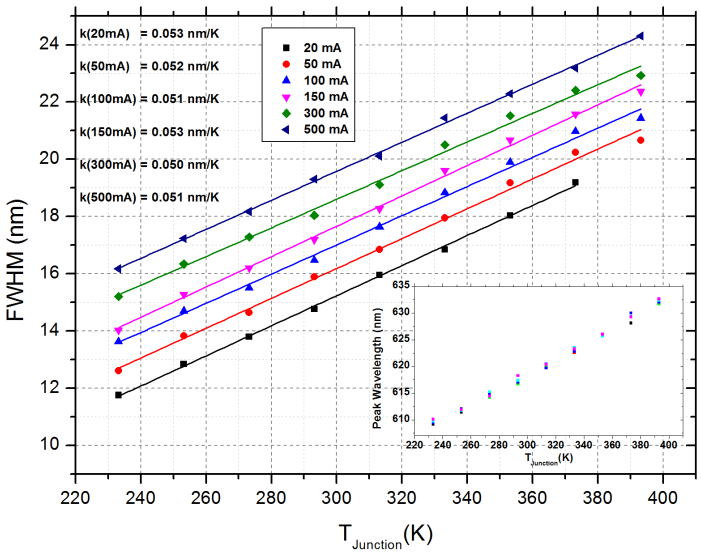

Figure 7.3.: Change of full width at half maximum (FWHM) with respect to junction temperature T_{Junction} and injection current level. The slopes k of the linear fit are listed. Insert shows the peak wavelength behavior for the same current levels with respect to junction temperature T_{Junction}.

7.3.1. Low temperature emission behavior

Already presented was the main emission peak E_p with respect to JT and pulsed injection current in the low temperature region (figure 7.1). However the detailed investigation of the emission spectra at low temperatures brings forward distinct characteristics of AlGaInP-based LEDs.

Figure 7.4 shows the behavior of the emission spectra with respect to injection current at 4.2 K. Left panel illustrates DC injection current, right panel the respective pulsed injection current measurements. One can see a dominant emission peak (E2) evolving at around 2.05 eV for low DC currents (0.1 mA to 3 mA), further a high energy peak at around 2.08 eV arises as well (E1). This second peak (E1 at 2.08 eV) gets dominant for high injection current levels at and above 5 mA. On the right panel the pulsed injection current measurements are presented which start at a current injection level of 10 mA. Lower pulsed injection currents were not possible to measure due to the fact that the signal to noise ratio decreased to an unacceptable level.

The main emission peak for pulsed operation is again at around 2.08 eV (E1), and similar to the DC operation at 10 mA, a distinct side shoulder is observable (E2). This side shoulder has a peak maximum of around 2.06 eV (E2 is also 2.06 eV at 10 mA DC),

therefore it is assumed that the peak E2 (in pulsed operation) is originating from the same recombination center as the peak E2 in the DC measurement. The author wants to allude that the spectra in figure 7.4 are normalized regarding their respective peak maximum and shifted for clarity.

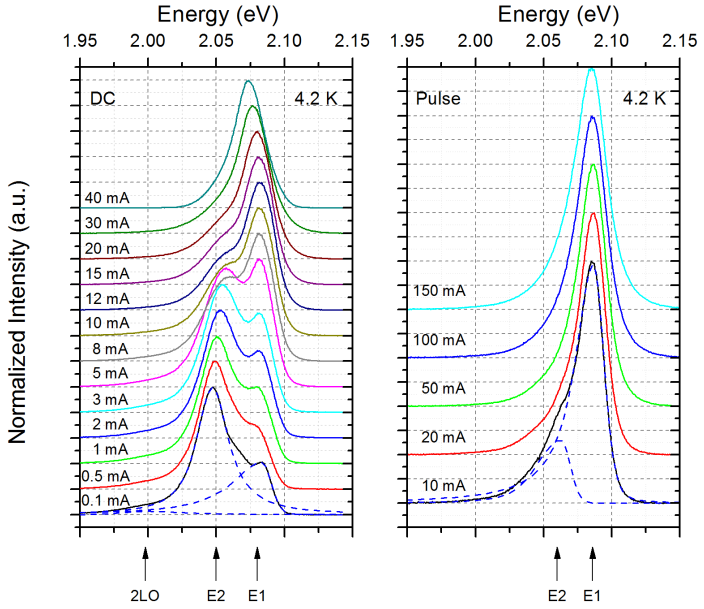

Figure 7.4.: Spectral behavior of an AlGaInP-based LED at 4.2 K with respect to various DC (left panel) and pulsed injection currents (right panel, pulse width was 500 ns, repetition rate was 500 µs, respectively). A "Split Voigt" profile fit for the lowest DC (0.1 mA) and pulse (10 mA) is illustrated (dotted line). The spectra are normalized to their respective peak maximum and shifted vertically for clarity.

To assign the certain peaks to recombination mechanisms, a couple of possibilities has to be taken into account:
We assign the emission at around 2.08 eV (E1) to the radiative recombination from excitons near the band edge of the main barrier. The low energy peak E2 at around 2.05 eV (2.06 eV) is assigned on the one hand to localized excitons. These are trapped due to impurities (defect related), and/or potential fluctuations and/or bound to neutral (D^0-X) and ionized (D^+-X) donors / neutral (A^0-X) and ionized (A^--X) acceptors. Localized excitons which are trapped lose their kinetic energy and therefore the recombination is red shifted with respect to the main emission [40]. The reason why this emission is so dominant at low DC levels is probably due to the fact that excitons are getting trapped to a certain level. If those traps are occupied, no more excitons can get trapped anymore, therefore the emission intensity is not further increasing. Further the degree of localization strongly depends on temperature. Higher DC injection leads to significant

higher temperature values of the pn-junction (self heating). This can also be identified out of the red shit of E1 occurring at higher DC levels and explains that the E2 peak gets slightly blue shifted with increasing DC current (temperature) as well.
The E2 peak occurring from trapped excitons does not disappear, rather the emission from the main barriers is getting so dominant that this peak is not resolved anymore.
One indication that trapped excitons are mainly responsible for this low energy emission is that at higher temperatures the localization becomes weaker because excitons thermalize out of the localized states in the QWs [123], [127]. This can be also seen in figure 7.5 where the emission spectra are plotted versus DC current (left panel) and pulsed injection current (right panel) at 77 K. The low energy side emission E2 is not as dominant anymore (even at low DC current levels) because the degree of localization decreases. Again the E2 peak is slightly shifted to higher energies if the temperature increases from 4.2 K to 77 K (around 12 meV in the 10 mA pulsed injection current measurement).
This behavior of E2 is similar to the exciton localization observed in GaN-based LEDs, however for GaN-based LEDs a blue shift of the main emission peak with temperature occurs (see section 6.4). Please be aware that all of the spectra shown in figure 7.5 are normalized to their respective peak maximum and shifted for clarity.
Indicated in figure 7.5 are fit functions used to obtain the peak values (details see below). It is very likely that LO phonon replica are superimposed (however unresolved) in the low energy side peak E2 of around 2.05 eV as well. Depending on the material, LO phonon replica energies for InP in between 42 meV and 45.2 meV [128], [129], [130] for GaP in between 45 meV and 47.6 meV [128], [129], [130], [131] and for AlP in between 55.8 meV and 56 meV [128], [129] were reported. For AlGaInP MWQ structure a LO phonon replica energy of 47 meV was reported [132] as well.
A 2LO phonon satellite of around 85 meV is observable at 4.2 K and at 77 K for low DC injection current (indicated in figure 7.4 and 7.5). This 85 meV correspond to a 42.5 meV 1LO phonon replica which fits with previous reported results [128], [129], [130], [131]. However, due to the dominant radiative recombination of localized excitons the 1LO phonon replica is not resolved.

As already discussed for high DC injection current the emission spectra get red shifted (at 4.2 K and 77 K). This results from the increase of JT due to self heating. Even at 10 mA direct comparison of DC and pulsed measurement show a slightly red shifted emission spectrum.

The author also wants to indicate that such peak splitting of the emission spectrum (in figure 7.4 and figure 7.5) is sometimes referred to exciton-polaritons, where a recombining exciton produces a photon which is getting absorbed immediately in the

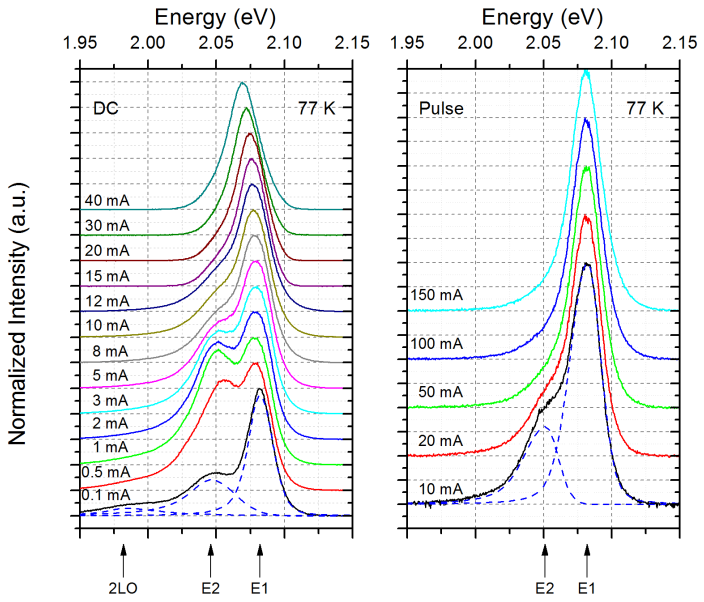

Figure 7.5.: Spectral behavior of an AlGaInP-based LED at 77 K with respect to various DC (left panel) and pulsed injection currents (right panel, pulse width was 500 ns, repetition rate was 500 µs, respectively). A "Split Voigt" profile fit for the lowest DC (0.1 mA) and pulse (10 mA) is illustrated. The spectra are normalized to their respective peak maximum and shifted vertically for clarity.

semiconductor structure [40]. However, if this would be the case, the two single peaks E2 at around 2.05 eV (2.06 eV) and E1 at around 2.08 eV, would merge to one peak if higher injection current is applied [133]. Further the phenomenon of exciton-polaritons in LEDs is, to the knowledge of the author, only observed in combination with a proper cavity which allows the re-absorption of the photon (e.g. in GaAs [133], [134]).
Another explanation of such peak splitting is the occurrence of strain which results in a split off of the heavy and light hole in the MQW. However this seems to be very unlikely in this case due to the fact that such observations were only achieved by inserting external mechanical pressure (e.g. diamond pressure cell [135]) or by certain growth conditions ([136], [137], [138]) to achieve such strain. Further it is not expected that such peak splitting will diminish with a higher injection current level.

The fit function used to evaluate the peak position is a "Split Voigt" profile (convolution of Lorentz profile and Gauss profile with two different FWHM on each side). The fit were just plotted for the respective lowest current levels (10 mA pulse injection current, 0.1 mA for DC injection) in figure 7.4 and figure 7.5. The fit function agrees well with the measured EL emission spectra.

7.3.2. Current-voltage behavior

Figure 7.6 shows the current-voltage (I-V) characteristics of the AlGaInP-based LED in the temperature region between 233 K and 393 K for pulsed operated LEDs. Insert in figure 7.6 illustrates the comparison between pulsed and DC operated I-V curves in the range between 0 mA and 25 mA in the same temperature range. For the pulsed operation the applied current was varied in the range between 10 mA and 150 mA, for the DC operation the current was varied between 0 mA and 40 mA (within the specifications), respectively. The I-V characteristic was obtained by measuring the voltage to the respective inserted preset current. For the DC I-V characteristic the DC current was injected 10 ms per measurement point (number of total measurement points was 200).
Out of the insert in figure 7.6 one can see that for high DC injection levels the I-V characteristics shifts to lower voltages. This can be assigned to the fact that DC injection leads to an increase of the JT which shifts the I-V curve to lower voltage values. This is obviously more curial at low temperatures, therefore the divergence between DC and pulsed operated I-V curve becomes more distinct at low temperatures.

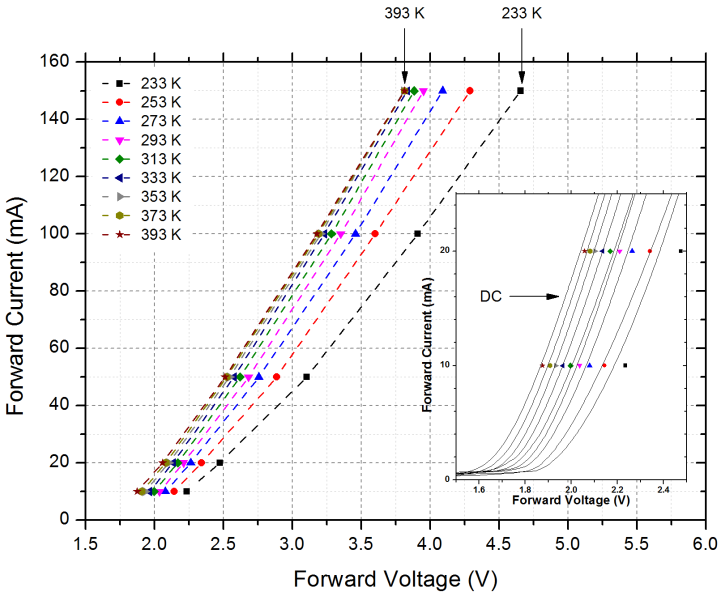

Figure 7.6.: Current voltage characteristic of an AlGaInP-based LED in the temperature range between 233 K and 393 K for pulsed operation. Insert shows the comparison between DC operation and pulse operation in the range between 0 mA and 25 mA in the same temperature range (DC was only applied between 0 mA and 40 mA).

Figure 7.7 shows the I-V behavior of the AlGaInP-based LED for the elevated temperature region (room temperature (293 K), upper boundary (393 K), lower boundary (233

K)) as well as for the low temperature range at 4.2 K and 77 K for pulsed injection current. Both axes are plotted on a logarithmic scale. The voltage change at 10 mA pulsed injection current is around 20.3 V (changing from 1.9 V at 393 K to 22.2 V at 4.2 K).
Insert in figure 7.7 illustrates the behavior of the I-V characteristics under DC injection for 4.2 K and 77 K. Comparison between DC and pulse operated LEDs shows a change of the forward voltage behavior (current was preset), where DC operation shifts the voltage to lower values. On top, at 4.2 K a back bending of the I-V curve is observable. A recent published paper by Lamp [139] observes a similar behavior of the I-V characteristics of AlGaInP-based LEDs at 4.2 K. The author of this publication associates this back bending to self heating in combination with the *Leidenfrost effect*[1] which together causes the elevation of the temperature of the diode [139].
However it is assumed by the author of this thesis that self heating is not the only reason for such strong back bending. Rather at very low temperatures most of the carriers freeze-out at shallow impurities (traps), therefore injection of charge carries in combination with a high electric field could lead to an ionization which will increase the current [140], [141], [142]. Due to the fact that for pulse operation the pulse width is only 500 ns, the charger carriers are not injected permanently. This influences the degree of ionization and explains the different behavior of the I-V characteristics of pulse and DC operation. A closer look at the shape of the forward voltage pulse at 4.2 K (150 mA) in figure 7.8 however indicates a similar behavior compared to DC injection. The voltage also drops (around 10 V) to maintain the preset current value of 150 mA.
After warming up of the LED back to room temperature the I-V characteristic behaves normally again. The process of back bending at low temperatures is reversible.

[1] Leidenfrost effect: An insulation vapor layer between a liquid and a solid object is produced by the fact that the object exhibits a higher temperature than the liquid's boiling point.

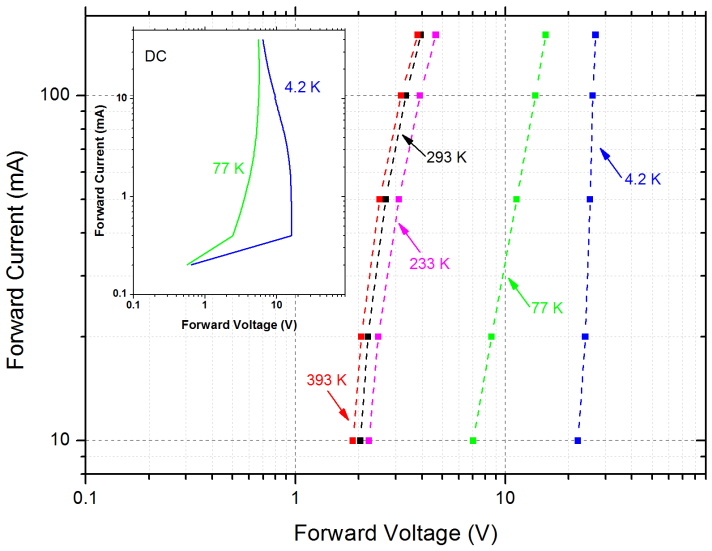

Figure 7.7.: Current-voltage characteristic of an AlGaInP-based LED in the temperature range between 4.2 K and 393 K for pulsed operation. Insert shows the DC operated current-voltage characteristic in the measurement regime between 0 mA and 40 mA.

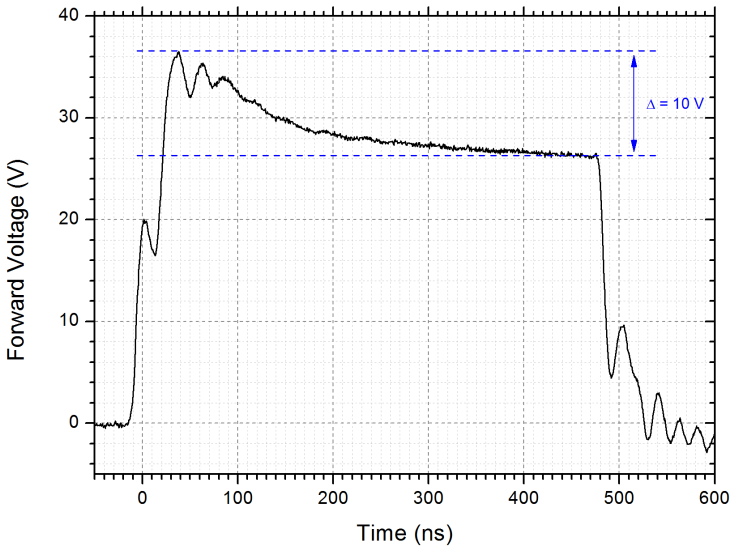

Figure 7.8.: Forward voltage versus injection time (500 ns) of the AlGaInP-based LED at 4.2 K. The injection current pulse is 150 mA.

7.4. Conclusion

The electroluminescence (EL) behavior of AlGaInP-based LEDs was investigated in the temperature region between 4.2 K and 400 K for several DC and pulsed injection currents. Pulsed injection current with a pulse width of 500 ns and a repetition rate of 500 µs (duty cycle = 0.1 %) was used to careful separate between current related and thermal influence of the spectral response.
The peak wavelength shifts linearly with temperature in the temperature region between 230 K and 400 K, further the FWHM shows also a linear behavior with temperature and its slope is independent of the injection current level.
Low temperature investigation were performed in liquid helium-4 (4.2 K) and liquid nitrogen (77 K) bath to ensure the JT of the device. Low current injection at low temperatures leads to the appearance of localized (trapped) excitons (e.g. due to defects) which radiatively recombine red shifted relative to the main barrier emission. Further 2LO phonon replica could be assigned to the emission spectra.
However the respective peak assignment is very difficult due to the fact that the particular MQW structure is unknown. Therefore transmission electron microscope (TEM) investigation would give further insights into the particular structure of those LEDs. On top of that, phonon satellites are superimposed with the radiative emission of localized excitons. Therefore on the one hand the 1LO phonon replica could not be resolved and on the other hand the emission peak due localized excitons get affected as well (convolution of several recombination processes).
Pulsed injection current below 10 mA was not possible because the signal strength of the EL spectra was too small compared to the noise produced by the CCD.

The unique behavior (back bending) of the current voltage characteristic at low temperatures is still under discussion. It is assumed that for AlGaInP-based LEDs self heating strongly influences the performance. In addition it is suggested that for the explanation of this extraordinary behavior other considerations (e.g. ionization processes, freeze-out of charge carriers) have also to be taken into account.

8. Patent: Method to operate an adjustable illuminant

In this chapter the general key aspects of the patent *Method to operate an adjustable illuminant* (German original title: *Verfahren zum Betreiben einer zum Emittieren von in seiner Helligkeit einstellbarem Licht eingerichteten Anordnung*) will be presented and summarized. The patent is currently in preparation and will be submitted to the German patent office.

To operate an LED module, a driver electronic is needed which adjusts the provided voltage supply to the certain requirements of the LED light engine. The driver electronic of an LED light engine usually produces current/voltage pulses with a certain duty cycle. The reason for the injection of current/voltage pulses is to reduce the heat of the pn-junction, which is highly effected by the amount of charge carriers injected per time segment. Temperature changes of the pn-junction lead to spectral changes and undesired shifts of the chromaticity coordinates. Furthermore an increase or decrease of the light output (dimming) of pulse driven LED light engines can be easily achieved by a change of the duty cycle (rather than by varying the height of the actual pulses).
One main issue of the pulsed injection current is the occurrence of flicker effects. The human vision recognizes and identifies pulse repetition rates up to 100 Hz. Such flickering frequencies are noticed as highly uncomfortable and disturbing. Moreover the human non-visual system still recognizes repetition rates at and above 100 Hz [143], [144].
Beyond that, LED illumination in combination with movie recording could lead to beats due to the superposition of the recording frequency and the illumination frequency. The only way to circumvent such problem is to synchronize the LED illumination frequency and the recording frequency which would result in a major technical effort. All of those reasons illustrate the importance of a DC driver solution.
However DC driver systems suffer from the problem that the level of injection current has to be reduced if the light output should get reduced. This leads to enormous junction temperature changes and therefore to shifts of the color coordinates of the LED system. Further, intended changes of the spectrum distribution, which allow to tune the color temperature of the white light (*Phosphor Innovation (PI) - LED technology*), can

be only achieved by changing the respective height of the current level for the various LEDs. This again leads to variations of the junction temperature of the single LED dice and therefore to chromaticity variations of the emission spectrum. Further the current level influences the spectra response (peak position and spectral shape) of the LED dice. Therefore, the aim is to operate an LED light engine with a constant current driver (DC driver) which allows to change the color temperature at least in the range between 2700 K and 6500 K throughout operation under maintaining the designated chromaticity value. Dimming of the light source must be possible under keeping the spectral distribution/intended color temperature constant.

The invention relates an LED module for general general illumination for producing white light of high quality, whereas the high quality is characterized by a high color rendering index (CRI) of at least 89 together with a high power efficiency of at least 65 lm/W together with a continuous tunability of the color temperature (CCT) between 2700 K and 6500 K following the Planckian locus in the CIE 1931 diagram. The LED light sources will be addressed by a DC driver which allows to change the color temperature at least in the region between 2700 K and 6500 K under maintaining constant color coordinates precisely as possible on the Planckian curve. The color coordinates should lie inside the MacAdam ellipses of 10, 6, 4 or 3 on the Planckian curve whereas smaller values are more preferred.
Further, dimming of the light source occurs by decreasing the injection current, whereas the chromaticity coordinates will remain constant, independent of the amplitude of the current level. The LED module consists out of minimum two different kinds of light sources, whereas a light source can be a primary emitter (LED) or a phosphor (color conversion) LED. Preferable three types of light sources which emit in the blue, green and red region of the visible spectrum are used. Moreover the LED light engine can also contain more than three types of LEDs.
To describe the color position in the CIE diagram, the dominant wavelength is used. The dominant wavelength is defined as the saturated color which lies on the intersection of a line which is determined by the connection between the white point (equal energy (EE) point) and the chromaticity point of the light source and the perimeter (figure 2.12 in section 2.2.5). The behavior of the color coordinate of the dominant wavelength (λ_d) with respect to temperature and current injection will be recorded in a calibration measurement. The behavior of λ_d will be obtained out of the variation of the peak wavelength λ_p and/or the full width half maximum (FWHM) change with respect to temperature and current. Moreover the slope of the high energy wing of the emission spectrum can be used for calibration.
Electrical parameters like forward voltage behavior of single LED and/or LED groups can be also used to obtain the junction temperature of the LED/LED group.

Performed Measurements:

To separate current effects and thermal impacts, the LEDs were calibrated under thermal equilibrium conditions. In a temperature controlled oven the temperature of the LEDs can be preset and the LEDs are operated with a pulsed injection current of 500 ns and a repetition rate of 500 µs, respectively. This low duty cycle of 0.1 % allows to neglect the current induced temperature increase. Therefore the behavior of the dominant wavelength of the single LEDs and/or LED groups with respect to injection current and temperature can be evaluated. This measurements were performed for blue as well as for red emitting LEDs. Storing and retrieving of such calibration measurement allows to calibrate the chromaticity coordinates relative to current and temperature changes of the LEDs and/or LED groups.
Figure 8.1 shows the behavior of the dominant wavelength of a blue and a red emitting LED with respect to junction temperature in the CIE 1931 diagram (top panel). A zoom out of the top panel for the blue emitting LED is illustrated in the middle panel of figure 8.1, for the red emitting LED in the bottom panel, respectively. For the blue emitting LED the change of the color coordinates (x_b,y_b) of the dominant wavelength λ_d in between -40°C and 120°C is Δx_b = 0.006 and Δy_b= 0.011. For the red emitting LED the change of the color coordinates (x_r,y_r) of the dominant wavelength λ_d is more distinct, however symmetric, whereas Δx_r and Δy_r change by 0.034 (in between -40°C and 120°C).

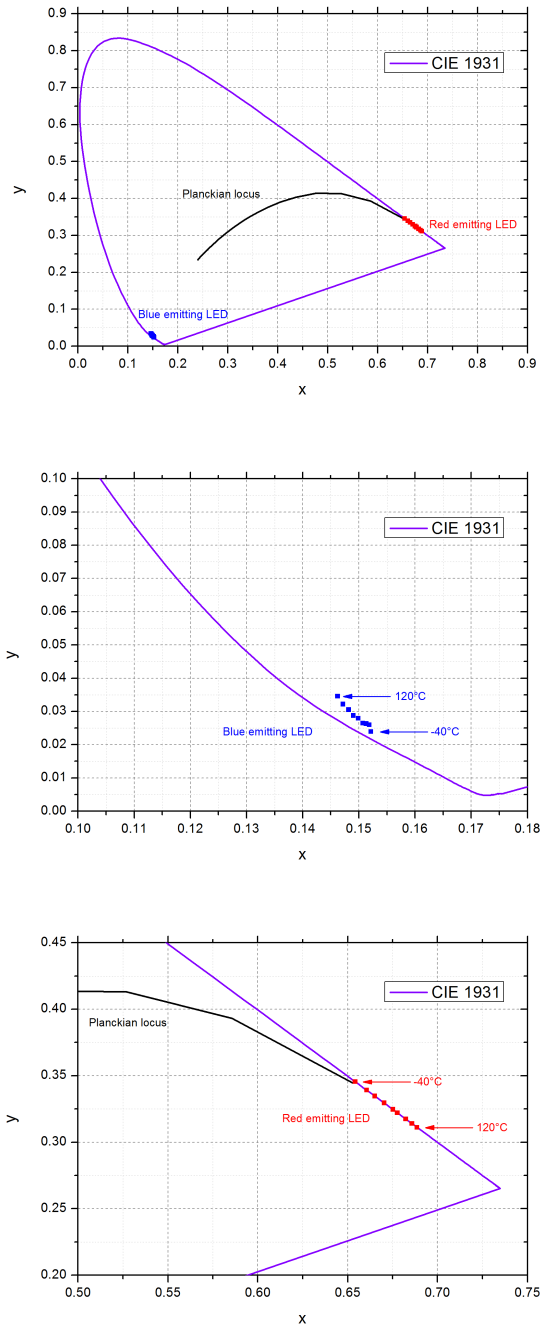

Figure 8.1.: Change of the color coordinates of the dominant wavelength of a blue and red emitting LED in the temperature range between -40°C and 120°C illustrated in the CIE 1931 chromaticity diagram. Middle Panel shows a cutout regarding the blue emitting LED, bottom panel a cutout regarding the red emitting LED.

What is claimed (compendium):

1. An LED module comprising at least one blue emitting light source in combination with at least one red emitting light source in combination with at least one phosphor/matrix coated blue LED to produce white light of high color quality whereas a constant current driver electronic (DC driver) controls each single emitter and/or certain emitter groups.

2. An LED module according to claim 1 whereas the color temperature of the LED module can be tuned at least in the range between 2700 K and 6500 K whereas the designated color temperature is achieved by the sum spectrum of the single emitters.

3. An LED module according to claim 1 whereas the color coordinates of the dominant wavelength of the sum spectrum stays constant and independent of the dimming level.

4. An LED module according to claim 1 whereas the color coordinates of the dominant wavelength of the sum spectra stays constant and independent of the preset color temperature.

5. An LED module according to claim 1 to claim 4 whereas the dominant wavelength of the sum spectrum of the single emitter lies as precise as possible on the Planckian locus, however at least in between the MacAdams ellipse of 10, preferable in between 6, more preferable in between 4 and most preferable in between 3.

6. An LED module according to claim 1 whereas the current dependence of the dominant wavelength of the single LED and/or a group of LEDs is stored on an EPROM / EEPROM.

7. An LED module according to claim 1 whereas the temperature dependence of the dominant wavelength of the single LED and/or a group of LEDs is stored on an EPROM / EEPROM.

8. An LED module according to claim 1 whereas a temperature sensor is located close to a single LED and/or an LED group which measures the temperature of the sin-

gle LED and/or the LED group and gives feedback to a communication unit.

One execution example of the regulation unit in combination with the light engine is shown in figure 8.2. The LEDs A to N are located on the array (2). The current through the diodes I_A to I_N is controlled by a microprocessor (3) which recalls the respective current values from the the EPROM/EEPROM (4). On the EPROM/EEPROM (4) the dependence of the dominant wavelength of one, two or more LEDs with respect to the injection current (I) and temperature (T) is stored. The start parameter (turn-on parameters) $I_{0,A}$ to $I_{0,N}$ are stored on the EPROM/EEPROM (4) as well. The actual temperature of the junction/device can be recalled by a sensor (5) located on array (2) or by an external sensor. Across a human interface (1) (e.g. switch, smart phone, tablet) the actual color temperature (CCT) or the dominant wavelength (via x,y) as well as the illuminance level can be adjusted. Instead of an human interface, a daylight senor or an external predefined regulation cycle could also be inserted.

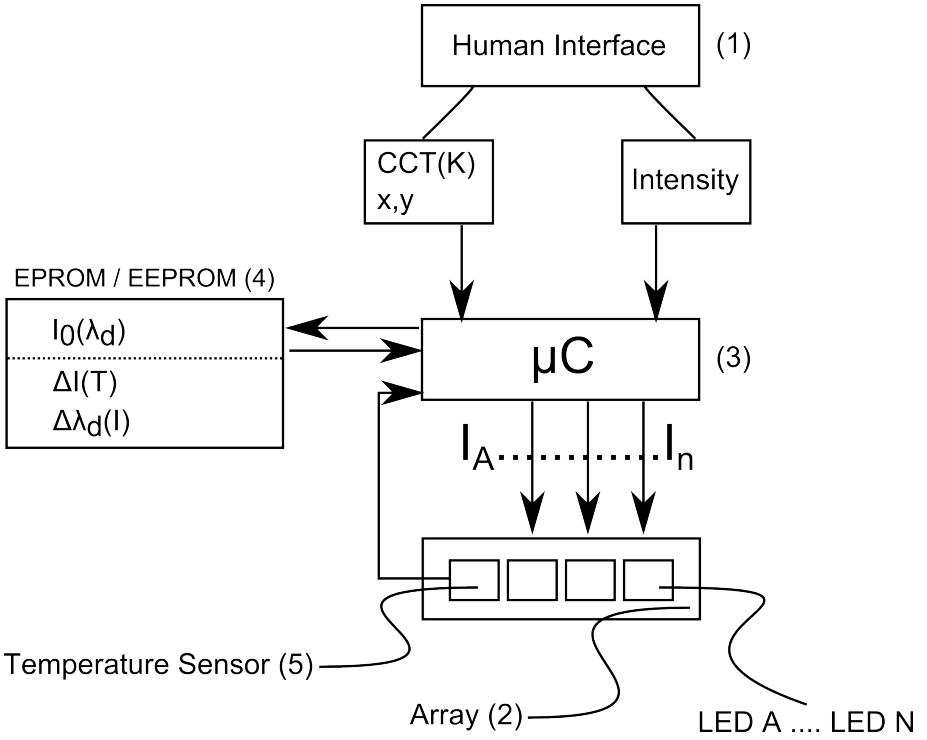

Figure 8.2.: Execution example of the regulation unit in combination with the light engine.

9. The coherence length of light emitted from LEDs

The contents of this chapter is taken and adapted form the SPIE Proceeding *Spectral Behavior and Coherence Length of GaN-, and AlGaInP-based Light-Emitting-Diodes* by Reinhold Hetzel and Günther Leising. The publication in its original form can be found in the appendix of this thesis.

9.1. Coherence length determination

For coherence length investigations a self-made Fabry-Perot Interferometer (FPI) was coupled with a closed cycle cryostat (figure 9.1). The LEDs were mounted on a copper plate using thermal conducting paste and electrically contacted with a 30 µm thick Au bonding wire. The samples were located in the focal point of a collecting lens (f = 50 mm) which created a parallel beam for the use of the FPI investigations. A variable aperture in front as well as a fixed aperture behind the FPI (diameter 1 mm, length 10 mm) were used for beam collimation. Two different kinds of high reflecting mirrors were used depending whether the red emitting LED (AlGaInP) or the blue emitting LED (GaN) was investigated. Figure 9.2 shows the reflectivity with respect to wavelength of the used mirrors. The emission spectra were recorded with a spectrometer containing a 2400 l/mm grid blazed at 250 nm. The vacuum in the closed cycle cryostat (Model 20/70 Cryogenic Technology) was 10^{-6} mbar throughout all measurements; the temperature was checked with a silicon diode mounted closely to the sample holder.

9.1.1. Coherence length of GaN-based and AlGaInP-based LEDs

LEDs provide attractive possibilities to implement them for holography (e.g. microscopy) due to the specific coherence properties this light source offers. Employing holography allows to construct a 3D-imaging microscope for nondestructive testing and quality control; further by using photorefractive holography the remote investigation of biological tissues is possible [145], [146]. Holography in combination with microscopy makes a

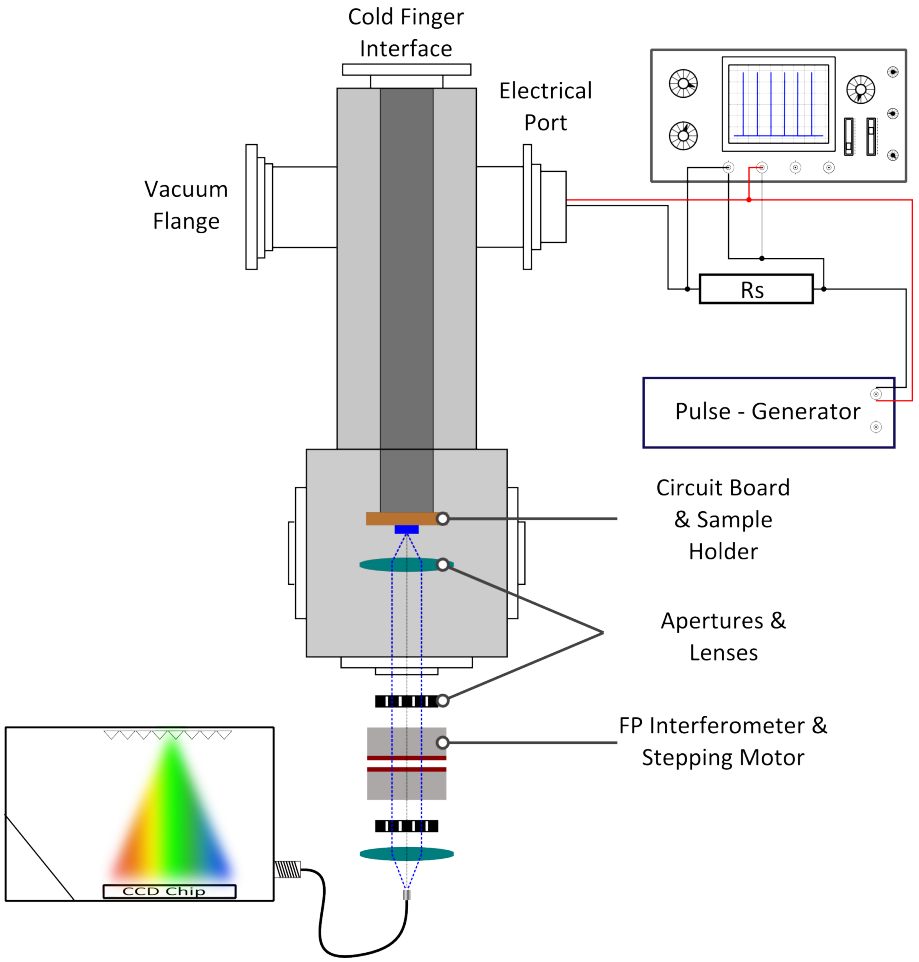

Figure 9.1.: Setup of the closed cycle cryostat in combination with an FPI for coherence length investigations.

quantitative phase contrast for high resolution topography analysis of micro and nano structured surfaces available [146]. However, the nature of coherence of solid state light sources is still not well understood and rarely specified.
Generally the temporal coherence length is defined via the coherence time (equation 9.1 following Ref.[42])

$$l_c = c\, t_c \tag{9.1}$$

whereas l_c is the temporal coherence length, t_c the coherence time and c the speed of light, respectively. For a Gaussian spectral distribution the spectral width $\Delta\nu$ and coherence time t_c are related by equation 9.2:

$$\Delta\nu = \sqrt{\frac{2\ln(2)}{\pi}}\frac{1}{t_c} \tag{9.2}$$

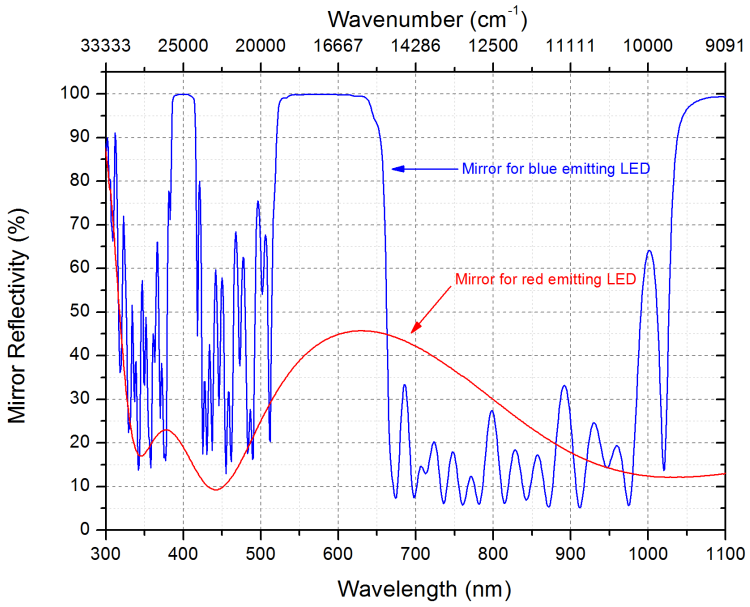

Figure 9.2.: Reflectivity of the two types of mirrors used for the Fabry-Perot interferometer. The spectra were obtained with a Shimadzu UV/VIS 1800 spectrometer.

Inserting equation 9.2 in equation 9.1 leads to the theoretical description of the coherence length given in equation 9.3:

$$l_c = \sqrt{\frac{2\ln(2)}{\pi}} \frac{\lambda}{\Delta\lambda} \tag{9.3}$$

Applying equation 9.3 for determining the coherence length assumes a Gaussian shape of the spectral distribution. Executing equation 9.3 on our measured emission spectra leads to coherence lengths at room temperature of 17.8 µm for the AlGaInP-based LEDs and 9.9 µm for the blue emitting GaN-based LEDs respectively (at 10 mA pulsed current). These results agree very well with previous reported coherence lengths [147]. However, measuring the coherence length with a FPI leads to total different situations. Figure 9.3 illustrates the interference fringes with respect to the mirror separation for the two types of investigated LEDs. The measurements were performed at room temperature and under DC current injection (10 mA for the GaN-based LED, 30 mA for the AlGaInP-based LED). For both types of LEDs we find remarkable coherence lengths which can be obtained directly out of the mirror separation. As shown in figure 9.3 bottom panel, interference fringes can be still identified at a mirror separation of 260 µm which correspond to a coherence length of at least 0.52 mm for the blue emitting GaN-based LED. For the red emitting AlGaInP-based LED interference fringes can be still observed at a mirror separation of 650 µm which corresponds to a coherence length

of at least 1.3 mm (figure 9.3 top panel). These obtained results do not mirror to the coherence length distribution of the light source and therefore cannot be taken as the average coherence length of the wave trains emitted from the LEDs. However the light sources we investigated emit wave trains which fulfill the interference conditions, therefore the LED provides wave trains with such long coherence length in the millimeter and sub-millimeter range. Intriguing about these results is that the number of wave trains with such long coherence lengths is obviously high which can be identified out of the amplitudes (constructive / destructive) of the observable interference fringes.
Although LEDs provide a single color (monochromatic) emission pattern (FWHM typically between 10 nm - 20 nm), the theoretical approach shown above to determine the coherence length is not satisfying in this case in comparisons to the gained experimental results.

9.2. Conclusion

Applying of Fabry-Perot interferometry allowed us to gain insights into the coherence length of the emitted wave trains of LEDs which leads to coherence lengths in the millimeter range for both types of the investigated LEDs. We could show that using numerical estimations for calculating coherence length gives misleading results and provides values which are far away from those determined experimentally. The main reason is that LEDs do not strictly provide monochromatic light emission.
Constitutive measurement in the low temperature region would be highly interesting and will provide further knowledge about the coherence length distribution.

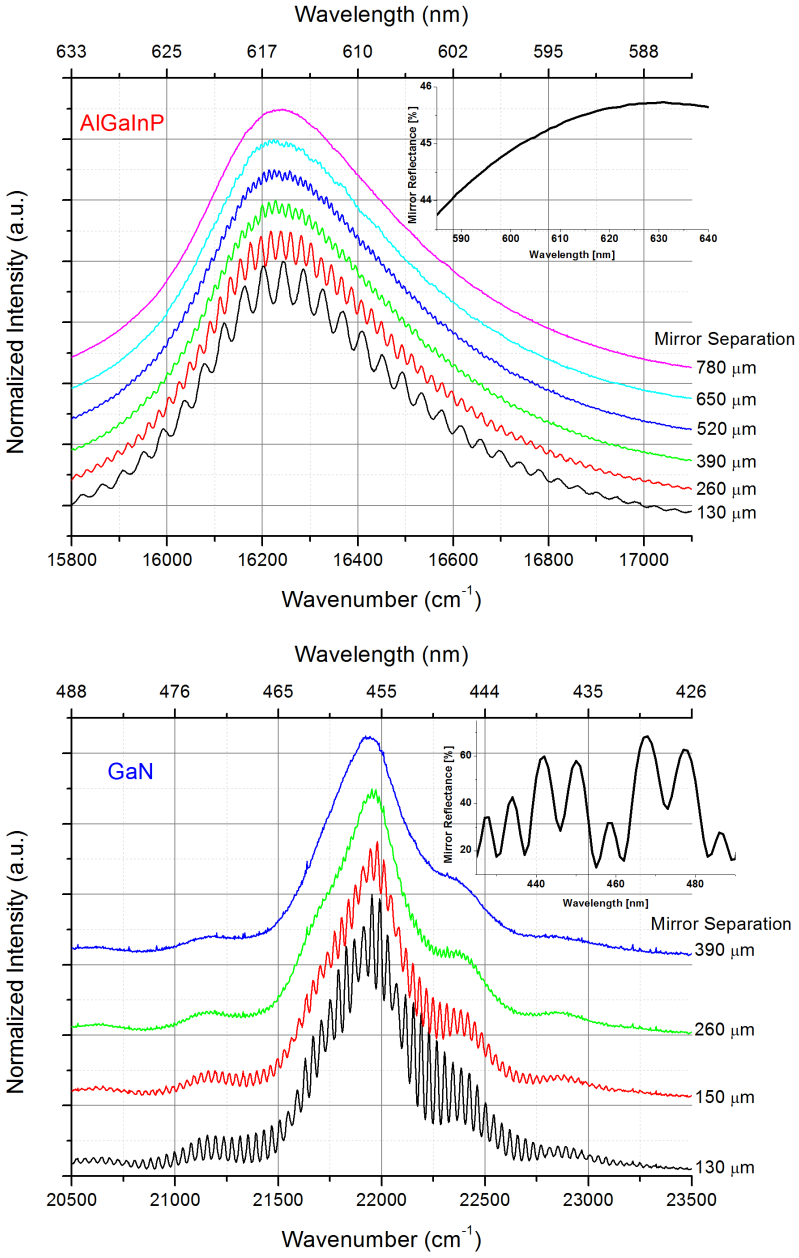

Figure 9.3.: Top Panel: Normalized emission spectra of an AlGaInP-based LED through a FPI in dependence of the mirror separation. The insert shows the reflectance behavior of the used mirrors in the FPI. Bottom Panel: Normalized emission spectra of a GaN-based LED through a FPI in dependence of the mirror separation. The insert shows the reflectance behavior of the used mirrors in the FPI. The spectra are normalized and shifted for clarity.

10. Optical properties of light converting materials

In this chapter experimental results of investigated color converting materials are presented. A general introduction into this topic can be found in section 3.3. Color conversion material are often named *Phosphors* or *phosphorous materials* in the lighting community. Unfortunate this nomenclature is misleading and has not be confused with with the chemical element phosphor (P). Color converting materials usually consists out of YAG (yttrium aluminum garnet) doped with rare earth materials. In this thesis the terminus phosphor is used only for color conversion luminescence particles which convert light of an excitation source to longer wavelength light.

10.1. Measurement of fluorescent lifetimes

To gain insights into the fluorescent lifetime of the investigated color conversion materials frequency domain lifetime measurements as described in section 3.3.1 was performed.
The actual measurement setup is shown in figure 10.1. The measurement device is an ISS Greg 200 with an ISS K2 software upgrade. Laser light (Coherent Innova 300, multi-line mirror) acts as sample excitation source, whereas through several prism (P) the light beam gets coupled into the main measurement setup. The linearly polarized beam gets depolarized first (D) due to the fact that the polarization direction of the laser is unknown. Afterwards, through a Glan-Thompson prism (GT), the light beam gets linearly polarized in the predominant direction which is needed for the Pockels cell. The linearly polarized light gets modulated within the Pockles cell whereas the light beam and the supplying voltage of the Pockels cell have to get adjusted in a way that the modulation m exceeds 0.1 at $\nu = 2$ MHz. To increase the Pockels effect, the light path hits a mirror (M) and travels again through the Pockels cell. The frequency measurement range is predetermined by the radio frequency amplifiers which allows to sweep the frequency in between 100 kHz and 250 Mhz (Hubert A 1020 RF amplifier).
After the Pockels cell the modulated light beam passes a monochromator (1300 l/mm) to a beam splitter (BS). One part is detected by a photo multiplier tube (PMT, type:

Hamamatsu R955), the second part hits the sample (S) or the reference liquid (R) respectively (sample and reference are located on a turret). The reference liquid is used to determine the origin of zero phase shift and to scale the modulation value properly. To obtain the phase value of the sample, the reference phase has to be subtracted, the modulation m of the sample is given by $m = \frac{m_{\text{sample}}}{m_{\text{reference}}}$. Glycogen in 18 Ω-water was used as the reference-scattering solution. A second PMT collects the light reflected from sample or reference. A cut off filter (F) is inserted in front of the second PMT to ensure that the excitation light does not influence the measurement.

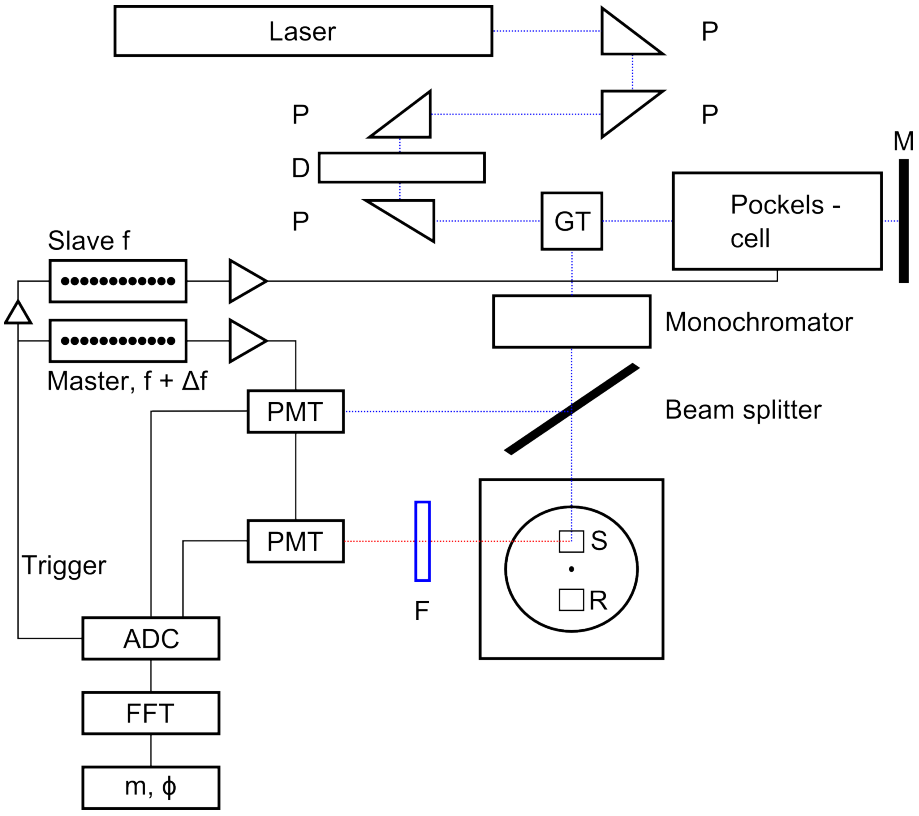

Figure 10.1.: Actual frequency domain lifetime measurement setup (following [148]). Laser light travels through several prism (P), a depolarizer (D), and a Glan-Thompson prism (GT). The light gets modulated in the Pockels cell and reflected back through a mirror (M). Sample (S) and reference (R) are mounted on a turret, a filter (F) prevents that the photo multiplier tube (PMT) measures the excitation light beam of the laser.

We determined the lifetime by embedding the light converting material in a silicon potting compound (XE14-B7892). The results are shown in figure 10.2. Lifetime values of τ=720 ns (out of the single exponential decay of the modulation m) and τ=970 ns (out of the single exponential decay phase ϕ) were obtained.

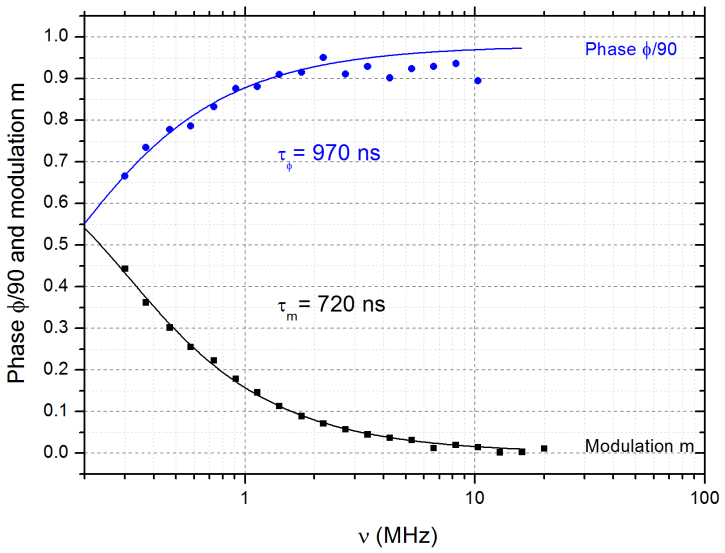

Figure 10.2.: Phase ϕ and modulation m of color converting material FA565 embedded in silicon potting compound (XE14-B7892). Lifetime values are obtained out of a single exponential decay (of phase ϕ and modulation m).

10.2. Determination of the quantum yield

In section 3.3.2 the definition of the quantum yield (QY) was established. For the experimental determination of the QY the following procedure was applied:

- Recording of the emission spectra of the sample and reference standard solution. Important is that the emission spectra has to be calibrated regarding the intensity axis. Further the background spectrum have to be recorded and subtracted from the respective emission spectrum. The excitation wavelength can be chosen in the limits where excitation is possible. The photoluminescence emission spectra were recorded with the Shimadzu RF 5301 PC. Important to note is that the Shimadzu (including a xenon lamp) should be turned on at least 30 minutes prior measurements are performed.
- Measuring of the absorption value of sample solution and reference standard solution for various concentrations. The absorption value of the chosen excitation wavelength (used for determining the photoluminescence emission) has to be recorded. At least four measurement points (concentrations) are required. Obviously the measurement accuracy increases with the number of data points. For

the result presented in this section the absorption was determined out of the transmission measured with an UV/VIS spectrometer (Shimadzu UV 1800). Again, the measurement system has to be turned on at least 30 minutes prior the measurements are carried out.

If those informations are available, one can plot the integrated emission (divided through the photon energy $(hc_0)^{-1}$) versus the absorption (1-transmission). This has to be done for the reference standard and for the sample solution as well. The gradient $grad$ of the linear fit leads to the QY of the sample Φ_S if the QY of the reference standard Φ_R is known:

$$\Phi_S = \Phi_R \frac{grad_S}{grad_R} \frac{n_S^2}{n_R^2} \tag{10.1}$$

whereas

$$grad = \frac{dF(\lambda_{ex})}{df(\lambda_{ex})} \tag{10.2}$$

and n_R, n_S the refracting index of the reference R and the sample S, respectively.

10.2.1. Reference standards

The reference standards were chosen in a way that they have similar emission/excitation behavior compared to the investigated samples. Obviously it is also very important that the QY of the reference standard is well reported in literature. Table 10.1 lists the QY of the used reference standard as well as the literature references. Table 10.2 lists the manufacturer details of the standard materials and the solvents which were investigated. A general list of reference standards can be found in the IUPAC technical report [149] as well as in reference [150].

Figure 10.3 shows the excitation/emission spectra (left panels), the absorbance (middle panels) as well as the integrated emission plotted over the absorption for various concentrations (right panels). The linear fit leads directly to the gradient $grad$ as discussed in equation 10.2. Please be aware that in the middle panels the absorbance is plotted (see equation 3.14), however in the right panels the absorption (1 - transmission) is plotted, respectively.

Table 10.1.: Literature values of the quantum yield (QY) of the used reference standard materials.

Reference materials	Reported QY	Literature reference
Rhodamine 6G in Ethanol	0.95, 0.99	[151], [152], [153]
Rhodamine B in Ethanol	0.65, 0.67	[151], [152]
Perylene in Cyclohexane	0.94	[154], [155]
Fluorescein in Ethanol	0.91, 0.97	[156], [157]

Table 10.2.: Manufacturer details of the reference standard materials as well as the solvents (including the index of refraction n).

Material / Solvent	Manufacturer Details	n
Rhodamine 6G	Lambda Physics, Lot Nr. 059001, LC5900, MW: 479.02	
Rhodamine B	Lambda Physics, Lot Nr. 039302, LC6100, MW: 479.02	
Perylene	CAS Nr.: 198-55-0	
Fluorescein	Fluka Chemicals, CAS Nr.: 2321-07-5 (from Sigma Aldrich)	
Silicon oil	Blazers Materials, Oil AN175, BD480126-T, Lot Nr.: 98-156859	1.52045 [158]
Ethanol	Sigma Aldrich, 34935, CAS Nr.: 64-17-5, 99.8%	1.3605 [159]
Cyclohexane	Fluka, 28932, CAS Nr. 110-82-7, 99.5%	1.4235 [160]

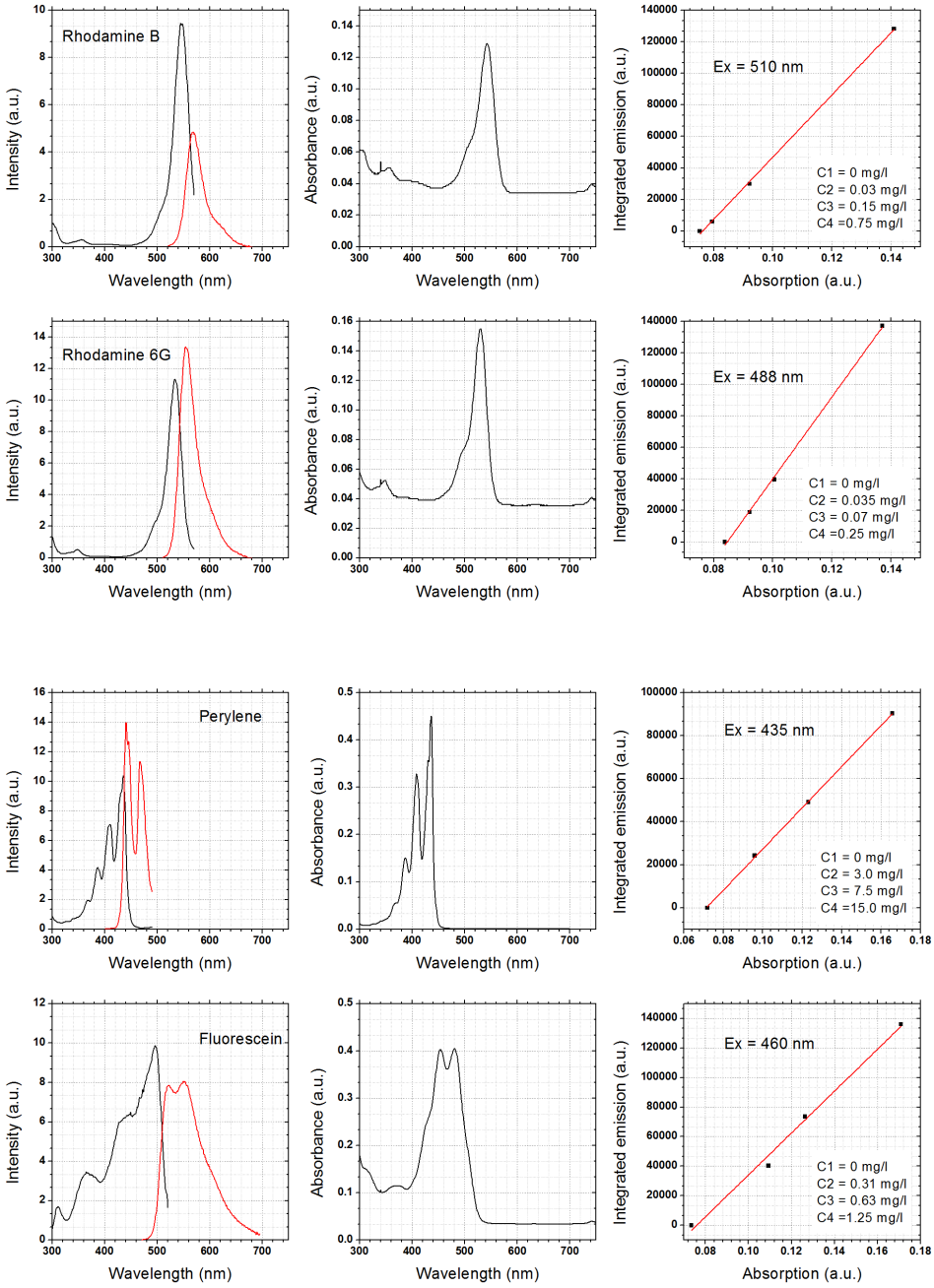

Figure 10.3.: Excitation/emission spectra (left panels), absorbance (middle panels) and integrated emission plotted over the absorption (right panels) for various concentrations of Rhodamine B, Rhodamine 6G and Fluorescein (all solved in Ethanol) as well as Perylene (solved in Cyclohexan). The excitation wavelength as well as the concentrations are labeled in the plot.

10.2.2. Quantum yield of solids

To determine the QY of a solid powder, the measurement setup has to be changed. To circumvent the problem of non solubility of the powder, the color converting particles were implemented in a silicon oil matrix (see table 10.2). This allows that the particles stay stable and are equally distributed in the interaction volume. However, performing such measurement in a quartz glass cuvette was not possible (measurements shown in figure 10.3 have been performed in a quartz glass cuvette) because it was hardly possible to establish a steady state situation where the luminescence particles did not move in the silicon oil. Therefore a homemade sample holder was built which is depicted in figure 10.4. The inner thickness of the sample holder was chosen to be very small (0.15 mm), which allowed that the particle distribution stayed constant in the silicon oil over a quite long time (orders of magnitude of the measurement time). Overall around 100 µl - 150 µl of the silicon oil / color converting material compound can be distributed in the sample holder. The sample holder in the photoluminescence measurement chamber was tilted by 30° to ensure that direct reflections of the excitation source are not detected by the fluorimeter (figure 10.4).
To compare those results with the reference standard samples, all the reference standard materials again were measured in this homemade sample holder.

Note: The matrix material where the color converting particles are getting embedded should be chosen in a way that the fluorescence properties of the investigated material will not be changed. Therefore for color converting materials no aqueous matrix compounds should be used (fluorescence decreases with potlife).

Figure 10.4.: Sample holder containing color converting particles in silicon oil. Top panel: Sample holder implemented in the fluorimeter with a tilt angle of 30° relative to the incoming light. Bottom panel: Excited color converting particles homogeneously distributed in the silicon oil matrix.

Color converting materials

Two types of color converting materials (YAG:Ce) where the QY was unknown were investigated. Figure 10.5 shows the excitation/emission spectra of the investigated materials (measured with home made sample holder as discussed before). All of the color converting materials are meant to be excited in the blue region and emit in the green/yellowish region. From the color converting material labeled ”Nemoto” a second batch called ”Nemoto Reference” was measured. Both (”Nemoto” and ”Nemoto Reference”) should have the same QY.

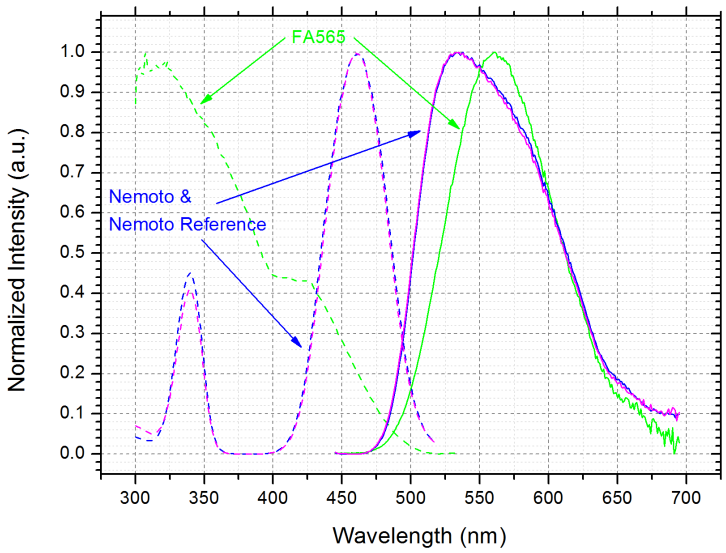

Figure 10.5.: Excitation/emission spectra of green/yellowish emitting color converting material labeled ”FA565” (wavelength position of the emission monochromator during the recording of the excitation spectra was at 550 nm, wavelength position of the excitation monochromator during the recording of the emission spectra was at 435 nm), ”Nemoto” and ”Nemoto Reference” (wavelength position of the emission monochromator during the recording of the excitation spectra was at 530 nm, wavelength position of the excitation monochromator during the recording of the emission spectra was at 435 nm).

The results of the obtained absolute QY are shown in table 10.3. For the ”FA565” a QY close to unity was measured. Due to the fact that those materials are labeled as highly efficient conversion materials such a high value was expected.
For the ”Nemoto” and the ”Nemoto Reference” the value of the two different batches varies by around 0.05. The discrepancy of the two batches can be assigned to measurement uncertainties occurring in the measurement setup. The inhomogeneous distribution of the particles in the sample holder as well as the slight particle movement lead to discrepancies of the slope of the fit (cf. figure 10.6). Slope changes lead to differences in the QY. Figure 10.6 shows the integrated emission energy versus the absorption for the three different color converting materials investigated.

Table 10.3.: Obtained quantum yield (QY) for the three investigated color converting materials using home made sample holder for solids. Reference standard material: *Perylene in Cyclohexane, **Fluorescein in Ethanol.

	Excitation wavelength	QY
FA565 (LITEC-LLL)*	410 nm	0.99
Nemoto**	460 nm	0.93
Nemoto Ref**	460 nm	0.88

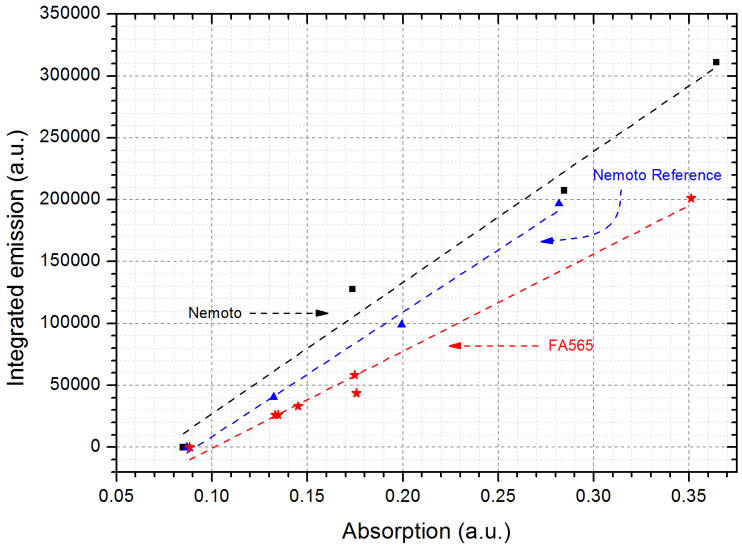

Figure 10.6.: Integrated emission energy over the absorption for the three investigated color converting materials. The concentrations vary between 0 and 230 g/l.

10.3. Conclusion

We investigated basic optical properties of color converting materials (luminescence pigments) which are used for color conversion of blue emitting LEDs. The motivation behind this work was to gain accurate information about data which is usually not provided by the distributor.

It was managed to built a measurement setup which allows to determine the absolute QY of a powder with quite high accuracy (uncertainty is around 5 %). Measurement uncertainties appear from the unstable distribution of the color converting particles in the matrix environment.

The fluorescent lifetime of a color converting material was determined by a time domain lifetime setup. An average lifetime in between 720 ns and 970 ns was observed.

11. Patent: Color converting material blends for a tunable white light engine

In this chapter the general key aspects of the patent *Color converting material blends for a tunable white light engine* (German title: *Anordnung zum Emittieren von in seiner Farbtemperatur variierbarem weissem Licht*) will be presented and summarized. The actual version was submitted to the German patent office in September 2013.

One essential parameter, which defines high quality white-light-sources, is the color rendering index (CRI) (see section 2.2.4). The CRI basically reflects the ability of a light source to render all feasible true colors of an object illuminated by the light source, whereas keeping in mind, that due to recent research results, the human eye can distinguish a variety of millions of colors. The CRI lies between 0 and 100 whereas 100 defines total rendering of all colors. A CRI of 100 is achieved if the light source has the same color rendering as the black body radiator with the same nominal color temperature. Therefore, a broad spectral distribution leads to high CRI values.
The *Phosphor Innovation (PI) - LED technology* allows to tune the color temperature of the emitted white light. The color temperature change is achieved by the rearrangement of the spectral distribution which therefore leads to different CRI values at different color temperatures.
One difficulty of such systems is that the light engines often provide a high CRI for one certain color temperature region; however, by changing the color temperature, the CRI drops to low values.
Therefore, the aim and, at the same time, the challenge is to provide high CRI values over the tunable color temperature region (2700 K - 6500 K).
The usual approach to provide high CRI is the combination of a blue, a red as well as a color converted light emitting diode. Due to the broad emission of the color conversion material (luminescence particles) in the green-yellow region this technique leads to higher CRI values compared to the classical combination of a red, green and blue light emitting diode (RGB technology).

11. Patent: Color converting material blends for a tunable white light engine

To overcome the problem that light sources usually provide high CRI values for just a certain color temperature region, we propose an arrangement, which consist out of at least two types (instead of one type) of color conversion materials (henceforth color conversion materials will be named phosphors).

The invention relates to an LED module for general illumination for producing white light of high quality, whereas the high quality is characterized by a high color rendering index (CRI) of at least 89 together with a high power efficiency of at least 65 lm/W together with a continuous tunability of the color temperature (CCT) between 2700 K and 6500 K following the Planckian locus on the CIE 1931 diagram, whereas strictly maintaining the high color rendering index (CRI) of at least 89 together with the high power efficiency of at least 65 lm/W over the whole CCT tuning range. Said module comprises at least one luminescent-conversion-LED consisting out of at least two types of phosphor conversion materials or at least one luminescent-conversion-LED group, whereas each LED or each group comprises a balanced mixture of one / two or three phosphors in a matrix with a broad emission spectrum together with at least one blue LED or a group of blue LEDs of a balanced emission color together with at least one red LED or one red LED group with a balanced emission color. The additive mixture of the various light colors and color distributions produces a white point that lies, as precise as possible, on the Planckian locus and fulfills the requirement of a high color rendering index of at least 89. Advantageously, only LEDs of one sort, preferably blue LEDs, are used for exciting the phosphor mixture(s). However the invention also suggests using red or green primary emitters as excitation source for particular phosphor materials. This specific completion will lead to a smaller Stokes shift and therefore to an increase of the general efficiency of the LED module. The intensity of individual light colors, single LEDs and LED groups can be adjusted by a separate control unit positioning the color locus exactly on the Planckian locus.

Abbreviation:

λ_p	Peak wavelength of a quasi-monochromatic light source
W_d	Dominant wavelength
$P1$	Phosphor (color converting material) 1 (W_d = 560 nm)
$P2$	Phosphor (color converting material) 2 (W_d= 570 nm)
Pb	Blend of $P1$ and $P2$

Performed Measurements:

The emission spectra of a single blue (λ_p = 456 nm), a single red (λ_p = 620 nm) as well as two separate types of phosphor converted LEDs ($P1$, W_d = 560 nm and $P2$, W_d = 570 nm, both excited by the same blue LED) were obtained.
Furthermore, the emission spectra of the light engine (three types of LEDs (blue, red, phosphor converted) assembled) were recorded for several color temperatures. The light engine contained either phosphor $P1$ converted LEDs or phosphor $P2$ converted LEDs. Out of the spectral data the CRI values for several color temperatures were determined.
Depending on the phosphor used as conversion material ($P1$ or $P2$), the CRI varies tremendously. Phosphor $P1$ (W_d = 560 nm) leads to high CRIs (>92) at 4000 K and above, however delivers low CRI values below 4000 K (e.g. 85 at 2700 K), respectively. On the other hand Phosphor $P2$ (W_d = 570 nm) leads to a moderate CRI of 90 at 2700 K but still quite low CRI values (< 80) for higher color temperatures.

Performed Calculations:

Calculations were performed using the data obtained from measured emission spectra. By blending (mathematically) of certain amount of phosphor $P1$ and phosphor $P2$ to a new phosphor blend Pb (which leads to a new W_d), the emission spectrum (sum-spectrum of red, blue and Pb converted LED) was calculated. The percentages of the blue, Pb and red emission were optimized in a way, that the chromaticity coordinates x and y (following CIE 1931 color space) of each spectrum, were always located on the Planckian locus for each color temperature. Out of these gained spectra the CRI values for several color temperatures was obtained.
By balancing the concentration of $P1$ and $P2$ of the phosphor blend, a mixture which allows a high CRI over the tunable color temperature region (2700 K to 6500 K) was gained. Hence, the CRI value can be improved to a level above 90 for nearly all color temperatures.
Further, by varying the concentration of $P1$ and $P2$, one can optimize the CRI for specific desired color temperatures. For example a blend containing 50 % of $P1$ and 50 % of $P2$ leads to high CRI values (above 90) in a color temperature region of 2700 K to 5000 K and to a moderate CRI value (above 87) beyond 5000 K. Blends containing 33 % of $P1$ and 66 % of $P2$ lead to CRIs above 89 over the whole color temperature region. Figure 11.1 illustrates the behavior of the CRI versus the correlated color temperature (CCT) in the range between 2700 K and 6500 K. In this example a blue LED (λ_p = 456 nm) and a red (λ_p = 620 nm) were combined with a phosphor blend. The phosphor blend contains two types of phosphors (called WD 560 and WD 570) whereas the

stoichiometric concentration of the various phosphors was changed in the ratios 1:1, 2:1 and, 3:1. Also indicated is the CRI behavior of the LED module if just one single phosphor is applied (dotted lines).

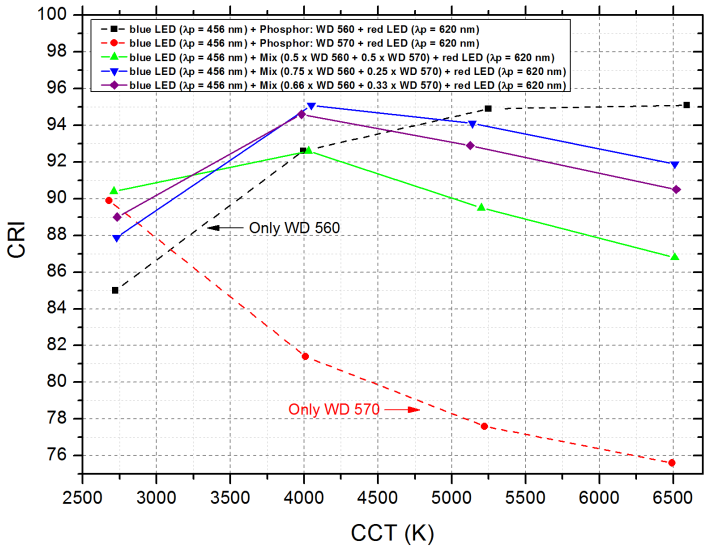

Figure 11.1.: Behavior of the color rendering index (CRI) versus the correlated color temperature (CCT) of an LED module with one blue emitter, one red emitter and one phosphor converted LED. The ratio of the phosphor blend is changed between 1:1 to 3:1. Dotted lines indicate the CRI trend if phosphor WD 560 (black dotted line) or WD 570 (red dotted line) is applied only.

What is claimed (compendium):

1. An LED module comprising at least one blue emitting light source in combination with at least one red emitting light source in combination with at least one phosphor/matrix coated blue LED to produce white light of color quality (CRI) having a CRI of at least 89 together with high power efficiency of at least 65 lm/W together with continuous tunability of the color temperature (CCT) between 2700 K and 6500 K following the Planckian locus, whereas the CCT accuracy is realized within the MacAdams ellipse of 10, 6, or 3 based on the 1931 CIE table following the Planckian locus. The phosphor / matrix is composed of a mixture of at least two phosphors.

2. An LED module according to claim 1, wherein the blue LED emission peaks between 430 nm and 480 nm, the red LED emission peaks between 600 nm and 640

nm and the phosphor/matrix emission containing a mixture of phosphors whereas phosphor A peaks between 500 nm and 590 nm and phosphor B peak between 550 nm and 650 nm; whereas the emission peak-wavelength of phosphor B is larger than the emission peak-wavelength of phosphor A.

3. An LED module according to claim 1 and claim 2, wherein the blue LED emission peaks between 430 nm and 480 nm, the red LED emission peaks between 600 nm and 640 nm and the phosphor/matrix emission containing a mixture of phosphors whereas phosphor A peaks between 500 nm and 590 nm and phosphor B peaks between 550 nm and 650 nm; whereas the quantity of phosphor A is between 0.4 and 0.8 and the quantity of phosphor B is in between 0.6 and 0.2, summing up to 1.

4. A LED module according to claim 1, wherein the blue LED emission peaks between 430 nm and 480 nm, the red LED emission peaks between 600 nm and 640 nm and the phosphor/matrix emission containing a mixture of phosphors whereas phosphor A peaks between 500 nm and 590 nm, phosphor B peaks between 550 nm and 650 nm, and phosphor C peaks between 530 nm and 580 nm. The emission peak-wavelength of phosphor A is smaller than the emission peak-wavelength of phosphor C and phosphor B. The emission peak-wavelength of phosphor B is larger than the emission peak-wavelength of phosphor C.

5. The blue and red light sources of the LED module according to claim 1 can be realized either by a primary emitter or as a phosphor converted light source whereas the emission peak is in the same region as described in the previous claims.

One execution example is illustrated in figure 11.2. On an array (1) two blue emitting LEDs (3) and (4) and a red emitting LED (5) are located, whereas a micro control unit (2) drives the array (1). One blue emitting LED (4) acts as excitation source for the phosphor matrix (6) which contains a blend of phosphor (7) and phosphor (8), whereas the dominant wavelength between phosphor (7) and phosphor (8) is different. Another execution example could also include a third type of phosphor with a different dominant wavelength compared to phosphor (7) and phosphor (8) in the phosphor blend matrix (6). In another execution example the red emitting LED (5) can be replaced by a blue or green emitting LED (which acts as excitation source) including a phosphor which emits in the red region of the visible spectrum. In another execution example phosphor (7) and phosphor (8) can be implemented in a separate phosphor matrix (6) located on a separate blue (or green) emitting diode each.

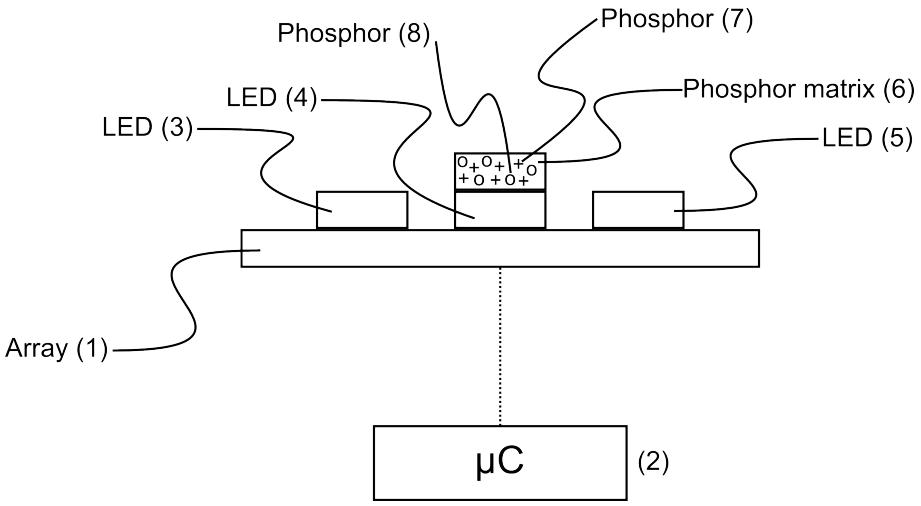

Figure 11.2.: Execution sample of a light engine containing primary emitter LEDs as well as phosphor converted LEDs.

12. Concluding remarks

During this thesis it was achieved to built a fully calibrated setup which allows to determine the junction temperature of LEDs in the broad temperature range between 4.2 K and 400 K. As mentioned several times in the thesis, DC operation leads to an increase of the junction temperature, therefore inserting short forward voltage/current pulses of 500 ns circumvents the thermal impact and leads to a steady state situation (thermal equilibrium).

Low temperature investigations in liquid helium and liquid nitrogen allowed to gain insight into the radiative recombination process at low temperatures.
GaN-based LEDs show a dominant radiative recombination due to localized excitons at low temperatures. Further mainly band filling (rather than screening of the piezoelectric field) leads to a blue shift of the electroluminescence spectrum with respect to injection current.
The peak energy as well as the FWHM of AlGaInP-based LEDs show a linear evolution in the elevated temperature region. Further neither band filling nor screening of piezoelectric fields was observed. At low temperatures excitons get trapped at defects and influence the emission behavior significantly. The conspicuous back bending of the I-V characteristics at low temperatures of AlGaInP-based LEDs is still under discussion and could not be totally explained right now.

Available analytical tools like FIB, EDX, and EBIC offered principle information about the structure of the LEDs, however to gain deeper insights, transmission electron microscopy (TEM) of the samples would be highly recommended.

This thesis clearly demonstrates that fundamental research is the required foundation for applicable process and product development. It was achieved to gain published scientific results and to implement those in a next step in product/process related patents.

Part IV.

Appendix

Bibliography

[1] R. Hetzel, S. Tasch, and G. Leising: Tunable natural light realized by phosphor-innovation light-emitting-diode technology. *e & i Elektrotechnik und Informationstechnik* (2012), 1–6.

[2] H. J. Round: A note on carborundum. **19** (1907), 309.

[3] R. Braunstein: Radiative transitions in semiconductors. *Physical Review* **99**(6) (1955), 1892.

[4] N. Holonyak Jr and S. F. Bevacqua: Coherent (visible) light emission from Ga (As1-xPx) junctions. *Applied Physics Letters* **1**(4) (2004), 82–83.

[5] R. Haitz and J. Y. Tsao: Solid-state lighting: The case 10 years after and future prospects. *physica status solidi (a)* **208**(1) (2011), 17–29. DOI: 10.1002/pssa.201026349.

[6] S. Pimputkar, J. S. Speck, S. P. DenBaars, and S. Nakamura: Prospects for LED lighting. *Nature Photonics* **3**(4) (2009), 180–182.

[7] R. V. Steele: The story of a new light source. *Nature photonics* **1**(1) (2007), 25–26.

[8] W. A. Hofstra and A. W. de Weerd: How to assess circadian rhythm in humans: a review of literature. *Epilepsy & Behavior* **13**(3) (2008), 438–444.

[9] J. R. Cameron and J. G. Skofronick: *Medical Physics. 1978*. New York: Wiley.

[10] G. C. Brainard et al.: Action spectrum for melatonin regulation in humans: evidence for a novel circadian photoreceptor. *The Journal of Neuroscience* **21**(16) (2001), 6405–6412.

[11] K. Thapan, J. Arendt, and D. J. Skene: An action spectrum for melatonin suppression: evidence for a novel non-rod, non-cone photoreceptor system in humans. *The Journal of physiology* **535**(1) (2001), 261–267.

[12] S. Hattar, H.-W. Liao, M. Takao, D. M. Berson, and K.-W. Yau: Melanopsin-containing retinal ganglion cells: architecture, projections, and intrinsic photosensitivity. *Science* **295**(5557) (2002), 1065–1070.

[13] M. G. Figueiro and M. S. Rea: The effects of red and blue lights on circadian variations in cortisol, alpha amylase, and melatonin. *International journal of endocrinology* **2010** (2010).

[14] C. Cajochen et al.: High sensitivity of human melatonin, alertness, thermoregulation, and heart rate to short wavelength light. *Journal of Clinical Endocrinology & Metabolism* **90**(3) (2005), 1311–1316.

[15] S. W. Lockley, G. C. Brainard, and C. A. Czeisler: High sensitivity of the human circadian melatonin rhythm to resetting by short wavelength light. *J Clin Endocrinol Metab* **88**(9) (2003), 4502–4505.

[16] T. Morita and H. Tokura: Effects of lights of different color temperature on the nocturnal changes in core temperature and melatonin in humans. *Applied Human Science* **15** (1996), 243–246.

[17] C. Cajochen: Alerting effects of light. *Sleep medicine reviews* **11**(6) (2007), 453–464.

[18] J. Phipps-Nelson, J. R. Redman, D.-j. Dijk, and S. M. Rajaratnam: Daytime exposure to bright light, as compared to dim light, decreases sleepiness and improves psychomotor vigilance performance. *Sleep* **26**(6) (2003), 695–700.

[19] P. R. Mills, S. C. Tomkins, and L. J. Schlangen: The effect of high correlated colour temperature office lighting on employee wellbeing and work performance. *Journal of Circadian Rhythms* **5**(1) (2007), 2.

[20] C. Barkmann, N. Wessolowski, and M. Schulte-Markwort: Applicability and efficacy of variable light in schools. *Physiology & behavior* **105**(3) (2012), 621–627.

[21] K. Bieske, D. Gall, C. Vandahl, and O. Dierbach: Influence of artificial daylight on gerontopsychiatric care of elderly people. *CIE 2cd expert symposium on light and health, CIEx*. **31**. 2006, 7.

[22] C. Sust, P. Dehoff, D. Lang, and D. Lorenz: Verbesserte Lebensqualitaet fuer demente Bewohner: Das Forschungsprojekt St. *Katharina in Wien. ABoVe GmbH, Zumtobel Research, Osram AG, Technische Hochschule Mittelhessen, Deutschland* (2012).

[23] G. Wyszecki and W. S. Stiles: *Color science 2nd Edition*. John Wiley & Sons, New York, 1982.

[24] J. J. Vos: Colorimetric and photometric properties of a 2 fundamental observer. *Color Research & Application* **3**(3) (1978), 125–128.

[25] V. DIN: *5031-100 Strahlungsphysik im optischen Bereich und Lichttechnik-Teil 100: Ueber das Auge vermittelte, nichtvisuelle Wirkung des Lichts auf den Menschen-Groessen, Formelzeichen und Wirkungsspektren. Juni 2009*. German.

[26] D. H. Brainard and A. Stockman: *Colorimetry*. Vol. 3rd edition. 2008.

[27] E. F. Schubert, T. Gessmann, and J. K. Kim: *Light emitting diodes*. Wiley Online Library, 2005.

[28] *CVRL main*. URL: http://www.cvrl.org/ (visited on Mar. 25, 2014).

[29] A. Stockman and L. T. Sharpe: The spectral sensitivities of the middle-and long-wavelength-sensitive cones derived from measurements in observers of known genotype. *Vision research* **40**(13) (2000), 1711–1737.

[30] D. L. MACADAM: Visual Sensitivities to Color Differences in Daylight. *Journal of the Optical Society of America* **32**(5) (1942), 247–273. DOI: 10.1364/JOSA.32.000247.

[31] C. S. McCamy: Correlated color temperature as an explicit function of chromaticity coordinates. *Color Research & Application* **17**(2) (1992), 142–144. DOI: 10.1002/col.5080170211.

[32] Y. Ohno and W. Davis: Rationale of color quality scale (2010).

[33] M. S. Rea and J. P. Freyssinier-Nova: Color rendering: A tale of two metrics. *Color Research & Application* **33**(3) (2008), 192–202.

[34] *Farbwiedergabe: DIN 6169. Farbwiedergabe-Eigenschaften von Lichtquellen in der Beleuchtungstechnik*. Beuth, 1976. 12 pp.

[35] D. B. Judd: The 1931 ICI standard observer and coordinate system for colorimetry. *JOSA* **23**(10) (1933), 359–373.

[36] D. A. B. Miller: Semiconductor Optoelectronic Devices. Lecture Notes Course EE243. 1999.

[37] S. L. Chuang: *Physics of Optoelectronic Devices*. Wiley, 1995. 736 pp.

[38] T. D. Moustakas and J. I. Pankove: *Gallium Nitride (GaN) I*. Acad. Press, 1998. 517 pp.

[39] S. M. Sze: Semiconductor Devices Physics and Technology. *ISBN: 0-471-33372-7* (2002).

[40] I. Pelant and J. Valenta: *Luminescence Spectroscopy of Semiconductors*. Oxford ; New York: Oxford University Press, USA, 2012. 600 pp.

[41] S. M. Sze: Physics of semiconductor devices, 2nd. *John & Sons* (1981).

[42] B. E. A. Saleh and M. C. Teich: *Fundamentals of photonics*. Wiley, 1991. 1000 pp.

[43] J. Piprek: Efficiency droop in nitride-based light-emitting diodes. *physica status solidi (a)* **207**(10) (2010), 2217–2225.

[44] M.-H. Kim et al.: Origin of efficiency droop in GaN-based light-emitting diodes. *Applied Physics Letters* **91**(18) (2007), 183507. DOI: 10.1063/1.2800290.

[45] M. F. Schubert et al.: Polarization-matched GaInN/AlGaInN multi-quantum-well light-emitting diodes with reduced efficiency droop. *Applied Physics Letters* **93**(4) (2008), 041102. DOI: 10.1063/1.2963029.

[46] Q. Dai et al.: Carrier recombination mechanisms and efficiency droop in GaInN/GaN light-emitting diodes. *Applied Physics Letters* **97**(13) (2010), 133507. DOI: 10.1063/1.3493654.

[47] G.-B. Lin et al.: Analytic model for the efficiency droop in semiconductors with asymmetric carrier-transport properties based on drift-induced reduction of injection efficiency. *Applied Physics Letters* **100**(16) (2012), 161106. DOI: 10.1063/1.4704366.

[48] S. M. a. Sze: *Physics of semiconductor devices*. Hoboken, N.J.: Wiley-Interscience, 2007.

[49] W. Bludau: *Halbleiter-Optoelektronik: die physikalischen Grundlagen der LED's, Diodenlaser und pn-Photodioden*. Muenchen; Wien: Hanser, 1995.

[50] J. R. Lakowicz: *Principles of Fluorescence Spectroscopy*. Springer, 2007. 961 pp.

[51] J. N. Demas and G. A. Crosby: Measurement of photoluminescence quantum yields-Review. *Journal of Physical Chemistry* **75**(8) (1971), 991.

[52] C. Wuerth, M. Grabolle, J. Pauli, M. Spieles, and U. Resch-Genger: Comparison of methods and achievable uncertainties for the relative and absolute measurement of photoluminescence quantum yields. *Analytical chemistry* **83**(9) (2011), 3431–3439.

[53] S. Reyntjens and R. Puers: A review of focused ion beam applications in microsystem technology. *Journal of Micromechanics and Microengineering* **11**(4) (2001), 287. DOI: 10.1088/0960-1317/11/4/301.

[54] H. Kuzmany: *Solid-State Spectroscopy - An Introduction*. Springer, 2009.

[55] H. J. Leamy: Charge collection scanning electron microscopy. *Journal of Applied Physics* **53**(6) (1982), R51–R80. DOI: 10.1063/1.331667.

[56] M. Faccinelli: Spatially resolved measurements of charge carrier properties in proton doped silicon. PhD thesis. Graz: Graz University of Technology, 2013. 98 pp.

[57] Y. S. Touloukian and D. P. DeWitt: *Thermal radiative properties: metallic elements and alloys*. IFI/Plenum, 1970. 1670 pp.

[58] H. Masui et al.: Equivalent-circuit analysis for the electroluminescence-efficiency problem of InGaN/GaN light-emitting diodes. *Japanese Journal of Applied Physics* **47**(4) (2008), 2112.

[59] J. Reader, C. J. Sansonetti, and J. M. Bridges: Irradiances of spectral lines in mercury pencil lamps. *Applied optics* **35**(1) (1996), 78–83.

[60] C. J. Sansonetti, M. L. Salit, and J. Reader: Wavelengths of spectral lines in mercury pencil lamps. *Applied optics* **35**(1) (1996), 74–77.

[61] W. J. Hwang, T. H. Lee, L. Kim, and M. W. Shin: Determination of junction temperature and thermal resistance in the GaN-based LEDs using direct temperature measurement. *physica status solidi (c)* **1**(10) (2004), 2429–2432.

[62] M. Tchounkeu, O. Briot, B. Gil, J. P. Alexis, and R.-L. Aulombard: Optical properties of GaN epilayers on sapphire. *Journal of Applied Physics* **80**(9) (1996), 5352–5360. DOI: 10.1063/1.363475.

[63] J.-C. Wang et al.: The effect of junction temperature on the optoelectrical properties of InGaN/GaN multiple quantum well light-emitting diodes. *Journal of Luminescence* **132**(2) (2012), 429–433.

[64] J. Cho, C. Sone, Y. Park, and E. Yoon: Measuring the junction temperature of III-nitride light emitting diodes using electro-luminescence shift. *physica status solidi (a)* **202**(9) (2005), 1869–1873.

[65] A. Keppens, W. R. Ryckaert, G. Deconinck, and P. Hanselaer: High power light-emitting diode junction temperature determination from current-voltage characteristics. *Journal of Applied Physics* **104**(9) (2008), 093104.

[66] Y. Xi et al.: Junction and carrier temperature measurements in deep-ultraviolet light-emitting diodes using three different methods. *Applied Physics Letters* **86**(3) (2005), 031907–031907.

[67] Z. Vaitonis, P. Vitta, and A. Zukauskas: Measurement of the junction temperature in high-power light-emitting diodes from the high-energy wing of the electroluminescence band. *Journal of Applied Physics* **103**(9) (2008), 093110.

[68] A. J. Nozik: Spectroscopy and hot electron relaxation dynamics in semiconductor quantum wells and quantum dots. *Annual Review of Physical Chemistry* **52**(1) (2001), 193–231.

[69] C.-K. Sun, F. Vallee, S. Keller, J. E. Bowers, and S. P. DenBaars: Femtosecond studies of carrier dynamics in InGaN. *Applied physics letters* **70**(15) (1997), 2004–2006.

[70] H. Ye, G. W. Wicks, and P. M. Fauchet: Hot electron relaxation time in GaN. *Applied physics letters* **74**(5) (1999), 711–713.

[71] K. T. Tsen et al.: Nonequilibrium electron distributions and phonon dynamics in wurtzite GaN. *Applied physics letters* **68**(21) (1996), 2990–2992.

[72] C.-K. Sun, Y.-L. Huang, S. Keller, U. K. Mishra, and S. P. DenBaars: Ultrafast electron dynamics study of GaN. *Physical Review B* **59**(21) (1999), 13535.

[73] K. T. Tsen, J. G. Kiang, D. K. Ferry, and H. Morkoc: Subpicosecond time-resolved Raman studies of LO phonons in GaN: Dependence on photoexcited carrier density. *Applied physics letters* **89**(11) (2006), 112111–112111.

[74] J. A. Ferrer-Perez et al.: Photoluminescence-Based Electron and Lattice Temperature Measurements in GaN-Based HEMTs. *Journal of Electronic Materials* **43**(2) (2014), 341–347.

[75] A. Matulionis et al.: Hot-electron energy relaxation time in AlGaN/GaN. *Semiconductor science and technology* **17**(3) (2002), L9.

[76] A. Matulionis et al.: Hot-electron energy relaxation time in AlInN/AlN/GaN 2DEG channels. *Semiconductor Science and Technology* **23**(7) (2008), 075048.

[77] Y. P. Varshni: Temperature dependence of the energy gap in semiconductors. *Physica* **34**(1) (1967), 149–154.

[78] E. Berkowicz et al.: Measured and calculated radiative lifetime and optical absorption of InxGa1-x N/GaN quantum structures. *Physical Review B* **61**(16) (2000), 10994.

[79] T. Wang, J. Bai, S. Sakai, and J. K. Ho: Investigation of the emission mechanism in InGaN/GaN-based light-emitting diodes. *Applied Physics Letters* **78**(18) (2001), 2617–2619.

[80] N. Nepal, J. Li, M. L. Nakarmi, J. Y. Lin, and H. X. Jiang: Exciton localization in AlGaN alloys. *Applied physics letters* **88**(6) (2006), 062103–062103.

[81] P. G. Eliseev, P. Perlin, J. Lee, and M. Osinski: Blue temperature-induced shift and band-tail emission in InGaN-based light sources. *Applied physics letters* **71**(5) (1997), 569–571.

[82] K. L. Teo et al.: An analysis of temperature dependent photoluminescence line shapes in InGaN. *Applied physics letters* **73**(12) (1998), 1697–1699.

[83] R. W. Martin, P. G. Middleton, K. P. O'Donnell, and W. Van der Stricht: Exciton localization and the Stokes shift in InGaN epilayers. *Applied physics letters* **74**(2) (1999), 263–265.

[84] T. Wang et al.: Effect of silicon doping on the optical and transport properties of InGaN/GaN multiple-quantum-well structures. *Applied Physics Letters* **76**(13) (2000), 1737–1739.

[85] P. Corfdir et al.: Temperature-Dependence of Exciton Radiative Recombination in (Al,Ga)N/GaN Quantum Wells Grown on a-Plane GaN Substrates. *Japanese Journal of Applied Physics* **52**(8) (2013), 08JC01. DOI: 10.7567/JJAP.52.08JC01.

[86] C.-M. Lee et al.: Photoluminescence investigation of In0. 15Ga0. 85N/GaN multiple quantum wells. *Journal of the Korean Physical Society* **45**(2) (2004), L243–L247.

[87] P. G. Eliseev: The red sigma2/kT spectral shift in partially disordered semiconductors. *Journal of applied physics* **93**(9) (2003), 5404–5415.

[88] I. Vurgaftman and J. R. Meyer: Band parameters for nitrogen-containing semiconductors. *Journal of Applied Physics* **94**(6) (2003), 3675–3696.

[89] K. B. Nam, J. Li, J. Y. Lin, and H. X. Jiang: Optical properties of AlN and GaN in elevated temperatures. *Applied physics letters* **85**(16) (2004), 3489–3491.

[90] T. Wang, D. Nakagawa, M. Lachab, T. Sugahara, and S. Sakai: Optical investigation of InGaN/GaN multiple quantum wells. *Applied physics letters* **74**(21) (1999), 3128–3130.

[91] K. Kazlauskas et al.: Excitation power dynamics of photoluminescence in InGaN/GaN quantum wells with enhanced carrier localization. *Journal of Applied Physics* **97**(1) (2005), 013525. DOI: 10.1063/1.1826220.

[92] T. Kuroda and A. Tackeuchi: Influence of free carrier screening on the luminescence energy shift and carrier lifetime of InGaN quantum wells. *Journal of applied physics* **92**(6) (2002), 3071–3074.

[93] B. Arnaudov, D. S. Domanevskii, S. Evtimova, C. Ivanov, and R. Kakanakov: Band-filling effect on the light emission spectra of InGaN/GaN quantum wells with highly doped barriers. *Microelectronics Journal* **40**(2) (2009), 346–348.

[94] R. A. Hogg, C. E. Norman, A. J. Shields, M. Pepper, and N. Iizuka: Comparison of spontaneous and piezoelectric polarization in GaN/Al0.65Ga0.35N multi-quantum-well structures. *Applied Physics Letters* **76**(11) (2000), 1428–1430.

[95] T. Takeuchi et al.: Determination of piezoelectric fields in strained GaInN quantum wells using the quantum-confined Stark effect. *Applied physics letters* **73**(12) (1998), 1691–1693.

[96] L. Guo, X. Wang, H. Xiao, and B. Wang: The influence of internal electric fields on the transition energy of InGaN/GaN quantum well. *Journal of crystal growth* **298** (2007), 522–526.

[97] H. S. Kim et al.: Piezoelectric effects on the optical properties of GaN/AlxGa1-xN multiple quantum wells. *Applied physics letters* **73**(23) (1998), 3426–3428.

[98] F. D. Sala et al.: Free-carrier screening of polarization fields in wurtzite GaN/InGaN laser structures. *Applied Physics Letters* **74**(14) (1999), 2002–2004. DOI: 10.1063/1.123727.

[99] D. A. B. Miller et al.: Electric field dependence of optical absorption near the band gap of quantum-well structures. *Physical Review B* **32**(2) (1985), 1043.

[100] L. K. Teles, J. Furthmueller, L. M. R. Scolfaro, J. R. Leite, and F. Bechstedt: First-principles calculations of the thermodynamic and structural properties of strained InxGa1-xN and AlxGa1-xN alloys. *Physical Review B* **62**(4) (2000), 2475.

[101] F. Bernardini, V. Fiorentini, and D. Vanderbilt: Spontaneous polarization and piezoelectric constants of III-V nitrides. *Physical Review B* **56**(16) (1997), R10024.

[102] H. Iwanaga, A. Kunishige, and S. Takeuchi: Anisotropic thermal expansion in wurtzite-type crystals. *Journal of materials science* **35**(10) (2000), 2451–2454.

[103] K. Wang and R. R. Reeber: Thermal expansion and elastic properties of InN. *Applied Physics Letters* **79**(11) (2001), 1602–1604. DOI: 10.1063/1.1400082.

[104] L.-C. Xu, R.-Z. Wang, X. Yang, and H. Yan: Thermal expansions in wurtzite AlN, GaN, and InN: First-principle phonon calculations. *Journal of Applied Physics* **110**(4) (2011), 043528.

[105] R. R. Reeber and K. Wang: Lattice parameters and thermal expansion of important semiconductors and their substrates. *MRS Proceedings*. **622**. Cambridge Univ Press, 2000, T6–35.

[106] Y.-H. Cho et al.: S-shaped temperature-dependent emission shift and carrier dynamics in InGaN/GaN multiple quantum wells. *Applied physics letters* **73**(10) (1998), 1370–1372.

[107] L. Zhu and B. Liu: Optical properties studies in InGaN/GaN multiple-quantum well. *Solid-State Electronics* **53**(3) (2009), 336–340.

[108] M. Grundmann: *The Physics of Semiconductors: An Introduction Including Nanophysics and Applications*. Springer, 2010. 875 pp.

[109] D. M. Graham et al.: Optical and microstructural studies of InGaN/ GaN single-quantum-well structures. *Journal of applied physics* **97**(10) (2005), 103508.

[110] R. Pecharroman-Gallego, P. R. Edwards, R. W. Martin, and I. M. Watson: Investigations of phonon sidebands in InGaN/GaN multi-quantum well luminescence. *Materials Science and Engineering: B* **93**(1) (2002), 94–97.

[111] P. P. Paskov et al.: Phonon-Assisted Photoluminescence in InGaN/GaN Multiple Quantum Wells. *physica status solidi (b)* **234**(3) (2002), 755–758.

[112] J. A. Davidson et al.: Photoluminescence studies of InGaN/GaN multi-quantum wells. *Semiconductor science and technology* **15**(6) (2000), 497.

[113] O. Celik, E. Tiras, S. Ardali, S. B. Lisesivdin, and E. Ozbay: Determination of the LO phonon energy by using electronic and optical methods in AlGaN/GaN. *Central European Journal of Physics* **10**(2) (2012), 485–491.

[114] S. Kalliakos et al.: The Effects of Localization and of Electric Fields on LO-Phonon-Exciton Coupling in InGaN/GaN Quantum Wells and Quantum Boxes. *physica status solidi (a)* **190**(1) (2002), 149–154.

[115] D. S. Meyaard et al.: Analysis of the temperature dependence of the forward voltage characteristics of GaInN light-emitting diodes. *Applied Physics Letters* **103**(12) (2013), 121103. DOI: 10.1063/1.4821538.

[116] A. Chitnis et al.: Self-heating effects at high pump currents in deep ultraviolet light-emitting diodes at 324 nm. *Applied Physics Letters* **81**(18) (2002), 3491–3493. DOI: 10.1063/1.1518155.

[117] Y. Xi and E. F. Schubert: Junction-temperature measurement in GaN ultraviolet light-emitting diodes using diode forward voltage method. *Applied Physics Letters* **85**(12) (2004), 2163–2165.

[118] S. Chhajed, Y. Xi, Y.-L. Li, T. Gessmann, and E. F. Schubert: Influence of junction temperature on chromaticity and color-rendering properties of trichromatic white-light sources based on light-emitting diodes. *Journal of Applied Physics* **97**(5) (2005), 054506.

[119] T. Gessmann and E. F. Schubert: High-efficiency AlGaInP light-emitting diodes for solid-state lighting applications. *Journal of applied physics* **95**(5) (2004), 2203–2216.

[120] P. Manninen and P. Orrevetelaeinen: On spectral and thermal behaviors of AlGaInP light-emitting diodes under pulse-width modulation. *Applied Physics Letters* **91**(18) (2007), 181121.

[121] N. C. Chen et al.: Spectral shape and broadening of emission from AlGaInP light-emitting diodes. *Journal of Applied Physics* **106**(7) (2009), 074514.

[122] P. Altieri et al.: Internal quantum efficiency of high-brightness AlGaInP light-emitting devices. *Journal of applied physics* **98**(8) (2005), 086101.

[123] E. M. Daly, T. J. Glynn, J. D. Lambkin, L. Considine, and S. Walsh: Behavior of In 0.48 Ga 0.52 P/(Al 0.2 Ga 0.8) 0.52 In 0.48 P quantum-well luminescence as a function of temperature. *Physical Review B* **52**(7) (1995), 4696.

[124] R. Hetzel and G. Leising: Spectral behavior and coherence length of GaN-and AlGaInP-based light-emitting diodes. *SPIE OPTO*. International Society for Optics and Photonics, 2014, 900318–900318.

[125] R. Paessler: Parameter sets due to fittings of the temperature dependencies of fundamental bandgaps in semiconductors. *physica status solidi(b)* **216**(2) (1999), 975–1007.

[126] K. Chen and N. Narendran: Estimating the average junction temperature of AlGaInP LED arrays by spectral analysis. *Microelectronics Reliability* **53**(5) (2013), 701–705.

[127] M. D. Dawson and G. Duggan: Exciton localization effects and heterojunction band offset in (Ga, In) P-(Al, Ga, In) P multiple quantum wells. *Physical Review B* **47**(19) (1993), 12598.

[128] T. Kita, M. Sakurai, K. Yamashita, and T. Nishino: Energy relaxation by multi-phonon processes in partially ordered (Al0.5Ga0.5)0.5In0.5P. *Indium Phosphide and Related Materials, 1999. IPRM. 1999 Eleventh International Conference on*. IEEE, 1999, 159–162.

[129] D. J. Mowbray, O. P. Kowalski, M. S. Skolnick, M. Hopkinson, and J. P. R. David: Optical spectroscopy of AlGaInP based wide band gap quantum wells. *Superlattices and microstructures* **15**(3) (1994), 313.

[130] S. P. Najda, A. H. Kean, M. D. Dawson, and G. Duggan: Optical measurements of electronic bandstructure in AlGaInP alloys grown by gas source molecular beam epitaxy. *Journal of applied physics* **77**(7) (1995), 3412–3415.

[131] J. Novak et al.: Photoluminescence and TEM characterization of (AlyGa1-y)1-xInxP layers grown on graded buffers. *physica status solidi (c)* **4**(4) (2007), 1503–1507.

[132] J.-R. Dong et al.: 650-nm AlGaInP multiple-quantum-well lasers grown by metalorganic chemical vapor deposition using tertiarybutylphosphine. *Applied physics letters* **83**(4) (2003), 596–598.

[133] S. I. Tsintzos, N. T. Pelekanos, G. Konstantinidis, Z. Hatzopoulos, and P. G. Savvidis: A GaAs polariton light-emitting diode operating near room temperature. *Nature* **453**(7193) (2008), 372–375.

[134] H. Deng, G. Weihs, C. Santori, J. Bloch, and Y. Yamamoto: Condensation of Semiconductor Microcavity Exciton Polaritons. *Science* **298**(5591) (2002). PMID: 12364801, 199–202. DOI: 10.1126/science.1074464.

[135] O. P. Kowalski et al.: GaInP-AlGaInP band offsets determined from hydrostatic pressure measurements. *Applied physics letters* **66**(5) (1995), 619–621.

[136] M. D. Dawson, G. Duggan, and D. J. Arent: Optical measurements of electronic band structure in tensile strain (Ga, In) P-(Al, Ga, In) P quantum wells. *Physical Review B* **51**(24) (1995), 17660.

[137] J. Shao, A. Dornen, R. Winterhoff, and F. Scholz: Effective mass and exciton binding energy in ordered (Al) GaInP quantum wells evaluated by derivative of reflectivity. *Journal of applied physics* **91**(4) (2002), 2553–2555.

[138] L. Zhu, J. Shao, X. Lu, S. Guo, and J. Chu: Competition of compressive strain with substrate misorientation in CuPt-type ordered GaInP/AlGaInP quantum wells. *Journal of Applied Physics* **109**(1) (2011), 013509.

[139] J. W. Lamb: Evaluation of biasing and protection circuitry components for cryogenic MMIC low-noise amplifiers. *Cryogenics* **61** (2014), 43–54. DOI: 10.1016/j.cryogenics.2014.02.005.

[140] K. Seeger: *Semiconductor Physics: An Introduction*. Springer, 2004. 556 pp.

[141] J. Liu, W.-S. Tam, H. Wong, and V. Filip: Temperature-dependent light-emitting characteristics of InGaN/GaN diodes. *Microelectronics Reliability* **49**(1) (2009), 38–41.

[142] J.-I. Shim et al.: Efficiency droop in AlGaInP and GaInN light-emitting diodes. *Applied Physics Letters* **100**(11) (2012), 111106. DOI: 10.1063/1.3694044.

[143] J. D. Bullough, K. S. Hickcox, T. R. Klein, and N. Narendran: Effects of flicker characteristics from solid-state lighting on detection, acceptability and comfort. *Lighting Research and Technology* **43**(3) (2011), 337–348.

[144] J. A. Veitch and S. L. McColl: Modulation of fluorescent light: Flicker rate and light source effects on visual performance and visual comfort. *Lighting Research and technology* **27**(4) (1995), 243–256.

[145] M. Tziraki, R. Jones, P. M. W. French, M. R. Melloch, and D. D. Nolte: Photorefractive holography for imaging through turbid media using low coherence light. *Applied Physics B* **70**(1) (2000), 151–154.

[146] B. Kemper, S. Stuerwald, C. Remmersmann, P. Langehanenberg, and G. von Bally: Characterisation of light emitting diodes (LEDs) for application in digital holographic microscopy for inspection of micro and nanostructured surfaces. *Optics and Lasers in Engineering* **46**(7) (2008), 499–507.

[147] D. S. Mehta, K. Saxena, S. K. Dubey, and C. Shakher: Coherence characteristics of light-emitting diodes. *Journal of Luminescence* **130**(1) (2010), 96–102.

[148] P. Mayrhofer: *Photophysical Properties of Rubicene Experimental Investigations on the Route to an Organic Laser*. Saarbruecken: AV Akademikerverlag, 2013.

[149] A. M. Brouwer: Standards for photoluminescence quantum yield measurements in solution (IUPAC Technical Report). *Pure & Applied Chemistry* **83**(12) (2011).

[150] J. Olmsted: Calorimetric determinations of absolute fluorescence quantum yields. *Journal of Physical Chemistry* **83**(20) (1979), 2581–2584.

[151] R. F. Kubin and A. N. Fletcher: Fluorescence quantum yields of some rhodamine dyes. *Journal of Luminescence* **27**(4) (1983), 455–462.

[152] P. C. Beaumont, D. G. Johnson, and B. J. Parsons: Photophysical properties of laser dyes: picosecond laser flash photolysis studies of Rhodamine 6G, Rhodamine B and Rhodamine 101. *Journal of the Chemical Society, Faraday Transactions* **89**(23) (1993), 4185–4191.

[153] M. Fischer and J. Georges: Fluorescence quantum yield of rhodamine 6G in ethanol as a function of concentration using thermal lens spectrometry. *Chemical physics letters* **260**(1) (1996), 115–118.

[154] Isadore Berlman: Handbook of fluorescence spectra of aromatic molecules. *Academic Press, New York and London, 2nd. edition,* **13**(1) (1972), 473. DOI: 10.1016/0022-2860(72)87041-8.

[155] X. Liu, Y. Mao, S. A. Ruetten, and J. K. Thomas: Charge transfer and charge trapping in zeolites and similar media. *Solar Energy Materials and Solar Cells* **38**(1) (1995), 199–219. DOI: 10.1016/0927-0248(94)00226-6.

[156] R. W. Douglas Magde: Fluorescence quantum yields and their relation to lifetimes of rhodamine 6G and fluorescein in nine solvents: improved absolute standards for quantum yields. *Photochemistry and photobiology* **75**(4) (2002), 327–34. DOI: 10.1562/0031-8655(2002)0752.0.CO;2.

[157] M. M. Martin: Hydrogen bond effects on radiationless electronic transitions in xanthene dyes. *Chemical Physics Letters* **35**(1) (1975), 105–111.

[158] R. M. Metzger: *The Physical Chemist's Toolbox*. John Wiley & Sons, 2012. 960 pp.

[159] M. I. Aralaguppi, C. V. Jadar, and T. M. Aminabhavi: Density, Viscosity, Refractive Index, and Speed of Sound in Binary Mixtures of Acrylonitrile with Methanol, Ethanol, Propan-1-ol, Butan-1-ol, Pentan-1-ol, Hexan-1-ol, Heptan-1-ol, and Butan-2-ol. *Journal of Chemical & Engineering Data* **44**(2) (1999), 216–221. DOI: 10.1021/je9802219.

[160] T. M. Aminabhavi, V. B. Patil, M. I. Aralaguppi, J. D. Ortego, and K. C. Hansen: Density and Refractive Index of the Binary Mixtures of Cyclohexane with Dodecane, Tridecane, Tetradecane, and Pentadecane at (298.15, 303.15, and 308.15) K. *Journal of Chemical & Engineering Data* **41**(3) (1996), 526–528. DOI: 10.1021/je950280b.

Wiley Online Library
Early View publication on www.wileyonlinelibrary.com
(issue and page numbers not yet assigned;
citable using Digital Object Identifier – **DOI**)

Phys. Status Solidi A, 1–8 (2014) / **DOI** 10.1002/pssa.201431046

physica status solidi a
www.pss-a.com
applications and materials science

Current density impact on the emission behavior of GaN-based blue emitting LEDs in the temperature range of 4.2–400 K

Reinhold Hetzel[*,1,2] **and Günther Leising**[**,1]

[1] Institute of Solid State Physics, Graz University of Technology, Petersgasse 16, 8010 Graz, Austria
[2] LUMITECH Produktion und Entwicklung GmbH, Technologiepark 10, 8380 Jennersdorf, Austria

Received 23 January 2014, revised 13 March 2014, accepted 10 April 2014
Published online 7 May 2014

Keywords current density, junction temperature, GaN, light-emitting diodes

[*] Corresponding author: e-mail reinhold.hetzel@tugraz.at, Phone: +43 316 873 8979, Fax: +43 316 873 8466
[**] e-mail g.leising@tugraz.at, Phone: +43 316 873 8470, Fax: +43 316 873 108470

Blue emitting GaN-based light emitting diodes (LEDs) show a distinct spectral behavior with respect to temperature and injection current density. Operating LEDs with short current pulses of 500 ns provides a steady state situation, which allows investigating the emission behavior of LEDs at a certain device temperature thereby maintaining thermal equilibrium. The LEDs were examined in a temperature range between 4.2 and 400 K and in a current density range between 2 and 50 A cm^{-2}. Low temperature investigations showed a blue shift of the electroluminescence spectra (EL) with respect to junction temperature, which is assigned to the radiative recombination of localized excitons. In the elevated temperature region a distinct red shift due to energy gap shrinkage was observed. Further we expect an exciton lifetime reduction at 4.2 K. Additionally, the influence of the driving parameters (pulse injection current or direct current (DC)) in the presence of piezoelectric fields is discussed and separated into band filling effect and occurrence of fields, which screen the quantum confined Stark effect. Low temperature investigations indicate that band filling is mainly responsible for the blue shift of the EL spectra with respect to the injection current.

1 Introduction Recent insights into the human non-image forming visual system gained tremendously the interest in tuneable white light engines (changing color temperature) in the last couple of years. Hence, the requirements for modern light emitting diodes (LEDs) are stable emission spectra, independent of the modality of current injection [pulse width modulated (PWM) or direct current (DC)]. These driving parameters are mainly responsible for the temperature increase of the pn-junction, which leads to unwanted spectral variations during operation of the LEDs [1]. In white light illuminants, especially blue emitters play a prevailing role because they are used as primary emitter and also as excitation source for the phosphor conversion technology. GaN layers reveal great thermal stability as well as crystalline robustness, which make this III–V direct semiconductor compound widely used for short wavelength light emission in optoelectronic devices for general illumination purposes [2, 3]. The understanding of the detailed nature of the emission process occurring in blue emitting LEDs and its particular behavior under different driving conditions is mandatory to design LED modules with stable and constant color coordinates.

The emission response is influenced by several internal device parameters. One important parameter, which dictates efficiency drops and influences the emission characteristics of LEDs is the junction temperature (JT) of the device [4]. However, the JT of LEDs is very difficult to access as neither sensing elements nor infrared (IR) cameras can be used for determination. Sensing elements probe the temperature remote from the junction; IR cameras suffer from the problem that images have to be calibrated regarding the often unknown emission coefficients and they look at best at the surface temperature and not at the JT of the device. If measured on the final LED module, emitted IR radiation gets

absorbed in the globe top material, which consists typically of hydrocarbon/silicon polymers. Implementing phosphor conversion materials (i.e. rare earth doped sulphides, nitrides, aluminium garnets etc.) into the globe top matrix will further sufficiently increase the IR absorption. Consequently, in the last couple of years methods have been developed which allow determining the JT out of the peak wavelength shift, the slope of the high energy wing or the forward voltage behavior of the LED [5–8]. Those measurements are performed at thermal equilibrium in a temperature-controlled oven.

We describe the current density impact on the temperature and therefore on the emission behavior of GaN-based LEDs by comparing pulsed and DC injection operated LEDs. We distinguish between pure temperature effects and pure carrier (current) impacts on the emission characteristics of GaN layer structures, which we achieve by operating the LEDs with short current pulse widths and low duty cycles. To achieve thermal equilibrium at low temperatures, the spectral response of the LEDs was measured in a liquid helium and nitrogen bath.

2 Experimental setup and sample preparation The measurements were performed at 4.2 and 77 K and in the range between 230 and 400 K. To ensure the intended device temperature (JT), all measurements were performed in thermal equilibrium. Low temperature measurements were carried out by contact cooling in a liquid helium bath (4.2 K) and a liquid nitrogen bath (77 K). The investigated LEDs consist of 8 μm thick GaN grown on a 140 μm thick Al_2O_3 substrate followed by an AlGaN/InGaN/GaN multiple quantum well (MQW) structure. A transparent SiO_x passivation layer is located on top of the whole diode area. The LEDs were mounted with a two component thermally conducting paste on an aluminum heat sink (5.0 mm × 6.3 mm × 4.8 mm) and contacted with 30 μm thick Au bond wires down to a printed circuit board (PCB). The device dimensions were 500 μm × 1000 μm with a device thickness (substrate and semiconductor layer) of 150 μm. The emission spectra were recorded with a spectrometer containing a 1200 lines mm^{-1} grid blazed at 500 nm. The spectrometer contains a CCD image sensor with a total number of 3648 pixels (pixel dimension 8 μm × 200 μm). Intensity calibration of the spectrometer (including fiber optics) was performed with a tungsten lamp standard; the wavelength calibration with a mercury argon lamp. The photometric linearity of the CCD detector was determined which causes that the signal intensity must be in the range between 5 and 90% of the total available measurement interval. For each recorded spectrum, the corresponding dark current was measured immediately afterwards and subtracted for data analysis. For the low temperature measurements (4.2 and 77 K) a 250 μm diameter fiber optics (NA = 0.29) was fixed on top of the LED using transparent glue. Emission/excitation photoluminescence measurements of the glue were carried out to ensure that the used glue does not affect the emission characteristics of the samples. Moreover, we quantified that the shape of the emission spectra and the peak position is independent of the detector angle relative to the sample position. We furthermore did not observe any preferred polarization direction of the collected light.

For the measurements in the range between 230 and 400 K a temperature-controlled chamber was used (temperature accuracy 0.1 K). To ensure the preset temperature of the chamber an additional Pt100 resistance on a separate heat sink was placed inside. During the whole experiment, the chamber was purged with dry air to avoid icing effects. In front of the entrance slit of the fiber optics input side an aperture with an acceptance angle of 5.72° was inserted. The samples were stored for at least 30 min per measurement point in the chamber to ensure thermal equilibrium between the junction and the chamber environment.

To operate the samples, forward current pulses (HP 214 B pulse generator) as well as DC current (Keithley 2601 B source measure unit) were injected. The forward current pulse width was 500 ns and the repetition rate was 500 μs (duty cycle 0.1%), respectively. A 20 Ω series resistance was installed in the setup to determine the injection current. The pulsed injection current (density) was varied between 10 mA (2 A cm^{-2}) and 250 mA (50 A cm^{-2}). Current voltage characteristics in DC mode were recorded consecutively from 0 to 200 mA with a 10 ms current injection time per measuring point. The DC current emission spectra were recorded after the device was turned on for 3 s.

3 Results and discussion One key parameter of light emitting junctions is the JT of the heterostructured LED. The JT is understood as the lattice temperature of the semiconductor alloy. Carriers injected into the quantum wells are denoted to hot carriers, which possess a higher temperature than the JT [9]. Those injected hot carriers undergo certain pathways of thermalization. One thermalization process occurs due to carrier–carrier scattering of the injected hot carriers as well as due to the interaction with already present charge carriers [10, 11]. Moreover, an energy transfer from the hot carriers to the lattice by the emission of phonons takes place [10, 11]. Thermalization due to carrier–carrier scattering occurs quite fast (<100 fs), e.g. for GaN 15–20 fs (at 25 K) were reported [9, 12]. Thermalization by the emission of phonons is occurring in the ps range where for GaN values between 0.2 and 2.5 ps [11, 13–15] and for InGaN epitaxial films 5 ps [10] at room temperature were reported.

For AlGaN/GaN heterostructures 1.4 ps and for AlInN/AlN/GaN heterostructures a hot carrier energy relaxation time of 6 ps (at room temperature) were experimentally determined [16, 17]. So, current pulse widths of 500 ns are orders of magnitude longer than the reported hot carrier relaxation times. Therefore, carrier temperature is expected to be equal to the JT. On the other hand, combining this current pulse width of 500 ns with a very low duty cycle of 0.1% allows neglecting the contribution of the average integrated power impact on the JT and leads to a steady state

situation. Operating LEDs with pulsed injection currents and a very low duty cycle in combination with a short current pulse width (500 ns) allows us to study the current impact on the charge carrier distribution in the potential wells of the MQW structure at certain preset temperature values. Further we gain insights into impact of the JT on the electroluminescence (EL) spectra.

3.1 Junction temperature investigations Figure 1 illustrates the behavior of the emission-peak energy E_p with respect to the JT for several pulsed injection currents, which was obtained from the respective measured EL spectra. For temperatures above 230 K a red shift of the EL spectra with respect to the JT occurs, which shows a nonlinear behavior (quadratic) up to 300 K and a linear relation for higher temperatures. This red shift can be attributed to a temperature induced energy gap shrinkage of the MQW structure which can be understood as an interaction of the temperature dependent expansion of the lattice as well as the temperature dependent electron lattice interaction [18]. In this temperature region between 230 and 400 K we measured a broadening of the emission spectra of approx. 8 nm, which occurs from the interaction of charge carriers with phonons (acoustical as well as optical) and unavoidable alloy composition fluctuations [8, 19].

We found an additional distinct red shift of the EL spectra with decreasing temperatures (i.e. blue shift with increasing temperature) for the low temperature range (4.2 and 77 K), which is an indication for exciton localization [20–26]. In semiconductor materials excitons are localized at low temperatures and quasi-free at high temperatures [27]. Structural defects (e.g. composition fluctuations, impurity density states, and lattice defects) lead to highly efficient traps for excitons [21, 22, 24, 26, 28]. Hence, the captured exciton loses its kinetic energy and therefore the photon emission energy that corresponds to the recombining bound electron–hole pair is reduced by the binding energy. This leads to induced electronic states in the energy gap of the material and therefore to a red shift at low temperatures (where excitons dominate the radiative recombination). Equation (1) presents the total exciton energy E_f in the ground state, whereas E_X stands for the binding energy of the exciton, m_e/m_h for the electron/hole mass, E_g reflects the actual energy gap, k the Boltzmann constant and $\hbar$ is equal to the Planck constant divided by 2π [23]. For trapped excitons the kinetic energy term vanishes and the total exciton energy E_f is given by the actual gap energy E_g minus the binding energy of the exciton E_X.

$$E_f = E_g - E_X + \frac{\hbar^2 k^2}{2(m_e + m_h)}. \quad (1)$$

To gain insight into the degree of the localization of the excitons (which apparently dominate the emission at low

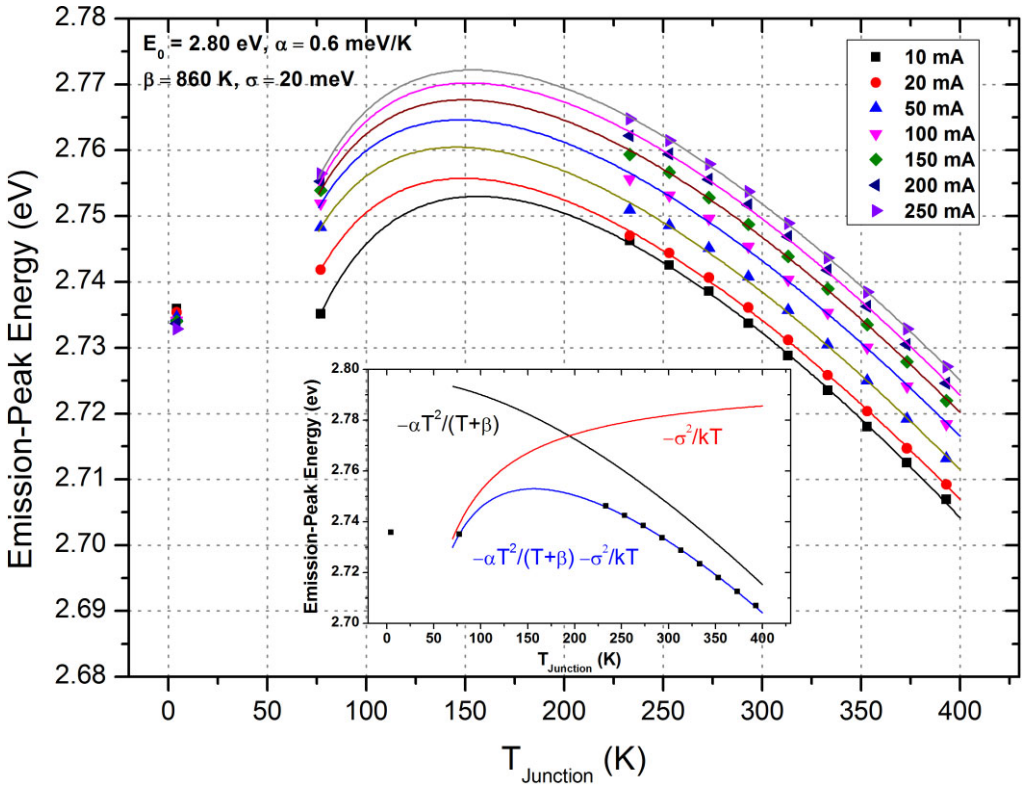

Figure 1 Behavior of the emission-peak energy E_p as a function of the junction temperature $T_{Junction}$ and the pulsed injection current. The solid lines are the fitting curves based on Eq. (2). Insert shows the individual contribution of the respective terms of the model in Eq. (2) for a 10 mA injection current.

temperatures) we apply a model in Fig. 1, which describes the behavior of the peak emission with respect to temperature as suggested in Refs. [22, 29]. The emission-peak energy as a function of temperature $E_p(T)$ can be then fitted with Eq. (2)

$$E_p(T) = E_{g,0} - \frac{\alpha T^2}{T+\beta} - \frac{\sigma^2}{kT}, \quad (2)$$

whereas $E_{g,0}$ represents the fundamental gap energy at the limit $T = 0$ K, α, and β are the Varshni parameters and T is the JT of the device, respectively. The last term $-\sigma^2/kT$ describes the Stokes-type red shift whereas from the σ value the degree of localization of the excitons can be obtained [20–22, 26, 29]. We found a σ value of around 20 meV, which is a qualitative indication of a high degree of localization and in good accordance to previous reported results [20, 22, 29]. As indicated in Fig. 1, Eq. (2) is just applicable for the temperature range at and above 77 K which again agrees with previously reported results in Refs. [20, 22, 29]. However, Eq. (2) cannot describe the distinct behavior of the EL-peak at 4.2 K, which will be elaborated below.

Insert in Fig. 1 separates the respective contribution of the two terms in Eq. (2). The first term $-\alpha T^2/(T+\beta)$ includes the Varshni parameters and allows the description of the energy gap shrinkage with increasing temperature whereas the second term $-\sigma^2/kT$ includes the excitonic behavior. Out of the applied model we obtained Varshni parameters of around 0.6 meV K^{-1} for α and 860 K for β, which are comparable to reported literature values for such types of materials [20, 26, 30, 31].

3.2 Injection current influence At 77 K and in the temperatures region between 230 and 400 K, a distinct blue shift when increasing the injection current is observed (Fig. 1). Two kinds of effects can be dominantly assigned to this current-induced blue shift namely the band filling effect (BFE) as well as the screening of the occurring piezoelectric (PE) field [32, 33]. Charge carriers at higher confined levels in a MQW structure contribute to the radiative recombination process, due to the fact that lower states are occupied [34, 35]. Therefore a shift to higher energies with respect to the charge carrier injection can be expected and assigned to the BFE. The BFE usually shifts the emission-peak energy linearly to higher energies when increasing the injection current [34]. This behavior is explained by the step-like density of states in the quantum well structure [35, 36].

However as reported previously, the lattice mismatch of GaN, AlN and InN gives rise to PE fields, which tilt the potential wells and therefore reduces the effective energy gap [37–40]. The injection of charge carriers creates a field that counteracts the PE field and therefore reduces the occurring quantum confined Stark effect (QCSE) [34, 40–42]. As reported in [43] lattice mismatches as well as the difference in thermal expansion coefficients furthermore lead to strain and therefore to PE fields in GaN based semiconductor alloys. Table 1 lists literature values for the piezoelectric modules ε_{33} and ε_{31} [44] as well as the thermal expansion coefficients α_n (normal to c-axis) and α_p (parallel to c-axis) at room temperature for GaN, AlN, and InN, respectively [45, 46]. From Table 1, we find that the origin of PE field can be mainly assigned to the lattice mismatch. Nevertheless, we note that the behavior of the thermal expansion coefficient for wurtzite III–V nitrides at low temperatures is quite complex due to the fact that negative values for temperatures below 50 K for InN [47] and at 75 K and below for AlN [48] were reported. However as described in Ref. [47], the difference between the several expansion coefficients of those materials diminishes for very low temperatures (below 10 K). This concludes that the combination of different thermal expansion coefficients with the distinct lattice mismatches leads to PE fields, which tilt the quantum well, where it can be expected that the lattice mismatch is the predominant effect.

Table 1 Thermal expansion coefficients α_p/α_n [45, 46] and piezoelectric modules $\varepsilon_{33}/\varepsilon_{31}$ [44] for GaN, AlN, and InN at room temperature.

	α_p at 300 K (10^{-6} K^{-1})	α_n at 300 K (10^{-6} K^{-1})	ε_{33} (C m^{-2})	ε_{31} (C m^{-2})
GaN	3.340	3.430	0.73	−0.49
AlN	3.480	4.350	1.46	−0.60
InN	2.751	3.830	0.97	−0.57

The behavior of the emission-peak energy of the EL spectra with respect to the injection current for the low temperature region (4.2 and 77 K) is shown in Fig. 2, for the high temperature region (230 to 400 K) in Fig. 3, respectively. Neither for measurements performed at 77 K nor in between 230 and 400 K, we find a strictly linear behavior of the emission-peak energy (which would be an indication for pure band filling) with respect to the pulsed injection current over the whole applied current range (left panel in Fig. 2 and Fig. 3). Only for higher pulsed injection current levels (i.e. above 100 mA) a linear behavior can be observed (left panel in Fig. 2 and Fig. 3).

Further, the increase of the full width at half maximum (FWHM) of around 16 meV with respect to the injection current at 77 K (Fig. 4) is an indication for band filling as the peak line width would be reduced if the QCSE is screened (as reported in Refs. [28, 42]). At 4.2 K, a very small red-shift (!) of 3 meV (corresponding to 0.1% change of the respective emission-peak energy) with respect to the injection current is measured (left panel in Fig. 2). This supports our explanation that the screening of the PE field is not responsible for the blue shift with increasing current at elevated temperatures [20]. If screening of the occurring PE fields would be mainly responsible for the blue shift, such shift will be also observable at 4.2 K, besides, the FWMH will get reduced as well. However, neither a blue shift (left panel in Fig. 2) nor a FWHM change (Fig. 4) is observed. Therefore we conclude that band filling is the dominant process for the blue shift of the EL spectra with increasing current at 77 K and above.

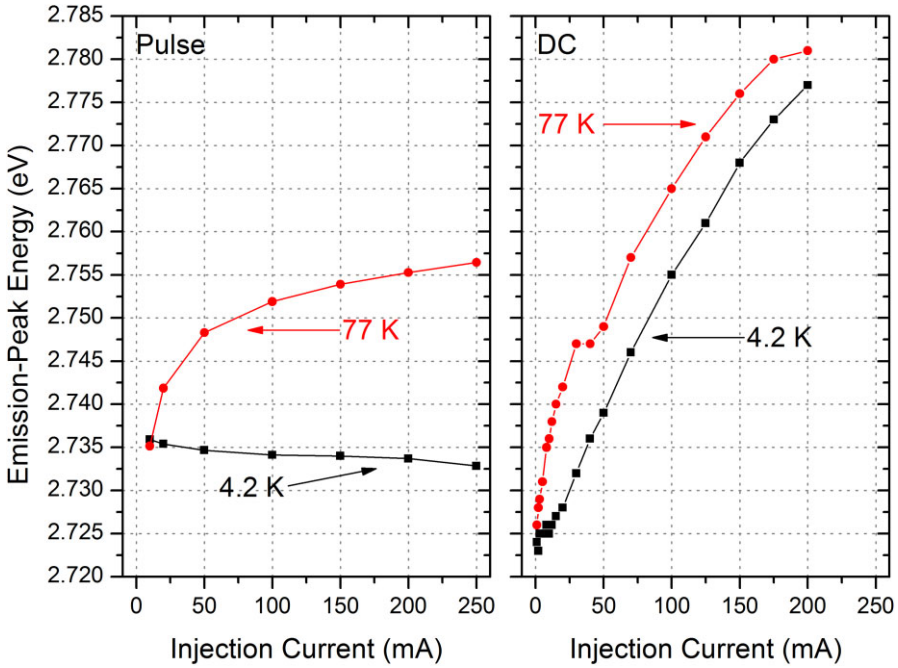

Figure 2 Influence of pulsed (left panel) and DC (right panel) injection current levels on the emission-peak energy E_p at 4.2 and 77 K.

However, since the emission-peak energy does show a non-linear behavior in the low current regime (<100 mA) and for temperatures above 77 K, an interplay between BFE and screening of the PE field in the low current range cannot be entirely excluded. The impact of PE fields in the low current region (<100 mA) and at elevated temperatures (at and above 77 K) cannot be further specified by taking the emission-peak behavior at 4.2 K into account.

We expect that the lifetime of the excitons decreases significantly at low temperatures, since neither the emission-peak energy (left panel in Fig. 2), nor the spectral shape (left panel in Fig. 5) do change significantly when increasing the pulsed injection current at 4.2 K (which was applied in the range between 10 and 250 mA) [27, 49]. Due to the decreasing lifetime of bound excitons at 4.2 K the recombination occurs from low lying energy levels. This reduction in carrier lifetime is also supported by the fact that no blue shift (and therefore no BFE) is observable at 4.2 K.

We note that for temperatures above 230 K the behavior of the emission-peak energy with respect to the injection current is slightly different and independent of the JT

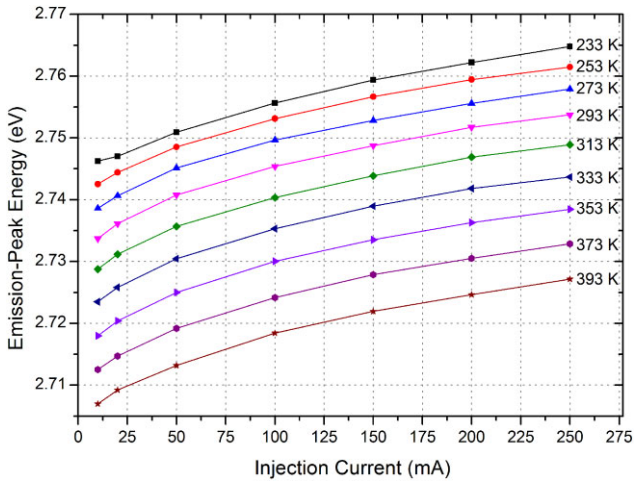

Figure 3 Influence of pulsed injection current on the emission-peak energy E_p in the range of 230 and 400 K.

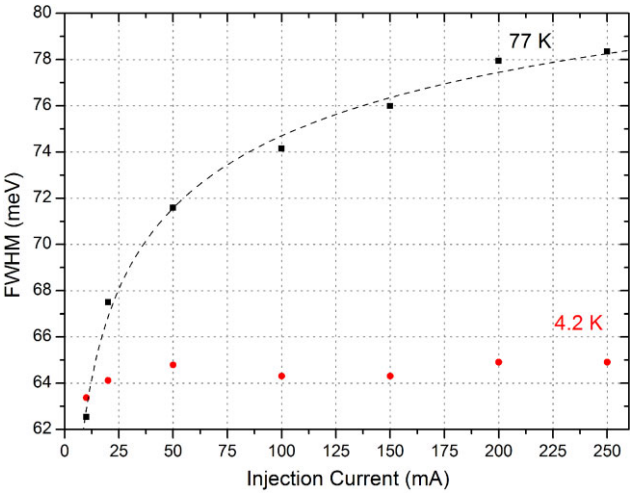

Figure 4 FWHM with respect to pulsed injection current at 4.2 and 77 K.

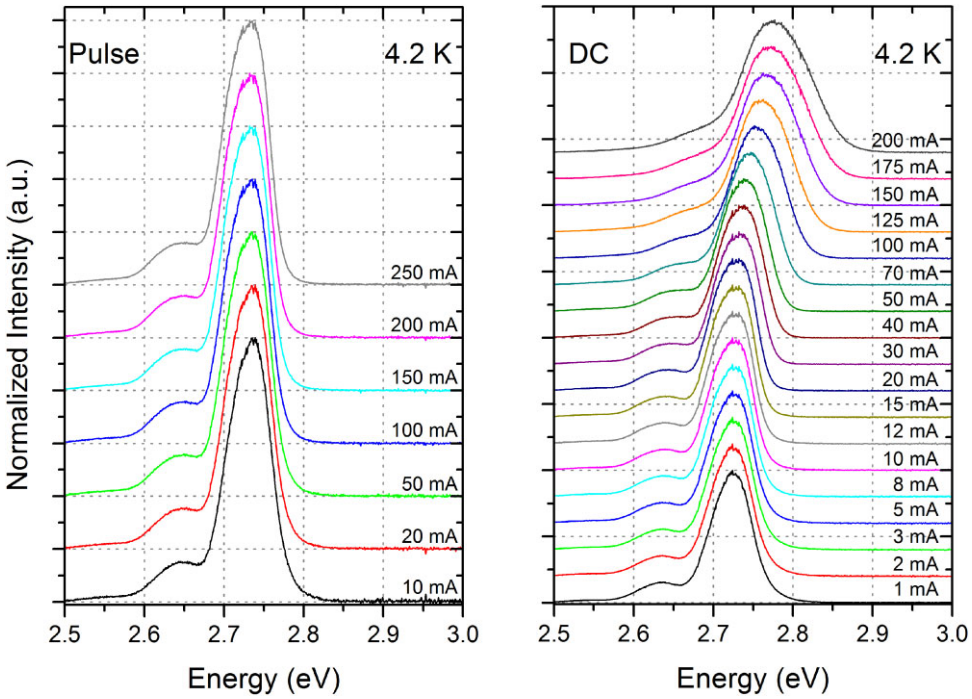

Figure 5 Spectral behavior of GaN based LEDs at 4.2 K. Left panel shows pulsed current injection, right panel DC current injection, respectively. The spectra are shifted vertically for clarity.

(Fig. 3). Deviations between low temperature (77 K) and high temperature (above 230 K) performance might be due to the fact that trapped excitons are not mainly involved in the radiative recombination process at such high temperatures anymore [27].

Essential to mention is that even low DC currents heat up the JT of the device, therefore non-thermal equilibrium situations are present and all discussed effects (lattice heating, carrier lifetime changes, screening of the PE field, band filling, etc.) do occur simultaneously and are hardly distinguishable anymore. With increasing temperature the lifetime of the charge carriers increase which allow them to relax into lower energy levels and explains the slightly red shifted emission spectra in Fig. 2 between pulse and DC injection current (<30 mA) [49]. Therefore, a redistribution of the charge carriers occurs. However, the lifetime gets also influenced by the amount of charge carriers, because more charge carriers in the quantum well reduce the average spatial separation between electrons and holes which reduces the lifetime [34]. This explains the different results of DC and pulse measurements performed at 4.2 and 77 K in Fig. 2 especially for high current levels. Figure 5 shows the spectral behavior at 4.2 K depending whether pulse or DC current is injected.

These findings support our approach that the only way to extract reliable informations from the emission data is by depositing low pulse power. We further found a big difference between the measured current voltage characteristic of pulsed operated and DC driven LEDs for temperatures between 4.2 and 300 K. Although the recording time of the current voltage characteristics of the LEDs was very short (10 ms) a distinct shift to lower voltages and therefore to higher temperatures was measured.

We also performed temperature investigations by IR technique, which supports our assumption that the pulse injection current does not increase the temperature of the device.

4 Conclusions Our measurements on GaN-based LEDs showed that thermal as well as electrical effects highly influence the emission behavior. Due to our approach using pulsed injection current with a very low duty cycle and a short pulse width, we could distinguish between prevailing thermal related shifts as well as carrier (current) dominated induced shifts. In the very low temperature region (4.2 and 77 K), the emission-peak energy of GaN-based LEDs is red shifted with decreasing temperature (i.e. blue shifted with increasing temperature) due to the dominating radiative recombination of localized excitons from traps. Furthermore, we expect that the exciton lifetime decreases significantly at 4.2 K. At 230 K, trapped excitons do not dominate the radiative emission anymore and thermalize out of the quantum wells. Hence, the observed red shift with increasing JT occurs due to the decrease of the effective energy gap.

We found that the blue shift with respect to injection current density can be dedicated mainly to band filling instead of screening of the QCSE.

Important to mention is that the JT as well as the lifetime of the charge carriers is strongly influenced by DC current. Therefore, investigations of the emission behavior of LEDs

have to be performed using short current/voltage pulses and low duty cycles. To reach a steady state situation and ensure a defined JT in the low temperature region, investigations were performed in liquid environment, which is the only possibility to ensure thermal equilibrium at such low temperatures.

Optical and electrical parameters gained from the presented experimental method can be in assigned to a two-dimensional calibration array, which allows the determination of the JT during operation of an LED by recalling those parameters. This gives the opportunity to counteract against current as well as temperature induced shifts of the color coordinates during operation of LED modules.

Further evaluating the JT out of spectral data is more preferred than extracting it out of the forward voltage behavior (so called forward voltage method), due to the fact that the equivalent circuit of the measurement setup used for calibration is not equal to the commonly used PWM or DC driver circuits.

Acknowledgements The authors would like to acknowledge LUMITECH Produktion und Entwicklung GmbH for providing samples as well as the Austrian Research Promotion Agency (FFG) for financial support. Further they thank Harald Plank and Sebastian Rauch for FIB and EDX measurements (Institute for Electron Microscopy and Nanoanalysis (FELMI) of Graz University of Technology).

References

[1] R. Hetzel, S. Tasch, and G. Leising, e & i Elektrotechnik und Informationstechnik **129**(7-8), 460 (2012).
[2] W. J. Hwang, T. H. Lee, L. Kim, and M. W. Shin, Phys. Status Solidi C **1**, 2429 (2004).
[3] M. Tchounkeu, O. Briot, B. Gil, J. P. Alexis, and R. L. Aulombard, J. Appl. Phys. **80**, 5352 (1996).
[4] J. C. Wang, C. H. Fang, Y. F. Wu, W. J. Chen, D. C. Kuo, P. L. Fan, J. A. Jiang, and T. E. Nee, J. Lumin. **132**, 429 (2012).
[5] J. Cho, C. Sone,1 Y. Park, and E. Yoonet, Phys. Status Solidi A **202**, 1869 (2005).
[6] A. Keppens, W. R. Ryckaert, G. Deconinck, and P. Hanselaer, J. Appl. Phys. **104**, 093104 (2008).
[7] Y. Xi, J.-Q. Xi, Th. Gessmann, J. M. Shah, J. K. Kim, E. F. Schubert, J. Fischer, M. H. Crawford, K. H. A. Bogart, and A. A. Allermanet, Appl. Phys. Lett. **86**, 031907 (2005).
[8] Z. Vaitonis, P. Vitta, and A. Zukauskas, J. Appl. Phys. **103**, 093110 (2008).
[9] A. J. Nozik, Annu. Rev. Phys. Chem. **52**, 193 (2001).
[10] C.-K. Sun, F. Vallée, S. Keller, J. E. Bowers, and S. P. DenBaars, Appl. Phys. Lett. **70**, 2004 (1997).
[11] H. Ye, G. W. Wicks, and P. M. Fauchet, Appl. Phys. Lett. **74**, 711 (1999).
[12] K. T. Tsen, R. P. Joshi, D. K. Ferry, A. Botchkarev, B. Sverdlov, A. Salvador, and H. Morkoç, Appl. Phys. Lett. **68**, 2990 (1996).
[13] C.-K. Sun, Y.-L. Huang, S. Keller, U. K. Mishra, and S. P. DenBaars, Phys. Rev. B **59**, 13535 (1999).
[14] K. T. Tsen, J. G. Kiang, D. K. Ferry, and H. Morkoç, Appl. Phys. Lett. **89**, 112111 (2006).
[15] J. A. Ferrer-Perez, B. Claflin, D. Jena, M. Sen, R. Vetury, and D. Dorsey, J. Electron. Mater. **43**, 341 (2014).
[16] A. Matulionis, J. Liberis, L. Ardaravicius, M. Ramonas, I. Matulioniene, and J. Smart, Semicond. Sci. Technol. **17**, L9 (2002).
[17] A. Matulionis, J. Liberis, E. Šermukšnis, J. Xie, J. H. Leach, M. Wu, and H. Morkoc, Semicond. Sci. Technol. **23**, 075048 (2008).
[18] Y. P. Varshni, Physica **34**, 149 (1967).
[19] E. Berkowicz, D. Gershoni, G. Bahir, E. Lakin, D. Shilo, E. Zolotoyabko, A. C. Abare, S. P. Denbaars, and L. A. Coldren, Phys. Rev. B **61**, 10994 (2000).
[20] T. Wang, J. Bai, S. Sakai, and J. K. Ho, Appl. Phys. Lett. **78**, 2617 (2001).
[21] N. Nepal, J. Li, M. L. Nakarmi, J. Y. Lin, and H. X. Jiang, Appl. Phys. Lett. **88**, 062103 (2006).
[22] P. G. Eliseev, P. Perlin, J. Lee, and M. Osiski, Appl. Phys. Lett. **71**, 569 (1997).
[23] I. Pelant and J. Valenta, Luminescence Spectroscopy of Semiconductors (Oxford University Press, Oxford, 2012), p. 164.
[24] K. L. Teo, J. S. Colton, P. Y. Yu, E. R. Weber, M. F. Li, W. Liu, K. Uchida, H. Tokunaga, N. Akutsu, and K. Matsumoto, Appl. Phys. Lett. **73**, 1697 (1998).
[25] R. W. Martin, P. G. Middleton, K. P. O'Donnell, and W. V. Stricht, Appl. Phys. Lett. **74**, 263 (1999).
[26] T. Wang, H. Saeki, J. Bai, T. Shirahama, M. Lachab, S. Sakai, and P. Eliseev, Appl. Phys. Lett. **76**, 1737 (2000).
[27] P. Corfdir, A. Dussaigne1y, H. Teisseyre, T. Suski, I. Grzegory, P. Lefebvre, E. Giraud, M. Shahmohammadi, R. T. Phillips, J. D. Ganiere, N. Grandjean, and B. Deveaud, Jpn. J. Appl. Phys. **52**, 08JC01 (2013).
[28] C. M. Lee, S. H. Choi, C. S. Kim, S. K. Noh, J. I. Lee, K. Y. Lim, and I. K. Han, J. Korean Phys. Soc. **45**, 243 (2004).
[29] P. G. Eliseev, J. Appl. Phys. **93**, 5404 (2003).
[30] I. Vurgaftman and J. R. Meyer, J. Appl. Phys. **94**, 3675 (2003).
[31] K. B. Nam, J. Li, J. Y. Lin, and H. X. Jiang, Appl. Phys. Lett. **85**, 3489 (2004).
[32] T. Wang, D. Nakagawa, M. Lachab, T. Sugahara, and S. Sakai, Appl. Phys. Lett. **74**, 3128 (1999).
[33] K. Kazlauskas, G. Tamulaitis, J. Mickeviius, E. Kuokštis, A. Žukauskas, Y. C. Cheng, H. C. Wang, C. F. Huang, and C. C. Yang, J. Appl. Phys. **97**, 013525 (2005).
[34] T. Kuroda and A. Tackeuchi, J. Appl. Phys. **92**, 3071 (2002).
[35] B. Arnaudov, D. S. Domanevskii, S. Evtimova, Ch. Ivanov, and R. Kakanakov, Microelectron. J. **40**, 346 (2009).
[36] B. E. A. Saleh and M. C. Teich, Fundamentals of Photonics (John Wiley & Sons, New York, 1991), pp. 569–573.
[37] R. A. Hogg, C. E. Norman, A. J. Shields, M. Pepper, and N. Iizuka, Appl. Phys. Lett. **76**, 1428 (2000).
[38] T. Takeuchi, C. Wetzel, S. Yamaguchi, H. Sakai, H. Amano, I. Akasaki, Y. Kaneko, S. Nakagawa, Y. Yamaoka, and N. Yamada, Appl. Phys. Lett. **73**, 1691 (1998).
[39] L. Guo, X. Wang, H. Xiao, and B. Wang, J. Cryst. Growth **298**, 522 (2007).
[40] H. S. Kim, J. Y. Lin, H. X. Jiang, W. W. Chow, A. Botchkarev, and H. Morkoc, Appl. Phys. Lett. **73**, 3426 (1998).

[41] F. D. Sala, A. D. Carlo, P. Lugli, F. Bernardini, V. Fiorentini, R. Scholz, and J. M. Jancu, Appl. Phys. Lett. **74**, 2002 (1999).
[42] D. A. B. Miller, D. S. Chemla, T. C. Damen, A. C. Gossard, W. Wiegmann, M. Hill, T. H. Wood, and C. A. Burrus, Phys. Rev. B **32**, 1043 (1985).
[43] L. K. Teles, J. Furthmueller, L. M. R. Scolfaro, J. R. Leite, and F. Bechstedt, Phys. Rev. B **62**, 2475 (2000).
[44] F. Bernardini, V. Fiorentini, and D. Vanderbilt, Phys. Rev. B **56**, 10024 (1997).
[45] H. Iwanga, A. Kunishige, and S. Takeuchi, J. Mater. Sci. **35**, 2451 (2000).
[46] K. Wang and R. Reeber, Appl. Phys. Lett. **79**, 1602 (2001).
[47] L. C. Xu, R. Z. Wang, X. Yang, and H. Yan, J. Appl. Phys. **110**, 043528 (2011).
[48] R. R. Reeber, Mater. Res. Soc. Symp. Proc. **622**, T6.35.1–T6.35.4 (2000).
[49] Y. H. Cho, G. H. Gainer, A. J. Fischer, J. J. Song, S. Keller, U. K. Mishra, and S. P. DenBaars, Appl. Phys. Lett. **73**, 1370 (1998).

Elektrotechnik & Informationstechnik DOI 10.1007/s00502-012-0105-1

Tunable *natural light* realized by phosphor-innovation light-emitting-diode technology

R. Hetzel, S. Tasch, G. Leising

The nature and quality of artificial lighting are becoming more and more recognized and debated issues concerning their impact on comfort, well-being and even human's health (chronobiology). Therefore, the target must be to emulate natural (sun) light for indoor illumination. In this paper parameters which are responsible for the nature and quality of light sources are elaborated. Leading edge high quality light sources, realized by light emitting diodes (LEDs) for emulating natural light, are presented.

The junction temperature of electroluminescence devices is a key parameter which influences emission wavelength, light output (power efficiency), light degradation and lifetime of the LEDs. We present experimental data and a model which allows one to derive the junction temperature of LEDs under operation.

Keywords: light emitting diodes; PI-LED; natural light; junction temperature; white light emitter; chronobiology

Veränderbares natürliches Licht realisiert mit Phosphor-Innovation Licht-Emittierender-Dioden-Technologie.

Die Natur und die Qualität künstlicher Lichtquellen und deren Auswirkungen auf Komfort, Wohlbefinden und Gesundheit werden immer stärker wahrgenommen und diskutiert (Chronobiologie). Daraus folgt nahezu zwingend die Forderung, natürliches (Sonnen-) Licht im Bereich der Innenraumbeleuchtung nachzubilden. In dieser Arbeit werden wesentliche Parameter, welche die Natur und die Qualität von Lichtquellen bestimmen, behandelt. Präsentiert werden technologisch führende und hoch qualitative Lichtquellen zur Erzeugung von „natürlichem" Licht unter Verwendung von Licht emittierenden Dioden (LEDs).

Die Temperatur der Grenzschicht ist ein Schlüsselparameter, der die Emissionswellenlänge, die Lichtausbeute (Effizienz), die Lichtdegradation und letztlich die Lebensdauer von LEDs bestimmt. Wir präsentieren Messergebnisse zur Grenzschichttemperatur und ein Modell, welches erlaubt, die Temperatur der Grenzschicht der LED im Betrieb zu bestimmen.

Schlüsselwörter: Licht emittierende Dioden; PI-LED; Natürliches Licht; Grenzschichttemperatur; Weißlicht-Emitter; Chronobiologie

Received July 6, 2012, accepted October 15, 2012

1. Introduction

Round (*1907*) noticed in 1907 that SiC crystals (carborundum) emit light of different colors by applying an electric field. This was the first published evidence for solid state lighting (*Schubert et al. 2006a*). In 1955, *Braunstein* (*1955*) reported radiative transitions through direct recombination of electron-hole pairs in several semiconductor alloys. One of the first visible Light Emitting Diodes (LEDs) was published in 1962 by Nick Holonyak et al. (*Holonyak and Bevacqua 1962*). The light emission in the red region of the visible spectrum was achieved with a $Ga(As_{1-x}P_x)$ semiconductor alloy.

Subsequently, the development of LEDs was pushed forward and the technology became commercially available in opto-couplers, alphanumeric displays and pocket calculators at the beginning of the 1970s. Since the late 1960s, the lumen per lamp efficiency for the most powerful commercially available red LEDs increased roughly by a factor of $1.5 \cdot 10^5$ (*Haitz and Tsao 2011*). During the last decade, the efficiency of the commercially offered white LEDs increased by a factor of $1 \cdot 10^3$ (*Haitz and Tsao 2011*). This exponential rise of the light output and the efficiency made the technology available for a large field of new applications. Amongst others, LED technology is now settled in the automotive and medical sector and is well established in the entertainment industry e.g. for large area display applications. Additionally, since LED light provides high luminous efficacies of 150 lm/W and more (*Pimputkar et al. 2009*) the conventional incandescent light bulb (around 12 lm/W) gets replaced by this technology. It is expected that most of the classical light sources will be replaced by LEDs soon.

Several types of semiconductor alloys being available today allow LEDs to operate at wavelengths from deep ultra violet (UV) up to the near infrared region (IR) covering the entire visible spectrum (VIS).

2. LED for general illumination purposes

Major advantages like long lifetime (beyond tens of thousands of hours) and high efficiencies make LEDs more and more common in the field of general illumination for homes and offices. Furthermore, in contrast to thermally radiating light sources (tungsten bulbs, halogen lamps, etc.), LEDs offer dimming capabilities while keeping the spectral distribution constant (*Steele 2007*). To benefit from the LED technology in these areas, the development of high quality white light was one of the basic challenges.

Hetzel, Reinhold, Dipl.-Ing., Graz University of Technology, Institute of Solid State Physics, Petersgasse 16, 8010 Graz, Austria, and LUMITECH Produktion und Entwicklung GmbH, Technologiepark 10, 8380 Jennersdorf, Austria (E-mail: reinhold.hetzel@tugraz.at); **Tasch, Stefan, Dipl.-Ing. Dr.,** LUMITECH Produktion und Entwicklung GmbH, Technologiepark 10, 8380 Jennersdorf, Austria; **Leising, Günther, Univ.-Prof. Dipl.-Ing. Dr.,** Graz University of Technology, Institute of Solid State Physics, Petersgasse 16, 8010 Graz, Austria

Table 1. List of correlated color temperatures (CCT), color rendering indices (CRI) and lumen efficacies (η) for different light sources (adapted from *Figueiro et al. 2006*)

Light Source	CCT [K]	CRI	η [lm/W]
Incandescent bulb	2800	100	12
Ceramic metal halide	4100	93	90
Phosphor converted LED	4000	90	94
'Full-spectrum' fluorescent	5500	88	55
RE80 fluorescent	3500	81	89
Cool White fluorescent	4000	62	55
High pressure sodium	2000	16	119

One essential parameter for the quality of a general lighting source is the *Color Rendering Index* (CRI). This index reflects the ability of the light source output to render the true colors of a physical object. The CRI varies between 0 and 100, whereupon 100 means total rendering of all colors. This is achieved if the light source has the same color rendering as the black body source with the same nominal *color temperature* (CT, given in units of Kelvin [K]). By convention, all black body emitters have a CRI of 100. This makes sense, considering that the sun's radiation (not taking atmospheric contributions into account) is close to a black body radiation of 5777 K. For indoor illumination CRI values larger than 90 are required.

Up to know it was generally accepted that high efficiencies involve low CRI values and vice versa. One of the prime examples are sodium gas discharge lamps which provide high lumen efficacies but very low CRI values, respectively (compare to Table 1). Hence, LED technology stands for a quite new understanding of providing high CRI values with high efficiencies and high lifetimes.

Another quantity which plays an important role in dynamic lighting systems is the CT which is the temperature of a Planckian black body radiator. Unlike the CT, the *correlated color temperature* (CCT) of a white light source is "*the color temperature corresponding to the point on the Planckian locus which is nearest to the point representing the chromaticity of the illuminant considered, on an agreed uniform-chromaticity-scale diagram*" (*Schanda and Dányi 1977*).

Tuning the CT of classic white light sources, results in spectral changes of the emitted light. Due to that fact, the CRI value changes by changing the CT. As a result, high quality dynamic lighting systems have to provide high CRI values over the whole tunable CT region. Table 1 lists CRI values, CCT, as well as the lumen efficacies for several light sources. One can see that the listed parameters for the ceramic metal halide light source are in the range of the phosphor converted LED however, the picture changes completely if one looks closer into the advantages/disadvantages of these two technologies. Phosphor converted LEDs have significant longer lifetimes (over 50 000 hours compared to around 10 000 hours for ceramic metal halide (*GE Lighting 2003*)). Ceramic metal halide light sources suffer from poor lifetime color stability (±200 K (Philips *1996*)) compared to the highly defined CT of phosphor converted LEDs. Furthermore phosphor converted LEDs provide high efficacies (more than 100 lm/W) together with high CRI values (above 90) over the tunable CT region (2700 K–6500 K).

2.1 White light generation

There are two general approaches to generate white light. One technique is by additive mixing of two or more colors from different light sources, alternatively wavelength converters allow to modify spectra in a way that white light is emitted. Figure 1 summarizes the different approaches for white light generation (adapted from *Schubert 2006b*).

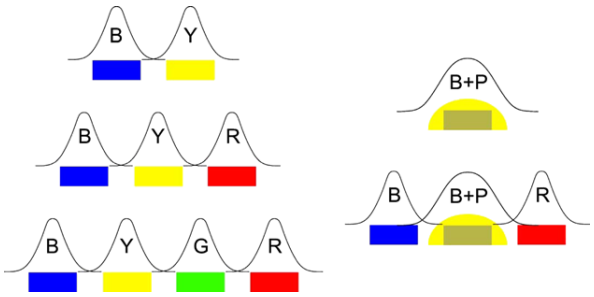

Fig. 1. Approaches to generate white light (blue (*B*), yellow (*Y*), green (*G*), red (*R*), phosphor (*P*)). *Left*: Additive color mixing of different LEDs emitting in two or more visible wavelength regions. *Right*: Use of phosphor converters (Adapted from *Schubert 2006b*)

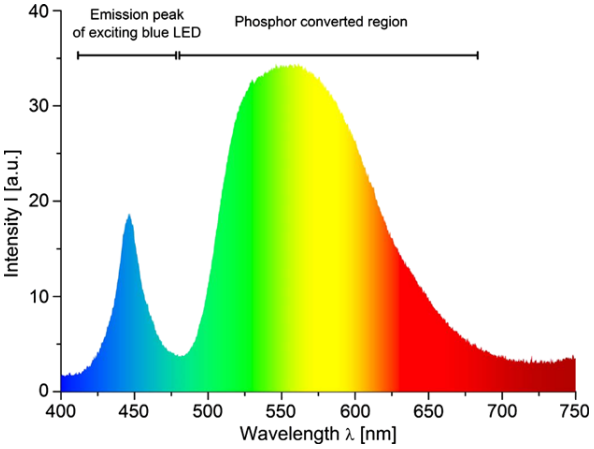

Fig. 2. Spectrum of a phosphor converted LED. The *blue peak* is due to the unconverted light fraction of the exciting blue LED

The approach, illustrated on the right hand side of Fig. 1, occurs via fluorescence. In this case the LED (usually UV or blue LED) excites a phosphor (e.g. Yttrium Aluminum Granat (YAG) doped with rare earth materials) which emits light in a certain visible wavelength range. Figure 2 demonstrates the characteristic spectrum of a phosphor converted LED. The blue peak in the spectrum at approximately 450 nm occurs due to the unconverted light fraction of the exciting blue LED.

Combining a phosphor converted LED with red and blue LEDs allows on the one hand to achieve high CRI values and on the other hand to tune the CT over a broad region. Figure 3 shows an example of an LED module combining three blue, six phosphor-converted and eight red LEDs, respectively (LUMITECHs Phosphor Innovation (PI) LED Technology). This setup allows CRI values above 90 over the allocated CT region, from 2700 K till 6500 K. Specifically, to address the appearance of an object, the LED module in Fig. 3 allows, by slightly varying the color composition of the emitting light, to adjust the CRI value of the object and therefore emphasizes the object. The spectral distributions of such an LED module for several CTs are shown in Fig. 4.

In general, the CRI increases with the number of LED sources distributed over the visible spectral range (*Schubert et al. 2006a*). One major benefit, phosphor converted LEDs provide, is the combination of high efficiencies and broadband emission (Fig. 2) which is mainly responsible for the high CRI values compared to multi LED additive mixing.

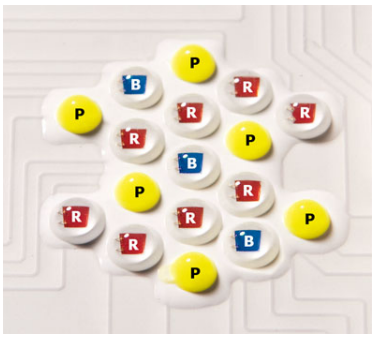

Fig. 3. LED module using six phosphor converted (*P*) LEDs in combination with three blue (*B*) and eight red (*R*) LEDs. This allows tuning the CT from 2700 K to 6500 K and providing a CRI above 90 over the whole tunable CT region (Courtesy of LUMITECH Produktion und Entwicklung GmbH)

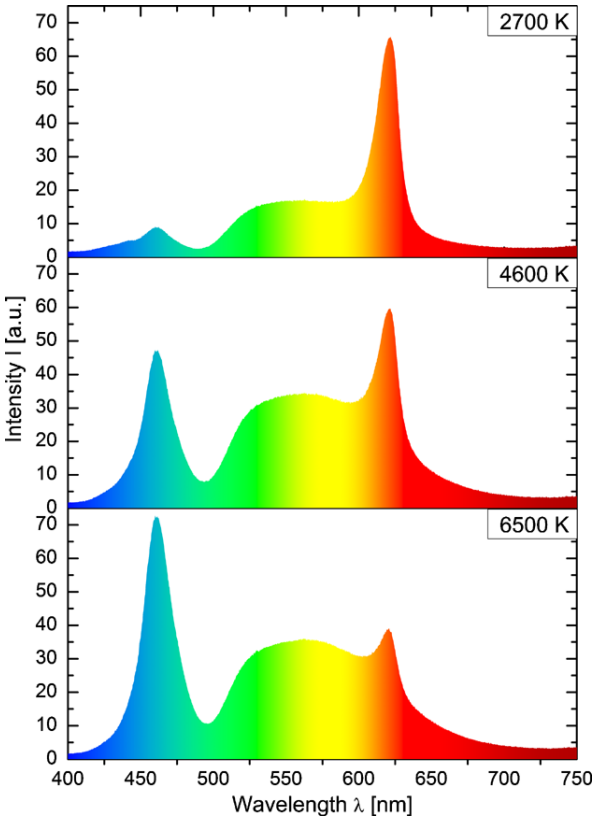

Fig. 4. Emission spectrum of the LED module presented in Fig. 3 for different CTs. For low CTs a significant fraction of the visible spectrum lies in the *red region*, for high CTs the *blue part* of the spectrum is dominant, respectively

3. Natural light quality from dynamic LED light

Light emitted by the sun is essential for life on earth and therefore the standards on artificial lighting systems must be quite high to compete with the natural light quality.

Dynamic lighting systems enable changing individually and continuously illuminance and CT over the day. Therefore, a high quality dynamic lighting system emulates natural light which allows to bring specific natural light conditions, with all its amenities, into buildings.

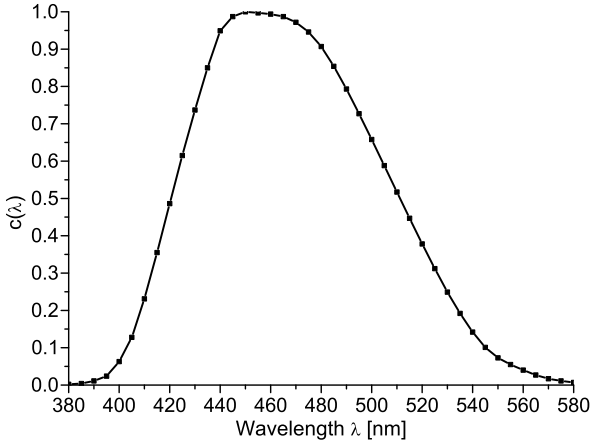

Fig. 5. Action spectrum of the melatonin suppression with respect to wavelength (according to DIN V 5031-100:2009-06)

Hence, the now commonly accepted human biological clock is getting more and more important. The intrinsic period of the biological clock is about 24.2 hours long which is slightly longer than our 24 hour's day. The biological clock synchronizes every day by external "Zeitgeber" which are e.g. social stimulations, sleep behavior and eating habits. However, known so far, light is the most important Zeitgeber which controls the human circadian clock (*Hofstra and Weerd 2008*).

Once light enters the human eye sensor, photons strike light sensitive photoreceptor cells in the retina. The obtained information gets transmitted through the retinal ganglion cells (RCGs) to the human brain. This image-forming visual system contains rod and cone photoreceptor cells. For the *Photopic* vision (color vision) three types of cones (L, M, S), for the *Scotopic* vision (night vision) only one type of rod cells are responsible. Each human eye contains in sum around 6.5 million cones and roughly 120 million rods, respectively (*Cameron and Skofronick 1978*). However, in 2001 Brainard (*Brainard et al. 2001*) and Thapan (*Thapan et al. 2001*) discovered a third type of photoreceptor that regulates the melatonin concentration over the day which is mainly responsible for setting the *circadian rhythm*. This non-image-forming system does not arise from rods or cones. The opsin-like protein melanopsin triggers the non-image-forming visual functions (*Hattar et al. 2002*). The circadian rhythm—also called sleep-wake cycle—controls, amongst others, the hormone level of melatonin and cortisol, the core body temperature, and the heart rate (*Figueiro and Rea 2010* and *Cajochen et al. 2005*). Hence, the circadian rhythm reflects physical properties and defines different chronotypes.

Especially short wavelength light (blue–green) suppresses the hormone melatonin efficiently which leads to a shift of the sleep-wake cycle (*Lockley et al. 2003*). Lockley et al. showed further, that exposure to light, using a monochromatic light source with a wavelength of 460 nm (linewidth (FWHM) = 10 nm), results in a phase delay of about 3 hours, compared to a phase shift of about 1.7 hours for 555 nm, respectively. The sensitivity spectrum for the melatonin suppression is illustrated in Fig. 5 (following DIN V 5031-100:2009-06); the peak maximum of this sensitivity curve is between 445 and 465 nm. As a result, polychromatic light sources offering a high CCT (e.g. 6500 K) show a significant stronger impact on the melatonin suppression than light sources with lower CCT values (e.g. 3000 K) (*Morita and Tokura 1996*). The quantity which expresses the influence of the light source on the biological clock, concerning the

melatonin suppression, is given by the circadian action parameter a_{cv} (Eq. (1), according to DIN V 5031-100:2009-06).

$$a_{cv} = \frac{\int_{\lambda_1}^{\lambda_2} X(\lambda)c(\lambda)d\lambda}{\int_{380\ nm}^{780\ nm} X(\lambda)V(\lambda)d\lambda} \tag{1}$$

The remaining question at this point is, by what means does the melatonin suppression influence the actual living situation? *Cajochen* (*2007*) showed a positive linear correlation between the subjective alertness and the suppression of melatonin. Suppressing the melatonin concentration results in less tiredness and therefore, in higher alertness ratings. Further, daytime exposure to bright light showed a significant decrease of sleepiness (*Phipps-Nelson et al. 2003*).

Especially for shift and late night workers dynamic lighting can help to get rid of sleep problems, fatigue and deactivation. A study from 2007 revealed that an increase of the CCT of general illumination systems in offices from 2900 K to 17000 K, leads to higher concentration and alertness of office workers. On the other hand the fatigue as well as the sleepiness decreased. Essentially, the subjective work performance of the office workers increased by 19.4 % (*Mills et al. 2007*).

Recent studies showed that dynamic lighting systems improve the performance of high school students (*Barkmann et al. 2012*). Appropriate use of different lighting programs with CCT ranges from 3800 K to 11000 K in class rooms lead to a positive effect regarding reading speeds and error reduction in concentration tests.

Other fields where light plays an important role are health care facilities and hospitals. Studies pointed out that artificial daylight illumination significantly improves the well-being and the life quality of elderly people in health care facilities (*Bieske et al. 2006* and *Sust et al. 2012*). Residents show better vitality and orientation and claimed to have a better sleep quality by applying dynamic lighting systems in common social environments (e.g. living room). Sust et al. also indicated that the residents of health care facilities start to communicate more in such environments.

Knowing this, the consequences of light on the physical and on the psychological system of the human body have to be considered by applying light designs, including variable light sequences, for offices, medical and health care facilities as well as homes.

4. Challenges for white light sources

High standards for dynamic lighting systems are required when emulating the changing day light situations. Light sources should possess a broad tunable CT region as well as high CRI values over this range. In addition, modern light sources have to provide high efficiencies especially for general lighting applications. Leading edge LED technology is capable to satisfy such high requirements.

One key parameter for the performance of LEDs is the device temperature, more specifically, the *junction temperature* (JT) of the active region. The consequences of high JT are reduced light output (efficiency), shifts of the emission spectra, light degradation as well as device lifetime shortening. Non-radiative recombinations and the peculiar temperature behavior of resistances in the equivalent circuit of the device increase the JT.

The aim is to derive the JT of individual LEDs in assembled light engine modules. Since a direct measurement of the JT is not possible we are studying the behavior of the different static and dynamic driving parameters (e.g. forward voltage, energy gap, etc.) to obtain the JT.

The theoretical background of the temperature dependence of the forward voltage can be obtained from Shockley equation

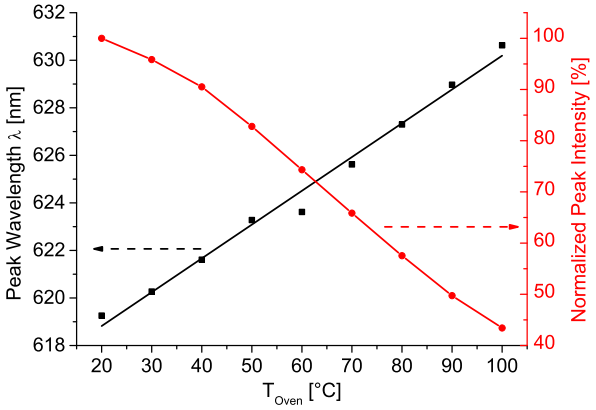

Fig. 6. Peak wavelength shift and light output drop with respect to device temperature. The red emitting AlGaInP LED was operated with a 20 mA pulse current (pulse width = 500 ns, repetition time = 500 µs)

(Eq. (2)) (following Xi et al. *2005a*, *2005b*, and *Xi and Schubert 2004*)

$$J_f = J_s\left(e^{eV_f/nkT} - 1\right) \tag{2}$$

Where J_f expresses the diode current in forward direction, J_S the saturation current, V_f the forward voltage, n the diode ideality factor, k the Boltzmann constant, e the elementary charge, and T the absolute temperature. For $V_f \gg kT/e$, the derivative regarding temperature from Eq. (2) leads to Eq. (3).

$$\frac{d}{dT}V_f = \frac{d}{dT}\left[\frac{nkT}{e}\ln\left(\frac{J_f}{J_s}\right)\right] \tag{3}$$

The saturation current J_S (Eq. (4)) can be expressed in terms of the intrinsic carrier concentration n_i, the diffusion constants of electrons D_n and holes D_p, the minority carrier lifetimes of electrons τ_n and holes τ_p as well as the donor density N_D and the acceptor density N_A, respectively.

$$J_S = e\left[\sqrt{\frac{D_n}{\tau_n}}\frac{n_i^2}{N_D} + \sqrt{\frac{D_p}{\tau_p}}\frac{n_i^2}{N_A}\right] \tag{4}$$

Taking into account the temperature dependence of the diffusion constants of electrons and holes ($D \propto T^{-1/2}$), the effective density of states at the valence and conduction band edge ($N_{C,V} \propto T^{3/2}$), the band gap energies as well as the lifetimes of electrons and holes lead to Eq. (5):

$$\frac{d}{dT}V_f = \frac{eV_f - E_G}{eT} + \frac{1}{e}\frac{d}{dT}E_G - \frac{3k}{e} \tag{5}$$

This relationship reflects the fundamental temperature dependence of the forward voltage. It is the starting point in order to characterize the JT of a pn-junction.

The measurements of the emission spectra and the driving parameters were performed in thermodynamic equilibrium in a chamber furnace with precise temperature control. To probe the LED device it must be driven in a manner that there is a negligible temperature increase due to the driving power. Therefore, the LED device is operated with a current which is generated by voltage pulses with a very small duty cycle (0.1 %, pulse width = 500 ns, repetition time = 500 µs). Consequently, we can assume that the measured oven temperature is equal to the JT.

Figure 6 shows the behavior of the peak emission wavelength as well as the reduction of the light output with respect to temperature

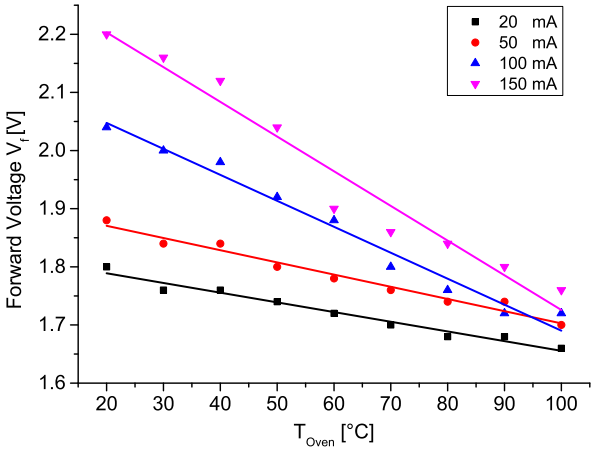

Fig. 7. Forward voltage dependence of a red light emitting AlGaInP LED with respect to temperature for different pulsed injection currents (pulse width = 500 ns, repetition time = 500 µs)

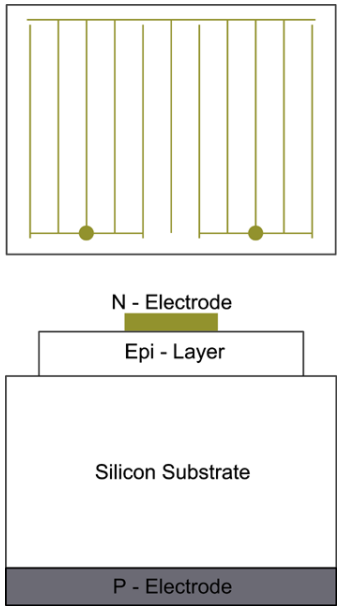

Fig. 8. Device geometry (*bottom view*) and electrode (*top view*) of the measured AlGaInP LED chip

of a red light emitting AlGaInP LED. The LED was operated with a pulsed injection current of 20 mA. The induced temperature mean peak wavelength shift is 0.14 nm/K, the reduction of the light output is 0.7 %/K, respectively. Figure 7 indicates the behavior of the forward voltage with respect to the oven temperature for four different pulsed injection currents (20 mA, 50 mA, 100 mA, 150 mA). The voltage drop lies between −1.67 mV/K (20 mA) and −5.97 mV/K (150 mA), respectively. The device geometry (bottom view) and the electrode (top view) of the measured red light emitting AlGaInP LED are illustrated in Fig. 8 (chip size 1066 µm × 1066 µm, chip thickness 225 µm).

To determine the actual JT during operation, rather than pulsed current, the device is driven with constant current until the thermodynamic equilibrium is reached. Measuring of the forward voltage during operation (in thermodynamic equilibrium) and the combination of the temperature behavior of the forward voltage obtained out of Fig. 7, lead to the actual JT of the device.

5. Conclusion and outlook

LED based modern light engines are highly efficient and provide long lifetimes above 50.000 hours. They offer to change the CT individually and are dimmable without changing the spectral distribution. Variable white lighting systems have a significant positive effect on health, wellbeing, performance, and satisfaction of humans in the working as well as in the private environment.

To harvest all the mentioned advantages, the thermal management of LED devices must be totally under control. Although many research groups worldwide have investigated temperature effects and their impact on the LED performance, a number of influences of the JT on the device characteristics are still not well understood. Particularly the impact of internal resistances and other parameters on the electric as well as optical properties of LED devices must be investigated thoroughly. In cases where the white light production is realized via phosphor converted LEDs, the influence of the device temperature on the phosphor performance must be examined as well. Luminescence quenching and degradation effects as well as spectral changes of the light emission as a consequence of thermal power produced by the junction, has to be studied and modeled.

In summary, the understanding of such temperature effects is a prerequisite to provide light engines delivering high efficiencies, long lifetimes as well as high quality light in terms of high CRI values and tunable CT.

References

Barkmann, C., Wessolowski, N., Schulte-Markwort, M. (2012): Applicability and efficacy of variable light in schools. Physiol. Behav., 105(3), 621–627.

Bieske, K., Gall, D., Vandahl, C., Dierbach, O. (2006): Influence of artificial daylight on gerontopsychiatric care of elderly people. In CIE 2cd expert symposium on light and health, CIEx 031:2006, 7.-8.9. Ottawa.

Brainard, G. C., Hanifin, J. P., Greeson, J. M., Byrne, B., Glickman, G., Gerner, E., Rollag, M. D. (2001): Action spectrum for melatonin regulation in humans: evidence for a novel circadian photoreceptor. J. Neurosci., 21(16), 6405–6412.

Braunstein, R. (1955): Radiative transitions in semiconductors. Phys. Rev., 99(6), 1892–1893.

Cajochen, C. (2007): Alerting effects of light. Sleep Med. Rev., 11(6), 453–464.

Cajochen, C., Munch, M., Kobialka, S., Krauchi, K., Steiner, R., Oelhafen, P., Orgul, S., Wirz-Justice, A. (2005): High sensitivity of human melatonin, alertness, thermoregulation, and heart rate to short wavelength light. J. Clin. Endocrinol. Metab., 90(3), 1311–1316.

Cameron, J. R., Skofronick, J. G. (1978): Medical physics (pp. 337–384). New York: Wiley.

Figueiro, M. G., Rea, M. S. (2010): The effects of red and blue lights on circadian variations in cortisol, alpha amylase, and melatonin. Int. J. Endocrinol., 2010, 829351.

Figueiro, M. G., Appleman, K., Bullough, J. D., Rea, M. S. (2006): A discussion of recommended standards for lighting in the newborn intensive care unit. J. Perinatol., 26, 19–26.

GE Lighting (2003). CMH single ended G8.5 product information for OEMs. General Electric Company. Ver. 1.0.

Haitz, R., Tsao, J. Y. (2011): Solid-state lighting: 'The case' 10 years after and future prospects. Phys. Status Solidi, a Appl. Mater. Sci., 208(1), 17–29.

Hattar, S., Liao, H. W., Takao, M., Berson, D. M., Yau, K. W. (2002): Melanopsin-containing retinal. ganglion cells: architecture, projections, and intrinsic photosensitivity. Science, 295(5557), 1065–1070.

Hofstra, W. A., Weerd, A. W. D. (2008): How to assess circadian rhythm in humans: a review of literature. Epilepsy Behav., 13(3), 438–444.

Holonyak, N., Bevacqua, S. F. (1962): Coherent (visible) light emission from $Ga(As_{1-x}P_x)$ junctions. Appl. Phys. Lett., 1(4), 82–83.

Lockley, S. W., Brainard, G. C., Czeisler, C. A. (2003): High sensitivity of the human circadian melatonin rhythm to resetting by short wavelength light. J. Clin. Endocrinol. Metab., 88(9), 4502–4505.

Mills, P. R., Tomkins, S. C., Schlangen, L. J. (2007): The effect of high correlated colour temperature office lighting on employee wellbeing and work performance. J. Circadian Rhythms, 5(2).

Morita, T., Tokura, H. (1996): Effects of lights of different color temperature on the nocturnal changes in core temperature and melatonin in humans. Appl. Hum. Sci., 15(5), 243–246.

Philips (2012): Lamp Description MasterColor® CDM ED28 standard.

Phipps-Nelson, J., Redman, J. R., Dijk, D. J., Rajaratnam, S. M. W. (2003): Daytime exposure to bright light, as compared to dim light, decreases sleepiness and improves psychomotor vigilance performance. Sleep, 26(6), 695–700.

Pimputkar, S., Speck, J. S., DenBaars, S. P., Nakamura, S. (2009): Prospects for LED lighting. Nat. Photonics, 3(4), 180–182.

Round, H. J. (1907): A note on carborundum. Electr. World, 19, 309.

Schanda, J., Dányi, M. (1977): Correlated color temperature calculations in the CIE 1976 chromaticity diagramm. Color Res. Appl., 2(4), 161–163.

Schubert, E. F. (2006b): Light-emitting diodes, 2nd ed. (pp. 332–366). Cambridge: Cambridge University Press.

Schubert, E. F., Kim, J. K., Luo, H., Xi, J. Q. (2006a): Solid-state lighting—a benevolent technology. Rep. Prog. Phys., 69(12), 3069–3099.

Steele, R. V. (2007): The story of a new light source. Nat. Photonics, 1(1), 25–26.

Sust, C. A., Dehoff, P., Lang, D., Lorenz, D. (2012): Verbesserte Lebensqualität für demente Bewohner: Das Forschungsprojekt St. Katharina in Wien. Zumtoble Research.

Thapan, K., Arendt, J., Skene, D. J. (2001): An action spectrum for melatonin suppression: evidence for a novel non-rod, non-cone photoreceptor system in humans. J. Physiol., 535(1), 261–267.

Xi, Y., Schubert, E. F. (2004): Junction-temperature measurement in GaN ultraviolet light-emitting diodes using diode forward voltage method. Appl. Phys. Lett., 85(12), 2163–2165.

Xi, Y. G., Gessmann, T., Xi, J. Q., Kim, J. K., Shah, J. M., Schubert, E. F. (2005a): Junction temperature in ultraviolet light-emitting diodes. Jpn. J. Appl. Phys., 44(10), 7260–7266.

Xi, Y., Xi, J. Q., Gessmann, T., Shah, J. M., Kim, J. K., Schubert, E. F., Fischer, A. J., Crawford, M. H., Bogart, K. H. A., Allerman, A. A. (2005b): Junction and carrier temperature measurements in deep-ultraviolet light-emitting diodes using three different methods. Appl. Phys. Lett., 86(3), 031907.

Authors

Reinhold Hetzel
was born in Austria in 1986. Studying for one year in Georgia, USA, he obtained his M.Sc. in Physics (2011) from the Graz University of Technology, Austria. He currently pursues his Ph.D. in the group of Prof. Günther Leising (Institute of Solid State Physics, Graz University of Technology) in cooperation with LUMITECH Produktion und Entwicklung GmbH, where he focuses on the improvement of optical and electrical properties of light engines containing light emitting diodes.

Stefan Tasch
was born in Austria 1968. Physicist, Ph.D. in Solid State Physics, Organic Optoelectronic Devices. Scientific assistant and teacher for Solid State Physics at the Graz University of Technology, Austria. Together with Prof. G. Leising founder of the White-LED technology and manufacturing in Austria (LUMITECH, 1997). Research periods at the Case Western Reserve University Cleveland (USA), University of California at Santa Barbara (USA) and University of Potsdam (Germany). Author of over 75 scientific publications and inventor of 90 registered patents. He was co-founder and managing director of LUMITECH Produktion & Entwicklung, Tridonic Jennersdorf (former Tridonic Optoelectronics) and Lexedis Lighting. Viktor Kaplan medal (2002). Austrian Innovation Award 2007 (LUMITECH). Six Sigma Black Belt Champion. Since 2010 CEO of the LUMITECH Holding.

Günther Leising
was born in Austria in 1952. Physicist, Ph.D. and habilitation in Solid State Physics. Visiting professorships in Nantes, Paderborn, Cambridge, Santa Barbara. Fritz Kohlrausch Award (1988); Viktor Kaplan medal (2002). Since 1995 Univ.-Prof. at the Institute of Solid State Physics (Graz University of Technology, Austria) for experimental Solid State Physics. Author of over 650 scientific publications; 13 patents. Research and teaching in photophysics, nanotechnology and the physics and chemistry of advanced materials. Founder of the White-LED technology and manufacturing in Austria together with Dr. Stefan Tasch (LUMITECH, 1997). Founder and director of the Institute of Nanostructured Materials and Photonics, Joanneum Research (1999–2007). Senior Vice President Technology of AT&S (2000–2005). Austrian Innovation Award 2007 (LUMITECH). Innovation and Business Angel for new technologies.

Spectral Behavior and Coherence Length of GaN-, and AlGaInP-based Light-Emitting-Diodes

R. Hetzel*[a,b] and G. Leising[a]
[a]Graz University of Technology, Petersgasse 16, 8010 Graz Austria, [b]Lumitech Produktions und Entwicklungs GmbH, Technologiepark 10, Jennersdorf, Austria

ABSTRACT

The coherence length of electromagnetic waves created by different light sources is a largely overlooked parameter. Since the coherence length and its spectral distribution are essential for the entire field of interference, ranging from unintended destructive and constructive pattern to intended interference determining the nature of structural colors. We studied the spectral emission behaviour of GaN- and AlGaInP-based Light-Emitting-Diodes (LED) under thermodynamic equilibrium conditions driven by direct current as well as by short current pulses (500 ns) in the temperature range from 4.2 to 390 Kelvin. The coherence length under the different driving conditions was measured via a Fabry-Perot interference setup. We discuss the validity and limitations of the conventional determination method from the emission linewidth and lineshape. Besides the distinct shifts of the emission wavelength accompanied by significant changes of the full width at half maximum, we found quite high values for the coherence length exceeding 0.15 millimeters for the blue emission and 0.4 millimeters for the red emission at room temperature, respectively. Furthermore this contribution will also discuss the nature and interrelationships of coherence length, emission peak wavelength and the spectral distribution (lineshape and linewidth) of the investigated LEDs.

Keywords: Junction temperature, light emitting diodes, coherence length, GaN, AlGaInP, spectral behavior

1. INTRODUCTION

The nature and quality of artificial lighting are becoming more and more recognized and debated issues concerning their impact on comfort, well-being and even human's health (chronobiology). So general lighting has to fulfill this demand towards an integral understanding of sustainability with high quality light sources. Recent insights into the non-visual imaging system of the human eye brought forward the fundamental importance of the now commonly accepted biological clock. Light is the most important parameter which influences the circadian rhythm and controls hormone levels of melatonin and cortisol[1]. Light emitting diodes (LEDs) are the first kinds of light sources which allow tuning the color temperature of white light and still maintaining high color quality in terms of color rendering. Tunable white light engines which provide changing color temperature open new dimensions in terms of human comfort and health. Furthermore, LEDs have sufficient potential to reduce significantly the energy consumption in the general lighting application. Much longer lifetimes and higher efficiencies make incandescent as well as fluorescent lighting systems becoming a dying segment[2].

However, intense discussions are going on regarding the total energy consumption (footprint) of LEDs in comparison to conventional lighting systems. The life cycle of LEDs is a highly debated issue, due to the fact that the world occurrence of used resources may diminish in the future. Additionally, transport costs, manufacturing efforts, as well as the use of certain raw materials are always confronted with the gained energy reduction in solid state lighting systems[3].

This paper focuses on LEDs which are assigned to white light engines with tunable white light. However, the circumstance that the color temperature is controllable throughout operation leads to the enormous problem that driving parameters change as well, which leads to undesirable variations of the pn-junction temperature (JT). Such temperature variations reduce the lifetime and the efficiency of the LEDs. Additionally, high temperatures of a single LED device heat up the whole luminaire and therefore, the driver electronic, which is usually mounted closely to the LED module, gets affected by this dissipated heat. This produced heat in the driver electronics leads to a failure of the electronics which is a highest ranked reason that LED systems totally fail[4].

*reinhold.hetzel@tugraz.at; phone +43 316 873-8477; fax +43 316 873-8466; if.tugraz.at

Light-Emitting Diodes: Materials, Devices, and Applications for Solid State Lighting XVIII, edited by Klaus P. Streubel, Heonsu Jeon, Li-Wei Tu, Martin Strassburg, Proc. of SPIE Vol. 9003, 900318

Therefore, understanding the behavior of the JT and its monitoring and tuning is a prerequisite to design and operate light engines with long lifetimes as well as high efficacies.

In our paper we present an experimental setup which allows to determine the JT of GaN- and AlGaInP-based LEDs in a temperature range between 230 K and 400 K very accurately. Especially GaN LEDs play a dominant role in white light engines due to the fact that they are implemented as primary emitter and excitation source for phosphor conversion materials. Out of the actual JT of the device we can study the influence of several driving parameters (pulse width modulation (PWM) as well as direct current injection (DC)) on the temperature throughout operation. We also examine the coherence properties of LEDs which offers us details about the ongoing radiative recombination process and provides a deeper knowledge of the nature of the electron-hole recombination process. Further we present low temperature measurements at 4.2 K and 77 K which allow investigating the interaction of charge carriers with quasiparticles like excitons and phonons.

1.1 Junction temperature determination methods

Thermo resistances (e.g. PT 100), thermocouples, or diodes are sensing devices which allow measuring the temperature with high accuracy. The difficulty of such methods is that depending where the sensing element is located and mounted, rather the environmental temperature than the actual JT is measured. Hence the obtained temperature value is not equal to the JT due to the fact of a non-thermal equilibrium of the device environment and the die.

A very common and comfortable instrument for thermal measurements and heat flow determinations are infra-red (IR) cameras. They are based on the fact that each object, which exhibits a temperature higher than 0 K, emits IR radiation in a certain wavelength range which follows Planck's radiation law. Advantages of IR cameras are that the temperature can be probed without any contact between the sample and the measurement system. Further, due to the fast picture processing time, thermal images can be taken basically in real time and therefore fast temperature changes of the device can be followed.

However, generally IR cameras can be set to only one emission coefficient; hence variations of different emission coefficients of the measured materials lead to wrong indicated temperature values. Therefore, each pixel of the IR image has to be calibrated regarding the emission coefficients. Moreover, imaging an LED covered with the generally used globe top leads to the problem that the IR radiation measured by the camera is strongly altered by the characteristic IR absorptions of the globe top hydrocarbon/silicon polymer. The specific transmission properties (complicated by the anharmonic vibrational behavior of the polymer hydrocarbons, overtones, combined resonances, etc.) of the globe top solid have to be taken into account. Figure 1 shows the IR absorption spectra of a transparent globe top material (two compound (ratio 1:1) silicon rubber) on a silicon substrate including black body radiation curves for three common LED JTs. The x-axis in figure 1 indicates the detection range of an amorphous silicon detector (19200 pixels, 25 µm x 25 µm per pixel; IR camera: Optris Pi160). Most of the emitted IR radiation gets absorbed in the transparent globe top, which implies that no direct conclusion of the actual JT can be drawn out of the characteristic IR emission behavior. Moreover, if no globe top material is used, at best the surface temperature instead of the actual JT of the die can be determined.

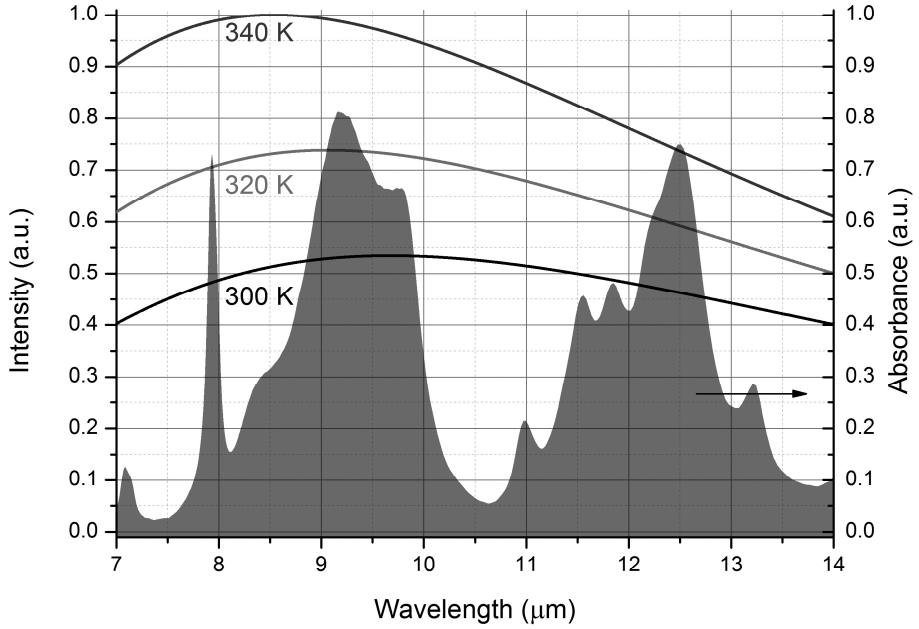

Figure 1: Comparison of black body radiation and absorbance spectra of a silicon hydrocarbon polymer used as glob top material in the detection range of an amorphous silicon IR detector.

2. EXPERIMENTAL SETUP

To investigate the emission as well as the voltage/current behavior of the LEDs in the temperature range between 230 K and 400 K the measurements were carried out in a temperature controlled oven (figure 2). To ensure thermodynamic equilibrium the samples were stored for at least 30 minutes in the chamber (Weiss–Vötsch VT4002) before characterization was performed. The temperature accuracy of the oven was 0.1 K; an additional PT 100 thermo resistance was installed on a separate aluminum heat sink to ensure the preset oven temperature. The whole chamber was purged with dry air to avoid icing effects. To ensure that the injection current does not increase the temperature of the junction during operation, the LED samples were operated with very short forward voltage pulses with a small duty cycle (0.1%, pulse width = 500 ns, repetition time = 500 μs). Consequently we can assume that the preset temperature of the oven equals the JT of the device. The forward voltage pulses were produced with a pulse generator (HP 214 B); using a 20 Ω series resistance the forward current of the device was determined. The voltage pulses were logged with a digital oscilloscope (Hameg HMO 3524). The DC current-voltage characteristics were recorded with a Keithley 2601B source measure unit.

A CCD spectrometer containing a 1200 lines/mm grid blazed at 500 nm (Thorlabs CCS 100) was used to record the emission spectra of the LEDs. In front of the input slit of the fiber optics input side an aperture with an acceptance angle of 5.72° was inserted.

The wavelength calibration was done with a mercury argon lamp (LSP035 LOT Oriel Group). For each recorded spectrum the corresponding dark current was recorded and subtracted. The intensity calibration (spectrometer including fiber optics and aperture) was performed with a tungsten lamp standard. The linearity of the CCD array of the spectrometer was calibrated by comparing the transmission spectra of optical density filters measured with the CCD spectrometer and an UV/VIS spectrometer (Shimadzu UV/VIS 1800). 10 filters with a transmission between 2% and 95% (at 460 nm) were used for linearity investigation. The calibration leads to the result that the photometric linearity is valid in the range between 5% and 90% of the total available measurement range.

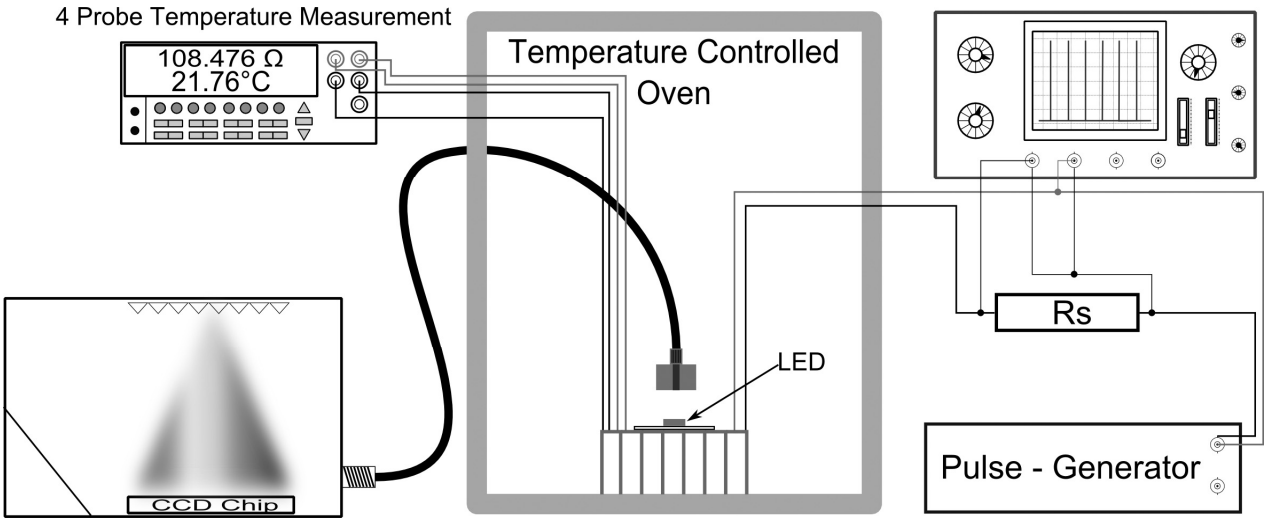

Figure 2: Setup for determining the JT in the temperature range between 230 K and 400 K.

2.1 Low temperature measurements

To gain insight into the emission processes occurring in LEDs the samples were characterized at very low temperatures of 4.2 K and 77 K. To ensure thermodynamic equilibrium at such low temperatures the LEDs were dipped into a bath of liquid helium (4.2 K) or liquid nitrogen (77 K). Hence the JT of the LED was preset. To record the emission in the liquid bath environment a 4 m long waveguide (Newport F-MLD, 100 µm core diameter, 140 µm cladding diameter NA = 0.290) was used. As elaborated above, the spectrometer including the waveguide was calibrated regarding the wavelength and intensity axis. To couple the fiber optics to the LED chip during the measurement, transparent glue was used on top of the LED as well as on the fiber optics. Photoluminescence excitation/emission measurements of the glue were carried out to certify that the recorded emission spectra do not get influenced by the glue. Moreover we confirmed that the shape as well as the peak position of the LEDs is independent of the sample position relative to the detector. We did not observe any preferred polarization direction of the emitted light.

2.2 Coherence length investigation

For coherence length investigations a self-made Fabry Perot Interferometer (FPI) was coupled with a closed cycle cryostat (figure 3). The LEDs were mounted on a copper plate using thermal conduction paste and electrically contacted with a 30 µm thick Au bonding wire. The samples were located in the focal point of a collecting lense (f = 50 mm) which created a parallel beam for the use of the FPI investigations. A variable aperture in front as well as a fixed aperture behind the FPI (diameter 1 mm, length 10 mm) were used for beam collimation. Two different kinds of high reflecting mirrors were used depending whether the red emitting LED (AlGaInP) or the blue emitting LED (GaN) was investigated (inserts in figure 7 and figure 8 show the reflectivity in respect to wavelength of the used mirrors). The emission spectra were recorded with a spectrometer containing a 2400 l/mm grid blazed at 250 nm. The vacuum in the closed cycle cryostat (Model 20/70 Crygenic Technology) was 10-6 mbar throughout all measurements; the temperature was checked with a silicon diode mounted closely to the sample holder.

2.3 Samples and diode mounting

The LED dice on a sapphire (AlO_3) substrate were mounted with thermally conducting paste on an aluminum heat sink (dimensions 5.0 mm x 6.3 mm x 4.8 mm). With a thin 30 µm Au bonding wire the devices were connected to a printed circuit board. To investigate the structure as well as the composition of the used samples focused ion beam (FIB) and electron disperse x-ray spectroscopy (EDX) measurements were performed. The dimension of the blue emitting GaN LED is 500 µm x 1000 µm with an overall thickness (substrate and semiconductor) of 150 µm whereas the active layer

consists out of a 8 µm thick GaN layer followed by a 150 nm thick AlN based p-type layer. The red emitting AlGaInP LEDs are grown on an AlO_3 substrate whereas a 2.5 µm AlInP layer follows a 9.5 µm thick GaP based layer. The device dimensions are 300 µm x 300 µm with an overall thickness of 100 µm. Both types of LEDs were covered with a SiOx passivation layer.

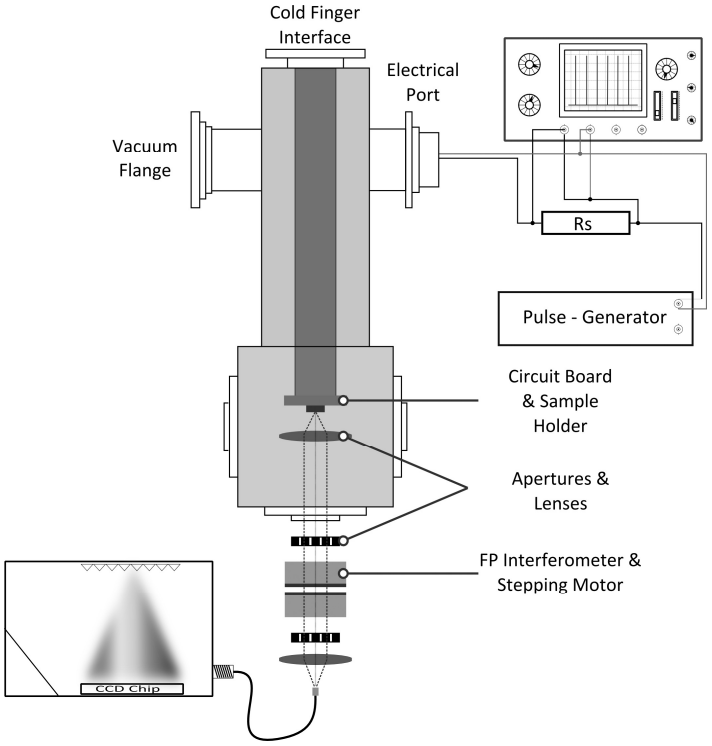

Figure 3: Setup of the closed cycle cryostat in combination with an FPI for coherence length investigations.

3. RESULTS

Figure 4 shows the behavior of the energy gap of a blue emitting GaN LED with respect to the pulsed injection current in the temperature range between 230 K and 400 K. The band gap energy E_g was extracted out of the peak energy E_p reduced by ½ kT [5]. With increasing temperature a shift of the peak to lower energy levels occurs. This red shift is designated to the reduction of the band gap energy with increasing temperatures[6]. Due to the applied small voltage pulses the current induced temperature increase can be neglected. Notable is the blue shift (shift to higher energies) of the band gap energy with increasing injection current. The reason for such behavior can be dedicated to charge carriers of higher confined levels in the quantum well structure which participate to the radiative recombination process. Hence an effective increase of the band gap energy occurs which is the so called band-filling effect[7,8]. This effect especially occurs for higher injection current levels and shows a linear behavior due to the fact that the density of states in the quantum wells increases linearly as well. The band filling effect interplays with the screening of the piezoelectric fields which occurs from the lattice mismatch in GaN LEDs[9,10]. Especially at low temperatures excitons dominate the emission. Those excitons gets polarized by the piezoelectric field, however instead of field ionization of the exciton, the electrons get pulled to the quantum well on the one side, the holes get pulled in the other direction, respectively. Hence the wall of the quantum well prevents the excitons from field ionization. In this constellation the electron and hole are still close together, thus they feel the Coulomb potential. For that reason the exciton can still exist as a particle for a long time, the absorption peak does not get broadened because the exciton is not ionized by the field. Therefore the emission peak gets shifted to a higher wavelength which is assigned to the quantum confined stark effect (QCSE)[11].

Injecting charge carriers rise a field which is acting against the occurring piezoelectric field and this results in a blue shift with respect to the injection current level. Low temperature investigations exhibited that the blue shift at a low current level (< 50 mA) can be assigned to the screening of the piezoelectric field until the potential wells are in a non-zero field condition. For higher current densities the band filling effect gets predominant.

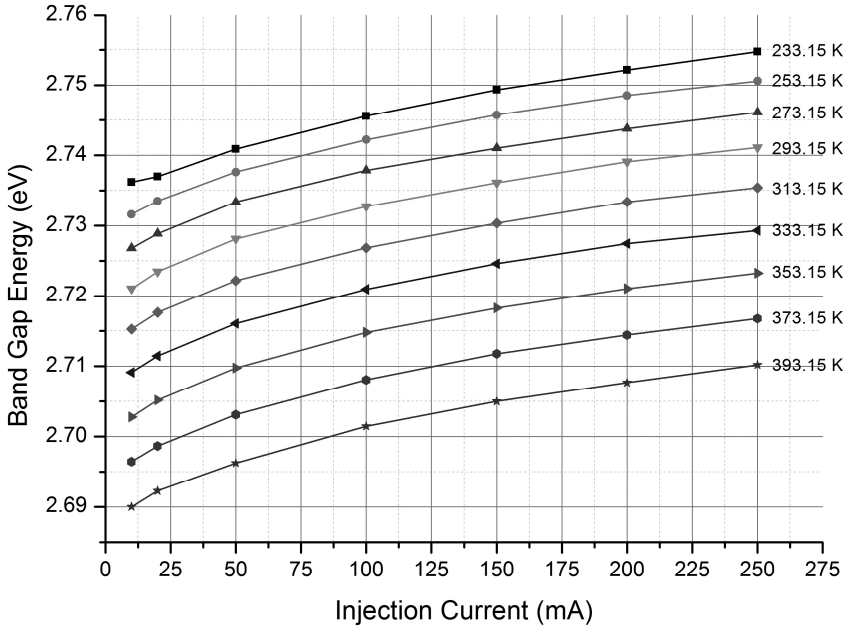

Figure 4: Energy gap behavior for several pulsed injection currents of a GaN blue emitting LED in the range of 230 K and 400 K

The spectral behavior of the red emitting AlGaInP LED in the temperature range between 230 K and 400 K for a forward current pulse height of 50 mA is illustrated in figure 5. The shown spectra are normalized regarding the maximum intensity value. Additionally plotted in figure 5 is the sensitivity curve of the L-cone of the human eye[12]. On top of the efficiency decrease with increasing temperature, due to the shift to higher wavelengths, a decrease of the subjective brightness occurs because the sensitivity of the human eye decreases significantly as well. Plotting the intensity logarithmically allows determining the slope of the high energy wing which can be used for JT determination[13].

Figure 6 shows the behavior of the band gap energy with respect to the JT in the region between 4.2 K and 400 K. Notable is that the energy gap is independent of the level of injection current. Further the peak wavelength behaves linearly for temperature values above 200 K. Therefore, after performing the calibration measurement in the temperature chamber, the peak wavelength behavior and/or the slope of the high energy wing lead to the actual JT of the device during operation (as reported in[14-16]).

The fit model used in figure 6 is obtained out of the data recorded with a 10 mA pulsed current and is given in equation (1)[6] (fit parameter see figure 7), whereas E_g represents the band gap energy, E_0 the energy gap at 0 K, β and γ are the fit parameters and T the JT of the device. The model fits well with the experimental data and implies that, in contrast to our investigated GaN-based LEDs, excitons do not dominate the recombination at low temperatures for the AlGaInP LEDs[17].

$$E_g = E_0 - \left(\frac{\beta \cdot T^2}{T + \gamma} \right) \tag{1}$$

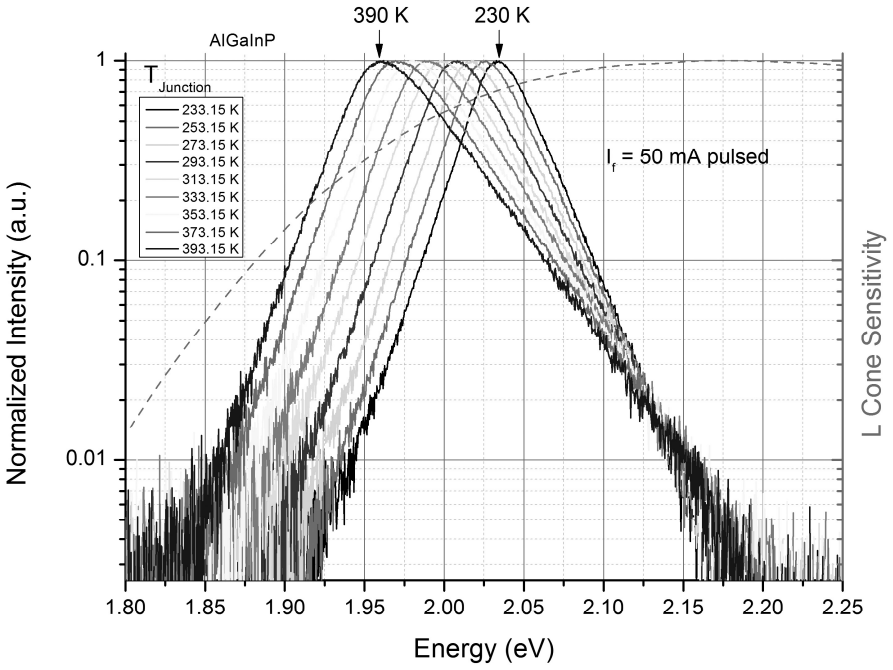

Figure 5: Emission behavior of a red emitting AlGaInP based LED in the temperature range of 230 K and 390 K in comparison to the sensitivity of the L-cone of the human eye.

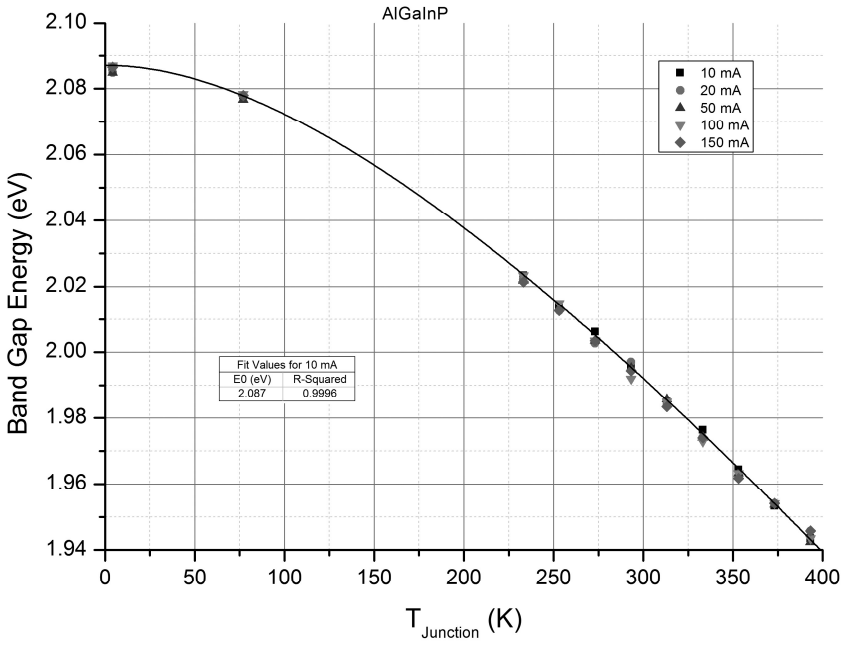

Figure 6: Band gap energy versus junction temperature of an AlGaInP LED.

3.1 Coherence length of GaN and AlGaInP LEDs

LEDs provide attractive possibilities to implement them for holography (e.g. microscopy) due to the specific coherence properties this light source offers. Employing holography allows to construct a 3D-imaging microscope for non-destructive testing and quality control; further by using photorefractive holography the remote investigation of biological tissues is possible[18, 9]. Holography in combination with microscopy makes a quantitative phase contrast for high resolution topography analysis of micro and nano structured surfaces available[19]. However, the nature of coherence of solid state light sources is still not well understood and rarely specified.

Generally the temporal coherence length is defined via of the coherence time (following Ref.[21])

$$l_c = ct_c \tag{2}$$

whereas l_c is the temporal coherence length, t_c the coherence time and c the speed of light, respectively. For a Gaussian spectral distribution the spectral width $\Delta\nu$ and coherence time t_c are related by

$$\Delta\nu = \sqrt{\frac{2\ln 2}{\Pi}}\frac{1}{t_c}. \tag{3}$$

Inserting equation (3) in equation (2) leads to the theoretical description of the coherence length given in equation (4).

$$l_c = \sqrt{\frac{2\ln 2}{\Pi}}\frac{\lambda^2}{\Delta\lambda} \tag{4}$$

Applying equation (4) for determining the coherence length assumes a Gaussian shape of the spectral distribution. Executing equation (4) on our measured emission spectra leads to coherence lengths at room temperature of 17.8 µm for the AlGaInP LEDs and 9.9 µm for the blue emitting GaN LEDs respectively (at 10 mA pulsed current). These results agree very well with previous reported coherence lengths[20]. However, measuring the coherence length with a FPI leads to total different situations. Figure 7 and figure 8 illustrate the interference fringes with respect to the mirror separation for the two types of investigated LEDs. The measurements were performed at room temperature and under DC current injection (10 mA for the GaN LED, 30 mA for the AlGaInP LED). For both types of LEDs we find remarkable coherence lengths which can be obtained directly out of the mirror separation. As shown in figure 7 interference fringes can be still identified at a mirror separation of 260 µm which correspond to a coherence length of at least 0.52 mm. For the red emitting AlGaInP LED interference fringes can be still observed at a mirror separation of 650 µm which corresponds to a coherence length of at least 1.3 mm. These obtained results do not mirror to the coherence length distribution of the light source and therefore cannot be taken as the average coherence length of the wave trains emitted from the LEDs. However the light sources we investigated emit wave trains which fulfill the interference conditions, therefore the LED provides wave trains with such long coherence length in the millimeter and sub millimeter range. Intriguing about these results is that the number of wave trains with such high coherence lengths is obviously high which can be identified out of the amplitudes (constructive / destructive) of the observable interference fringes.

Although LEDs provide a single color (monochromatic) emission pattern (FWHM typically between 10 nm – 20 nm), the theoretical approach shown above to determine the coherence length is not satisfying in this case in comparisons to the gained experimental results.

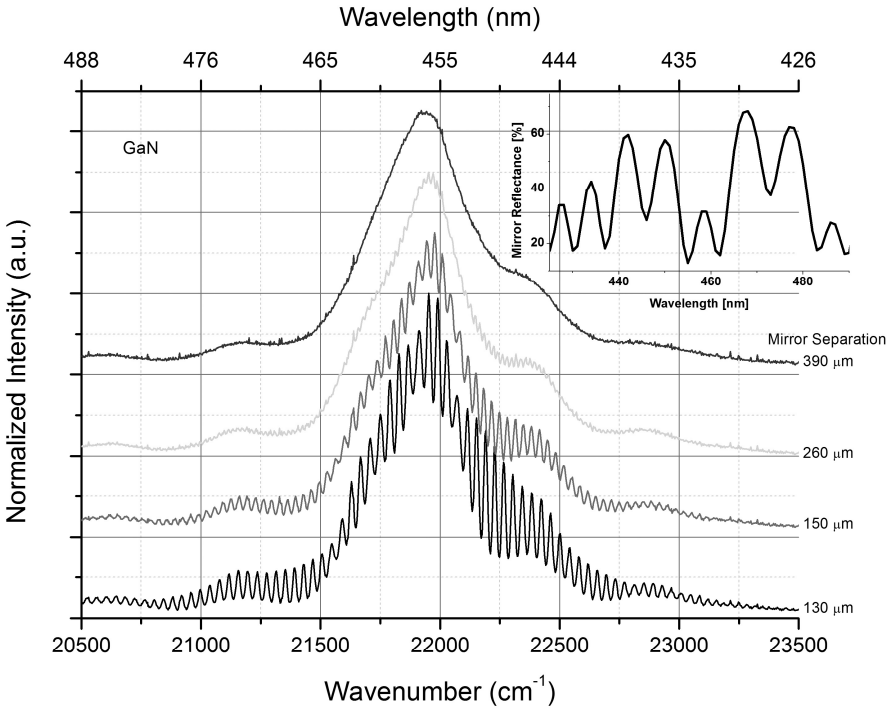

Figure 7: Normalized emission spectra of a GaN LED through a FPI in dependence of the mirror separation. The insert shows the reflectance behavior of the used mirrors in the FPI.

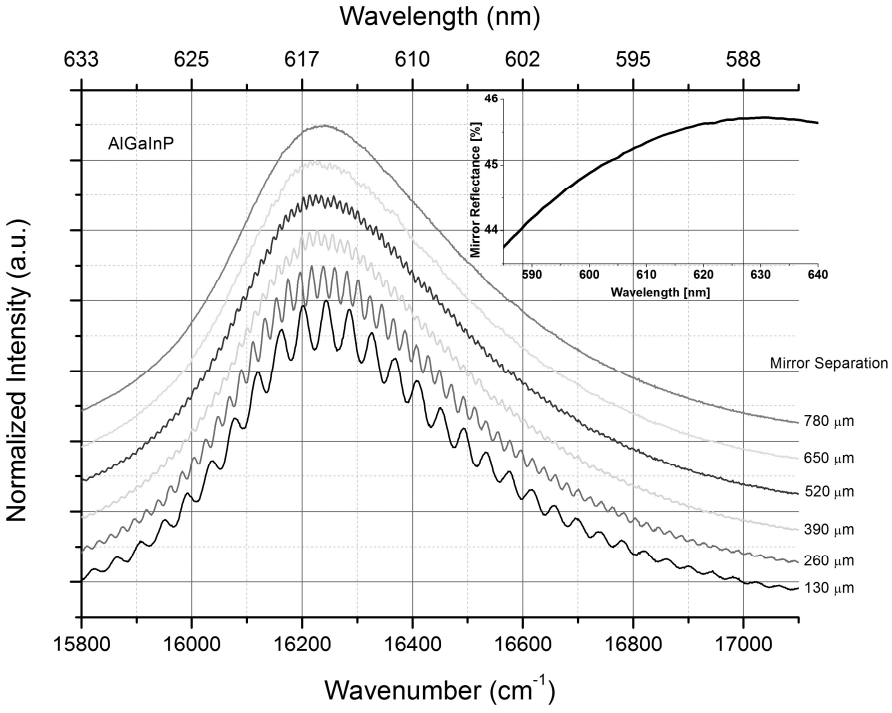

Figure 8: Normalized emission spectra of an AlGaInP LED through a FPI in dependence of the mirror separation. The insert shows the reflectance behavior of the used mirrors in the FPI.

4. CONCLUSION

The presented setup allows to determine the JT of LEDs very accurately. Injecting small voltage pulses leads to emission spectra whereby maintaining thermal dynamic equilibrium. Operating LEDs under DC leads to the fact that the JT of the device immediately changes and therefore a non-thermal equilibrium situation is present. We found that screening of the piezoelectric field as well as the band filling effect are responsible for the blue shift with increasing current injection level for blue emitting GaN LEDs. Low temperature investigations further illustrate that the band filling effect is dominant for the shift at high current levels. On the other hand we found that the band gap energy does not change with increasing current density for the red emitting AlGaInP LEDs. Therefore determining the JT out of the peak wavelength leads to accurate and satisfying results.

Applying of Fabry-Perot interferometry allows to gain insight into the coherence length of the emitted wave trains of LEDs which leads to coherence lengths in the millimeter range for both types of LEDs. We could show that using numerical estimations for calculating coherence length gives misleading results and provides values which are far away from those determined experimentally.

ACKNOWLEDGMENTS

The authors would like to acknowledge LUMITECH Produktions und Entwicklungs GmbH for providing samples as well as the Austrian Research Promotion Agency (FFG) and LUMITECH Produktions und Entwicklungs GmbH for financial support. Further they thank Harald Plank and Sebastian Rauch for FIB and EDX measurements (Institute for Electron Microscopy and Nanoanalysis (FELMI) of Graz University of Technology).

REFERENCES

[1] Hofstra, W. A. and Weerd, A. W. d., “How to assess circadian rhythm in humans: A review of literature,” Epilepsy and Behavior 13, 438-444 (2008).

[2] Hetzel, R., Tasch, S. and Leising, G., “Tunable natural light realized by Phosphor-Innovation Light-Emitting-Diode technology,” e & i 129 (7-8), 460-465 (2012).

[3] US Department of Energy, ”Life-Cycle Assessment of Energy and Environmental Impacts of LED Lighting Products,” Tech Report (2013), 12 November 2013, http://www1.eere.energy.gov/buildings/ssl/tech_reports.html.

[4] Lu, G., Yang, S. and Huang, Y., “Analysis on Failure Modes and Mechanisms of LED,“ Reliability Maintainability and Safety, 2009, ICRMS 2009, 1237 – 1241 (2009).

[5] Schubert, E. F., [Light-Emitting-Diodes], Cambridge University Press, New York, 90 (2006).

[6] Varshni, Y. P., “Temperature dependence of the energy gap in semiconductors,” Physica 34, 149-154 (1967).

[7] Kuroda, T. and Tackeuchi, A., “Influence of free carrier screening on the luminescence energy shift and carrier lifetime of InGaN quantum wells,” J. Appl. Phys. 92 (6), 3071-3074 (2002).

[8] Arnaudov, B., Domanevskii, D. S., Evtimova, S., Ivanov, Ch. and Kakankov, R., “Band filling effect on the light emission spectra of InGaN/GaN quantum wells with highly doped barriers,” Microelectronics Journal 40, 346-348 (2009).

[9] Takeuchi, T., Wetzel, C., Yamaguchi, S., Sakai, H., Amano, H. and Akasaki, I., “Determination of piezoelectric fields in strained GaInN quantum wells using the quantum-confined Stark effect,” Appl. Phys. Lett. 73 (12), 1691-1693 (1998).

[10] Hogg, A. A., Norman, C. E., Shields, A. J. and Pepper, M., "Comparison of spontaneous and piezoelectric polarization in GaN/Al0.65Ga0.35N multi-quantum-well structure," Appl. Phys. Lett. 76 (11), 1428-1430 (2000).

[11] Miller, D. A. B., Chemla, D. S., Damen, T.C., Gossard, A.C., Wiegmann, W., Wood, T. H. and Burrus, C.A., "Electric field dependence of optical absorption near the band gap of quantum-well structures," Physical Review B 32, 1043-1060 (1985).

[12] Color and Vision Research Labs, "Colour & Vision Research laboratory and database," CVRL, http://www.cvrl.org (30 August 2013)

[13] Chhajed, S., Xi, Y., Li, Y.-L., Gessmann, Th., and Schubert, E.F., "Influence of junction temperature on chromaticity and color-rendering properties of trichromatic white-light sources based on light-emitting diodes," J. Appl. Phys. 97, 054506 (2005).

[14] Cho, J., Sone, C., Park, Y., and Yoon, E., "Measuring the junction temperature of III-nitride light emitting diodes using electro-luminescence shift," Phys. Status Solidi A 202, 1869-1873 (2005).

[15] Keppens, A., Rychaert, W. R., Deconinck, G., and Hansalaer, P., "High power light-emitting diode junction temperature determination from current-voltage characteristics," J. Appl. Phys. 104, 093104 (2008).

[16] Xi, Y., Xi, J.-Q., Gessmann, Th., Shah, J. M., Kim, J.K., Schubert, E. F., Fischer, A. J., Crawford, M. H., Bogart, K. H. A. and Allerman, A. A., "Junction and carrier temperature in deep-ultraviolet light-emitting diodes using three different methods," Appl. Phys. Lett. 86, 031907 (2005).

[17] Wang, T., Bai, J., Sakai, S. and Ho, J. K.., "Investigation of the emission mechanism in InGaN/GaN-based light-emitting diodes," Appl. Phys. Lett. 78 (18), 2617-2619 (2001).

[18] Tziraki, M., Jones, R., French, P. M. W., Melloch, M.R. and Nolte, D. D., "Photorefractive holography for imaging through turbid media using low coherence light," Appl. Phys. B 70, 151-154 (2000).

[19] Kemper, B., Stürwald, S., Remmersmann, C., Langehanenberg, P. and v. Bally, G., "Characterization of light emitting diodes (LEDs) for application in digital holographic microscopy for inspection of micro and nanostructured surfaces," Optics and Lasers in Engineering 46, 499-507 (2008).

[20] Mehta, D. S., Saxena, K., Dubey, S. K. and Shakher, C., "Coherence characteristics of light-emitting diodes," Journal of Luminescence 130, 96-102 (2010).

[21] Saleh, B. E. A. and Teich, M. C., [Fundamentals of Photonics], John Wiley & Sons Inc., United States of America, 351-352 (1991).

Methods for Obtaining the Junction Temperature of LEDs

Reinhold Hetzel [*/**], Dipl.-Ing.,
Günther Leising [*], Univ.Prof.
Dipl.-Ing. Dr.tech.

* Institute of Solid State Physics,
Graz University of Technology,
Petersgasse 16, 8010 Graz, Austria

** LUMITECH Produktion und
Entwicklung GmbH,
Technologiepark 10,
8380 Jennersdorf, Austria

Abstract

The electrical and optoelectronic performance as well as the operation lifetime of electroluminescent devices are strongly linked to the temperature of the active region. This so called junction temperature is a key parameter regarding device lifetime and luminous efficacy. Furthermore, temperature changes throughout operation lead to spectral shifts and broadening of the emission spectrum which subsequently lead to changes of color temperature and color rendering index in white light LED systems. Therefore, understanding the behavior of the junction temperature and its monitoring are prerequisites to design and operate light engines with long lifetimes, high efficacies and excellent long term color quality.

Introduction

High efficiencies combined with long lifetimes make LED technology more and more becoming well established in a variety of fields and therefore LED lighting systems start to dominate the area of general illumination. Lifetime, efficiency, and reliability of electroluminescent devices are strongly linked to one important device parameter, namely the temperature of the LED device, to be more specific the temperature of the pn-junction volume. Moreover, optoelectronic properties are closely related to this so called junction temperature (JT). Shifts of the peak wavelength, broadening or narrowing of the emission spectra are the severe consequences of altering JTs. Hence during operation, variations of the JT lead to changes of the device characteristics i.e. color temperature and chromaticity coordinates. [1]

Due to chip encapsulation, in situ measurements of the junction temperature is practically not possible. There are several measuring methods which attempt to probe the temperature of the device (direct measuring (e.g. attached sensing elements) as well as indirect measurement (e.g. infra-red cameras)). However, most of them rather probe the temperature of the device environment than the actual junction temperature of the active region.

Our work is based on contactless methods for accurately deriving the junction temperature of LEDs in an assembled light engine under operation. Additionally we will show that the junction temperature can be obtained out of several externally accessible parameters (forward voltage, energy gap, etc.) on direct current (DC) and pulsed current driven devices.

This paper focuses on temperature measurement methods of electroluminescent devices and we will show a contactless measurement setup which allows to determine the JT of LED devices under operation [2 - 4]. Additionally we demonstrate the impact of the JT on optoelectronic properties.

Common Temperature Measurement Methods

There are several methods to determine the operation temperature of the device; however most of them rather probe the temperature of the device environment than the actual JT of the active region.

Direct measuring of the temperature using e.g. resistance thermometers or thermocouples leads to the problem that the temperature is measured outside of the place of interest. Hence the measured temperature is not equal to the JT due to the fact of a non-thermal equilibrium of the device environment and the die. Figure 1 shows the temperature of the device environment of an LED light engine measured with a K-type thermocouple (Nickel Chromium vs. Nickel Aluminum, reference temperature 0°C). The DC forward current of the device was 400 mA, 600 mA, and 1300 mA, respectively. The thermocouple was located on a heat sink next to the LED device which consists of four phosphor-converted-LEDs and two red-LEDs. After approximately 3000 seconds (60 minutes) a thermal equilibrium of the device environment is reached, however no conclusion about the actual JT of the active region of any of the LEDs can be drawn. Only the complete solution of the quite complex heat equation over the whole device area would give an estimate of the actual temperature distribution.

Very common and comfortable instruments for thermal measurements and heat flow determinations, are infra-red (IR) cameras. They are based on the fact that each object, which has a temperature higher than 0 K, emits IR radiation in a certain wavelength range which follows Planck radiation law. Advantages of IR cameras are that no direct

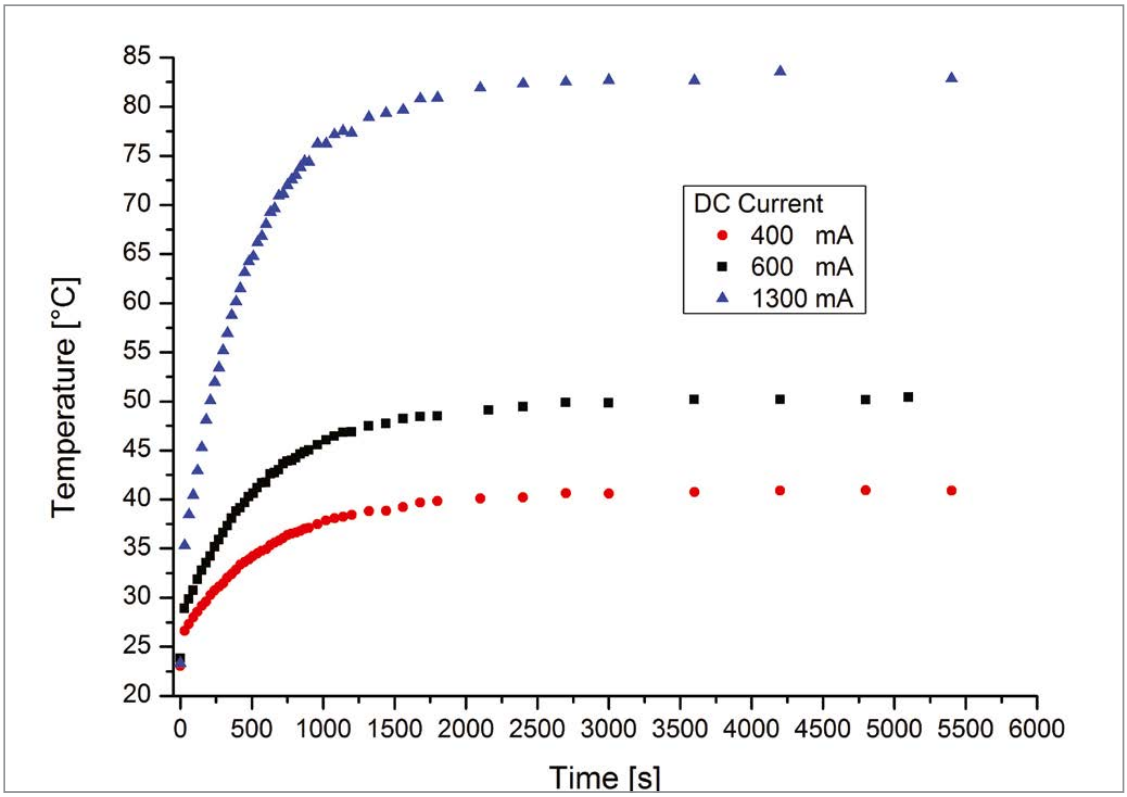

Figure 1: Temperature dependence vs. time of an LED module containing 4 phosphor converted and 2 red LEDs. Measurements were performed with a K-type thermocouple located on a heat sink next to the LED device

contact between the sample and the measurement system is needed.
Further due to the fast picture processing time, thermal images can be taken basically in real time and therefore fast temperature changes of the device can be followed.

However, imaging an LED covered with the generally used globe top leads to the problem that the IR radiation measured by the camera is strongly altered by the characteristic IR absorptions of the globe top polymer. Therefore, the specific transmission properties (complicated by the enharmonic behavior of the polymer hydrocarbons, overtones, combined resonances, etc.) of the globe top solid have to be taken into account. To gain accurate and correct temperature values, a calibration regarding the globe top transmission features is mandatory.

Theoretical Background

The theoretical background of the temperature dependence of the forward voltage and the energy gap can be obtained from Shockley equation (equation (1)) (following [2], [3] and [4])

$$J_f = J_s \left(e^{eV_f / nkT} - 1\right) \quad (1)$$

Where J_f expresses the diode current in forward direction, J_s the saturation current, V_f the forward voltage, n the diode ideality factor, k the Boltzmann constant, e the elementary charge, and T the absolute temperature. For $V_f \gg kT/e$, the -1 in equation (1) can be neglected and the derivative regarding temperature of the modified equation (1) leads to equation (2).

$$\frac{d}{dT} Vf = \frac{d}{dT} \left[\frac{nkT}{e} \ln\left(\frac{Jf}{Js}\right) \right] \quad (2)$$

The saturation current (equation (3)) can be expressed in terms of the intrinsic carrier concentration n_i, the diffusion constants of electrons D_n and holes D_p, the minority carrier lifetimes of electrons τ_n and holes τ_p as well as the donor density N_D and the acceptor density N_A, respectively.

$$J_s = e \left[\sqrt{\frac{D_n}{\tau_n}} \frac{n_i^2}{N_D} + \sqrt{\frac{D_p}{\tau_p}} \frac{n_i^2}{N_A} \right] \quad (3)$$

The intrinsic carrier concentration n_i is given by

$$n_i = \sqrt{N_C N_V} e^{\frac{-E_g}{2kT}}$$

where N_C and N_V are the effective density of states at the conduction and valence band edges

$$N_C = 2 \left(\frac{2\pi m_e kT}{h^2} \right)^{\frac{3}{2}}$$

$$N_V = 2 \left(\frac{2\pi m_h kT}{h^2} \right)^{\frac{3}{2}}$$

Taking into account the temperature dependence of the diffusion constants of electrons and holes $(D \propto T^{1/2})$, the effective density of states at the valence and conduction band edge $(N_{C,V} \propto T^{3/2})$, the band gap energies as well as the lifetimes of electrons and holes lead to equation (4):

$$\frac{d}{dT} Vf = \frac{eV_f - E_g}{eT} + \frac{1}{e} \frac{d}{dT} E_g - \frac{3k}{e} \quad (4)$$

This relationship reflects the fundamental temperature dependence of the forward voltage. It is the starting point in order to characterize the JT of a pn-junction.
The first term on the right hand side is due to the temperature dependence of n_i, the second term expresses the temperature dependence of the energy gap, the third summand occurs due to the temperature dependence of N_C and N_V.

The band-gap energy is given by

$$E_g = E_{T=0K} - \frac{\alpha T^2}{\beta + T}$$

where α and β are the Varshni parameters.

Experimental Setup

The principle parts of the measurement setup are shown in figure 2. The measurement of the emission spectra and the driving parameters were performed in thermodynamic equilibrium in a chamber oven with precise temperature control (Weiss – Vötsch VT4002). The temperature range was set between -40°C to 120°C with an accuracy of 0.1°C. One additional PT 100 resistor was mounted on a separate heat sink which was located in the oven to ensure the predetermined oven temperature. Before the measurements were performed, the samples were stored for at least 30 minutes in the chamber to guarantee the thermodynamic equilibrium of the devices. To avoid icing effects, the temperature oven was flushed with dry air during the whole experiment.

To probe the LED device it must be driven in a manner that there is a negligible temperature increase due to the driving power. Therefore, the LED device is operated with a current which is generated by voltage pulses with a very small duty cycle (0.1%, pulse width = 500 ns, repetition time = 500 µs). Consequently, we can assume that the JT is equal to the measured oven temperature. Voltage pulses were produced with a pulse generator (HP 214 B); using a series resistance Rs the forward current of the device was determined (the series resistance was selected individually: 9.78 Ω for 20 mA & 50 mA, 19.52 Ω for 100 & 150 mA or 46.31 Ω for 300 & 500 mA, respectively).

The voltage pulses were logged with a digital oscilloscope (Hameg HMO 3524).
The emission spectra were recorded with a CCD spectrometer (Thorlabs CCS 100) containing a grating with 1200 lines per mm, blazed at 500 nm. An aperture in front of the entrance slit of the spectrometer was used to define the acceptance angle ($\alpha = 5.72°$). The current-voltage characteristics were measured with a Keithley 2601B source measure unit.

AlGaInP red LED dice on a sapphire substrate (chip dimension 300 µm x 300 µm, Au electrodes) with a nominal dominant wavelength at room temperature between 610 nm and 620 nm were used. Through a thin 30 µm Au bonding wire the devices were connected to a circuit board. To ensure high heat dissipation the devices were mounted with thermally conducting paste on a heat sink (L = 5 mm, B = 6.3 mm, H= 4.8 mm).

Figure 3 shows the AC equivalent circuit of the measurement setup. Due to the narrow width of the voltage pulses (high frequency components), capacitances as well as the inductances of the coax cable and of the circuit board have to be considered. Furthermore, we also distinguish between horizontal as well as vertical resistances in the diode. The current Id in figure 3 represents four current components namely the leakage current, the radiative current, the non-radiative current as well as the carrier-overflow current [5].

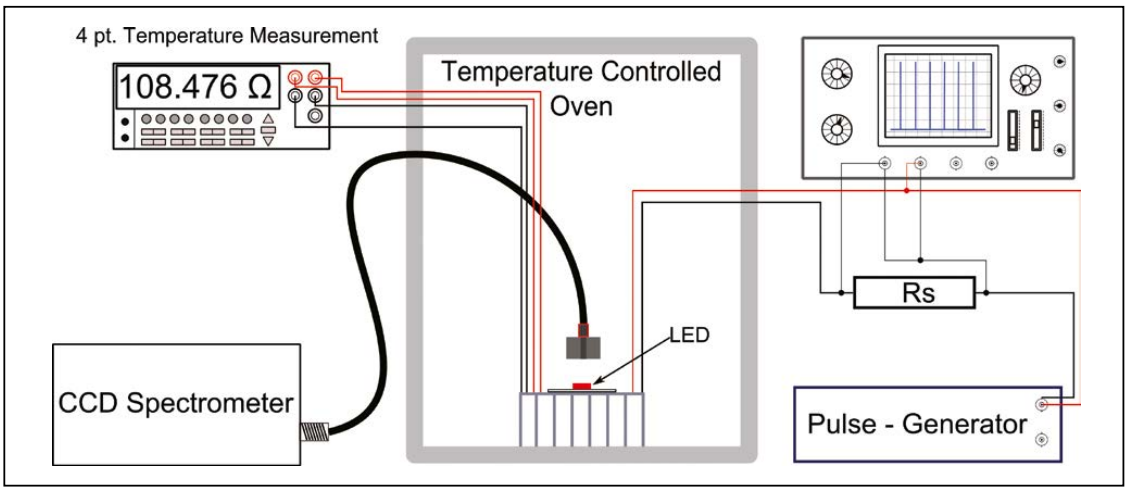

Figure 2: Measurement setup for determining the calibration curve for evaluating the JT

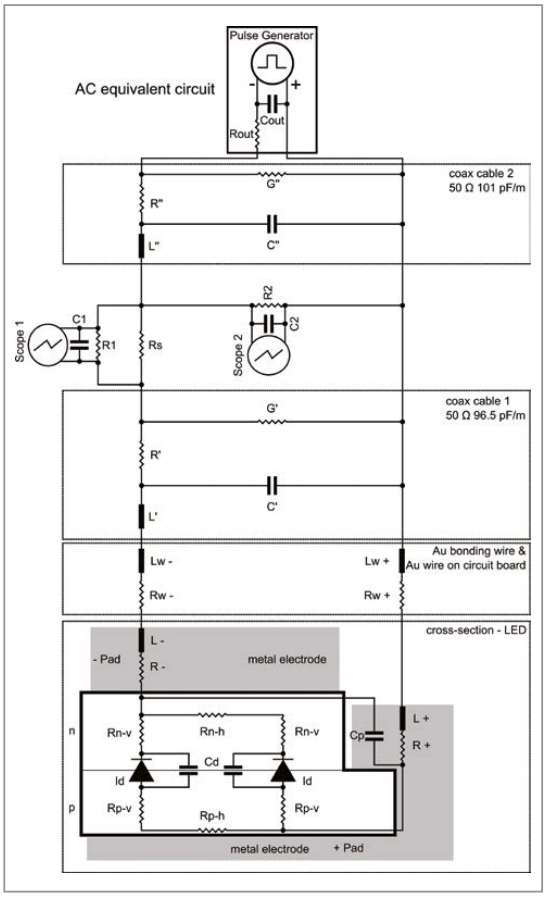

Figure 3: AC equivalent circuit of the measurement setup. The description of the denotation used in figure 3 can be found in table 1.

Table 1: Explanation of the denotation used in figure 3

R + / R -	Resistance of metal electrode of LED
L + / L -	Inductance of metal electrode of LED
Rn-v / Rp-v	Vertical resistance of the p-type / n-type semiconductor material
Rn-h / Rp-h	Horizontal resistance of the p-type / n-type semiconductor material
Id	Current components
Cd	Conductance occurring from the depletion zone
Cp	Conductance occurring from the electrodes (pads)
Rw + / Rw -	Resistance of Au bonding wire & Au wire on circuit board
Lw + / Lw -	Inductance of Au bonding wire & Au wire on circuit board
Rs	Series resistance for forward current determination
R' / R''	Resistance of coax cable 1 (') / 2 ('')
L' / L''	Inductance of coax cable 1 (') / 2 ('')
C' / C''	Capacitance of coax cable 1 (') / 2 ('')
G ' / G''	Conductance of the dielectric material between inner and outer conductor of coax cable 1 (') / 2 ('')
R1 / R2 / Rout	Input (output) resistances of scope 1(R1) / 2 (R2) / pulse generator (Rout)
C1 / C2 / Cout	Input (output) capacitances of scope 1 (C1) / 2 (C2) / pulse generator (Cout)

The DC equivalent circuit is much more simple and is derived from the AC equivalent circuit because neither capacitances nor inductances play a significant role and therefore just resistances have to be taken into account.

Results

Figure 4 shows the effects of the JT on the driving parameters of the diode. In the low temperature region (< 20°C), JT changes have greater impact on the driving parameter compared to the high temperature region (> 20°C). Hence the broadly proposed linear behavior of the forward voltage with respect to temperature does not apply anymore for such large temperature ranges (160 K).

Figure 5 (on page 200) illustrates the effect of the JT on the spectral behavior of the red LED for a pulsed current of 50 mA. The emission peak shifts between 610 nm at - 40°C to 632 nm at 120°C. The dashed line in figure 5 shows the sensitivity dependence of the L cone of the human eye (Styles and Burch [6]). It follows that a peak wavelength shift of 30 nm corresponds to a subjectively perceived change of brightness of around 50 % in this wavelength range.

Figure 6 shows the linear change of the full width at half maximum (FWHM) with respect to temperature and injected pulsed current over the whole temperature region.

As indicated in figure 7 (on page 200) the peak wavelength shifts linear with temperature (0.14 nm/K) and additionally it is independent of the pulsed driving current. This behavior proofs that the injected pulsed current does not influence the JT. For comparison figure 7 shows the intensity drop of the red LED with respect to temperature. The results are referred to the measurement performed at 20°C. Out of this data one can extract that the impact of the JT on the device performance is rather affected by temperatures above 20°C compared to temperatures below 20°C, respectively.

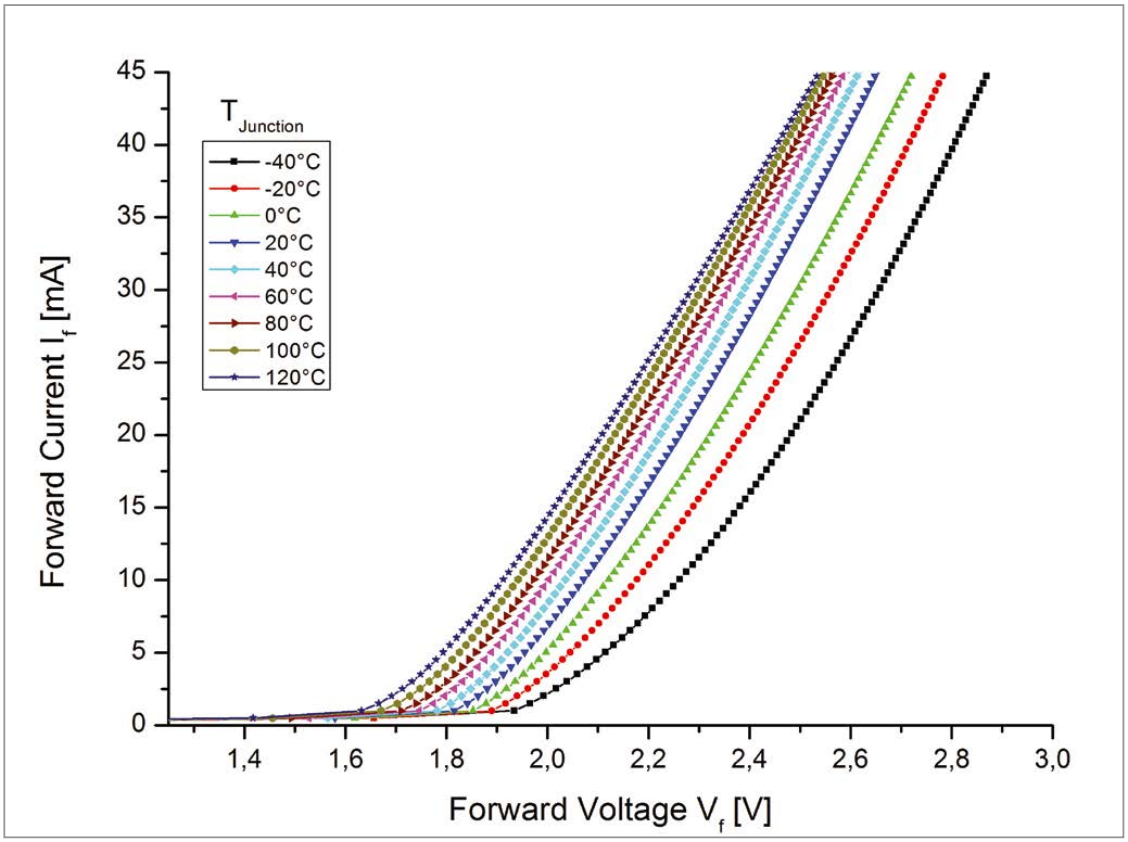

Figure 4: I-V characteristic of a red LED as function of temperature

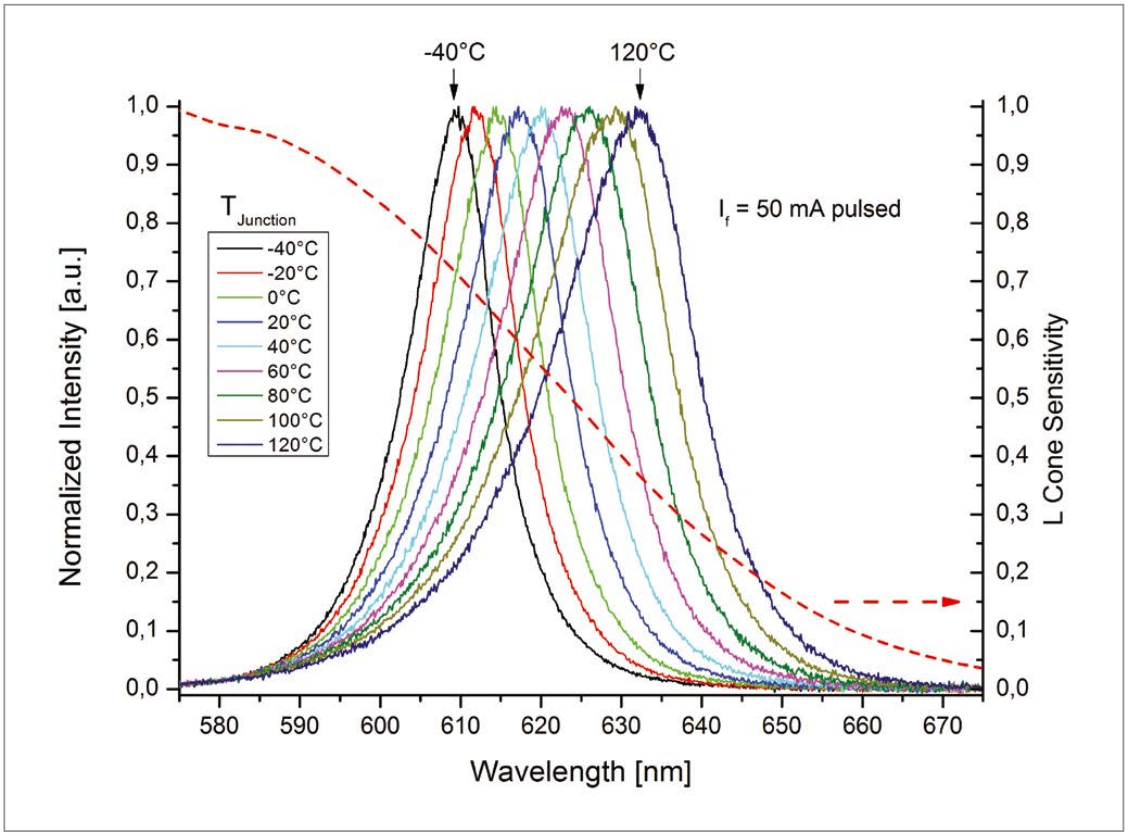

Figure 5: Spectral distribution with respect to temperature as well as L cone sensitivity curve

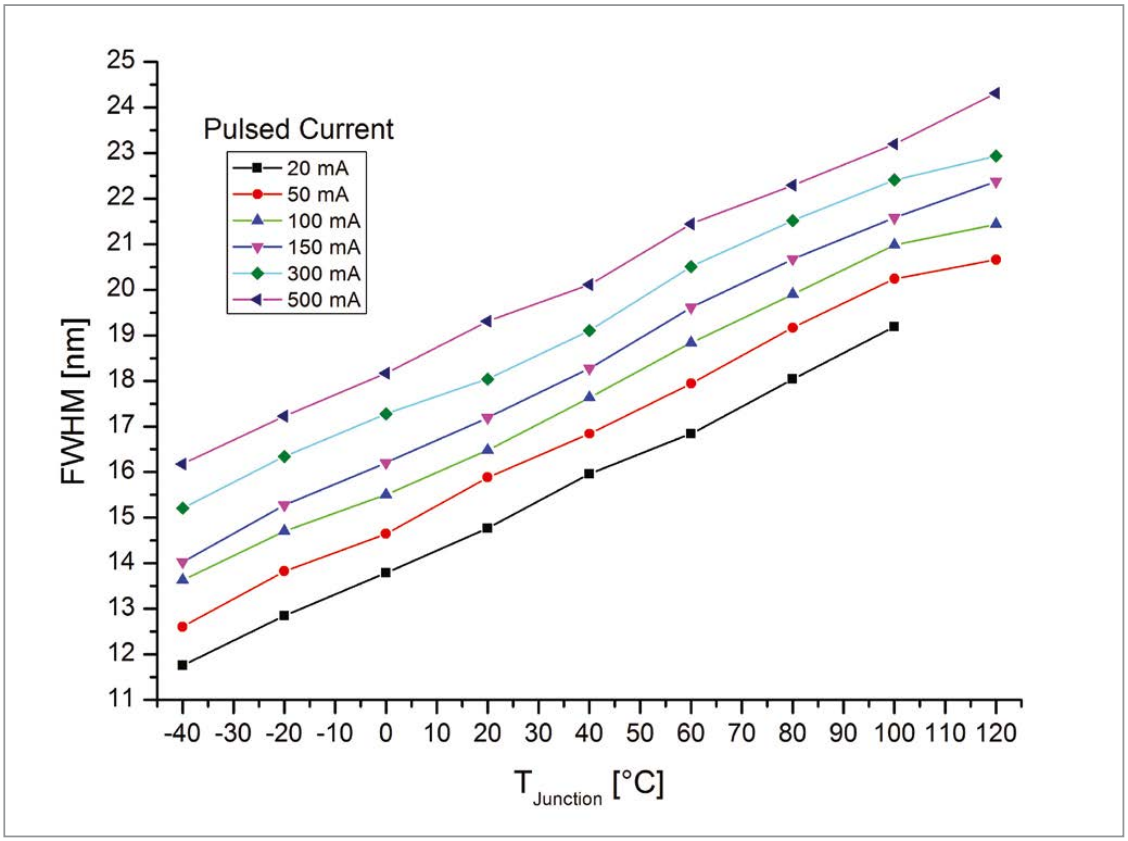

Figure 6: Dependence of the FWHM with respect to temperature and injection pulsed current

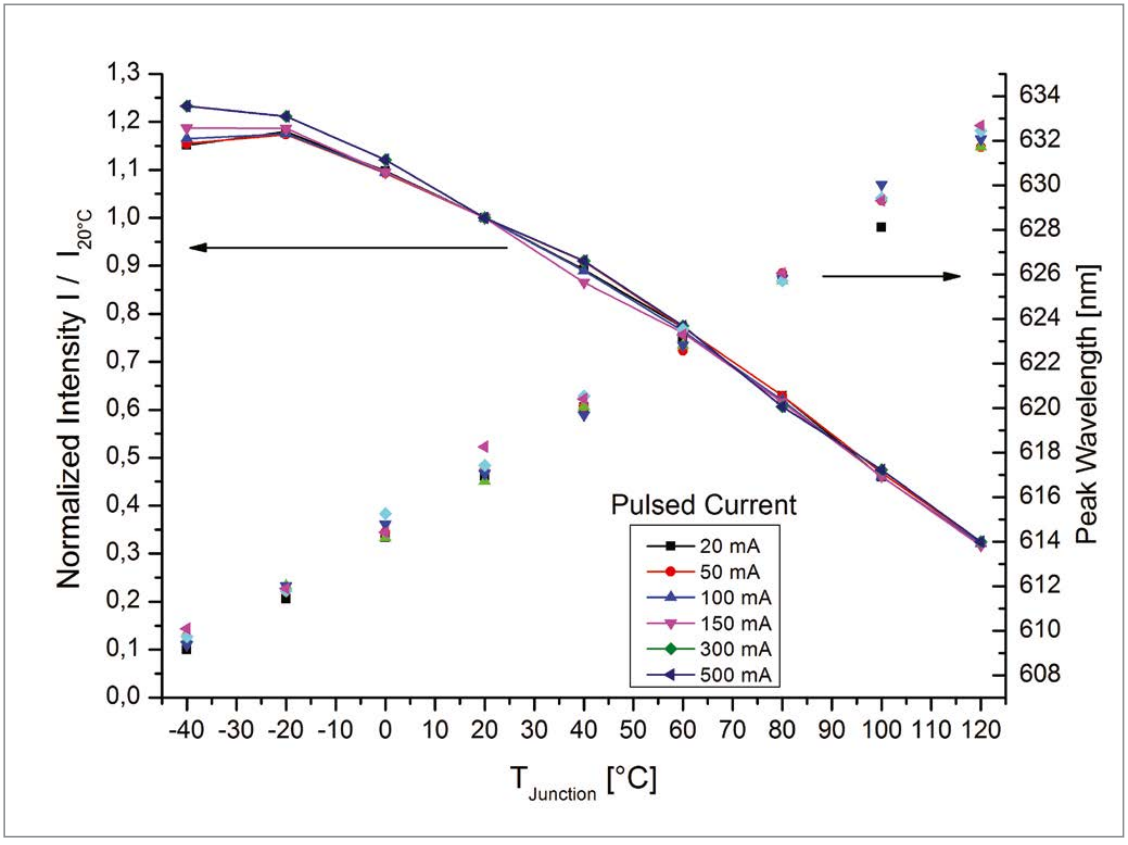

Figure 7: Peak wavelength and normalized intensity with respect to temperature of a red LED

With this gained spectral information the JT of an electroluminescent device during operation can be determined. Measuring of the forward voltage and the emission spectra during operation and the combination of the temperature behavior of the forward voltage/emission spectra obtained out of the calibration data, the actual JT of the device can be extracted. This approach is independent of the designated driving conditions of the device (pulsed current, pulse width modulation or DC).

Conclusion

All the well-known advantages of LED technology could only be harvested if the thermal management is totally under control. As shown in this paper, temperature changes lead to spectral changes (e.g. wavelength shifts, spectral broadening/narrowing) as well as intensity changes which directly effect the color temperature and the chromaticity coordinates of the device. We showed that out of the spectral information the actual JT during operation can be obtained.

Precise measurements of the temperature of the active region are a prerequisite for understanding the temperature behavior of LEDs and therefore allow providing light engine design with high efficiencies, long lifetimes as well as high quality light in terms of stable color temperature and color rendering.

All the above mentioned measures to extend energy efficiency, life expectancy and consumer comfort of LED lamps could be combined to create a superior product and to support a major breakthrough in solid state lighting on a broader basis - some at a higher cost but some even cost saving especially in terms of energy consumption, maintenance and payback with all the ecological side aspects of fossile resources, carbon footprint and climate. 300 lm/W efficiencies seem to be within reach and have the potential of cutting lighting energy consumption from 20% down to 1% off today's electric energy bill. All the intelligence required to take care of complex monitoring and control functions could be packed into very compact basic ultra low power microcontrollers at minimal cost. It doesn't take magic but a certain conceptual pradigm shift at the design, engineering, manufacturing, sales and last-not-least consumer level and should be worth the effort. ■

References:

[1] Hetzel et al., 2012, Tunable natural light realized by phosphor-innovation light-emitting-diode technology, e & i Elektrotechnik und Informationstechnik, 7-8, pp.460-465

[2] Xi et al. (2005). Junction temperature in ultraviolet light-emitting diodes. Japanese Journal of Applied Physics Part 1-regular Papers Brief Communications & Review Papers, 44(10), pp. 7260-7266

[3] Xi et al. (2005) Junction and carrier temperature measurements in deep-ultraviolet light-emitting diodes using three different methods. Applied Physics Letters, 86(3), 031907

[4] Xi et al. (2004). Junction-temperature measurement in GaN ultraviolet light-emitting diodes using diode forward voltage method. Applied Physics Letters, 85(12), pp. 2163-2165

[5] Masui et al., 2008, Equivalent-Circuit Analysis for the Electroluminescence-Efficiency Problem of InGaN/GaN Light-Emitting Diodes, Japanese Journal of Applied Physics, Vol. 47, No54, pp. 2112-2118

[6] Based on the Stiles & Burch 10-deg CMFs (adjusted to 2-deg), Color and Vision Research Labs, accessed 18.06.2013

